BRNO UNIVERSITY OF TECHNOLOGY

VYSOKÉ UČENÍ TECHNICKÉ V BRNĚ

CENTRAL EUROPEAN INSTITUTE OF TECHNOLOGY BUT

STŘEDOEVROPSKÝ TECHNOLOGICKÝ INSTITUT VUT

QUANTITATIVE COMPUTED TOMOGRAPHY

KVANTITATIVNÍ POČÍTAČOVÁ TOMOGRAFIE

DOCTORAL THESIS
DIZERTAČNÍ PRÁCE

AUTHOR   Ing. Jakub Šalplachta
AUTOR PRÁCE

SUPERVISOR   prof. Ing. Jozef Kaiser, Ph.D.
ŠKOLITEL

BRNO 2022

Summary

The main aim of this thesis is to study, explore and possibly move further the field of quantitative computed tomography (QCT) with specific focus on a laboratory-based submicron computed tomography (CT) system Rigaku nano3DX. This work is dealing with both aspects of the QCT, which are the acquisition of quantitative CT data and the utilization of CT data for quantitative analysis. Regarding the first aspect, specific focus is placed on assessment of current technological limits of submicron CT, where the technology-based tomographic artifacts are studied, and optimal reduction strategies are proposed. Also, practical aspects related to implementation of spectral CT in a form of dual-target CT (DTCT) using Rigaku nano3DX system, are solved by development of dedicated acquisition and data registration methodologies. For the quantitative analysis of CT data, two novel methods were developed. One was specifically designed for porosity analysis of additive manufactured samples with a respect to the crucial points of tomographic data processing, making it objective and reproducible. Second method was specifically designed for quantitative assessment of 3D models of biological tubular systems and was practically tested on a mouse model of Alagille syndrome.

Abstrakt

Hlavním cílem této práce je prostudovat, prozkoumat a případně posunout dále oblast kvantitativní počítačové tomografie (QCT) se specifickým zaměřením na laboratorní submikronový CT systém Rigaku nano3DX. Tato práce se zabývá oběma aspekty QCT, kterými jsou akvizice kvantitativních CT dat a využití CT dat pro kvantitativní analýzu. Pokud jde o první aspekt, specifický důraz je kladen na posouzení současných technologických limitů submikronového CT, kde jsou studovány tomografické artefakty způsobené právě technickými nedostatky a navrženy optimální redukční strategie. Také praktické aspekty spojené s implementací spektrálního CT ve formě dual-targetového CT (DTCT) pomocí systému Rigaku nano3DX jsou řešeny vývojem specializovaných metodologií pro akvizici a registrace dat. Pro kvantitativní analýzu CT dat byly vyvinuty dvě nové metody. Jedna z metod byla speciálně navržena pro analýzu porosity vzorků vyrobených metodou 3D-tisku a to s ohledem na klíčové aspekty zpracování tomografických dat, díky čemuž je tato metoda objektivní a reprodukovatelná. Druhá metoda byla speciálně navržena pro kvantitativní hodnocení 3D modelů biologických tubulárních systémů a byla prakticky testována na myším modelu Alagilleova syndromu.

Keywords

Quantitative Computed Tomography, QCT, CCD, sCMOS, tomographic artifacts reduction, dual-energy CT, porosity analysis, 3D models analysis

Klíčová slova

Kvantitativní počítačová tomografie, QCT, CCD, sCMOS, redukce tomografických artefaktů, duálně-energiové CT, analýza porosity, analýza 3D modelů

Rozšířený abstrakt

Hlavním cílem této práce je prostudovat, prozkoumat a případně posunout dále oblast kvantitativní počítačové tomografie (QCT) se specifickým zaměřením na laboratorní submikronový CT systém Rigaku nano3DX. Tato práce se zabývá oběma aspekty QCT, kterými jsou akvizice kvantitativních CT dat a využití CT dat pro kvantitativní analýzu. Tyto aspekty souvisí i s praktickou implementací metody spektrálního CT (více-energetického CT), jejímž cílem je celkové zvýšení kvality a přesnosti CT zobrazování a také implementace pokročilých kvantifikačních nástrojů pro charakterizaci analyzovaných vzorků.

Z hlediska prvního aspektu, specifický důraz je kladen na posouzení současných technologických limitů submikronového CT, kde jsou studovány tomografické artefakty způsobené právě technickými nedostatky a navrženy optimální redukční strategie. Nejprve byl nalezen optimální rekonstrukční proces pro submikronová CT data s využitím metody analytické rekonstrukce s optimalizovaným nastavením respektujícím dosažitelné prostorové rozlišení a kvalitu dat. Následně byly studovány tomografické artefakty související s technologickými limity, kdy byly studovány jejich jednotlivé příčiny a vlastnosti a byly navrženy optimální strategie redukce. Bylo zjištěno, že některé z nejvýznamnějších artefaktů z této skupiny – šum a kruhové artefakty, souvisejí se samotným detekčním systémem. Proto byly pro úlohu submikronové CT akvizice posouzeny tři typy detektorů a porovnány z hlediska kvality a přesnosti získaných dat a výsledky byly dále zapracovány do navržených redukčních postupů. Konkrétně byly vyvinuty nové postupy pro redukci kruhových artefaktů a potlačení všech typů šumu přítomných v datech z Rigaku nano3DX. Řešení redukce šumu konkrétně zahrnuje nové algoritmy pro redukci impulsního šumu a pro odhad absolutní odchylky šumu, a prakticky otestované nejmodernější metody pro redukci složky „shot" šumu. Dedikované řešení bylo také vyvinuto pro nestabilitu a nepřesnost rotační stage při submikronovém CT snímání. Tento vývoj zahrnoval také studium této nestability z hlediska tepelné závislosti a také v kontextu komerčních laboratorních CT systémů.

Pro řešení spektrálního zobrazování a jeho implementace pro získávání submikronových CT dat pomocí Rigaku nano3DX byly vyvinuty specializované metodiky akvizice a registrace DTCT dat. Z hlediska akvizice byl definován nový postup pro výběr optimálních parametrů měření pomocí vlastností šumu jako hodnotící metriky. Pro úlohu registrace byl použit vyvinutý držák vzorku s referenční oblastí, kdy výsledkem je plně automatické, robustní řešení s vysokou přesností. Pro kvantitativní analýzu CT dat byly vyvinuty dvě nové metody. Jedna z metod byla speciálně navržena pro analýzu porozity vzorků vyrobených metodou 3D-tisku a to s ohledem na klíčové aspekty zpracování tomografických dat, díky čemuž je tato metoda objektivní a reprodukovatelná. Druhá metoda byla speciálně navržena pro kvantitativní hodnocení 3D modelů biologických tubulárních systémů a byla prakticky testována na myším modelu Alagilleova syndromu.

I declare that I carried out this doctoral thesis *Quantitative computed tomography* independently, and only with the cited sources, literature and other professional sources.

Ing. Jakub Šalplachta

Table of Contents

Introduction

X-ray Computed Tomography (CT) is an imaging method used for a non-destructive evaluation (NDE) of internal structures of a sample. Although this technique was originally developed for medical applications, in the last decades it has been also utilized in various industrial and scientific fields. In principle, a set of projection images is acquired from various angles of a sample's rotation by X-ray beam illumination and detection of the attenuated radiation after sample passing. From such measured data, a 3D sample's information is retrieved using a reconstruction algorithm. The resulting CT data can be then utilized for various purposes from visualization to dedicated analysis of sample's properties – e.g., morphology, voids and pores detection, material properties and distribution etc. Especially in the recent years, the technical progress in field of high-resolution CT (referring to achievable spatial resolution on micron or submicron level) enabled utilization of this technique for quantitative analysis or as a dimensional metrology tool. [1; 2; 3]

However, CT technique suffers from many limitations of an acquisition process itself. The polychromatic nature of X-ray radiation used in standard CT scanners is responsible for dependence of attenuation properties of any sample's compound not only on its density and chemical composition but also on used CT system parameters and settings and moreover on the surrounding materials. Moreover, the accuracy of CT data can be further distorted by various tomographic artifacts. All those effects together distort the reliability and accuracy of resulting CT data. The main objective of Quantitative CT (QCT) is then a quantitative measurement of sample's properties based on undistorted attenuation information that is solely dependent on its internal composition. In industrial or scientific sphere of CT, these characteristics can, for instance, be: dimensional measurements [4], fibre's orientations [5], porosity analysis [6] or other parameters characterizing structures or material properties of given sample. The application of a high-resolution CT has already proven its applicability and benefits in various fields from R&D to basic research.

However, aiming for higher spatial resolution and implementation of advanced CT techniques (e.g., 4D CT or spectral CT), brings strict requirements for both the hardware and the software. Moreover, the crucial task for every technique used for any metrological assessment is determining measurement uncertainty, which requires analysis of all critical error sources. In recent years, spectral imaging methods (also known as multi-energy CT or dual-energy CT) have remerged in CT practise, that aim to increase the overall accuracy and quality of CT imaging and to practical implementation of advanced quantification tools for sample's characterization. However, practical implementation of spectral CT was lagged by the technological limits that were not solved up to recent years. Especially in sphere of high-resolution CT, the possibility of acquisition of undistorted CT data and its' further quantitative analysis is still highly limited by various technological aspects and lack of dedicated methodologies and correction solutions.

The main aim of this thesis is to study, explore and possibly move further the field of quantitative computed tomography (QCT) with specific focus on a laboratory-based submicron computed tomography (CT) system Rigaku nano3DX. This work is dealing with both aspects of the QCT, which are the acquisition of quantitative CT data and the utilization of CT data for quantitative analysis. Regarding the first aspect, specific focus is placed on an assessment of current technological limits of submicron CT, where the technology-based tomographic artifacts are studied, and optimal reduction strategies are proposed. Also, practical aspects related to implementation of spectral CT in a form of dual-target

CT (DTCT) using Rigaku nano3DX system, are solved by development of dedicated acquisition and data registration methodologies. For the quantitative analysis of CT data, two novel methods were developed. One was specifically designed for porosity analysis of additive manufactured samples with a respect to the crucial points of tomographic data processing, making it objective and reproducible. Second method was specifically designed for quantitative assessment of 3D models of biological tubular systems and was practically tested on a mouse model of Alagille syndrome.

Presented thesis can be divided into six main parts. In the first part, a theoretical background and literature review regarding the thesis topic is given. The focus is placed on subsection regarding tomographic reconstruction and technology-based tomographic artifacts, where existing solutions for their reduction are presented. Subsequently the aims of this thesis are described in more details. Following chapter contain description of CT devices, software and CT data quality assessment metrics used within scope of this work. Next three chapters contain overview and description of outcomes that have been achieved within the aims of this thesis. These are mainly focused on assessment of technology-based tomographic artifacts and development of dedicated reduction approaches. Further, the practical implementation of dual-target CT using Rigaku nano3D system is presented focused on development of dedicated acquisition and data registration methodologies. For the quantitative analysis of CT data, two novel methods are presented for porosity analysis of additive-manufactured samples and for analysis of 3D models of biological tubular systems.

1 Literature review and state of the art

In this chapter principles of CT technique as imaging modality are described with specific focus on X-ray radiation and its origin, X-ray detection and the process of tomographic reconstruction. This part is followed by description of limitations of CT acquisition process and corresponding tomographic artifacts. The last part is then dedicated to concept of QCT and spectral imaging with focus on material's decomposition.

1.1 X-ray computed tomography

Although the CT technology has undergone extensive development since the construction of the first CT device in 1971, the workflow of standard CT process and the core components of any CT device still remain the same. Those components are an X-ray source, a sample's stage and a detection system. Within the standard CT process, any CT measurement is followed by process of tomographic reconstruction and as final step the CT data are further processed in terms of data visualization and analysis. The principle of standard CT measurement is based on placing a sample between an X-ray source and a detection system and measuring the intensity of X-ray radiation after passing through the sample at various angular positions – this information is then recorded on detector in form of 2D projection images. Here two options are possible: either a rotation of source-detector pair around a static sample (predominantly in medical sphere of CT) or a rotation of the sample in between a static source and detector, where dedicated rotation sample's stages are used. After the set of projections is recorded the tomographic reconstruction takes place to retrieve 3D information about the sample. [1; 2; 3] In following sub-sections, the technical details of core CT components and process of tomographic reconstruction are explained in more details.

1.1.1 X-ray generation and X-ray spectra

X-ray radiation, like the visible light, is part of the electromagnetic spectrum. The energy *E* of X-ray photons is proportional to their frequency *f*, which is expressed by the following equation:

$$E = hf = \frac{hc}{\lambda},$$

(1-1)

where *h* is Plank's constant (6.626 · 10^{-24} *J·s*), *c* is the speed of light (2.998 · 10^8 ms^{-1}), and *λ* is the wavelength of the X-ray [7]. The characteristic wavelength of X-rays ranges from 0.01 to 10 nm, which corresponds to the interval of energies 100 eV – 100 keV. Based on the wavelength and the ability to penetrate through the matter, the X-rays can be classified as either "soft X-rays" (*λ* > 0.1 nm) or "hard X-rays" (*λ* < 0.1 nm). [7]

X-rays can be generated by means of various sources, within the scope of this work the principle of the most used source, an X-ray tube, will be further explained. The main components of an X-ray tube are a cathode and an anode (target), that are placed in the evacuated tube (see Figure 1). Electrons are emitted from a cathode consisting of a heated filament (usually made from tungsten or molybdenum) and further accelerated by an electrical field. The strength of the electrical field and the resulting energy of the electrons are determined by the tube voltage (usually within the interval of 30 kV-450 kV). The trajectory of the emitted electrons is then focused to hit the anode in a small region called focal spot. In the focal spot, the electrons interact with the target material, when most of their energy (over 99%) is dissipated as heat. Therefore, the tube design must ensure a very efficient cooling of the anodes. To fulfil such demand, rotating anodes were designed, where energy of the electron

beam is distributed on circular focal path. As the target materials, metals with high density and heat resistance are used, usually tungsten, molybdenum, or others. [1; 7]
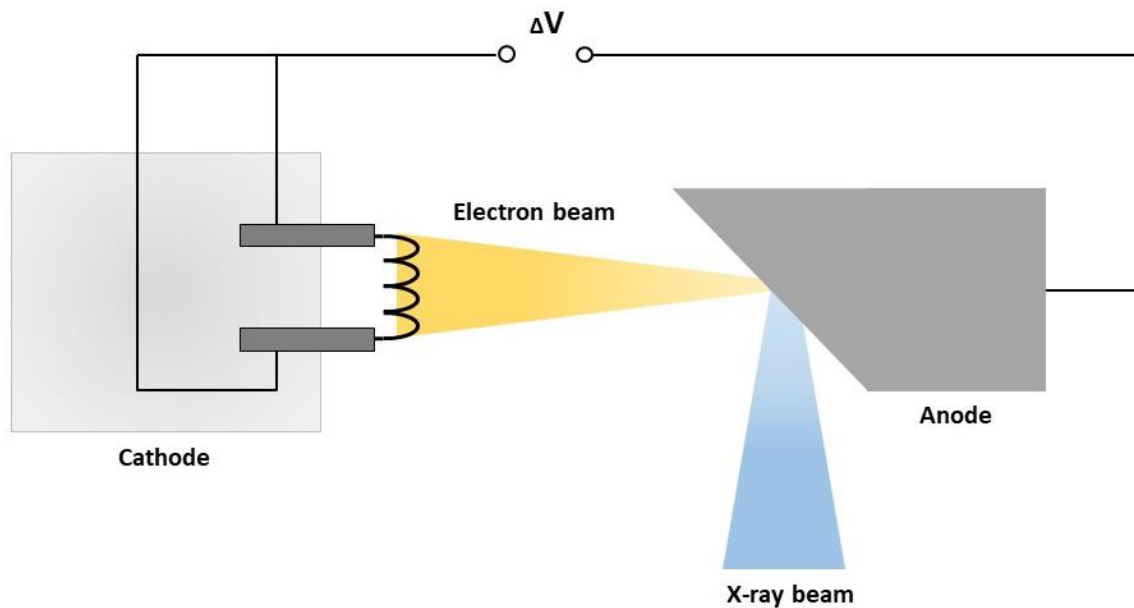
Figure 1: Illustrative scheme of an X-ray tube.

The remaining 1% of the energy is converted into X-rays. The fast electrons are decelerated in the atoms of anode material, in very proximity of their nuclei, and breaking radiation is emitted (also called as "Bremsstrahlung"). The accelerated electrons can also directly collide with the inner shell electrons of the target and knock them out from their atomic shell. Therefore, an atom is left ionized and in excited state. The vacant place is immediately filled by an electron transition from a more energetic shell. During these transitions, the photons with discrete characteristic energies (equal to the energetic differences between the shells) are emitted, which is referred as characteristic spectrum, which is unique for every material. The resulting X-ray spectrum is then a mixture of the Bremsstrahlung and the characteristic spectrum (see Figure 2). [1; 7]

The X-ray energy spectrum impacts the manner of the X-ray attenuation and can be affected by several factors: acceleration voltage, tube current, target material, filtration, and anode angle (see Figure 2). The acceleration voltage determines the energy interval and the amplitude, controlling both the "quality" and "quantity" of the X-ray beam (i.e., increasing tube voltage shifts the X-ray spectrum to the higher energies affecting penetration of a sample). On contrary, the tube current has no effect on the energy interval, but linearly affects the X-ray intensity (i.e., number of emitted X-ray quanta) and the size of focal spot. The characteristic part of the X-ray spectra is material specific and can be then controlled by used target material. The resulting X-ray spectra can be further affected by means of a filtration of the X-ray beam, which is used to modify the spectra for specific applications. In general, flat metal filters (Al, Cu, Mo, etc.) with specific thickness are placed between the X-ray source and the sample, to absorb the low-energy X-rays. This part of X-ray spectra has no contribution to the detected signal, because such X-rays are completely absorbed by the sample itself. Therefore, the filtration is beneficial for reduction of artifacts originating from the polychromatic X-ray radiation – e.g., beam hardening. Lastly an anode angle together with the tube current can control size of the focal spot. This factor important since it has direct influence on achievable spatial resolution and quality of detected signal. [7]
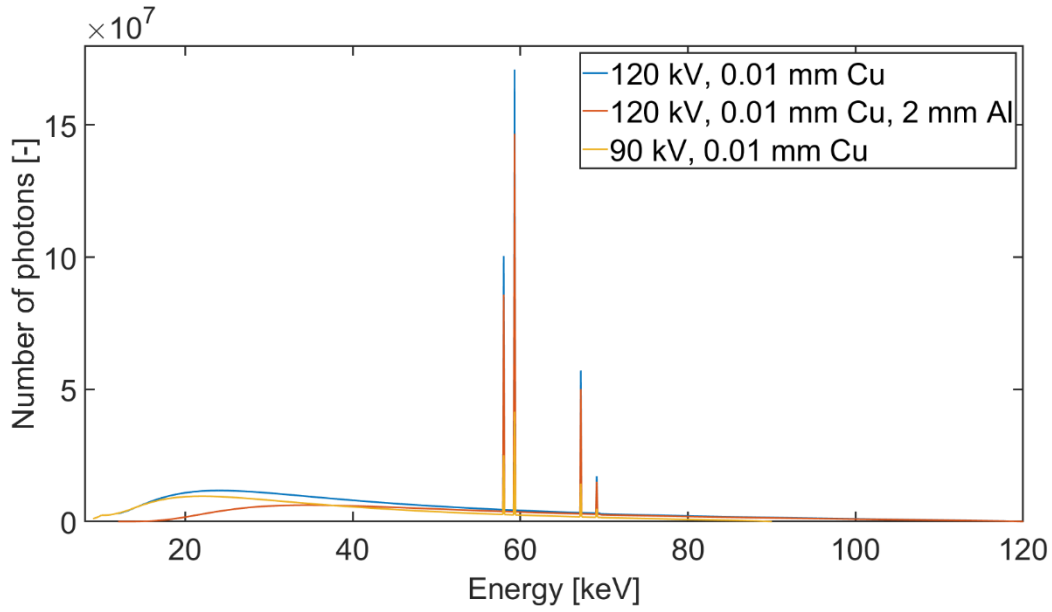
Figure 2: Example of X-ray spectra generated by tungsten target with 120 kV and 90 kV acceleration voltages and filtration using 0.01 Cu and 2 mm Al plates. For the simulations the Spekcalc software [8] was used.

1.1.2 Interaction of X-rays with matter

When X-rays pass through matter, the intensity of the X-ray beam is exponentially reduced due to changes in the number, energy, and direction of the incoming photons [7]. This process is called the attenuation and is expressed by linear attenuation coefficient μ. For monochromatic radiation and a homogeneous sample, the intensity I after sample's passing (also called transmission) is given by Beer-Lambert law:

$$I = I_0 exp(-\mu x) , \tag{1-2}$$

where I_0 is incident X-ray intensity and x is material thickness. This equation can be further adapted to consider positional dependency of μ along the linear path L and the polychromatic X-ray radiation:

$$I(L) = \int_0^{E_{max}} I_0(E) \exp\left(-\int_L \mu(E,x)dx\right), \tag{1-3}$$

where E is the energy of X-rays. Previous equation can be rearranged into line integral form for given energy E:

$$-log\frac{I(E)}{I_0} = \int_L \mu(E,x)dx, \tag{1-4}$$

and using substitution we can acquire form:

5

$$b = -\ln\frac{I}{I_0},$$

(1-5)

where quantity b is called the absorption.

The attenuation of a material is dependent on its mass density and chemical composition. Different physical mechanisms contribute to this process when individual contributions of these mechanisms are non-deterministic and depend on the energy of the X-ray beam (see Figure 3). The four primary interactions between the X-rays and the matter are [7]:

- **Photoelectric effect**
  This effect occurs, when incident photon has a higher energy E_p than the binding energy E_b of the atomic electrons in the irradiated sample [7]. Absorbing such photon, a photoelectron from a lower shell is ejected with kinetic energy E_k equal difference between E_p and E_b. The hole in the lower shell is immediately refilled by an outer shell electron and a characteristic fluorescence photon is emitted with energy equal an energy difference between the two electron levels involved. When such energy is high enough, an Auger electron can be further ejected. Photoelectric effect dominates at lower X-ray energies – below 50 keV (see Figure 3), and its probability depends on the atomic number Z of the sample. [7] [9]

- **Compton (incoherent) scattering**
  This type of interaction occurs, when a photon has considerably higher energy E_p than the binding energy E_b of the atomic electrons in the irradiated sample [7]. The incident photon ejects the electron from the atom but continues its movement with lower energy (i.e., higher wavelength) and different direction due to the scattering/deflection. The angle of scattering is dependent on the energy E_p – higher the energy smaller the angle. In general, this effect is predominant for higher X-ray energies (see Figure 3) and its probability depends on the electron density of the sample. [7] [9]

- **Rayleigh/Thompson (coherent) scattering**
  Rayleigh (or Thompson) scattering occurs when low-energy photons interact with atomic electrons in the irradiated sample by oscillation. This results into elastic scattering when photons with same energy but different direction are emitted. Compared to the Compton scattering or the Photoelectric effect, no energy is transferred, and no ionization takes place during this interaction. Rayleigh scattering is important only for low energies (see Figure 3) and its probability decreases with increasing X-ray energy. [7] [9]

- **Pair production**
  This interaction is based on the formation of an electron-positron pair and occurs for high X-ray energies above 1 MeV. The pair production process takes place inside the Coulomb field of an electron or a nucleus, where the newly emerged pair mutually annihilate, and two γ-rays are emitted [7].

The sum of the beforehand mentioned contributions then determines the total attenuation μ of X-rays in the penetrated object:

$$\mu = \mu_{PE} + \mu_{CS} + \mu_{RS} + \mu_{PP}, \tag{1-6}$$

where μ_{PE} is the attenuation coefficient due to the Photoelectric effect, μ_{CS} is the attenuation coefficient due to the Compton scattering, μ_{RS} is the attenuation coefficient due to the Rayleigh scattering and μ_{PP} is the attenuation coefficient due to the pair production [7]. However, for the X-ray energy range used within standard CT applications from approximately 10 keV to 150 keV, the only two major contributors to the total attenuation are the photoelectric effect and Compton (incoherent) scattering (see Figure 3). Contributions of the remaining mechanisms, especially pair production, can be in this energy interval neglected.
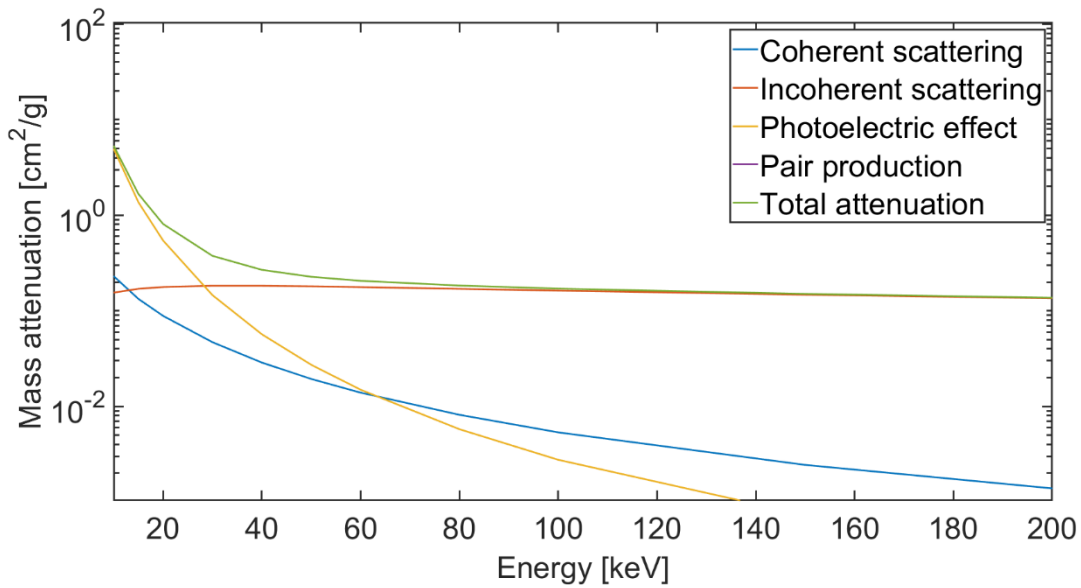
Figure 3: Contributions of individual physical mechanism to the mass attenuation function of water. Data taken from XCOM database [10].

1.1.3   X-ray detection

As introduced in the previous section, within the conventional attenuation-based CT, the X-rays are attenuated during their travel through matter by various means. The attenuated radiation is then detected by a digital X-ray detector, which captures the attenuated X-ray beam and converts it into electrical signal, which is further processed and finally reconstructed to represent a 2D or 3D distribution of attenuation values for a given object. The mentioned conversion of X-ray radiation into electrical signal can be either direct (i.e., X-ray energy is directly converted in electrical signal) or indirect (i.e., X-ray energy is first converted into a different form of radiation that is then converted in electrical signal). According to these two conversion principles (see Figure 4), the digital X-ray detectors can be classified into: gas ionisation detectors (direct conversion) and solid-state detectors (indirect conversion). Over the years, the major concern of the CT manufactures has been increasing the number of detection elements simultaneously illuminated by the X-rays, enabling faster acquisition, and thus improving the thermal efficiency of the X-ray tubes [7]. However, only solid-state detectors are generally expandable to multi-row or multi-slice arrays, whereas high-pressure gas detectors are not easily expandable to flat area detector systems [7].

Direct conversion

X-ray beam

Charge

Photoconductor

Read-out

Indirect conversion

X-ray beam

Visible light

Charge

Scintillator

Photodetector

Read-out
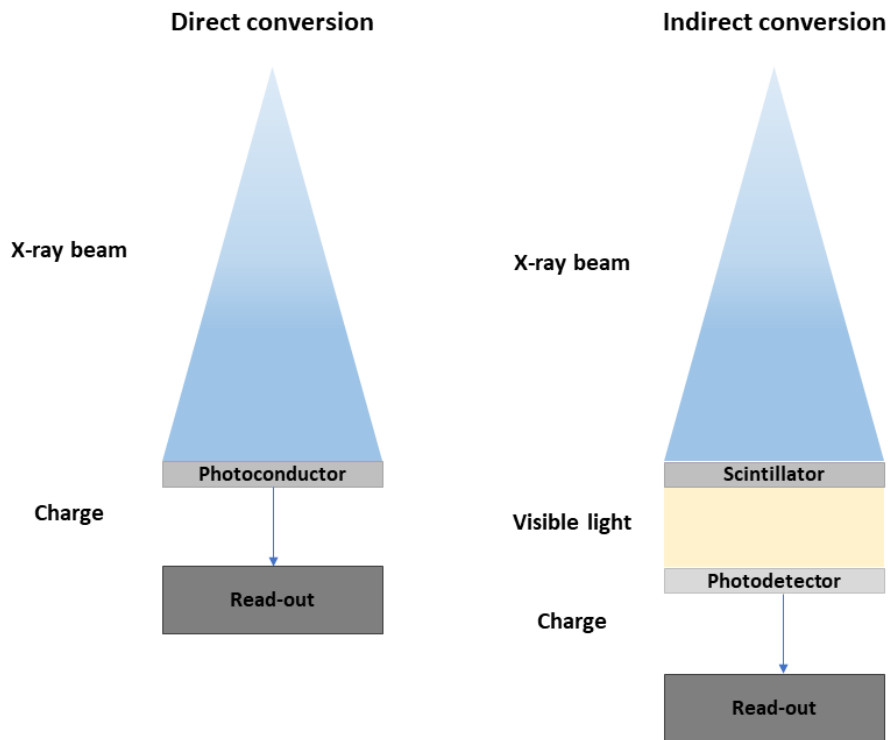
Figure 4: Illustrative scheme of X-ray detection principles.

The solid-state detectors are nowadays used in almost all modern CT systems. Standard solid-state detector consists of a scintillation crystal (scintillator) and a photon detector (sensor). Operational principle of solid-state detectors is based on conversion of X-ray radiation within the penetration of a scintillator into visible light and its subsequent detection. The emitted light is directed to a sensor, where the output signal is generated in the form of a digital number (DN) and represents the integrated number of photons or energy absorbed in a detector element (pixel) over specific exposure time. The choice of scintillator material is then crucial to overall functionality of a solid-state detector. The main parameters to be considered are the desired quantum efficiency for the X-ray to visible light conversion, when the range of emitted wavelengths should match peak efficiency range of the detector [3], absorbing power of the scintillator and the time constant of the conversion process, which determines the "afterglow" of the detector (i.e. persistence of the image even after turning off the radiation) [7]. Also, the scintillator must be defect-free, or at least possess a small number of defects, and emit relatively uniformly over areas of several square millimetres or larger [3]. Usually, the scintillators are made from materials such as sodium iodide doped with thallium caesium iodide cadmium tungstate ($CdWO_4$), zinc sulphide (ZnS), naphthalene, anthracene and other compounds based on rare earth elements, or gadolinium oxysulfide (Gd_2O_2S) [7]. Scintillators are then coupled to the photon detectors through a lens system or fibre-optic channel plate [3]. According to the output signal, the solid-state X-ray detectors can be further classified to integrating and counting detectors, which will be further described in following sections.

1.1.3.1 Integrating detectors

An ideal integrating detector produces a signal that is directly proportional to the complete incoming X-ray energy that represents the sum of all X-ray quanta. Such detector is based on the indirect

conversion principle, when the electrical signal from the photodiode is integrated over a given amount of time, also called as integration period. At the end of the integration period, the resulting charge is read-out and next integration period starts. The total amount of time including the integration period and the read-out time is then called as a reading. The integrated signal is then amplified, digitized, and further processed by an analog-to-digital converter, when the output signal in the DN units corresponds to the total detected energy of all incoming X-ray photons during one reading. Therefore, the individual detection events, relating to the particular X-ray quanta with specific energy, cannot be resolved in the output signal. Detected photon specifically contributes to the output signal with a weighting factor that is proportional to its energy, when higher energy photons contribute more to the signal than the lower energy ones. However, efficiency of this process is dependent on the energy of incoming X-ray photons. For photons with low energy this process is rather linear, when the amount of visible light photons generated in the scintillator is linearly dependent on the energy of an incoming X-ray photon. But for high energies above 100 keV, the scintillator sensitivity decreases because such high energy X-ray photons can pass through the scintillator layer without any form of interaction. The detector types incorporating this principle can be then classified into three main categories according to the technology they are based on:

- **Charge-coupled device (CCD) detectors**
  A CCD device is an integrated circuit consisting of an array of coupled metal oxide silicon (MOS) capacitors (photosensitive area) when each capacitor can transfer its electric charge to a neighbouring capacitor. During the detection process absorbed photons create electron-hole pairs and the electrons are accumulated in detector wells corresponding to individual pixels (see Figure 5). After the integration time, the pixels are read digitally by transferring charge from pixel to pixel until all columns of pixels have reached the read-out register [3] and are amplified and digitized by an AD converter. Unfortunately, this procedure is quite long taking about one second to read an image. [11] There exist several architectures of CCD sensors, such as full-frame, frame-transfer or interline that all differ in used shuttering strategy, or technologically evolved versions of standard CCD such as Electron Multiplying CCD (EMCCD).

- **Flat panel detectors (FPD)**
  Standard FPD consists of pixel matrix, where each element consists of a photodiode and a thin-film transistor (TFT) made of amorphous silicon on a single glass substrate. The pixel matrix is then coated with the scintillator layer made from caesium iodine (CsI). A thin aluminium cover is further used as a reflector and a carbon cover protects from any mechanical damage. Multi-chip modules are used as the read-out amplifiers at the edge of the detector field. [7]

- **Complementary metal-oxide semiconductor (CMOS) detectors**
  The principle of photon detection and charge accumulation in a potential well is the same as for CCD detector. The main difference between CMOS and CCD detectors is the additional complementary metal oxide semiconductor (CMOS) electronics which is engraved beside each potential well (see Figure 5) [11]. This electronics allows for the conversion of the accumulated charges into voltage and the amplification of the signal at each pixel when each pixel can be read without the need for a charge transfer. This results to high speed and low power consumption of CMOS sensor but also to low sensitivity as well as high Fixed Pattern Noise (FPN) due to fabrication inconsistencies in the multiple charge to voltage conversion circuits.
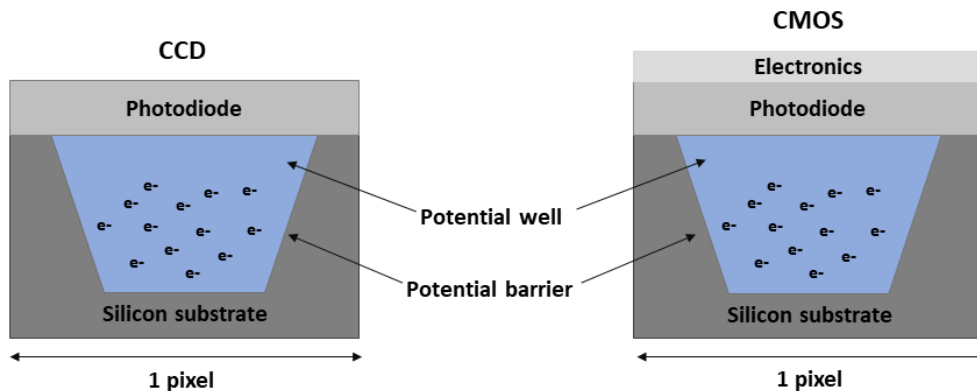
Figure 5: Illustrative scheme of CCD and CMOS sensors pixels.

The CCD sensors have for years dominated scientific imaging applications. Recently, CMOS detectors and amorphous silicon (α-Si) flat panel detectors have become its main challengers [12]. However, CCD detectors poses the high image fidelity in terms of readout noise, quantum efficiency and dynamic range which were hardly met by other sensor types [12]. However, the CCD architecture, where each pixel is read sequentially, results in slow readout rate [12], which prevents its usage for measurements of fast dynamic processes. For area of CT imaging with high resolution (submicron range), detectors with pixel sizes of several hundred nanometres are utilized. This significantly improves detectability of CT system at submicron resolution even for a laboratory-based CT system. To achieve the high image fidelity of CCD detector and preserve readout rate of standard CMOS sensors, new image sensors were recently developed specifically for scientific imaging applications and called the scientific CMOS (sCMOS) [13].

1.1.3.2 Counting detectors

Integrating solid-state detectors do not allow for discrimination between different X-ray photon energies, hence the polychromatic nature of X-ray spectra can cause so called beam hardening artefacts (see section 1.2), which hinders inspection of multi-material components [7]. In recent years, photon counting detectors (PCDs) started to be used for CT applications, overcoming previously mentioned limitations of standard integrating detectors. PCDS are predominantly based on direct conversion of X-ray photons in an electric charge that is proportional to the incident photon's energy [7]. This technology has its origins in high-energy particle physics experiments at the Conseil Européen pour la Recherche Nucléaire (CERN) in the 1980s [14] and can be considered as an assembly of hundreds of thousands of independent point detectors. The photon counting detector (PCD) standardly consists of a sensor layer made from direct conversion semiconductor crystals, where the X-ray photons are directly converted into an electrical signal. The absorption efficiency of the sensor depends on the energy of X-ray photons, the used material and its thickness. The energy range of the absorbed photons is directly determined by the used crystal material, when the most used high-resistivity silicon (Si) sensors efficiently absorb X-ray photons with energies between 2 keV and about 25 keV [14] and the higher energy photons can pass through the sensor undetected. Therefore, for higher X-ray energy applications, sensor materials with a higher stopping power are used such as gallium arsenide (GaAs) or cadmium telluride (CdTe), whose high quantum efficiency allows for detection of X-ray photons up to 50 keV for GaAs and up to 100 keV for CdTe [14]. The sensor layer is pixelized and micro-soldered with a step-size of 1 pixel to an electronic chip, where the counting chains

are engraved, by bump-bonding technique also called as hybridization. Each pixel then consists of a sensor part, responsible for X-ray photon detection, and which is hybridized to the electronics, where the individual photons are counted by their energy. According to this technological principle, various variants of naming this class of detectors exist – hybrid pixel detectors (HPD), photon counting detector (PCD) or hybrid photon counting detector (HPCD). [11]
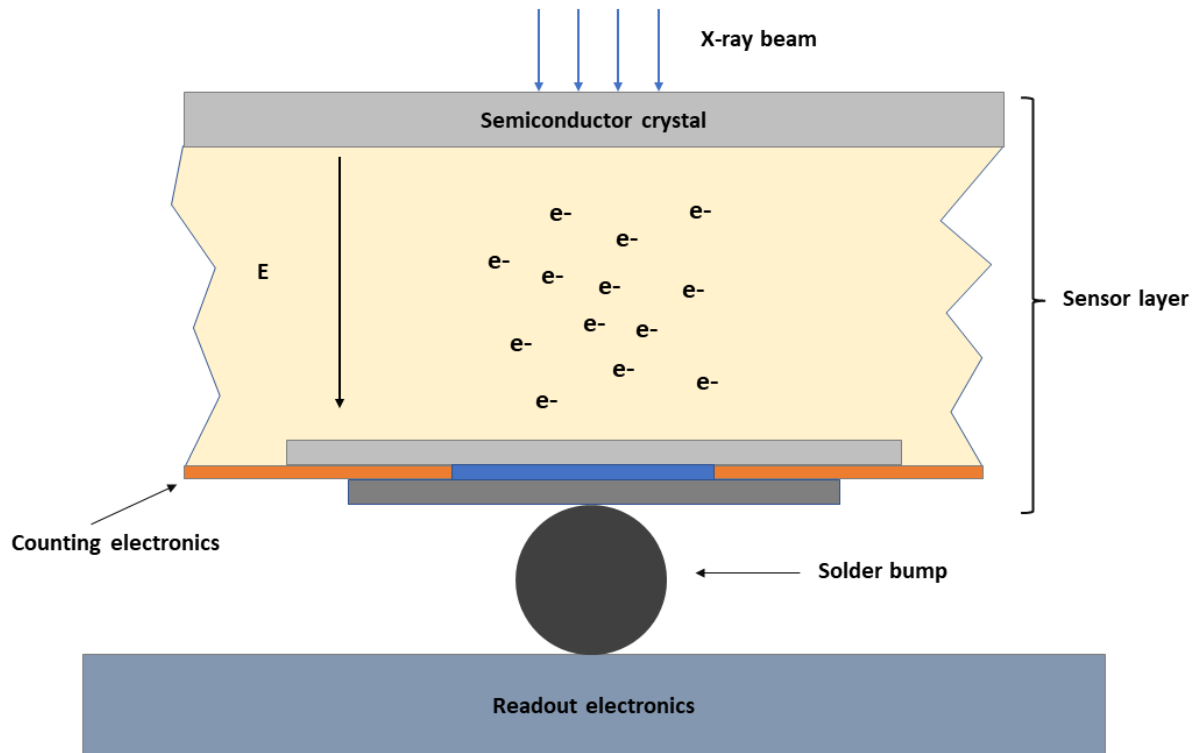
Figure 6: Illustrative scheme of PCD detector pixel.

Individual pixels work like a point detector, when the incident X-ray photon is absorbed in the sensor, the charge cloud, that is proportional to the energy of absorbed photon, made up from electron-hole pairs is generated (see Figure 6). Those electrons are then collected via the bump into the electronic counting chain and readout electronics with minimal point spread [14], where following operations are performed [11]:

1. Conversion of the collected electrons into an electrical impulse, its amplifications and formatting.
2. Comparison of the impulse to a reference energy threshold (set for every pixel) and validation (or not) of the counting event.
3. The discriminated impulse passes through a logic gate which is opened/closed by an externally controllable electrical signal using fast electronic shutter.
4. When the discriminated impulse is authorized to pass the shutter, it is counted (numerically integrated) and stored in the counter. The counters can be then addressed with row and column shift registers and read out in parallel.

11

PCD technology therefore allows for discrimination between different photon energies incident to the detector during a single projection acquisition, when the incident X-ray spectra can be discretized into specified energy intervals, usually from 2 to 8 energy bins. This results into advantages when scanning multi-material samples that are not only related to elimination of beam hardening artifacts but also to increasing the image contrast for low attenuating components by giving more weight to the lower photon energy intervals [7]. In terms of practical aspects and quality of acquired data, the PCD principle of detection allows for elimination of noise components that are common or inevitable for integrating detectors such CCDs or FPDs. This results to considerably improved detectability of fine details, contrast enhancement and increased signal to noise ratio (SNR) [15].

PCD technology related research has been focus of various laboratories and manufactures, which has resulted in several counting readout electronics designs and overall PCD arrangements. The detector group at the Paul Scherrer Institut (PSI) developed the original PILATUS and EIGER [16] chips. The detector technology based on these chips and their successors are manufactured and sold by company DECTRIS. The MEDIPIX collaboration (founded by CERN) has till today developed three generations of their eponymous chip [17; 18] and derivatives like TIMEPIX [19] and MEDIPIX3RX [20]. Detectors based on these chips are nowadays sold by several manufacturers, such as Advacam, Amsterdam Scientific, Quantum Detectors and others. [14],

1.1.3.3 Flat-field correction

Unfortunately, any 2D digital detector suffers from several limiting factors that affects quality of the acquired data. As introduced in the previous section, a 2D digital detector is composed of an array of light sensitive elements (pixels), when each pixel has its own unique light sensitivity characteristics due to manufacturing tolerances. In X-ray imaging applications, the acquired projection images generally suffer from fixed-pattern noise [21], that stems from not only the detector sensitivity variations but also other sources such as losses in charge transport, charge trapping, or variations in the performance of the readout [22]. Also, the scintillator may accumulate dust and/or scratches on its surface and in the bulk [21], or its thickness may vary over the active area [23] resulting in systematic patterns in every acquired X-ray projection image (see Figure 7). Such deviations from true output signal should be corrected, otherwise serious artifacts can appear in the final image data.

The conventional method to reduce stationary fixed pattern noise (i.e., the same in each acquired image) [21] is the flat-field correction. This method is based on normalization of acquired data using following notation:

$$I_c(x,y) = \frac{\left(I_R(x,y) - D(x,y)\right) \cdot (\bar{B} - \bar{D})}{\left(B(x,y) - D(x,y)\right)} = \left(I_R(x,y) - D(x,y)\right) \cdot G(x,y), \qquad (1\text{-}7)$$

where $I_c(x,y)$ is the flat-field corrected pixel intensity, $I_R(x,y)$ is the pixel intensity of the acquired raw data I_R (i.e. before flat-field correction), $D(x,y)$ corresponds to pixel intensity of the dark-field image D, $B(x,y)$ corresponds to pixel intensity of the bright-field image B and $G(x,y)$ is the pixel gain. The dark-field image D is an image which is captured by the detector without X-ray illumination. The signal detected in the absence of X-rays from the X-ray source includes both the true dark current (which is proportional to the exposure time), and the digitization offset, which is independent of exposure time [21]. The bright-field image I is on contrary acquired with X-ray illumination, but without the presence of the sample. It is used to measure and correct for inhomogeneities in the X-ray beam intensity profile and detector response [21]. Usually, the exposure time for the acquisition of both

dark-field and bright-field images is equal to that of the projection images, when those images are usually acquired at the beginning of a CT measurement [3].
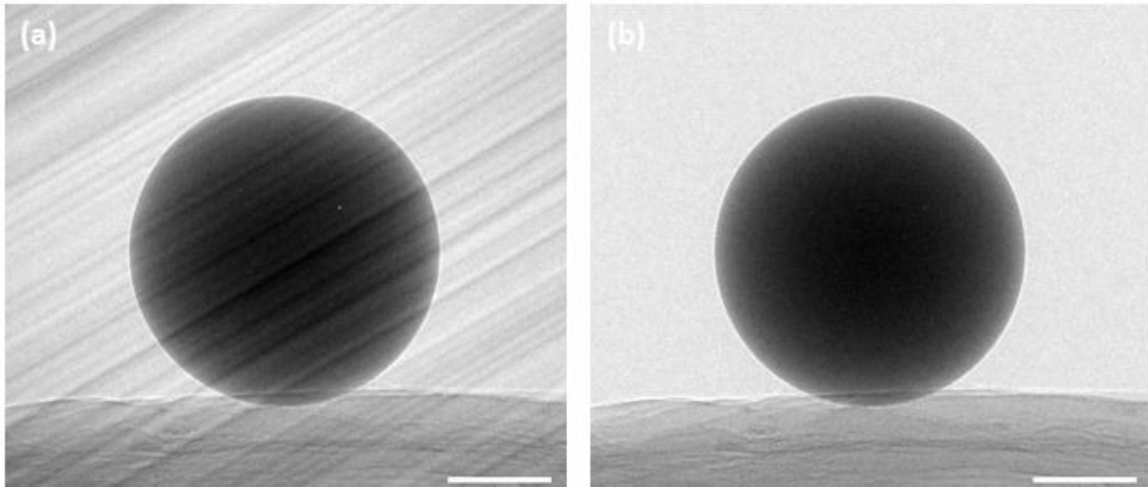
Figure 7: Effect of flat-field correction: a) original projection image; b) flat-field corrected projection image; device: Rigaku nano3DX; sample: ruby ball (Ø 0.3 mm), scale bar: 100 µm.

However, standard flat-field correction method relies on stationarity of the X-ray beam, scintillator and used detector sensitivity, when such assumption is in practise only approximately met [21]. To account for time dependent variations of detected signal, advanced flat-field correction methods were proposed in several recent works [21; 23; 24; 25; 26; 27]. Those techniques are based on specific acquisition scenarios combined with dedicated processing methodologies and incorporation of precise knowledge of used detection system. In the work by Nieuwenhowe et al. [21], the dynamic intensity normalization was proposed, when individual bright-field image is estimated for particular projection image using principal component analysis (PCA) of bright-fields acquired prior, during and/or posterior to the actual CT measurement. However, such requirements and dedicated measurement scenarios leading to significant prolongation of CT acquisition times, prevent general applicability of those methods, when conventional flat-field correction method is still primarily used.

1.1.4 Sample positioning system

Within the sphere of industrial and high-resolution CT, the stationary tube-detector systems arrangement is used, where three axes span a Cartesian coordinate system (see Figure 8). The magnification axis (Z-axis) is defined along the line from the X-ray source to the detector. The Y-axis is parallel to the rotation axis and the X-axis is orthogonal to both the Y- and Z-axes [7]. In this arrangement, the lateral opening of the X-ray bean is called the fan angle and the longitudinal opening is called the cone angle [7]. In this arrangement, the kinematic system (manipulator) is further used to position and rotate a sample during CT measurement. Due to high requirements for measurement performance, the geometrical alignment and stability of the kinematic system are crucial for overall system performance [7]. To consider any CT system well aligned, several conditions must be satisfied, as defined in [7]:

- the intersection of the magnification axis (Z-axis) with the detector is coincident with the centre of the detector,
- the magnification axis (Z-axis) is normal to the detector,

- the magnification axis (Z-axis) intersects the axis of rotation at a 90° angle, and
- the projection of the axis of rotation is parallel to the detector columns.

Further, for the kinematic system following conditions must be met during CT measurement [7]:

- the relative distance between all components is constant and the position of the rotation axis is fixed, and
- the plate of the rotation is perpendicular to the rotation axis.
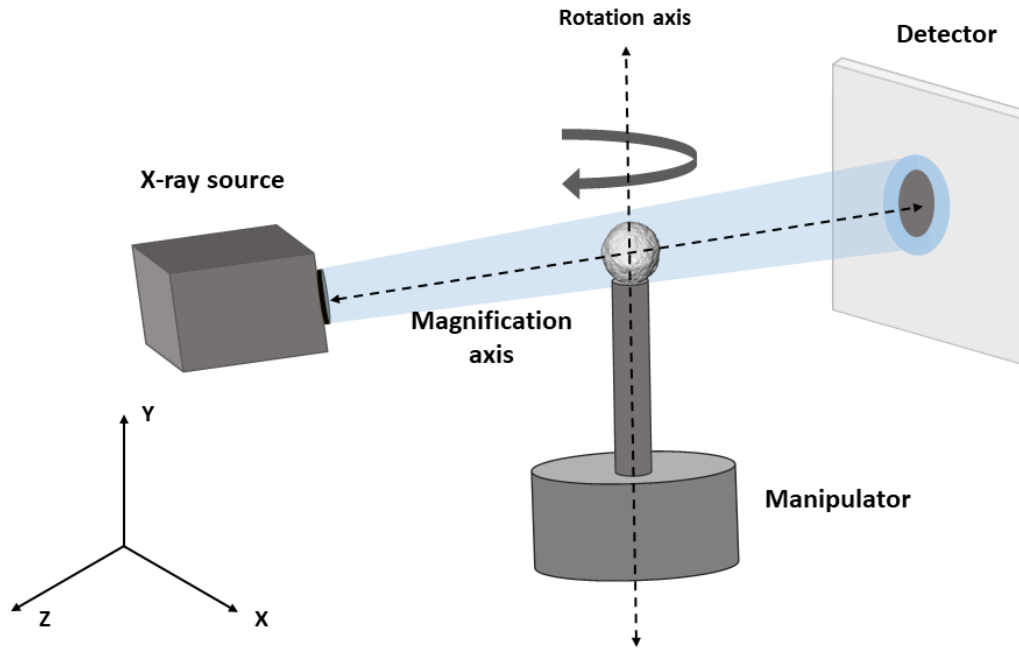
Figure 8: Schematic illustration of a standard CT system arrangement.

When any of those conditions is not met, tomographic artifacts can be present in the acquired data (see section 1.2). Therefore, high dimensional stability, precision, damping capacity and overall stiffness of kinematic system are required. Further, temperature is important aspect that can affect CT measurement results, when as a standard temperature for dimensional metrology 20°C is considered [7]. Differences from this standard temperature can result into expanding/shrinking of the object and possible thermal distortion of the CT system components, when it is essential to keep the temperature stable during CT measurement to avoid any thermal gradients and related distortions. Also, the exact knowledge of the sample position during a CT measurement, determined by the positioning system, is essential, as it will define voxel size (*vx*) and, therefore, the measurement resolution:

$$vx = \frac{p}{M} = p\frac{SSD}{SDD},$$ (1-8)

where p corresponds to pixel size of used detector and M is the geometric magnification defined as $M = \frac{SSD}{SOD}$, where SDD is source-to-detector distance and SSD is source-to-sample distance. According to this relation, the error in the voxel size can be caused by imprecisions of both SDD and SOD distances and the pixel size. Therefore, even minor displacement of the manipulator can yield errors

in subsequent dimensional assessment of the acquired data, and it is then essential that the sample positioning is done as accurately as possible [7].

In summary, high-quality mechanical components are required, when it is essential for them to reach precision and accuracy substantially smaller than the smallest voxel size that will be reconstructed [3]. Some imprecisions of sample positioning system can be reduced by data post-processing, but such software-based solutions are not always easily applicable and functional. Therefore, it is better to have hardware that does not require any correction steps [3].

1.1.5 Tomographic reconstruction

Tomographic reconstruction is a mathematical apparatus providing a link between acquired projection data and the 3D representation of the studied sample. After the acquisition of projection data, a reconstruction process is performed by means of mathematical algorithms to obtain the 3D volume (or a 2D slice representation) of the studied object, which describes its internal and external structure [7]. The resulting data then consists of voxels – the volumetric representation of pixels, where the width of the slices is also considered. From the perspective of the tomographic reconstruction, the object to be reconstructed is the 2D distribution of a function $f(x, y)$, which represents the linear attenuation coefficients of the object, in a Cartesian coordinate system parametrized by the two spatial variables (x, y). All the necessary information to recover this function is contained in the acquired projection data. As already described in the previous section (1.1.2), the X-ray beam is attenuated during passing through an object according to the Beer-Lambert law (1-2). This attenuated radiation is then recorded by the detector in form of intensity value for each pixel. This value represents the function of the attenuation coefficient μ along the ray path *L* through the sample (1-3). When we assume voxel representation of the sample, each voxel along the path *L* contributes to the total attenuation by μ_i. The total attenuation μ is then represented by X-ray projection describing line integral of individual voxel contributions as specified in equation (1-4). The task for tomographic reconstruction is then to assign correct value of μ_i for each voxel *i*, knowing the attenuated intensity values recorded by detector for a different number of orientations of the lines *L*, i.e., projections acquired at different angular positions [7].

The theoretical foundation of tomographic reconstruction was established in 1917 by Johann Radon, who provided a mathematical solution to uniquely determine the value of a function knowing its' line integrals [7]. Till today number of reconstruction algorithms have been introduced, which can be classified into analytical and iterative reconstruction methods. Analytical techniques are standard in CT. They model the object as a mathematical function and reconstruct this object by solving a continuous integral equation. Although these techniques are till today the most used, there are several limitations of their effectiveness that are described latter. The iterative reconstruction methods use iterative reconstruction schemes, where process of reconstruction is repeated until certain criteria are met. Those methods can in general acquire higher quality data compared to analytical methods, but at a cost of high computational demands, that prevents their general applicability. Recently novel reconstruction algorithms have appeared, which utilize machine learning methods during the reconstruction process, such as: [28; 29; 30; 31]. In this section, the fundamentals of this process and the basics of the standard reconstruction algorithms are presented.

1.1.5.1 Analytical reconstruction methods

Analytical reconstruction methods are based on a continuous representation of the reconstruction problem, where an analytical inverse formula of the Radon transform (RT) is discretized to obtain a reconstruction algorithm. Radon transform can be mathematically expressed as:

$$p_\theta(s) = \int_{-\infty}^{\infty} \int_{-\infty}^{\infty} f(x,y)\delta(x\,cos\theta + y\,cos\theta - s)\,dx\,dy, \qquad (1\text{-}9)$$

where p is Radon transform, r is distance from projection centre, θ is acquisition angle, f is the object function at spatial coordinates x,y and δ is Dirac delta function. The Radon transform describes the forward problem of how X-ray projection data are created for a parallel beam geometry. The output of the Radon transform, for all angles θ, is called the sinogram – the name comes from the fact that the point-like object is in Radon space represented by a sine curve (see Figure 9). [32] To obtain exact solution of inverse Radon transform several assumptions about the input projection data should be met, such as: continuous and noiseless character of the data and their acquisition using well-defined measurement geometry. However, such assumptions are not in practise met, therefore, the reconstruction results are only approximation of the real situation.
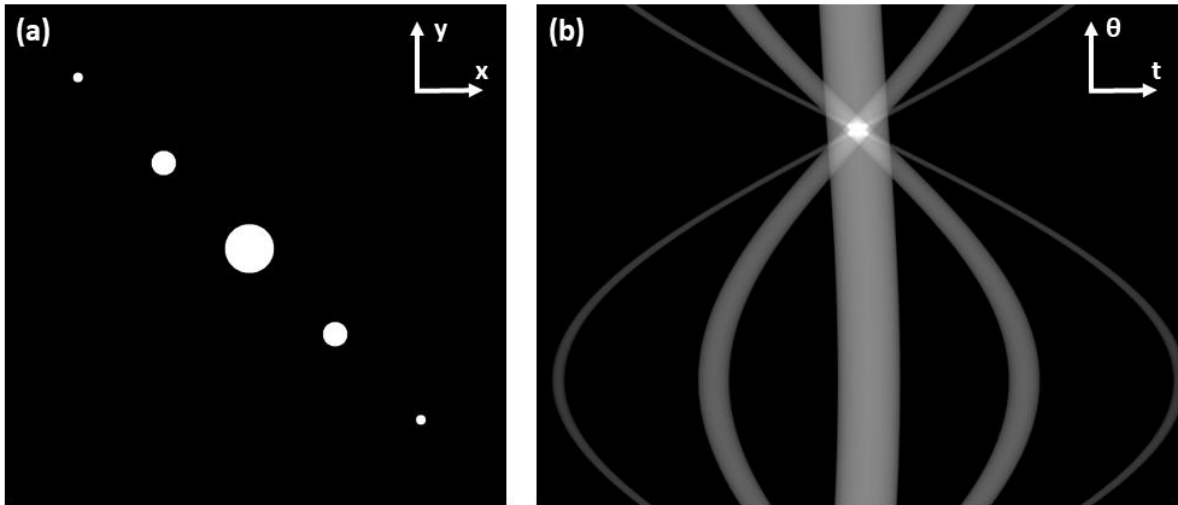
Figure 9: a) Test image containing circular-shaped objects with varying size; b) corresponding sinogram is shown with θ as the vertical axis with the range of ⟨0, π⟩. Contrast of the sinogram was enhanced for visualization purposes.

Tomographic reconstruction using analytical algorithms can be based on the Fourier slice theorem (also known as central slice theorem), which relates Radon transform with Fourier transform (FT). For 2D reconstruction and a parallel-beam geometry, the Fourier slice theorem states that the 1D Fourier transform of a projection of an object $f(x,y)$ acquired at angle θ describes a radial line in the Fourier space of the object, taken at the same angle (see Figure 10) [7]. If enough projections are acquired and the entire Fourier space is filled by performing 1D FT of each projection and inserting them into 2D spectrum at their corresponding angles θ, the object can be reconstructed by applying inverse 2D FT. If the projection data were noiseless and continuous, this method would yield straightforward and exact reconstruction of the analysed object. However, in practise only finite number of discrete and noisy projections is available. Moreover, within the practical implementation the Fast Fourier transform (FFT) is used due to discrete character of the input data, which requires input data arranged in a Cartesian grid. Unfortunately, the object's spectrum is sampled in polar coordinates, therefore a resampling is necessary to apply inverse 2D FFT. Such operation means that 2D spectrum is rearranged from a polar to a Cartesian grid using interpolation. Unfortunately, interpolation in the frequency domain causes artifacts in the reconstructed data, when such artifacts

are more severe for higher frequency components, which are sampled more sparsely due to further distance from the origin. [3] [7]
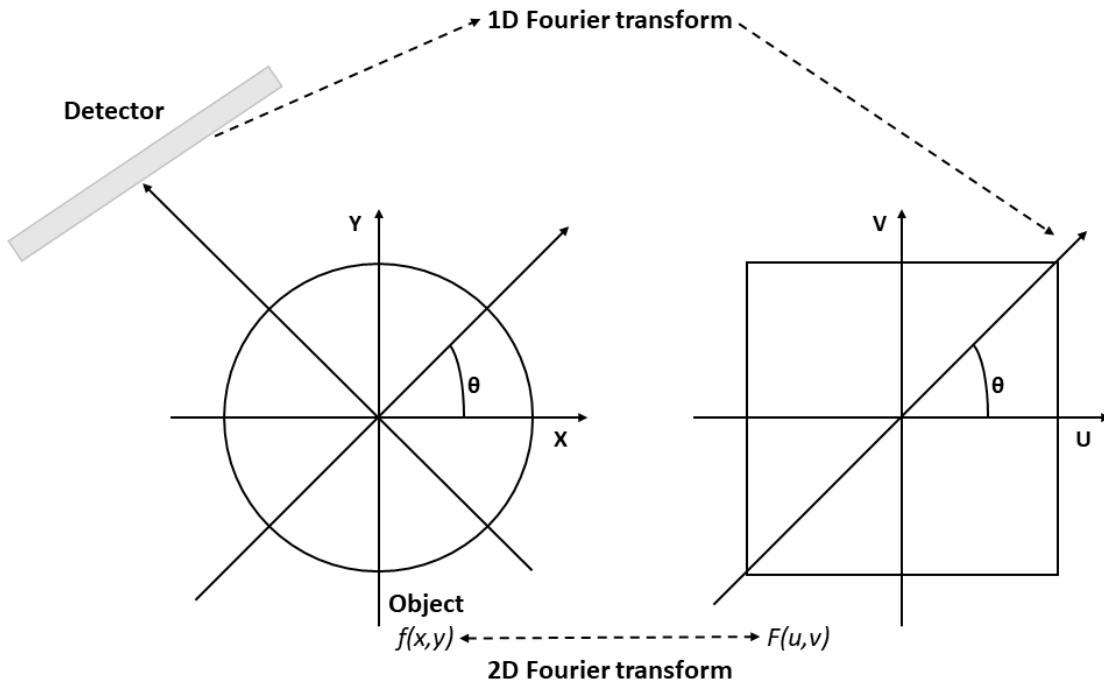
Figure 10: Graphical representation of the Fourier slice theorem. According to: [7].

The basic reconstruction method derived from Radon transform is the Back projection (BP), that can be for parallel beam geometry and acquisition over angular range π expressed as:

$$B[p_\theta(s)](x, y) = \int_0^\pi p_\theta(x\cos\theta + y\sin\theta)\, d\theta. \tag{1-10}$$

This process is sometimes referred as "smearing and summation", when all acquired 1D projections are smeared over reconstruction matrix at corresponding acquisition angles and subsequently summed, which however results in inaccurate approximation of recorded scene (see Figure 11). The resultant intensity value of each voxel of the grid is given by the sum of non-negative values corresponding to each projection, when each projection is a non-negative function, meaning that positive values are also assigned to voxels that do not contain the object [7]. This results to enhancement of low spatial frequencies leading to overall blurriness and reduced data quality.

To overcome such issues, Filtered Back projection (FBP) was proposed:

$$f(x, y) = \int_0^\pi q_\theta(x\cos\theta + y\sin\theta)\, d\theta = B[q_\theta](x, y), \tag{1-11}$$

where q_θ refers to filtered projection defined as:

$$q_\theta(s) = F_1^{-1}[F_1[p_\theta](\omega)\, |\omega|]\, (s), \tag{1-12}$$

17

where F_1 is 1D Fourier transform and F_1^{-1} its inverse and IωI refers to impulse characteristics of used high pass filter. As described by equations (1-11) and (1-12), the FBP involves filtering each object projection with a specific filtering function before applying BP reconstruction to compensate for its point-spread function. The FBP algorithm, is the most widely used reconstruction method, from which is derived the most implemented non-exact algorithm, the FDK algorithm [33] used for cone-beam geometry reconstruction [7]. [32]
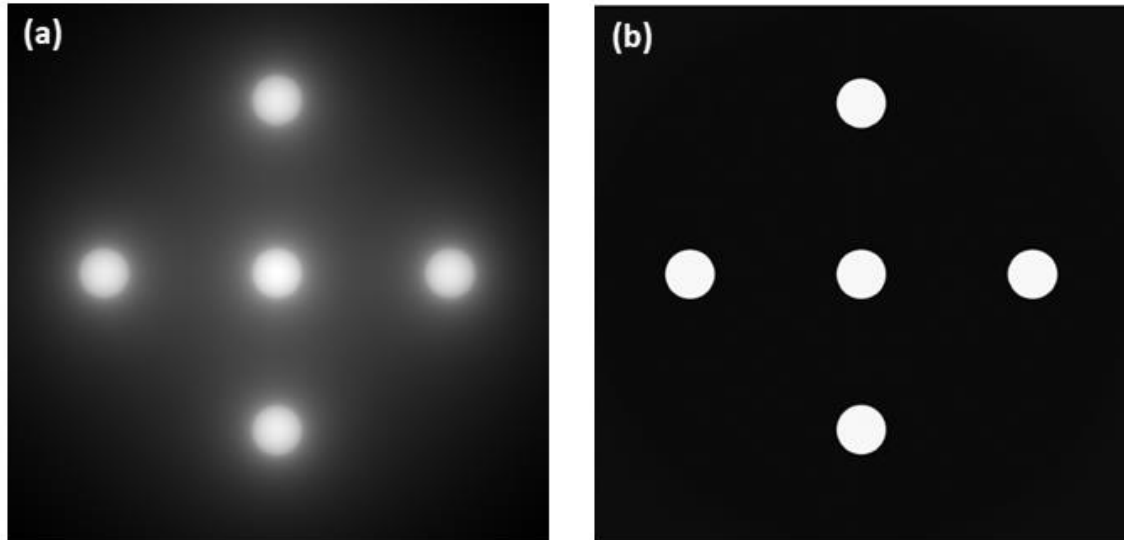
Figure 11: Comparison of BP reconstruction (a) and FBP reconstruction (b). [32]

The used high pass filter ideally preserves the response of the detector but adds negative tails to even out the positive contributions outside the object [7]. The filter is usually called a ramp because its impulse characteristics is shaped as an inclined ramp. Since projections are discrete and intrinsically band-limited, the ramp filter also needs to have a zero response outside the signal's frequency range, when according to Nyquist–Shannon sampling theorem the maximum frequency of a discrete signal is half of its sampling frequency f_s. Higher frequencies cannot be resolved and, when they are present in the original signal, they cause characteristic artifacts called aliasing in the sampled version [34]. Fortunately, in most cases, little energy is contained within these high frequencies, due to the limited spatial resolution of real imaging systems. The contribution of these high-frequency components to the object function is thus negligible. [34] As defined in equation (1-12), filtering by ramp filter is done by multiplication in frequency-domain. Unfortunately, noise spectrum's energy is contained in high-frequency components that are inevitably amplified by standard ramp filter (Ram-Lak filter). The noise can be partially suppressed by multiplying the Ram-Lak filter's frequency response by an additional apodizing function – selection standard apodized filters is shown in Figure 12. But high frequencies of the object function are also dampened resulting in reduction of spatial resolution. Therefore, selection of the apodized filter has high importance as the properties of the filter kernel are directly related to quality of the reconstructed data.
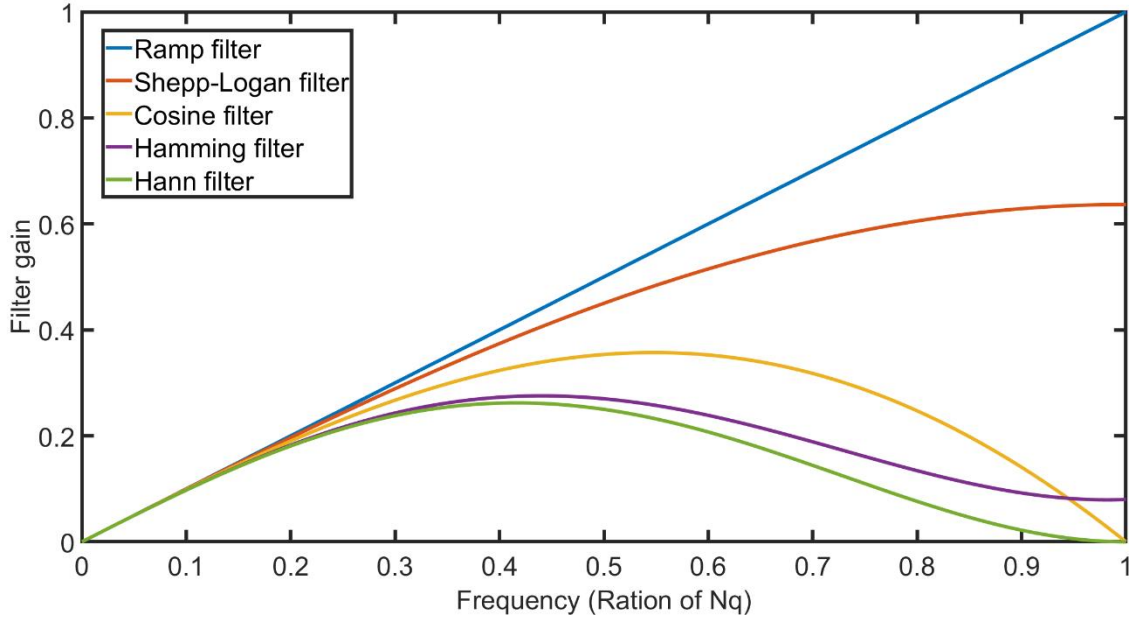
Figure 12: Frequency responses of standard FBP filters, Nq corresponds the highest frequency that can be displayed in the image (0.5 cycles/pixel)). [32]

1.1.5.2   Iterative reconstruction methods

Iterative reconstruction methods (IR) were originally used in the early days of CT but were given up when the amount of measured data increased because of their higher computational demands compared to the analytical methods (1.1.5.1) [35]. However, the increasing capacities of current workstations have led to their re-emergence as a realistic option for CT reconstruction and IR methods are a major and growing area of research in the field of CT and inverse problems in general. All IR algorithms consist of three major steps which are all iteratively repeated until a fixed number of iterations is reached, or solution converged to the predefined quality criterion. First, a forward projection of volumetric object estimate creates artificial raw data (empty image or image incorporating prior information: FBP reconstruction or a volume of a similar object) which, in a second step, are compared to the real measured raw data to compute a correction term [35]. In the last step the correction term is back projected onto the volumetric object estimate [35]. In general, the better the prior images match the final images, the faster the process converges towards a stable solution. [7; 35]

The simplest form of IR is the algebraic reconstruction technique (ART) [36], which was used for reconstruction of images from first CT systems [35]. ART method is based on Kaczmarz's method for solving linear systems of equations described by formula:

$$Ax = b, \tag{1-13}$$

where *A* is a system matrix used for producing the raw data, *b* are the pixels of the measured raw data and vector *x* is the solution which represents the reconstruction we want to compute. The system matrix *A* describes the scan geometry, when every ray is modelled separately and, therefore, no constraints on the shape of the scanning trajectory, detector position or tilt or other acquisition parameters are placed [34]. The entries of the *A* specifically correspond to rays from the X-ray source trough the object to the detector pixel, i.e., the line integrals of the linear attenuation coefficients. [35]

19

In the original ART algorithm, only a single ray sum through the current image is updated in each iteration leading to slow convergence towards a stable solution. This drawback was reduced by proposal of Simultaneous algebraic technique (SART [37]), and it's recent modifications: [38] or [39], where complete raw data are updated in every iteration. To further reduce reconstruction times while keeping high reconstruction quality, the principle of ordered subsets (OS) was incorporated to Simultaneous iterative reconstruction technique (SIRT) [40], and it's recent modification such as: [41] or [42]. In OS-based methods, the projection data is divided into groups called subsets and the update is performed for each group instead for the complete set of available projections [35].

In addition to ART-based methods, other IR algorithms have been proposed mainly incorporating some priory information about the acquisition process such as the statistical methods ([43; 44; 45]) or the model-based methods ([46; 47; 48; 49; 50]). The key idea of the statistical methods is to incorporate counting statistics of the detected photons in the reconstruction process [35] and thus reduce noise in the volumetric images. The model-based methods, in general, try to model the acquisition process as accurately as possible – the better a forward projector can model this process, the better at artificial image can be matched to the acquired raw data [35], leading to faster convergence.

The advantages of IR algorithms over analytical algorithms (1.1.5.1) are significant, including the flexibility in terms of acquisition geometry, better performance for incomplete, noisy, and sparse projection data, and the ability to incorporate prior knowledge about scanned object. Their only disadvantage lies in the high computational demands coming from their iterative nature. The computational cost is often several orders of magnitude larger than for analytical methods, even when using highly optimized implementations on graphic processor units (GPUs), which is in practice preventing their widespread use. [7; 35]

1.1.6 High-resolution CT

Industrial X-ray CT devices are commonly divided into several categories based on sample's size and achievable spatial resolution according to De Chiffre et al. [2]. Many factors influence the achievable spatial resolution of those devices, including focal spot size of the X-ray source, performance of the detector and others. CT systems with focal spot size larger than 0.1 mm are typically referred to as conventional CT or macro-CT [2]. Microfocus systems (micro-CT) have a spot size down to one or few micrometres with achievable spatial resolution in range 5-50 µm [51] and nanofocus systems (nanoCT, submicron CT) may reach sub-micrometric spot size, down to 0.4 µm [2] , and achievable spatial resolution in the submicrometric range [51] but at cost of limited Field of View (FOV) – usually less than 1 mm. [52]

Within scope of this work, the submicron CT systems are especially interesting. Those devices belong to the class of high-resolution CT systems with achievable spatial resolution in the submicrometric range [2; 51]. In some works, the CT systems with achievable spatial resolution from 0.4 − 1 µm are preferably labelled as submicron CT devices to avoid confusion with nanoCT devices that reach a spatial resolution in tens of nm, but general characteristics as nanoCT devices is also applicable. Such high resolution, in general, can be in general achieved in several ways, when those systems can be further categorized according to Zabler et al. [53] as source-based and detector-based submicron CT systems. The first type employs geometrical magnification of the cone-beam shape of X-rays: the sample is placed close to the X-ray source and is projected to the large-area detector placed in the certain distance, when the resolution is restricted by a small size of the focal spot. In the latter approach, the sample is placed far from the X-ray source with minimal sample-to-detector distance, when the resolution is achieved by small pixel size of used detector and coupled magnification optical

system (microscope lenses) [53; 54]. Both types have their benefits and drawbacks that are directly related to their operating principles, such as the high requirements on the used X-ray sources or X-ray detectors. [52]

1.2 Tomographic artifacts

In the field of X-ray computed tomography, the term artifact can be applied to any systematic discrepancy between the CT numbers in the reconstructed image and the true linear attenuation coefficients of the object [55]. Although this definition is broad enough to cover nearly all types of the discrepancies potentially present in the CT data, it has little practical value since nearly every image produced by a CT scanner contains an artifact by this definition [56]. From practical perspective, it is better to consider as artifacts only those discrepancies that significantly distort the informative value and decrease quality of the CT data. Tomographic data are inherently more prone to artifacts than conventional radiographs because the CT images are reconstructed from high number of the independent measurements [55]. The tomographic reconstruction process then assumes that all those measurements are consistent, so any error of the measurement will usually reflect itself as an error in the reconstructed image [55]. [7]

Tomographic artifacts can, in general, degrade the quality of CT data, sometimes even to the point of making them completely unusable for any further analysis. However, for any quality improvement or optimization it is necessary to understand the artifact's occurrence and how they can be prevented or suppressed. In general, the tomographic artifacts can appear as (see Figure 13): a) streaking: caused by projections inconsistencies, b) shading: related to gradual deviations of the group of projections from the true measurements, c) rings and bands: caused by errors or sensitivity deviations of detector elements and d) any form of distortions: related to tomographic reconstruction process. [7]
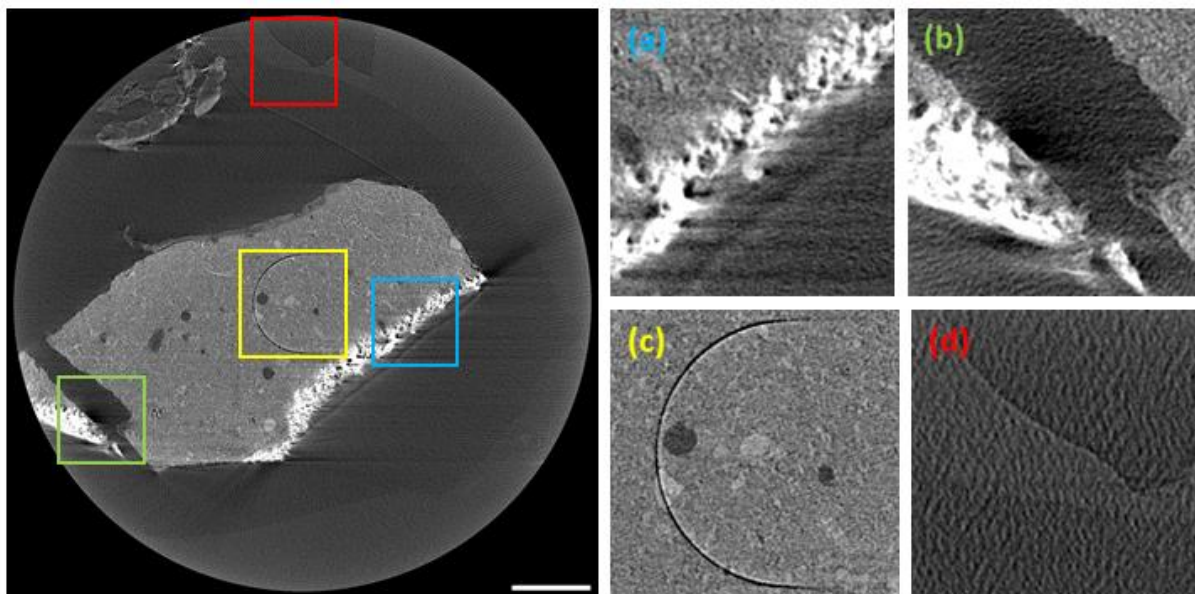
Figure 13: Exemplar overview of tomographic artifacts: a) streaking; b) shading; c) rings and bands; d) distortions. CT system: Rigaku nano3DX; sample: fragment of easel painting from 19th century; scale bar: 200 μm; contrast enhanced for visualization purposes.

In terms of their origin, the tomographic artifacts can be classified into a) technology-based artifacts including the scanner related artifacts and artifacts originating from the physical processes involved in the CT data acquisition, and b) sample-based artifacts that are caused by factors such as sample movement or the presence of metallic materials.

1.2.1 Technology-based artifacts

In the following chapter the most important artifacts related to CT technology and physical processes involved are described in more details including their origin, appearance and also reduction strategies.

1. **Beam-Hardening**
   - **Appearance:** a cupping effect in the CT data – a radial gradient in the values of linear attenuation coefficient with abnormally low values in the central region and high values at the periphery of an object, predominantly observable for a uniform sample.
   - **Cause:** increment of the average photon energy of the polychromatic X-ray beam dependent on the sample's thickness, due to the predominant absorption of the low-energy photons – resulting into the beam becoming "harder".
   - **Reduction:**
     - **Hardware-based:** aims to eliminate the low-energy part of X-ray spectra either by:
       - use of monochromatic radiation,
       - filtering the X-ray beam by metallic filters,
       - dual-energy CT.

       Functionality of the first two methods is limited either by small accessibility of monochromatic X-ray sources or small effectiveness of filtering – beam hardening is not totally eliminated, coupled with decreasing of signal-to-noise ratio of detected signal. Dual-energy CT is able, in theory, to overcome the beam-hardening artifacts because it allows for monochromatic data to be extracted from measurements at two separate polychromatic beam spectra. But the drawback of this method is the need for additional measurements.

     - **Software-based:** aims to transform the measured polychromatic attenuation data into monochromatic based on some assumptions such as: the used spectrum, the detector response, the physical attenuation and scatter properties of the intersected materials [57]. Here belong so-called linearization methods, that takes the correction into consideration before (pre-processing), [58; 59; 60], or after (post-processing) tomographic reconstruction, [61; 62; 63], using the polychromatic regression to normalize measured attenuation data into a linear function. There also exist class of empirical beam hardening correction methods which does not rely on prior knowledge: [57; 64; 65].

2. **Noise**
   - **Appearance:** unwanted variations of detected signal that result in non-exact representation of the original scene.
   - **Classification and cause:**
     - **Dark-current noise:** originating from generated electrons in the detector itself, i.e., without captured radiation, and is sometimes described as fixed pattern noise because it manifests as constant signal pattern that is thermally dependent.
     - **Readout noise:** noise represents a noise floor which is given by signal processing electronics.
     - **Random-valued impulse noise:** randomly distributed individual pixels or clusters of pixels with significant signal deviations caused by detection of cosmic ray during the CT acquisition process.
     - **Shot (photon) noise:** property of quantum nature of light that arises from statistical fluctuations in the number of photons emitted from the object following the Poisson statistics.
   - **Reduction:**
     - **Flat-field correction:** methods based of flat-field correction of detector (for more details see section 1.1.3.3) are mainly applicable for dark-current noise due its fixed pattern character, however practical applicability is limited by requirements on specific acquisition scenarios, priory knowledge of used detector and temporal dependence of noise properties during CT acquisition process.
     - **Hardware-based**:
       - **Signal enhancement:** using either the longer exposure times or higher accelerating voltage to increase the level of detected signal or spreading the histogram of detected signal by increasing the accelerating current. However, such strategies are not applicable for every CT acquisition process due temporal demands or contrast requirements especially for multi-material samples.
       - **Detector cooling:** decreasing the detectors temperature, especially for sensors based on CCD or CMOS technology, minimizes the thermally generated dark-current noise, but has no effect on other noise sources.
       - **Frames averaging:** acquiring several radiograms of static scene at given rotational position with same acquisition's settings, followed by averaging those images. This reduction method has positive effect on the statistically dependent and temporally variable noise but has no effect on the fixed pattern noise, having also strict requirements on imaging scene stability otherwise resulting in structural blurring.
     - **Image-processing:**
       - **Projection-/ Tomogram-domain:** according to noise type, they are dealing with, the denoising methods in this category can be classified as:
         - **Impulse noise reduction:** median filter [66] has been widely accepted as solution with high computational efficiency while on the other hand leading to blur and certain loss of information. Therefore, modified versions of it have been till now developed to overcome these drawbacks: adaptive median filter [67; 68; 69],

23

weighted median filter [70; 71], decision based median filter [72; 73], fuzzy median filters [74; 75; 76] or switching median filters [77; 78; 79].

- **Shot (photon) noise reduction:** historically reduced using filters such as averaging (mean) filter [34] or Gaussian filter [80] although having the same drawbacks as standard median filter. Recently replaced by more advanced methods: Non-Local means [81; 82; 83], Total variations denoising [84; 85], Block Matching algorithms [86; 87] or methods using neural networks [88; 89].

  However, noise in CT data is known to be spatially variant and correlated and its' statistics to be strongly dependent on used reconstruction process and therefore hard to model [90]. Therefore, it is more convenient to reduce noise in the projection domain, where the noise can be precisely characterized. [32]

  - **Reconstruction domain:** using either analytical FBP algorithm (described in the section 1.1.5.1) with carefully optimized apodized filter or IR methods (described in the section 1.1.5.2). Although IR methods have better denoising capabilities compared to analytical ones, they still remain highly computationally demanding.

- However, all the image-processing denoising methods share the importance of noise properties knowledge for their optimal functionality. Moreover, noise reduction can lead to certain loss of edge and structural information, which is inevitable by use of any traditional denoising method. Therefore, sophisticated methods in terms of noise reduction effectivity and preservation of structural information are needed especially in the sphere of high-resolution CT.

3. **Ring artifacts**
   - **Appearance:** ring-like features centred on rotation axis in the CT data, or straight lines in the sinogram.
   - **Cause:** miscalibration or defective detector elements or damaged scintillator areas.
   - **Classification:**
     - **High-level ring artifacts (HRA)**: the most prominent rings caused by malfunctioning detector elements or damaged scintillator areas.
     - **Low-level ring artifacts (LRA):** one pixel wide or wider rings with slight intensity differences compared to not-affected pixels, caused by miscalibrated detector elements.
   - **Reduction:**
     - **Flat-field correction:** methods based of flat-field correction of detector (for more details see section 1.1.3.3), however practical applicability is limited by requirements in terms of acquisition scenarios and priory knowledge of used detector.

- o **Hardware-based:** moving a detector in defined horizontal steps during CT acquisition [91; 92; 93], not effective when detector shifts are not accurately known or movement precision is worse than detector's pixel size.
- o **Image-processing:**
  - **Sinogram-based methods:** working in sinogram domain and filtering-out the artifact's frequency components [94; 95; 96; 97], or using detection-removal schemes [98; 99; 100; 101; 102; 103; 104; 105].
  - **Tomogram-based methods:** working with CT data and usually converting data from Cartesian to polar coordinate system (artifacts then appear as straight lines) before the reduction [106; 107; 108; 109; 110].
  - **Reconstruction-based methods:** using specific regularizations during tomographic reconstruction [111; 112; 26].

4. **Cone-beam ("Feldkamp") artifacts**
- **Appearance:** rhombus-like shading artifacts present in the top and bottom regions of the reconstructed data most prominent near high-density objects, the artifact's extent varies with the cone angle [7].
- **Cause:** Insufficiency of the data sampling in the peripheral regions – projection data for an off-centred planes are mathematically incomplete to solve the tomographic reconstruction problem.
- **Reduction:**
  - o **Hardware-based:** modifying the acquisition geometry either by enlarging the distance from X-ray source to the object (i.e., decreasing the cone angle) or incorporating specific trajectories e.g., saddle [113; 114] or helical [115; 116].
  - o **Software-based:** improving the reconstruction algorithm to handle insufficiency of data sampling of circular trajectory, parallel FDK [117], weighting FDK [118] or iterative reconstruction schemes [119; 120; 121].

5. **Centre of Rotation (CoR) misalignment**
- **Appearance:** tuning fork streak artifacts or double wedges [7], whose extent is dependent on the level of misalignment.
- **Cause:** shift of the rotation axis position from the centre of projection data.
- **Reduction:**
  - o **Prior-scan:** estimating the position of CoR using dedicated phantoms or procedures prior CT acquisition [122], followed by correction either by hardware (i.e., shifting the rotational stage) or software means (i.e., shifting the acquired data). However, the functionality is limited by the precision of the stage [123] or the CoR shift can be reintroduced by sample's manipulation or thermal expansion of system's components during the scan [124].
  - o **Post-scan:** estimating the position of CoR either manually or automatically. Within the manual estimation, the operator changes the CoR interactively and laboriously reviews the reconstructed data. The automatic estimation tries to mimic this process when effects of CoR shifts are quantitatively evaluated using objective metrics: Centre-of-mass (CoM) methods [124; 125], Opposite projection registration (OPR) methods [126; 127], Sinogram symmetry evaluation (SSE)

methods [128; 129; 130] or Reconstruction evaluation (RE) methods [131; 132; 133]. The CoR estimation can be further augmented using fiducial markers that are placed in the measurement Field of View (FoV) [134].

6. **Rotational stage wobble**
   - **Appearance:** shading or streak artifacts, whose magnitude is dependent on the level of stage "unwanted" movement.
   - **Cause:** perturbations in the geometrical parameters used in the acquisition process.
   - **Reduction:**
     - **Hardware-based:** using high-quality mechanical components with precision and accuracy substantially smaller than the smallest voxel size that will be reconstructed.
     - **Software-based (post-scan):**
       - Marker-based – alignment of consecutive projections using accurate tracking of fiducials (i.e., high density particles present in the FoV) [135].
       - Marker-less methods – various concepts applicable to compensate for mechanical inaccuracies and instability: cross-correlation-based [136] or feature-based [137; 138] alignment of consecutive projections, reference scans methods [139] or iterative refinement procedures [123; 138; 139; 140; 141].

1.3 Quantitative computed tomography

X-ray Computed tomography, in general, has transformed from a qualitative diagnostic tool to a quantitative characterization method. However, there is no exact definition of quantitative computed tomography (QCT), but in general two main understandings are perceived. Firstly, the QCT is related to the quantitative characterization of acquired CT data, such as the measurement of bone mineral density (BMD) [142] in medical CT or dimensional measurements [4], fibre orientation [5] and porosity [6] analysis and further industrial and scientific applications described in [143]. Secondly, the QCT is related to very acquisition of CT data and its accuracy in terms of acquired information, which should be in theory solely dependent on sample' properties (as described in the section 1.1.2). However, such quantitative and accurate sample's information is in practise hardly achievable due to the tomographic artifacts (introduced in the section 1.2) and other distortion factors [3]. In recent years, spectral imaging methods have remerged in CT practise, that aim to increase the overall accuracy and quality of CT imaging including methods for tomographic artifacts reduction (see the section 1.2) and to practical implementation of advanced quantification tools for sample's characterization.

1.3.1 Spectral imaging

Spectral CT, also known as multi-energy CT or dual-energy CT, was first hypothesized in the 1970s [144], when it was theoretically derived that the physical properties of materials being scanned, such as density and atomic numbers, can be obtained by utilizing multiple scanning energies [145]. In the conventional single energy CT, the CT voxel intensity is related to the magnitude of X-ray attenuation, which is, however, not unique to a given material, when substances with different chemical compositions can be represented by similar voxel intensities [146]. The spectral CT overcomes this by employing the energy dependence of X-ray attenuation in any material [146]. When various materials are simultaneously exposed by X-ray photons with different energies, X-ray attenuation differences reflect the differences in material's interactions with low- and high-energy photons. By measuring the

X-ray attenuation in two or more distinct energy bins, information about the object's elemental composition can be gained using a concepts of materials decomposition [147], making it possible to precisely distinguish between different materials [148]. Moreover, using the spectral CT the overall quality of acquired data can be improved by various manners, e.g., fusion of acquired data [149], or virtual monoenergetic imaging to reduce tomographic artifacts [150; 151].

However, practical implementation of spectral CT was lagged by the technological limits that were not solved up to recent years. In terms of practical implementation of spectral CT, two main concepts can be applied, either the detector-based or X-ray source-based. In practise, the spectral CT refers to producing multiple measurements of the same object with different X-ray spectra weightings, which are defined by X-ray tube spectrum and spectral sensitivity of used detection system. During the spectral CT either one these is changed to result into as little spectral overlap as possible. The detector-based implementation of spectral CT is linked to the advancement of photon-counting detector technology, as it has become possible to employ measurements at a larger number of energy levels. The photon-counting detectors (introduced in the chapter 1.1.3.2) can discriminate energy of individual X-ray photons and divide them into predefined energy bins. Thereby providing spectral analysis of transmitted X-ray beam [148], can be acquired withing one CT measurement. Dual-energy CT (DECT), i.e., scanning at two energy levels, is a special case of spectral CT that was up to now the mostly used in practise. With the technological development of CT technology dedicated systems were designed exclusively for DECT [7], utilizing concepts such as:

- **Dual kVp** – two subsequent CT scans are performed at different tube voltages,
- **Dual source** – similar concept to the dual kVp but two CT scans are being performed simultaneously by a two tube-detector pairs with a fixed angular offset,
- **kVp switching** – approach that switches the tube voltage between two readings,
- **Dual-layered or PCD detectors** – utilizing advanced detector technology of sandwich detectors or photon-counting detectors.

However, all the X-ray source-based approaches (i.e., dual kVp, dual source and kVp switching) are practically limited by possible misalignment of acquired data, therefore, data alignment procedures should be incorporated within their data processing workflows. [7; 152]

1.3.2 Basis material decomposition

As stated beforehand, the ability of spectral CT to decompose a sample into its constituent elements relies on the energy- and element-dependent nature of X-ray attenuation, mainly due to Compton scatter and Photoelectric effect in the standard CT energy range (described in the section 1.1.2), being a monotopic and smoothly varying function for elements without K- or L-edges within this energy range [153]. Since the X-ray attenuation is primarily dependent on those two interactions, any material's attenuation coefficient μ can be expressed as a linear combination of M energy-dependent material basis functions $f_j(E)$ [144]:

$$\mu(E, r) = \sum_j^M c_j(r) f_j(E),$$ (1-14)

where $c_j(r)$ are the spatially dependent coefficients. This equation can be for standard CT energy range rearranged into:

$$\mu(E,r) = \sum^{M} c_{CS}(r)f_{CS}(E) + c_P(r)f_P(E), \qquad (1\text{-}15)$$

where subscripts *CS* and *P* reflect Compton scatter and Photoelectric effect respectively. Modelling the dependence of Compton scatter and Photoelectric effect processes on material mass density and atomic number, a material specific information can be obtained [153]. Methods for spectral CT material decomposition can be divided into: direct decomposition [154], projection-domain [144; 155] or image-domain [156; 157; 158] methods. In either scheme, material decomposition is very sensitive to noise present in the data because the energy spectra of linear attenuation coefficients of basis materials are strongly overlapped with each other in the standard CT energy range, therefore, decomposed images have severely degraded signal-to-noise ratios (SNR) [158]. Moreover, regardless of the algorithm domain, accurate system calibrations, which establish the relationship between the projection measurements and known densities and thicknesses of basis materials, are essential [153].

2 Aims of Thesis

The general aim of this thesis is to study, explore and possibly move further the field of Quantitative CT, specifically dealing with submicron CT system Rigaku nano3DX. The content of this work can be divided into three major parts covering different aspects of QCT: the first part is dedicated to studying technical limitations of submicron CT and development of dedicated reduction strategies; second part is dedicated to practical implementation of spectral imaging in a form for dual-target CT; and the third part focuses on quantitative analysis of CT data.

2.1 Reduction of technology-based tomographic artifacts

The application of a high-resolution CT has already proven its applicability and benefits in various fields from R&D to basic research. However, aiming for higher spatial resolution and implementation of advanced CT techniques (e.g., 4D CT or spectral CT), brings strict requirements for both the hardware and the software. Especially in sphere of high-resolution CT, the possibility of acquisition of undistorted CT data is still highly limited by various technological aspects and lack of dedicated methodologies and correction solutions. In this work, specific focus is placed on assessment of the technological limits of submicron CT practically implemented using Rigaku nano3DX device, where the technology-based tomographic artifacts are studied, and optimal reduction strategies are proposed. Within realization of this aim several sub-tasks can be defined:

- determination of optimal reconstruction process for Rigaku nano3DX data using the ASTRA tomography toolbox,
- determination of optimal detector in terms of quality and accuracy of acquired data,
- development of noise reduction methodology for Rigaku nano3DX data,
- development of ring artifacts reduction solution for Rigaku nano3DX data,
- development of a solution for correction of rotational stage instability and inaccuracy during CT acquisition using Rigaku nano3DX.

2.2 Spectral imaging

Spectral CT, or multi-energy CT, is perceived as one of the key technologies for future development of CT in general. Spectral imaging methods generally aim to increase overall accuracy and quality of CT imaging including methods for tomographic artifacts reduction and to practical implementation of advanced quantification tools for sample's characterization. In terms of practical implementation of spectral CT, two main concepts can be applied, either the detector-based or X-ray source-based. The focus of this work is X-ray source-based dual-energy CT (DECT), which refers to scanning at two energy levels and is a special case of spectral CT. Dedicated CT systems were designed exclusively for DECT, such as the Rigaku nano3DX system, where this technique is implemented in a unique form of dual-target CT (DTCT). Using this device, not only two energy separate X-ray spectra but also material specific spectra can be achieved during DECT by switching the X-ray source target material. However, all the X-ray source-based approaches are practically limited by possible misalignment of acquired data and also by lack of knowledge about practical aspects of setting up DECT measurements. In this work, both these issues are addressed and practically implemented for Rigaku nano3DX device. The practical realization of this aim can be divided into following sub-tasks:

- determination of optimal DTCT acquisition process using Rigaku nano3DX,
- development of optimal registration procedure for DTCT data acquired by Rigaku nano3DX.

2.3   Quantitative analysis of CT data

CT data can be in general utilized for various purposes from visualization to dedicated analysis of sample's properties – e.g., morphology, voids and pores detection, material properties and distribution etc. However, there is still a lack of dedicated and fully automatic data processing tools for CT data, that would utilize its' full potential. This results into either using CT for visualization purposes only, or quantifying the CT data using non-standardized procedures based on operator's expertise and skills. However, these aspects rule out any trustworthy or reproducible results. Therefore, the aims of this work can be specified as:

- development of objective and reproducible porosity analysis procedure based on CT data,
- development of quantitative analysis tools for 3D models of biological tubular systems based on CT data.

3 Methods

In the following section, CT devices used for experiments in this doctoral thesis are described: Rigaku nano3DX, GE phoenix v|tome|x L240 and ThermoFisher Scientific Heliscan, all located at CEITEC Brno University of Technology. Apart from the utilized CT devices, the software tools, used evaluation metrics and standards are further described.

3.1 CT devices
3.1.1 Rigaku nano3DX

Most of the experiments and CT data presented in this work were acquired using laboratory-based CT system Rigaku nano3DX. Rigaku nano3DX is a detector-based submicron CT system. Achieving such high resolution is accomplished by using a high-power rotation anode X-ray source and high-resolution detection system. In the nano3DX, the magnification takes place in the detector using optical elements which results in small sample to detector distances. Using such settings, near-parallel beam geometry is achieved. This system also enables switching anode materials to optimize contrast for specific sample types, these materials are Cu and Mo. Apart from the material the targets also differ in terms of used tube current and voltage (Cu: 40 kV and 30 mA; Mo: 50 kV and 24 mA) and also in shape and size of a X-ray spot (effective size at 6° take-off angle: Cr and Cu – 0.07 mm circle; Mo – 0.15 x 0.1 mm ellipse). This machine has also possibility of utilization of a unique X-ray rotary target that enables Dual-Target CT (DTCT) measurements. Using such target not only two energy separate X-ray spectra but also material specific spectra are acquired.

3.1.2 GE phoenix v|tome|x L240

Industrial microCT system, GE phoenix v|tome|x L240, was used within analysis of rotational stage stability (section 4.5.1) and for application studies dealing with quantitative analysis of CT data (section 6). This microCT system is placed in the air-conditioned, walking cabinet where all components are on the granite-based 7-axis manipulator. This setup has the cone-beam geometry and is equipped with GE DXXR 250 flat panel detector. The sample limitations for this setup are: 500x800 mm^3 in terms of volume and 50 kg in terms of weight. This system can be equipped with two X-ray sources, which are the unipolar microfocus source and high-power nanofocus X-ray tube. Nominal parameters of these sources are stated in Table 1. [161]

Table 1: Nominal parameters of GE phoenix v|tomex|x L240 X-ray sources, LVS – linear voxel size.

X-ray source	Voltage/ Power	Maximal LVS
Microfocus tube	240 kV/ 320 W	~ 2 μm
Nanofocus tube	180 kV/ 15 W	~ 1 μm

3.1.3 ThermoFisher Scientific Heliscan

MicroCT system, ThermoFisher Scientific Heliscan, was used within analysis of rotational stage stability (section 4.5.1). This system is equipped with micro-focus X-ray source with tungsten target achieving 8W power and maximum accelerating voltage of 160 kV. The applicable focal spot size varies between 0.8 μm and 4 μm according to applied settings. The detector is a 16bit flat panel with 3072 × 3072 pixels and pixel size 139 μm. The setup has cone-beam geometry with maximum applicable SSD 130 mm and maximum applicable SDD 750 mm, using this arrangement voxel resolution up to 0.8 μm can

be achieved. For CT acquisition, several scanning trajectories are available: circular and helical with several options – single helix, double helix and space filling [162]. Using the helical scanning trajectory, tall samples, up to 100 mm, can be scanned without stitching.

3.2 Software

List of utilized software tools for data processing and analysis used within scope of this thesis is summarised in Table 2.

Table 2: List of software used in this thesis for data processing and analysis.

Software	Use
Matlab®	Data processing and analysis
ImageJ [163]	Data visualization and analysis
VGStudio MAX	Data visualization and analysis
ASTRA Toolbox [164]	Tomographic reconstruction

3.3 Practical assessment of a detector and image data quality

Several characteristics describe the quality of image data acquired by a detector, when these are mainly governed by noise and signal properties. In the Table 3, the utilized evaluation metrics are introduced together with ways of computing those measures from specific measurements.

Table 3: List of evaluated image quality metrics with corresponding calculations used in this work.

Category	Parameter	Definition/Calculation
Data quality	Contrast to Noise Ratio (CNR)	$$CNR = \frac{|\mu_o - \mu_b|}{\sigma_b},$$ where μ_o and μ_b are mean intensity values of object and background respectively and σ_b is standard deviation of background. [167]
	Signal to Noise Ratio (SNR)	$$SNR = \frac{\mu_o}{\sigma_b},$$ where μ_o is mean intensity value of object and σ_b is standard deviation of background. [167]
	Local Contrast (C)	$$C = \frac{g_{max} - g_{min}}{g_{max} + g_{min}},$$ where g_{max} and g_{min} denote the maximal respectively minimal intensity values in the region of interest defined by a support window R centred around i_0, j_0 spatial coordinates. [167]
	Variance (VAR)	$$VAR = \frac{1}{n} \sum_{(i,j) \in R_{i0,j0}} (g(i,j) - \mu_R),$$

		where n is number of pixels (voxels) in support window R centred around i_0, j_0 spatial coordinates, $g(i,j)$ is intensity value at spatial coordinates i, j and μ_R is mean intensity value in window R. [167]
	Sum of Modified Laplacians (SML)	$$SML(i_0, j_0) = \sum_{(i,j) \in R} (|-g(i+s,j) + 2g(i,j) - g(i-s,j)| + |-g(i,j+s) + 2g(i,j) - g(i,j-s)|),$$ where R is support window centred around i_0, j_0 spatial coordinates, g denotes intensity value at specified spatial coordinates and s is defined step parameter. [167]
	Just Noticeable Blur (JNB)	$$JNG = c \frac{\sum w(e_{i,j})}{E},$$ where $e_{i,j}$ denotes edge pixel at spatial coordinates i, j and w is corresponding edge width, E denotes number of all edge pixels and c is a real valued factor. [167]
Linearity	Linearity analysis	Graphical plot analysis of detected signal as a function of exposure time / evaluated for bright-field frames. Linearity was then expressed as the root mean square of the distances between detected signal points and the linear regression fit line (a linear least-squares regression model was used).
Noise properties	Readout noise	Readout noise was defined in the section 1.2. It was extracted from the set of bias frames (i.e., dark-field frames acquired with the minimal exposure) by subtraction of average bias frame and then quantified using standard deviation.
	Dark current	Dark current noise was defined in the section 1.2. For quantification linearity analysis of dark-field frames was used. Frames were acquired for exposures from 1 s to 30 s and from each frame mean bias frame was subtracted. Resulting dependence of average dark current signal on exposure time was then fitted using linear regression and the dark current was then defined as the slope of this fit.
	Total noise	Total noise is a compound of all noise sources. It was quantified from set of bright-field frames by subtraction of an average bright-field frame from intensity stabilized frames and then quantified using standard deviation calculation.
	Noise power spectrum (NNPS)	The NNPS is a characterization of the noise in the spatial frequency domain. In this work, we incorporated NNPS calculation as specified in IEC 62220-1: 2003(E) standard [165]: $$NNPS(u,v) = \frac{1}{S^2} \cdot \frac{\Delta x \Delta y}{M \cdot 256 \cdot 256} \cdot \left(|DFT2(n_{ij})|^2\right),$$ where S denotes average signal in the subset, Δx and Δy are the pixel size in horizontal respectively vertical directions, M is number of subsets, DFT2 denotes the discrete 2D Fourier transform and $n_{i,j}$ is extracted 2D noise image from given subset.

	Hot pixels	Hot pixels are pixels with dark current significantly above the average. They were detected based on analysis of dark-field frames with 10 exposure levels from 20 s to 30 s. From such frames mean bias frames were subtracted so only dark current map images remained. In these images extreme dark values were detected using this formula: $$g(x,y) = \begin{cases} 1, & if\ f(x,y) \geq M + 3 \cdot s \\ 0, & if\ f(x,y) < M + 3 \cdot s \end{cases}$$ where *f(x,y)* is analysed dark current frame for given exposure, *M* is median dark current value and s is the standard deviation (both calculated from *f*) and *g(x,y)* is binary value of output binary image g both at corresponding spatial coordinates x, y. As hot pixels were then considered pixels with extreme dark current values whose positions was not changing within analysed frames.
	Random hot pixels	These pixels are defined analogously as hot pixels but are mostly caused by scattered radiation. For detection similar scheme as for hot pixels was applied but in case of random hot pixels their positions were random within the frames.
Spatial resolution	JIMA RT RC-02B resolution test	Graphical analysis of minimal resolvable pattern – line profiles over selected pattern charts in both horizontal and vertical directions. For analysis representative frames were used – pixel-wise averaging of acquired frames with extreme values exclusion. To avoid any remaining effect of noise, analysed line profiles were taken through a band of 100 pixels thickness.
	Modulation transfer function (MTF)	MTF is considered as a measure of the spatial resolution of a liner imaging system. This function was calculated using procedure defined in: ASTM E1695-95(2013) standard [166]. As disk phantom a ruby ball with diameter 0.3 mm was used and corresponding CT data were acquired using acquisition parameters that simulated standard measurement scenario. From CT slice located at centre of used phantom the composite edge disk profile was generated and used for calculation of the edge response function (ERF). From this function the point spread function (PSF) was obtained as the derivate. MTF was then calculated as unity normalized amplitude of PSF Fourier transform. Spatial resolution (*SR*) calculation: $$SR = \frac{1}{2 \cdot MTF_{10\%}} \cdot vx,$$ $MTF_{10\%}$ is a frequency value [lp/voxel] at 10 % of MTF and *vx* is voxel-size value.

4 Reduction of technology-based tomographic artifacts

In this chapter, are presented results, that have been achieved dealing with the topic of reduction of technology-based tomographic artifacts, that were introduced in the section 1.2.1. These results are mostly focused on studying such artifacts and development of dedicated reduction strategies with specific focus on Rigaku nano3DX system.

4.1 Optimization of parameters for analytical tomographic reconstruction

Although it may seem that tomographic reconstruction is not related to the topic of technology-based tomographic artifacts, the truth is the opposite. As it was introduced in the section 1.1.5, it is an essential step of CT data acquisition process, when a selection of specific reconstruction algorithm and its settings has key importance for reconstructed CT data quality. This is valid especially for the class of analytical reconstruction methods (see chapter 1.1.5.1), where the selection of the shape of apodized filter and its cut-off frequency is crucial using FBP-based algorithms. Therefore, this section is focused on searching optimal analytical reconstruction procedure using ASTRA tomography toolbox [162] for reconstruction of submicron CT data acquired by Rigaku nano3DX device. [32]

4.1.1 Materials and methods

Using implementation of FBP in ASTRA toolbox (v1.9.0), two parameters can be selected. These are: filter type and the cut-off point in the frequency domain. Regarding the filter type, 16 filters are available in ASTRA, where the Ramp filter can be considered as a standard. This filter is the high-pass filter with zero transmission of DC component and linear increase towards the highest frequencies, which leads to accentuation of high frequencies (i.e., image details and noise component). Therefore, for tomographic reconstruction of data that contain noise, it is better to weight the Ramp filter by specific function (see Figure 12). The actual shape of the filter's transmission function has the effect on high frequencies reduction during the reconstruction process affecting the spatial resolution and noise properties in tomogram data. All the filters aim at reduction the frequency information through an amplitude of their transmission functions, i.e., adjusting this function inside the frequency interval from 0 Hz to Nyquist frequency (Nq). Specifically, Cosine and Hamming filters achieve good results in terms of noise suppression, but they do not preserve edges and details (their transmission reaches zeros zero quickly near the highest frequencies, see Figure 12). The cut-off point in the frequency domain specifies the threshold above which higher frequencies are eliminated (see Figure 14). Setting this value to 1.0 will include the whole filter range without any effect on the transmission function shape (cut-off point value times the Nq frequency = the highest frequency that can be displayed in the image (0.5 cycles/pixel)). High value of this parameter leads to improvement of spatial resolution but neglecting the noise reduction. Values higher than 1.0 amplifies the transmission of high frequencies, which can be advantageous for some filter types in terms of details preservation. For images containing a high degree of complexity, the trade-off between the noise removal and features preservation needs to be find (i.e., compromise between the extent of noise reduction and fine details suppression). [32]
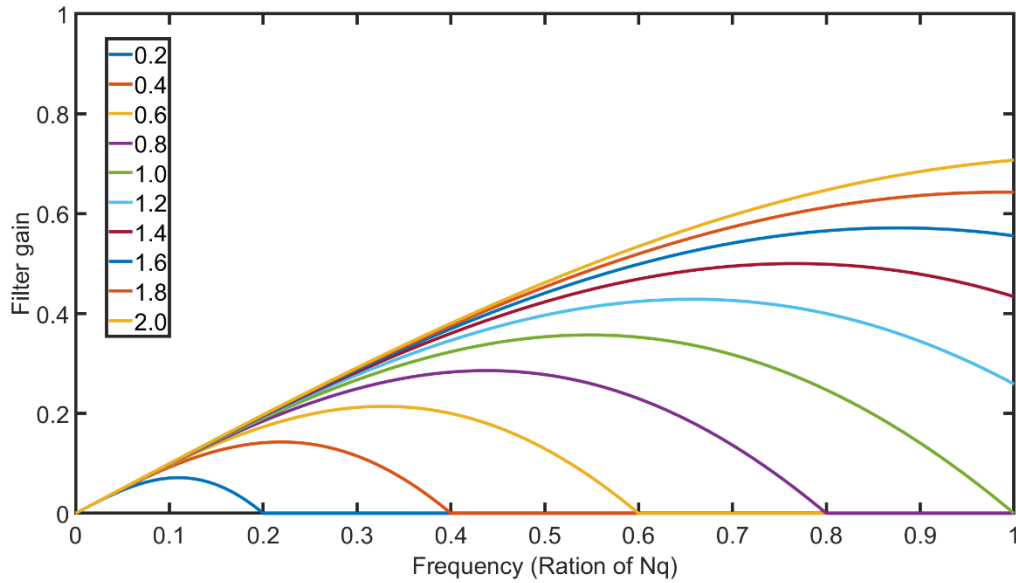
Figure 14: Dependence of Cosine filter transmission functions in frequency domain based on used cut-off point values (used range from 0.2 to 2). [32]

Specifically, all available 16 filters in ASTRA Toolbox were evaluated for range of cut-off points from interval 0.1 to 5.0 with step 0.1. This optimization was done using brute-force search with quantitative performance evaluation using two numerical metrics. These were: the peak signal-to-noise ratio (PSNR) and structural similarity index (SSIM) [166]. Apart from optimization of filtering settings, the dependence of noise reduction together with spatial resolution preservation on filtering settings were also studied. For evaluation of noise reduction, Signal to Noise Ratio (SNR) was used and in case of spatial resolution evaluation, the line profile analysis was conducted. For this evaluation synthetic data were generated. Specifically, 4 types of data were used (see Figure 15). These images were generated in image (tomogram) domain and then forward projected to sinogram domain. The data were simulated to have similar parameters as real nano3DX data, specifically to have pixel size 0.54 μm, used detector width 1648 pixels and to follow acquisition of 800 projection angles from angular range of 0° to 180°. To further test the effect of filter settings on noise reduction, Gaussian distributed noise with standard deviation 0.01 (reflects noise properties of real projection data) was added to generated sinograms. [32]
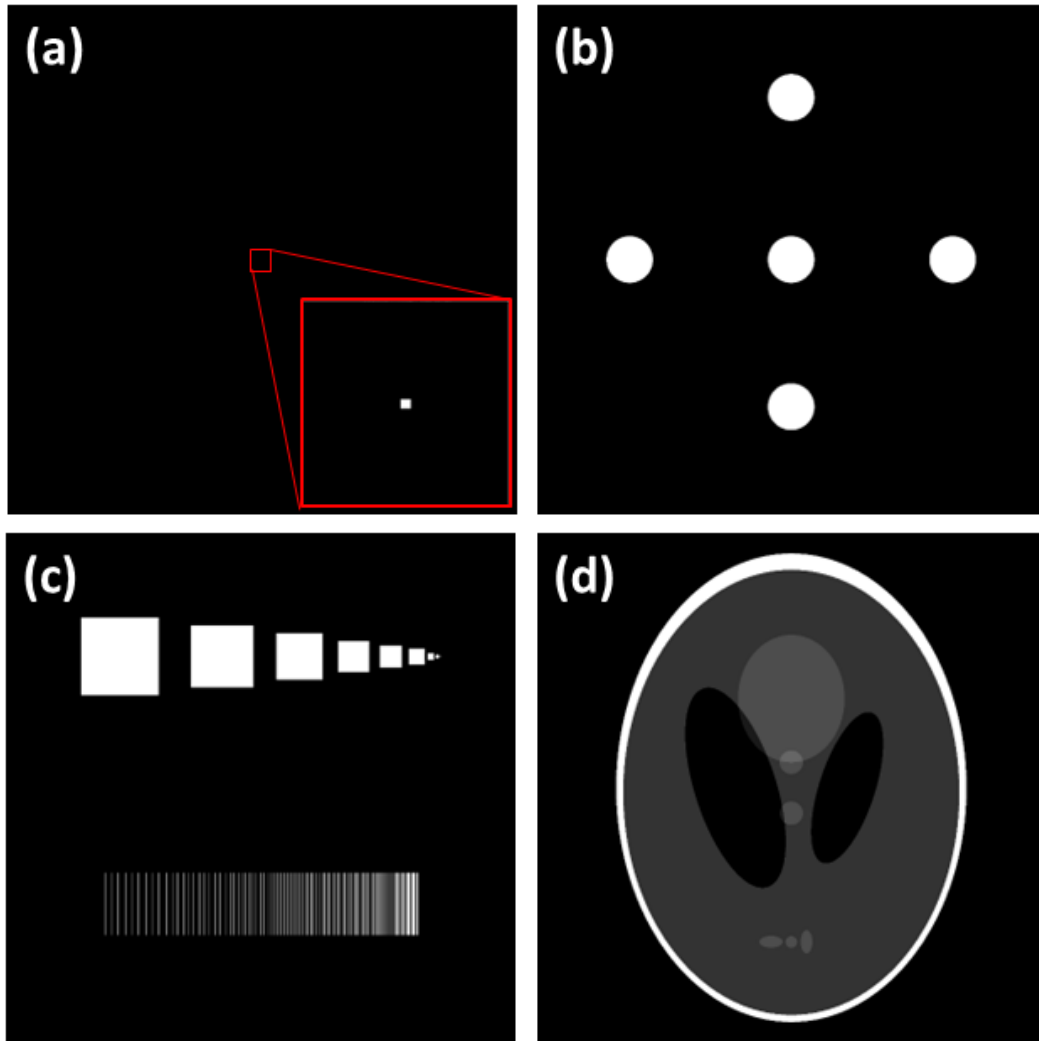
Figure 15: Generated synthetic data for optimization of FBP filtering setting: a) Dirac delta function; b) circles phantom; c) spatial resolution phantom and d) Shepp-Logan phantom. [32]

4.1.2 Results

4.1.2.1   Filtration settings evaluation for ideal data

It should be stated that this optimization was done assuming ideal conditions i.e., no noise and other tomographic artifacts presence in the data. The optimal filtration settings were estimated for each of 4 phantom images separately and then overall optimal settings was evaluated. It was revealed that FBP based reconstruction even with optimal settings is not an ideal system, when its response to Dirac delta function is not a point-spread function (see Figure 16). From line profile analysis of reconstruction results using filtration settings with the best score (see Figure 17), it is evident that in all the cases intensity was decreased and that the point-spread function was blurred. The best overall score achieved filtration settings using cosine filter with cut-off point 2.0 (see Table 4). From Figure 18, it is evident that transmission functions of filtration settings with best overall score are having almost the same course, forming an ideal transmission function for noise- and artifacts-free data. [32]
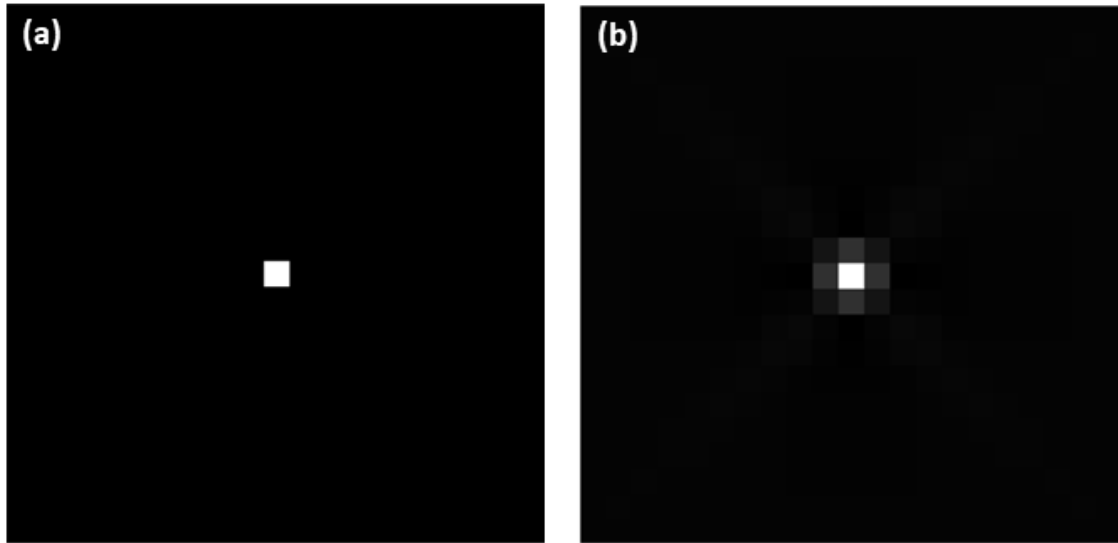
Figure 16: Comparison of responses to Dirac impulse by ideal reconstruction system and real reconstruction system (used filter with best results for this phantom – Hamming filter with cut-off point = 1.8): a) Ideal reconstruction system and b) real reconstruction system. [32]
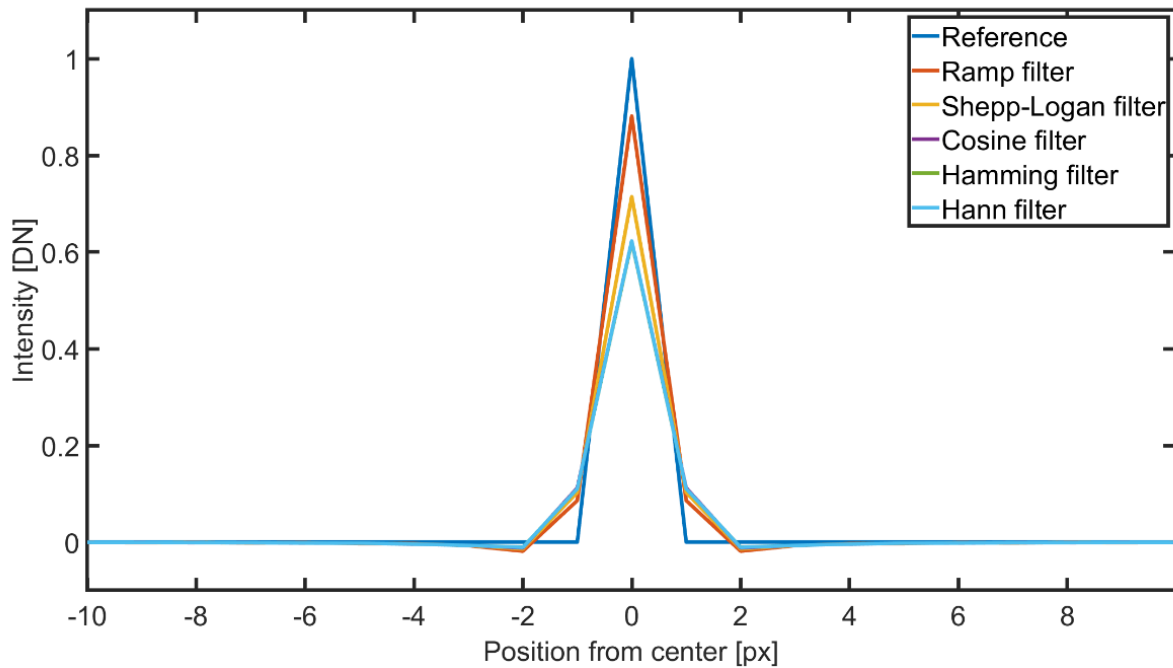
Figure 17: Line profiles in horizontal directions over central area of Dirac impulse tomograms reconstructed with filtration settings that achieved best results for this phantom. [32]

Table 4: Overall optimal filtration settings for ideal data. [32]

Rank	Filter type	Cut-off point
1.	Cosine	2.0
2.	Hann	2.8
3.	Shepp-Logan	1.1
4.	Hamming	2.7
5.	Ramp	1.0
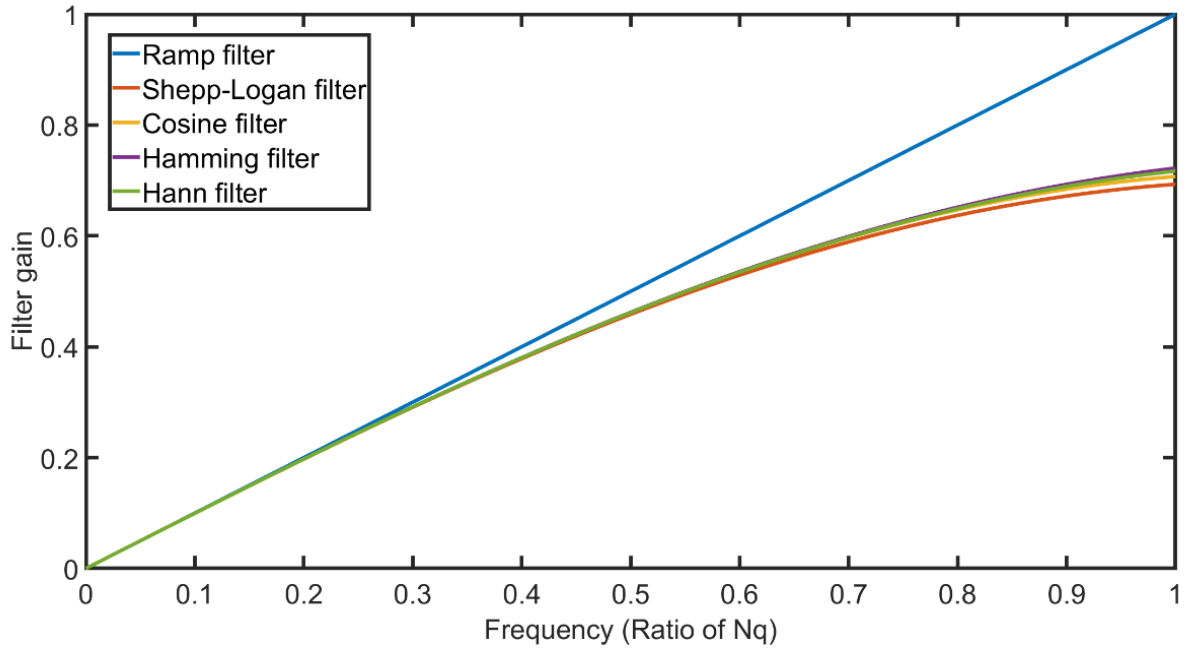
Figure 18: Transmission functions in frequency domain of estimated optimal filtrations settings for ideal data. [32]

4.1.2.2   Spatial resolution dependence on used reconstruction settings

Using spatial resolution phantom, the effect of used cup-off point on achieved spatial resolution was studied. As filter type, the cosine filter was used due to its best overall results in previous section. This analysis was done using line profiles analysis over the chart-pattern (see Figure 19) covering the resolution areas from 4.0 µm to 0.5 µm. The assumption that with higher values of cut-off point the achieved spatial resolution increases, was confirmed. But it was found out that for used cosine filter the spatial resolution improvements were not significant from the cut-off point value 1.2. Even with the cut-off point 0.9 the highest tested resolution 0.5 µm was achieved. [32]
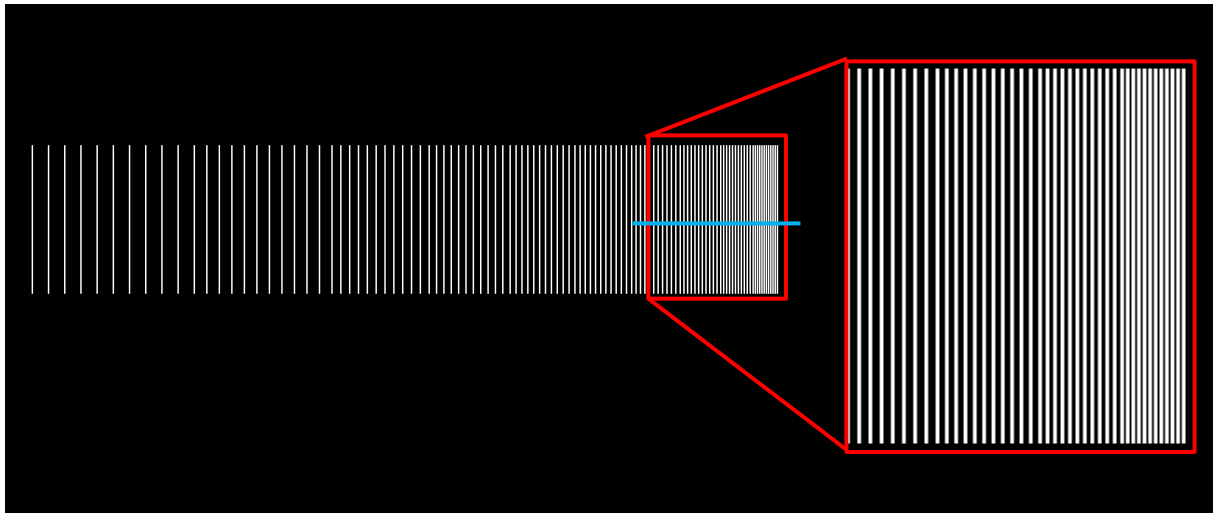
a)   Chart pattern of used spatial resolution phantom, by blue color is labeled the area used for line profile analysis: 4.0 μm – 0.5 μm.

b) Cut-off point 0.3.

c) Cut-off point 0.6.

d) Cut-off point 0.9.
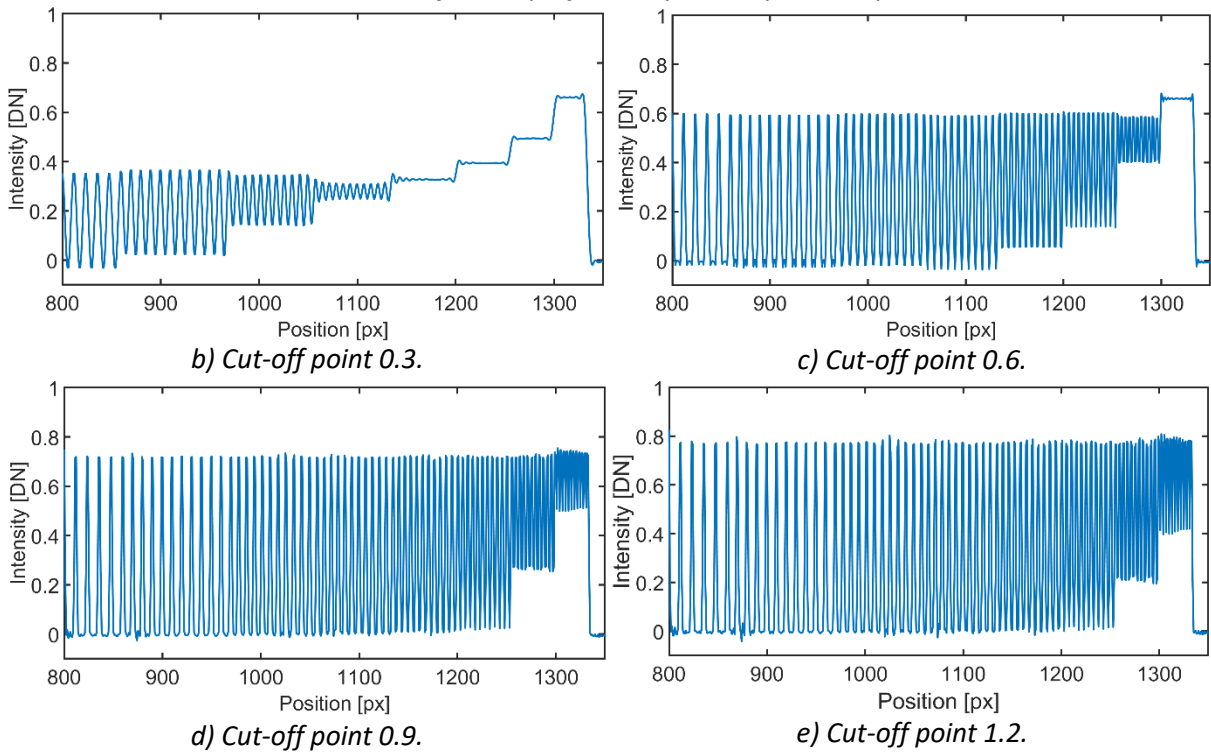
e) Cut-off point 1.2.

Figure 19: Dependence of achieved spatial resolution on used cut-off point value for Cosine filter. [32]

4.1.2.3   SNR dependence on used reconstruction settings

For this study, Gaussian distributed noise with standard deviation 0.01 (reflects noise properties of real projection data) was added to sinograms of phantom images: circles phantom and spatial resolution phantom. For SNR calculation according to definition in section 3.3, the areas of signal and background were manually selected. The assumption, that with higher cut-off point values the SNR values decreases, was confirmed. The actual dependence of SNR on used filter type and used cut-off point

value is shown in Figure 20. This dependence was evaluated for filter types with best optimization score from previous study (4.1.2.1) and for cut-off point values from 0.1 to 5.0 with step 0.1. It was found out that this dependence has exponential course when the highest decrease of SNR values lies between cut-off points from 0.1 to 0.5 and that from cut-off point value 1.0 towards higher values this decrease is almost negligible. Overall best SNR results achieved the Hann, Hamming and cosine filters. However, it was found out that the first two named filters do not reach comparable resolution as cosine filter when having same SNR values. Specifically, it was found out that Hann or Hamming filters would need cut-off point values higher than 1.0 to achieve comparable spatial resolution as cosine filter with cut-off values less than 1.0. Therefore, cosine filter is selected as the optimal filter, in terms of acquired spatial resolution and noise reduction, with cut-off point values from 0.8 to 1.0. [32]
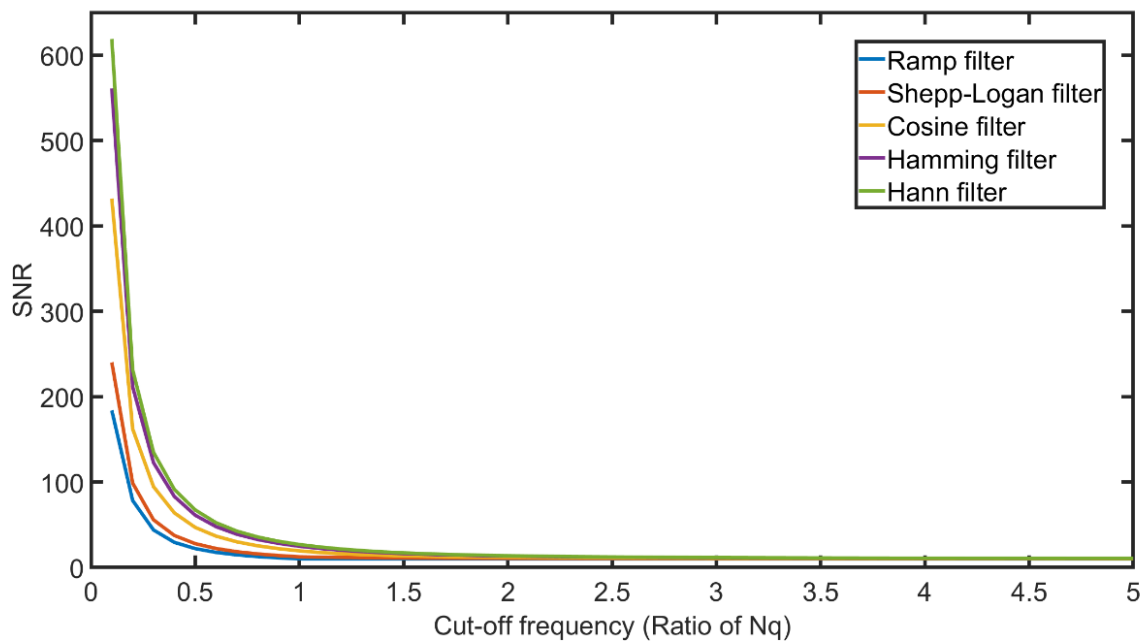
Figure 20: Circles phantom – SNR dependence on used filter type and cut-off point value. [32]

4.1.3 Summary

When dealing with FBP-based reconstruction of submicron CT data, there exists a compromise between the achieved spatial resolution and level of noise suppression during the reconstruction process. It was verified that Ram-Lak and Shepp-Logan filters do not provide optimal results for noisy data compared to the Hamming, Hann and Cosine filters that achieved the best results in terms of noise reduction. It is suggested that, for reconstruction of noisy projection data, the cut-off point should be selected less than 1.0 (< Nq) but not too low to preserve sufficient spatial resolution. In this interval the Cosine filter achieved the best results in terms of spatial resolution preservation compared to other filters. Therefore, Cosine filter is selected, and the optimal cut-off values interval is proposed to be $0.8 - 1.0$, depending on data type and amount of noise. Such defined FBP reconstruction is further used within scope of this work. [32]

4.2 Practical assessment of detectors for submicron CT applications

The key component of any CT system is a detection system (see section 1.1.3). Despite the technical development, the current detector's technology is still limited by various technical aspects that influence achievable spatial resolution of a CT system and overall quality of acquired data by presence of tomographic artifacts such as ring artifacts or noise (see section 1.2). However, for their optimal reduction it is essential understand their cause and study their properties. In the sphere of submicron CT, the integrating detectors based on CCD or CMOS technology are predominantly used, when historically the CCD-based sensors were considered as golden standard in terms of achievable data quality. In this study, performance of three integrating detectors (one CCD- and two sCMOS-based) is conducted for laboratory-based submicron CT system Rigaku nano3DX to assess possibilities of current sCMOS technology. Properties of each detector were evaluated as well as the quality and noise properties of acquired data. Part of the results have been already presented at international conference, Industrial Computed Tomography (ICT 2019), for more details please refer to: [167].

4.2.1 Materials and methods

For purposes of this work Rigaku nano3DX was equipped with Rigaku's scientific X-ray CDD camera (XSight™ Micron LC X-ray CCD camera [168]), scientific X-ray sCMOS camera (XSight™ Micron LC X-ray sCMOS camera [169]) and Rigaku's prototype camera using sCMOS technology, these cameras were labelled as CCD, sCMOS1 and sCMO2 respectively. Summary of cameras' nominal parameters without an optical lens unit is listed below in Table 5.

Table 5: Nominal parameters of tested cameras without an optical lens unit.

Technical features	CCD	sCMOS 1	sCMOS 2
Array size	3320(H) x 2500(V)	2048(H) x 2048(V)	2560(H) x 2160(V)
Pixel size	5.4 µm	6.5 µm	6.5 µm
Sensor diagonal	22.5 mm	18.8 mm	21.8 mm
Nonlinearity	< 1%	<0.2%	<0.2%
Dynamic range	2300: 1	21 400: 1	21 400: 1
Acquisition gain	0.45 e-/ADU	0.52 e$^-$/ADU	0.52 e$^-$/ADU
Readout noise	11 e- rms	1.4 e$^-$ rms	1.4 e$^-$ rms
Readout rate	8 Mpix./s (≈ 1 fps)	40 fps (@ 16 bit)	30 fps (@ 16 bit)
Dark current	0.001 e-/pix./s -35ºC	0.14 e$^-$/pix./s @ 0ºC	0.0169 e$^-$/pix./s @ -10ºC
Binning	Independent on-chip binning in x, y	2 x 2, 3 x 3, 4 x 4, 8 x 8	2 x 2, 3 x 3, 4 x 4, 8 x 8
Peak quantum efficiency	56% @ 540 nm	82% @ 550 nm	58% @ 550 nm
Shutter type	Electromechanical	Rolling shutter	Rolling shutter
Data interface	USB 2.0	USB 3.0	USB 3.0

For comparison of all tested cameras various data types were acquired which are stated in Table 6, with used acquisition settings and evaluated parameters – for more detail about evaluated parameters refer to Table 3. For measurements with CCD and sCMOS 1 camera, the sensors temperature was kept at 0 °C. For second tested sCMOS camera, the sensor temperature was set to -10 °C to evaluate effect of cooling on noise properties. Used exposure times for X-ray projection data were selected based on optimal contrast (dependent on amount of detected signal) and on intended

analysis purpose of the data. For comparison of all systems in terms of CT data acquisition, the exposure time was first selected for CCD camera based on optimal contrast and the exposure for sCMOS based cameras was subsequently derived to achieve equal detected signal level as for CCD. The evaluated CT data of a ruby ball (0.3 mm diameter) and a glass cup sample were reconstructed, from only background and flat-field corrected projections, using reconstruction settings specified in section 4.1. No data processing or corrections such as noise or ring artefacts reduction were used in our study. For some analysis DN (Digital numbers) of acquired data were converted to number of detected electrons using vendor's conversion specifications.

Table 6: List of acquired data with corresponding acquisition parameters and evaluated parameters.

Data	Acquisition parameters			Evaluated parameters
	CCD	sCMOS 1	sCMOS 2	
Bias frames	Exposure: 10 ms; Binning: 1x1; Pixel size: 5.5 μm; Frames: 10	Exposure: 10 ms; Binning: 1x1; Pixel size: 6.5 μm; Frames: 10	Exposure: 10 ms; Binning: 1x1; Pixel size: 6.5 μm; Frames: 10	Read-out noise
Dark background frames	Exposure: 1-30 s; Binning: 1x1; Pixel size: 5.5 μm; Frames: 30	Exposure: 1-30 s; Binning: 1x1; Pixel size: 6.5 μm; Frames: 30	Exposure: 1-30 s; Binning: 1x1; Pixel size: 6.5 μm; Frames: 30	Dark current Hot pixels Random hot pixels
Bright frames	Target: Cu; Exposure: 1-30 s, 60 s; XD = 0.7 mm; Binning: 1x1; Pixel size: 0.27 μm; Frames: 30, 20	Target: Cu; Exposure: 1-30 s, 30 s; XD = 0.7 mm; Binning: 1x1; Pixel size: 0.32 μm; Frames: 30, 20	Target: Cu; Exposure: 1-30 s, 30 s; XD = 1.1 mm; Binning: 1x1; Pixel size: 0.32 μm; Frames: 30, 20	Noise properties Linearity
JIMA RT RC-02B frames	Target: Cu; Exposure: 30 s, 60 s; XD = 0.9 mm; Binning: 1x1; Pixel size: 0.27 μm; Frames: 10/ chart position	Target: Cu; Exposure: 30 s; XD = 0.7 mm; Binning: 1x1; Pixel size: 0.32 μm; Frames: 10/ chart position	Target: Cu; Exposure: 30 s; XD = 1.1 mm; Binning: 1x1; Pixel size: 0.32 μm; Frames: 10/ chart position	Spatial resolution Data quality
CT data – Ruby ball (0.3 mm diameter)	Target: Mo; Exposure: 13 s; XD = 0.2 mm; Binning: 2x2; Voxel size: 0.53 μm; Projections: 802	Target: Mo; Exposure: 4.5 s; XD = 0.2 mm; Binning: 2x2; Voxel size: 0.64 μm; Projections: 802	Target: Mo; Exposure: 6 s; XD = 0.2 mm; Binning: 2x2; Voxel size: 0.64 μm; Projections: 802	Spatial resolution Data quality
CT data – Glass capillary*	Target: Mo; Exposure: 16 s; XD = 0.2 mm; Binning: 2x2; Voxel size: 0.53 μm; Projections: 802	Target: Mo; Exposure: 6 s; XD = 0.2 mm; Binning: 2x2; Voxel size: 0.64 μm; Projections: 802	Target: Mo; Exposure: 8 s; XD = 0.4 mm; Binning: 2x2; Voxel size: 0.64 μm; Projections: 802	Data quality

* For sCMOS 2 CT measurement not the same sample as for CCD and sCMOS 1 was used – only same structure.

4.2.2 Results

4.2.2.1 Noise properties analysis

Numerical results of conducted noise properties analysis are presented in Table 7. It is evident that CCD camera poses higher readout noise and also the dark current compared to sCMOS 1, when cooling both sensors to 0 °C. Second tested sCMOS camera had slightly higher readout noise than sCMOS 1, but much lower dark current compared to both other tested cameras, confirming the thermal dependence of dark current noise. Both tested sCMOS cameras had higher total noise than CCD camera which is evident from numerical results and also from both 1D and 2D normalized noise power spectra (Figure 21 and Figure 22). Specifically, in 2D total noise NNPS are evident high intensity crosses (Figure 22) for tested sCMOS cameras. The worst hot pixels and random hot pixels results achieved sCMOS 1, contrary to sCMOS 2 achieved the best hot pixels results which again reflects the positive effect of cooling.

Table 7: Results of noise properties analysis.

	Readout noise [e⁻ rms]	Dark current [e⁻/pix/s]	Total noise [e⁻ rms]	Hot pixels [%]	Random hot pixels [% / frame]
CCD	10.67	0.102	101.53	0.06	0.24
sCMOS 1	1.32	0.057	118.75	0.47	0.74
sCMOS 2	1.35	0.007	103.68	0.04	0.73
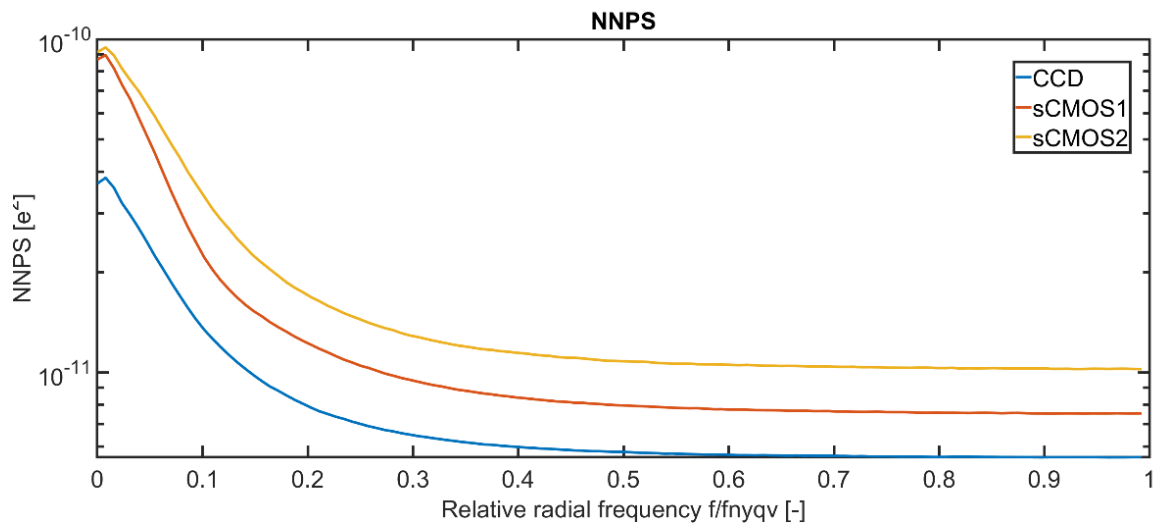
Figure 1

Figure 21: Comparison of 1D NNPS for all tested cameras.

a) CCD

b) sCMOS 1

c) sCMOS 2
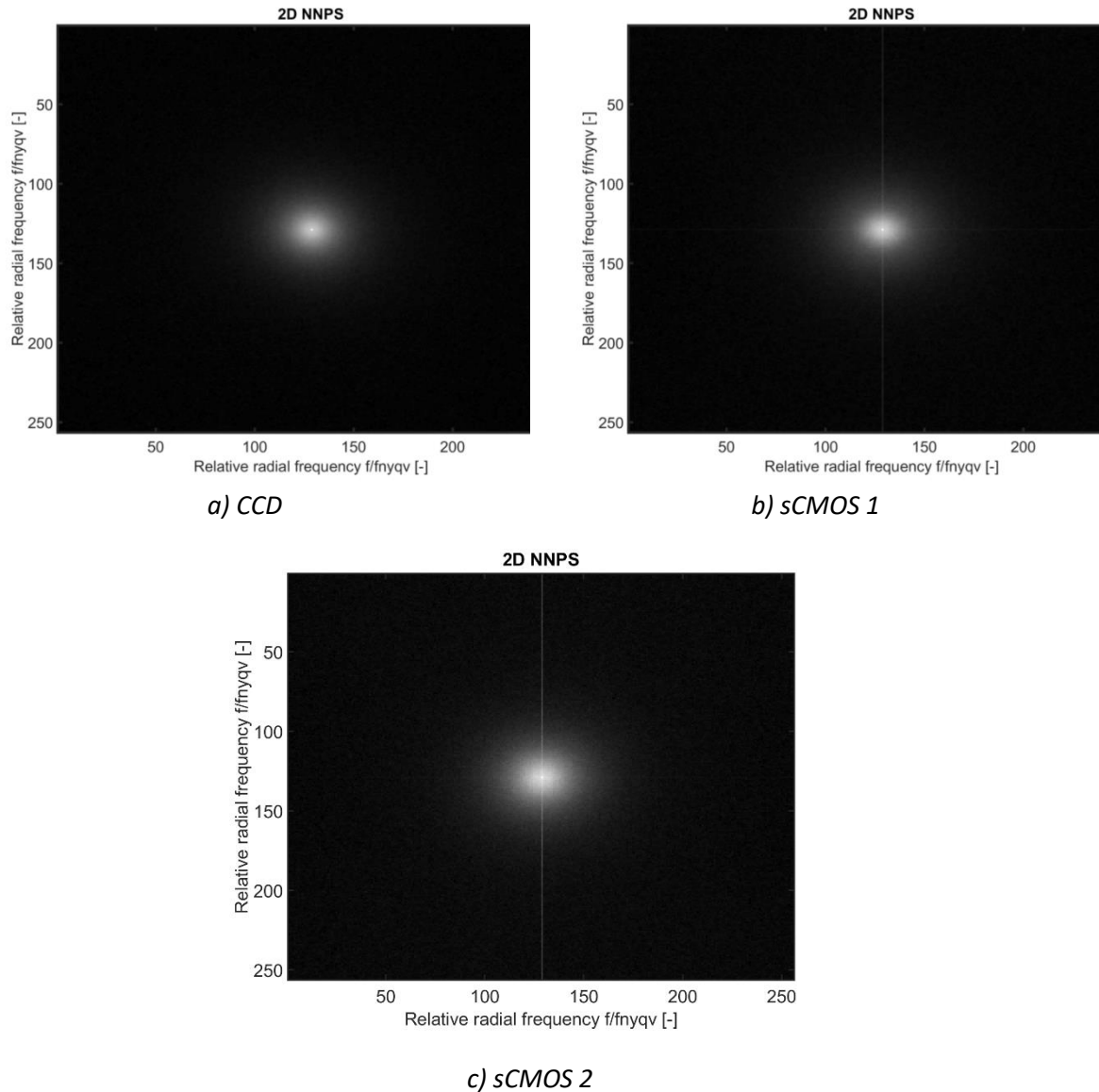
Figure 22: 2D NNPS for all tested cameras.

4.2.2.2 Spatial resolution analysis

Achievable spatial resolution of Rigaku nano3DX system was evaluated for all tested cameras in both projection and tomogram domain using JIMA RT RC-02B resolution test and MTF analysis (defined in section 3.3). It was revealed that in projection domain and the system was able to reach 0.5 μm resolution in both horizontal and vertical directions for all tested cameras. In case of CCD camera, the resolution was comparable in both spatial direction (see Figure 23). However, in case of sCMOS cameras, it was revealed that the resolution was higher in horizontal direction (see Figure 23). The results of spatial resolution estimation in CT domain according to ASTM E1695-95 are stated in the Table 8. The best achievable spatial resolution was for CCD camera, which corresponds to its smallest voxel-size value and good data quality. Although, both sCMOS cameras had same voxel-size value, the sCMOS2 has worse achievable spatial resolution. This correspond to results of JIMA RT RC-02B resolution test (Figure 23), where is sCMOS 2 had blurrier line profile in vertical direction.

45
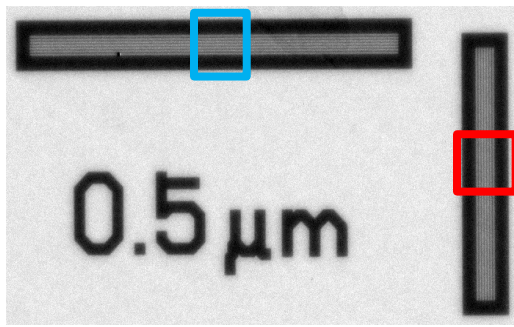
a) CCD
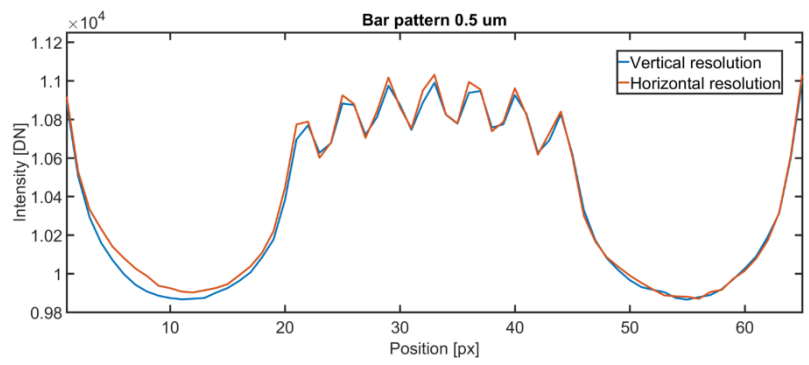
b) CCD
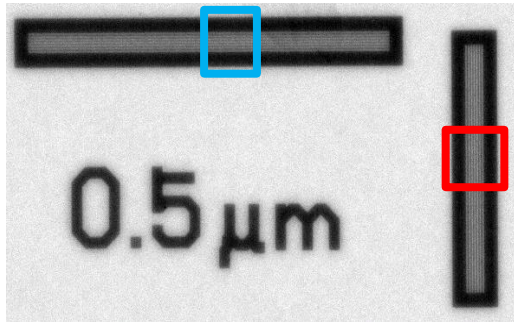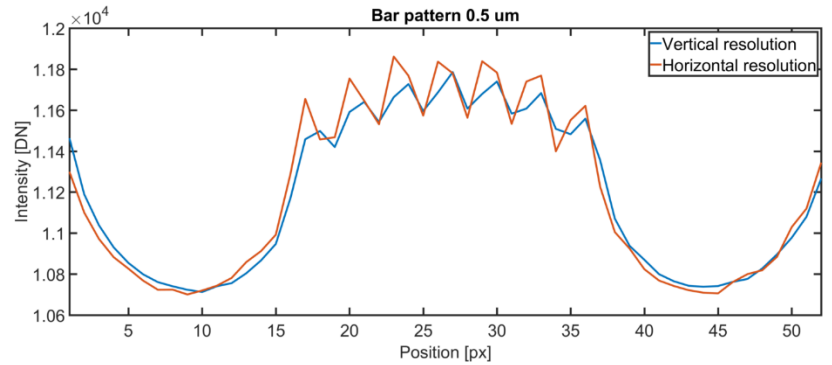
c) sCMOS 1

d) sCMOS1
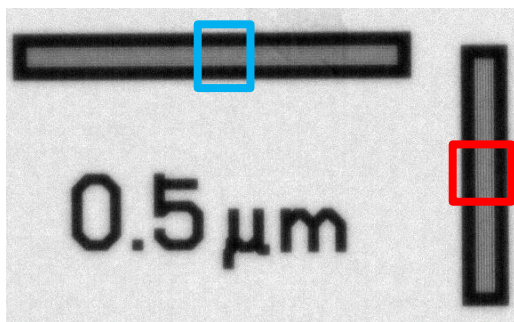
e) sCMOS 2
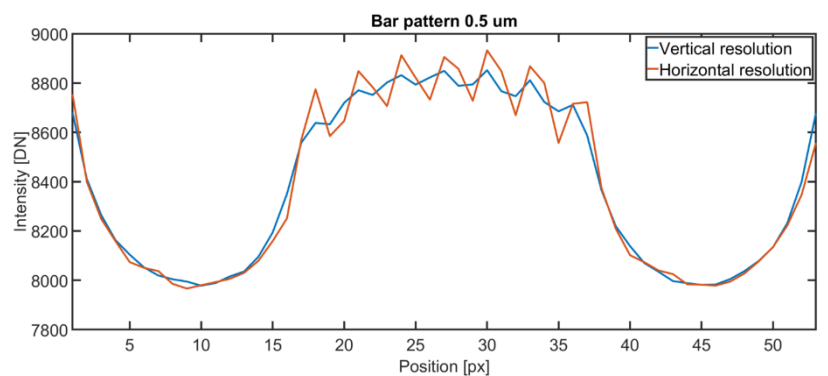
d) sCMOS2

Figure 23: JIMA RT RC-02B resolution test: JIMA 0.5 µm chart; labelled areas were used for resolution line profile analysis.

Table 8:Results of MTF analysis

Camera	MTF 10 % level [lp/µm]	Spatial resolution [µm]
CCD	0.307	0.863
sCMOS1	0.342	0.933
sCMOS2	0.286	1.115

4.2.2.3   Linearity analysis.

Based on conducted linearity analysis, it was revealed that all cameras have responses linearly proportional to amount of incident photons (Figure 24). For all cameras the root mean square error (RMSE) of the distances between detected signal points and the linear fit was found to be negligible (Table 9).

a) CCD

b) sCMOS1

c) sCMOS2
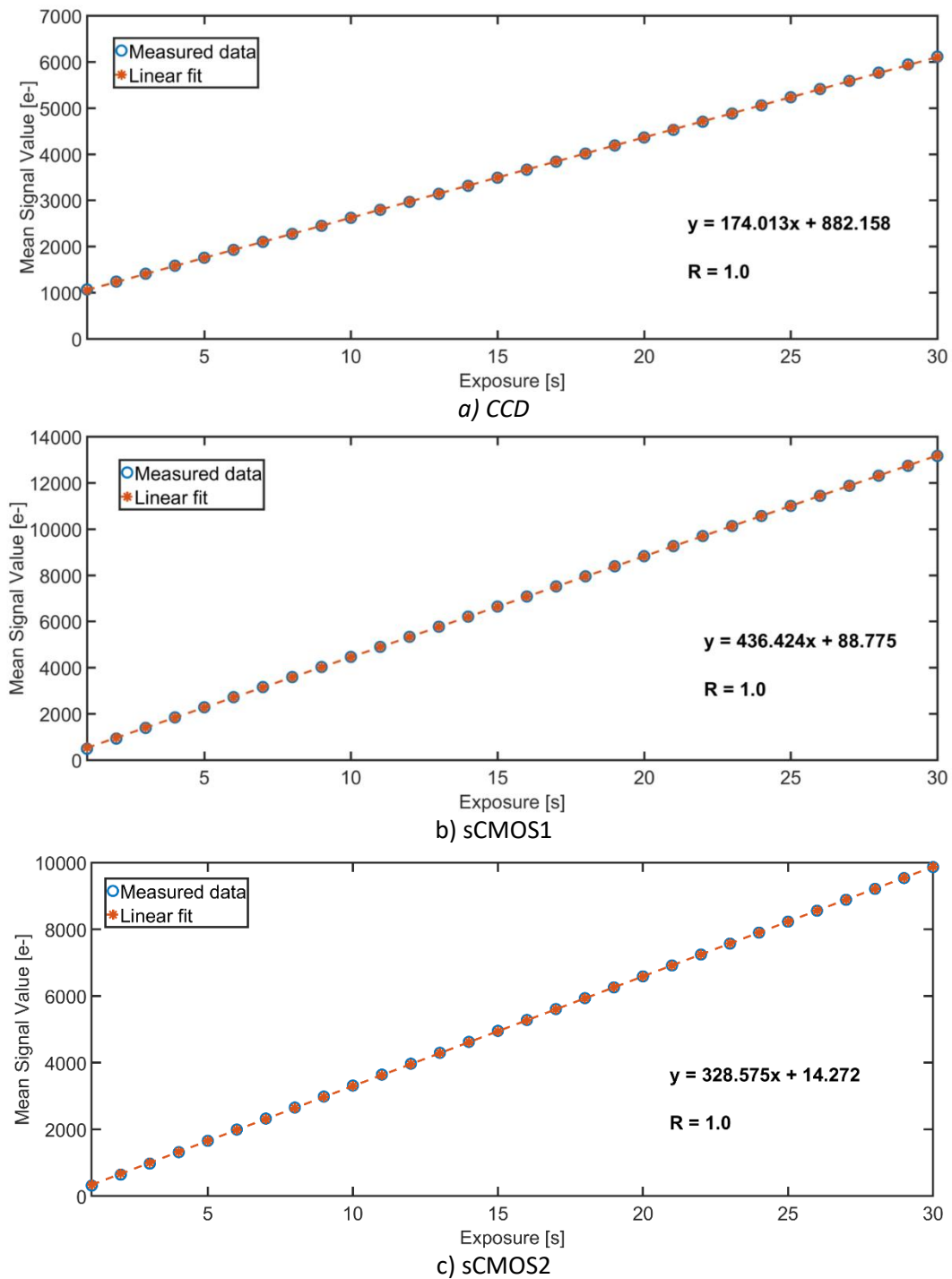
Figure 24: Bright-field frames linearity analysis.

Camera	RMSE [%]
CCD	9.93e-11
sCMOS1	2.05e-10
sCMOS2	7.22e-11

4.2.2.4 Data quality

Quality of acquired data was evaluated quantitatively and qualitatively. In projection domain, there were no significant data quality differences between all cameras except the vertical pattern that was visible in both sCMOS 1 and sCMOS 2 data (Figure 25). However, this pattern was visible only in central area of the projection images – detector rows covering sample area. This resulted to severe ring artifacts present in CT data acquired by tested sCMOS cameras (Figure 26). These artifacts were also present in CCD acquired data but not in such extent (Figure 26), which corresponds with results from hot pixels' analysis (Table 7). For quantitative evaluation six measures were calculated in both projection and tomogram domain and the results are presented in Table 10 and Table 11. For all evaluated data, the CCD camera reached higher SNR. Low SNR results in case of both rested sCMOS cameras can correspond to hot pixels population that could affect the analysis, specifically in tomogram domain (Table 11). In case of same exposure for all tested cameras (JIMA chart pattern), sCMOS 1 reached the best overall results compared to CCD and sCMOS 2, which corresponds to level of detected signal. Also, for situations, when comparable signal was detected by all tested sensors, sCMOS cameras reached better or comparable results to CCD camera.
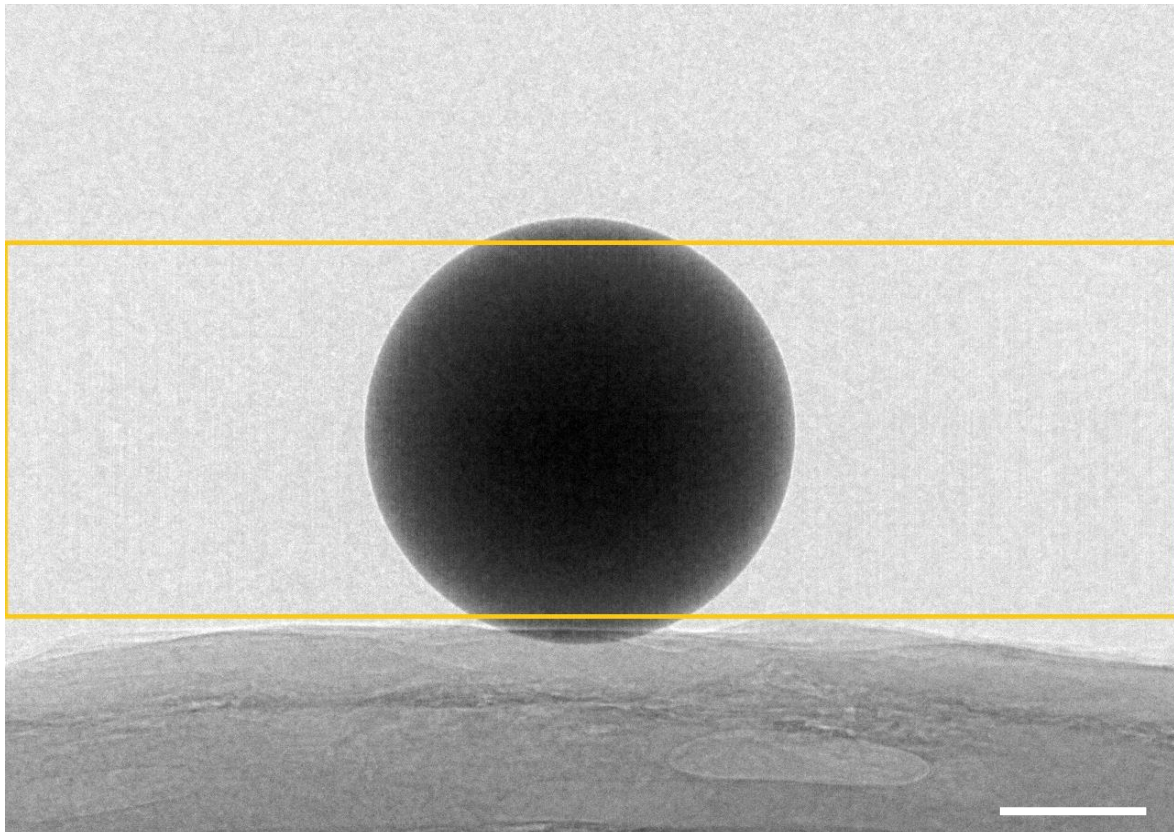
Figure 25: Example of projection image of Ruby ball – acquired by sCMOS 2. The vertical pattern is visible in central area – labelled by yellow rectangle; scale bar: 100 µm.

a) Ruby ball – CCD

b) Glass capillary – CCD

c) Ruby ball – sCMOS 1

d) Glass capillary – sCMOS 1

e) Ruby ball – sCMOS 2

f) Glass capillary – sCMOS 2
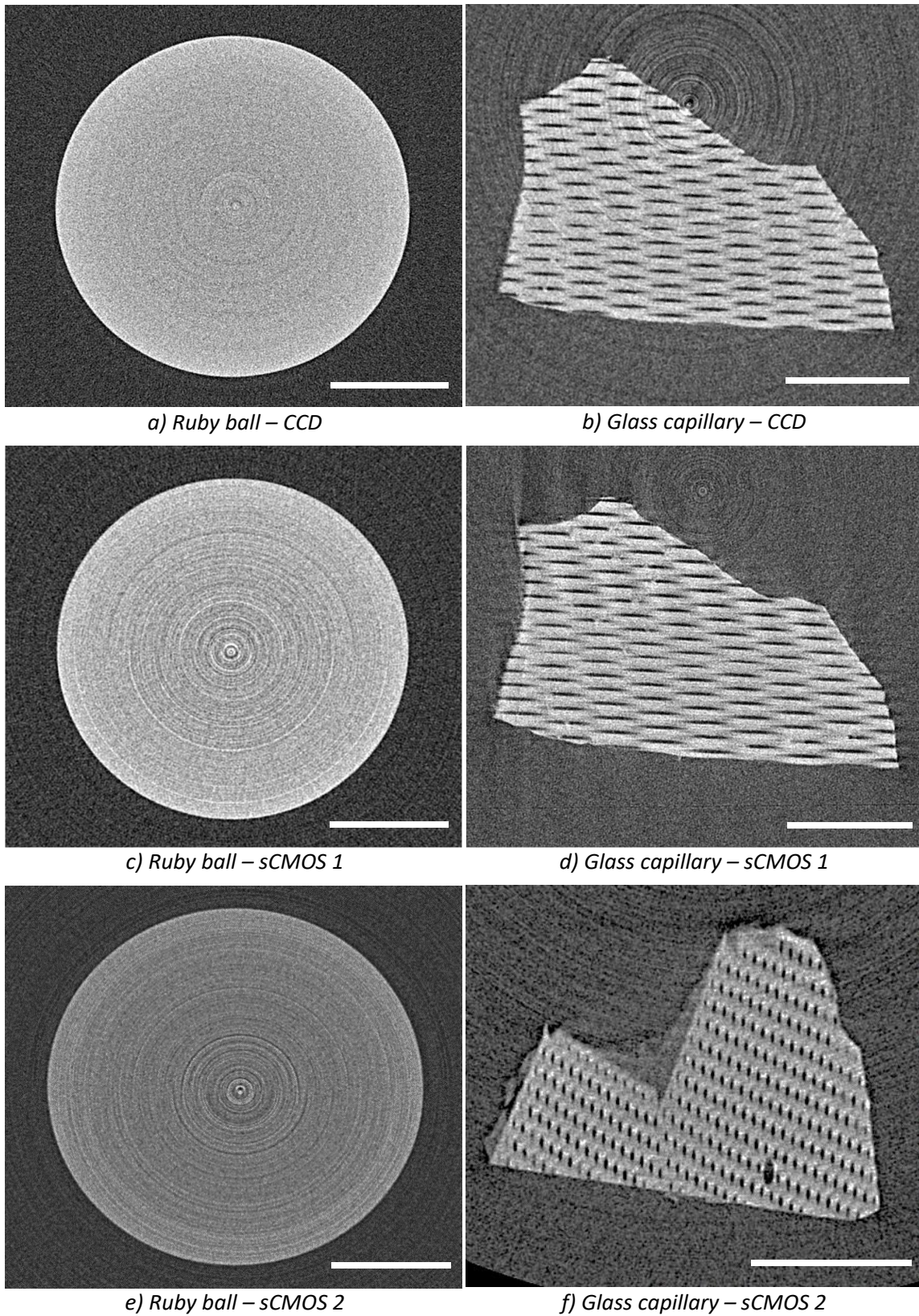
Figure 26: Comparison of raw CT images without any processing (no ring artifacts and noise reduction) acquired by tested cameras; central areas are shown; scale bar: 100 μm.

Table 10: Results of data quality analysis for acquired projection data.

	CCD				sCMOS 1			sCMOS 2		
	JIMA (30 s)	JIMA (60 s)	Ruby ball	Glass cap.	JIMA (30 s)	Ruby ball	Glass cap.	JIMA (30 s)	Ruby ball	Glass cap.
CNR	7.07	10.15	28.83	28.80	10.51	17.75	25.52	10.20	21.20	27.30
SNR	8.73	9.10	3.53	51.0	6.89	3.17	9.60	4.26	3.99	15.97
C	0.56	0.61	1.0	0.14	0.72	1.0	0.48	0.88	1.00	0.53
VAR	3e-3	4e-3	1.85e-5	1.47e-4	0.01	1e-3	8.91e-4	2.7e-3	1.5e-3	4.4e-3
SML	184.76	185.48	381.94	280.53	164.25	3778.60	137.63	137.41	6303.33	162.45
JNB	1.39	2.61	0.98	2.09	3.20	0.63	2.75	2.51	0.81	3.08

Table 11: Results of data quality analysis for tomographic data.

	CCD		sCMOS 1		sCMOS 2	
	Ruby ball	Glass cap.	Ruby ball	Glass cap.	Ruby ball	Glass cap.
CNR	6.15	4.44	6.11	4.41	6.13	5.33
SNR	79.28	278.15	26.63	26.06	27.38	34.47
C	0.08	0.03	0.39	0.40	0.40	0.34
VAR	1.98e-4	1.03e-4	2e-3	0.01	1.4e-3	6.4e-3
SML	1158.71	106.31	1682.12	519.72	1754.90	187.52
JNB	7.89	4.52	6.94	5.13	11.94	16.22

4.2.3 Summary

In this study, comparison of CCD- and two sCMOS-based detectors in field of submicron CT was conducted using Rigaku nano3DX system. All detectors were compared in terms of their properties and also acquired data quality. For that, image data of phantoms as well as selected samples from material sciences were acquired and evaluated in projection and tomogram domain. Acquired results showed that there were not negligible differences between all tested cameras, specifically in terms of noise properties, achieved spatial resolution and number of hot pixels. However, it was shown that both sCMOS-based detection systems can be used for the task of submicron CT. Specifically, they had better quality and noise properties results for low exposure time measurement scenarios compared to situation when CCD sensor was used. Therefore, those detectors can be used for imaging of fast dynamic processes where it is crucial to keep the acquisition time as low as possible.

4.3 Noise reduction for submicron CT data

In this section work regarding noise reduction in the sphere of submicron CT is presented and summarized. First, noise properties were studied and then several algorithms were tested for reduction of all noise compounds found in the data. All acquired knowledge was then used for proposal of optimal noise reduction procedure in 3D projection data acquired by means of submicron CT system Rigaku nano3DX using XSight™ Micron LC X-ray CCD camera [168]. Part of the results have been already presented in form of a poster at 12th International Conference on Computer Graphics, Visualization, Computer Vision and Image Processing (CGVCVIP 2018) in Madrid, Spain: [170]. [32]

4.3.1 Noise model

Results regarding noise properties from previous study (4.2.2.1) were used and further extended. Here, the focus was placed on estimating a noise distribution model which is an essential parameter for optimal noise reduction. First, the total noise was extracted from set of bright-field frames (acquisition parameters are specified in Table 6) by subtraction of an average bright-field frame from intensity stabilized frames. Such extracted noise was further analysed using normal probability plot analysis (Figure 27). It was revealed that two main components can be separated from the extracted total noise: one following Gaussian distribution (Shot noise) and the second outside this distribution with values around borders of used intensity dynamic range (classified as random valued impulse noise). The first and major noise component (in terms of number of affected pixels) was further analysed to confirm its distribution (Figure 28), when the actual distribution of this component was compared to reference Gaussian distribution having the same characteristics, i.e. mean value and variance. [32]
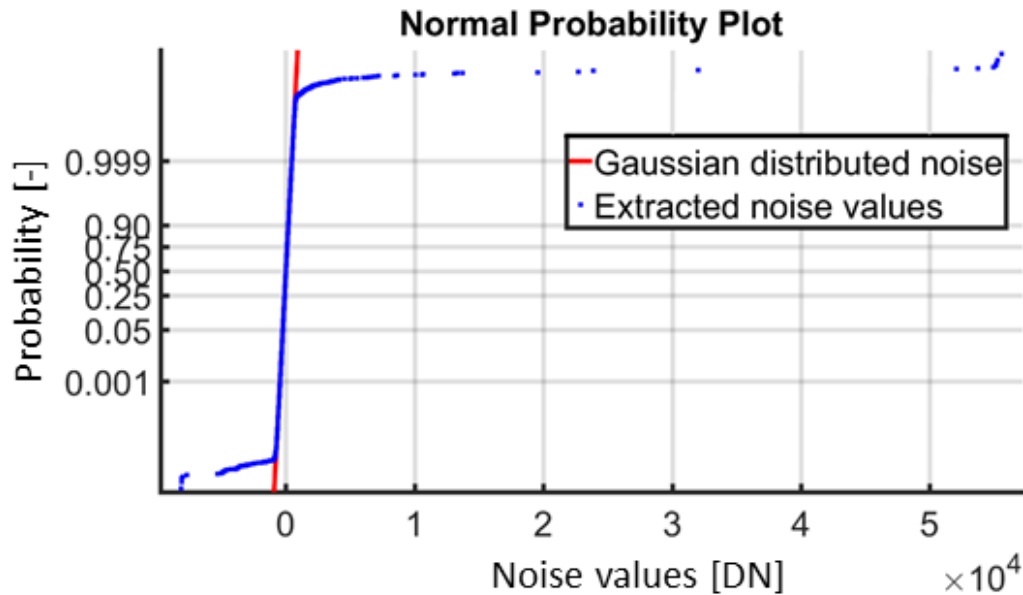
Figure 27: Normal probability plot analysis of extracted total noise. [32]
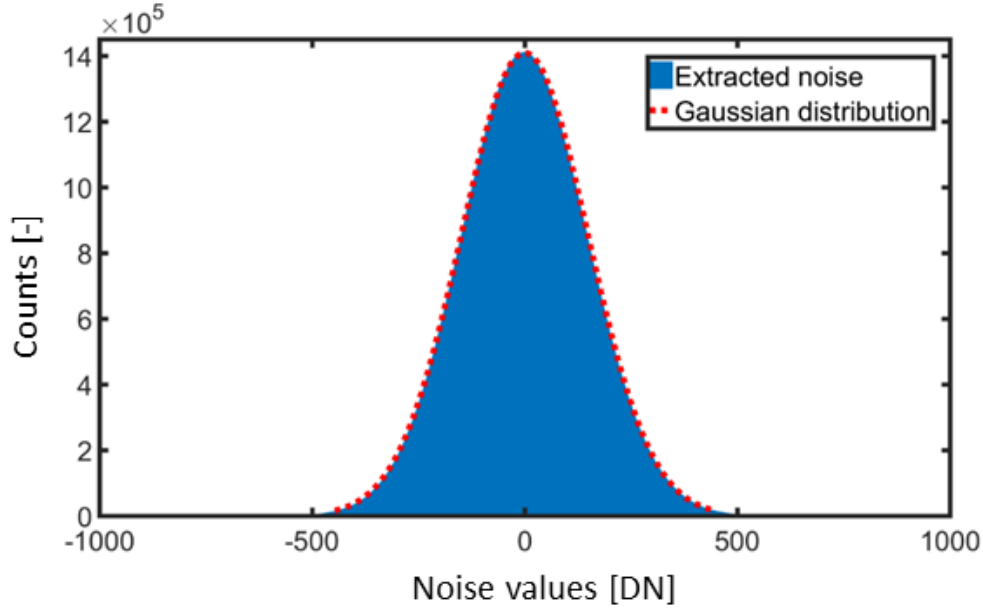
Figure 28: Comparison of shot noise distribution with reference Gaussian distribution having the same characteristics, i.e., mean value and variance. [32]

4.3.2 Proposed algorithm for estimation of noise absolute deviation

As beforehand mentioned, exact noise characteristics are essential for optimal noise reduction. Specifically, in case of Gaussian distributed noise, most denoising algorithms sets their parameters based on standard deviation of noise present in data. In this work, new algorithm was proposed for exact noise absolute deviation estimation. This algorithm is based on Imearkear method [171] and inspired by its modification published by Tai [172]. [32]

In original algorithm noise variance is calculated as weighted average of convolution result of input image with 2D kernel:

$$N = \begin{bmatrix} 1 & -2 & 1 \\ -2 & 4 & -2 \\ 1 & -2 & 1 \end{bmatrix}. \tag{4-1}$$

This kernel was derived to be insensitive to the Laplacian of an image. However, it was revealed that this assumption is not always fulfilled. Especially in highly textured images, thin lines and other small structures can be perceived as noise, resulting in noise over-estimation. Therefore, Tai in his work [172] proposed to first perform edge detection using Sobel operator and then follow Imearkear approach [171], but exclude detected edge pixels from variance calculation. However, it was found that even this modification is not sufficient for highly textured images with low levels of noise, where the noise standard deviation was in many cases overestimated. [32]

Our proposed approach was inspired by Tai's method [172], but different edges and structures detection approach is used. These features are detected using local standard deviation calculation followed by global thresholding with automatic threshold selection based on statistical evaluation. Specifically, as edge pixels are considered the pixels with high local standard deviation values. Using

this detection approach all structural pixels can be precisely identified and then excluded from absolute deviation calculation using the formula:

$$\sigma = \sqrt{\frac{\pi}{2}} \frac{1}{6 \sum(1-G)} \sum |(I(x,y) * N)(1-G)|, \tag{4-2}$$

where $I(x,y)$ is the input image at spatial coordinates x,y; N is the convolution kernel described by equation (4-2) and G is result of edge and remaining structures detection. [32]

4.3.2.1   Results

Functionality of proposed algorithm was tested using Shepp-Logan phantom with several levels of Gaussian distributed noise added to its original values. For this analysis, the input data were normalized to intensity range from 0 to 1. Results were also compared to previously mentioned methods and stated in Table 12. The proposed algorithm achieved superior results for low levels of noise and in total reached the minimal overall deviation to reference standard deviation values compared to the other tested methods. [32]

Table 12: Comparison of noise estimation methods. [32]

Reference value σ_{ref}	Immerkear σ	Tai σ	Proposed method σ
0.0	0.002	0.001	0.000
0.001	0.003	0.002	0.001
0.005	0.007	0.006	0.005
0.01	0.012	0.011	0.010
0.05	0.051	0.051	0.050
0.1	0.101	0.101	0.100
0.25	0.251	0.250	0.250
0.5	0.501	0.501	0.501
0.75	0.750	0.750	0.750
1.0	1.003	1.003	1.003
$\sum |\sigma_{ref} - \sigma|$	**0.014**	**0.010**	**0.004**

4.3.3 Proposed algorithm for impulse noise reduction

As introduced in the section 1.2.1, median filter [66] has been widely accepted as solution for impulse noise reduction with high computational efficiency while on the other hand leading to blur and certain loss of information. Therefore, modified versions of it have been till now developed to overcome these drawbacks: adaptive median filter [67; 68; 69], weighted median filter [70; 71], decision based median filter [72; 73], fuzzy median filters [74; 75; 76] or switching median filters [77; 78; 79]. However, till today not fully acceptable and universal solution exists for the submicron CT data. In this work, new impulse noise reduction algorithm was proposed specifically for such data.

This algorithm is a switching median filter, having the first step noise affected pixels detection and followed by correction of those pixels in second step. Detection of affected pixels is based on a local image statistic called ROAD ("Rank-Ordered Absolute Differences") published by Garnett [78]:

$$ROAD_m(x) = \sum_{i=1}^{m} r_i(x), \tag{4-3}$$

where r_i is the ith smallest absolute intensity difference of the pixels in squared shaped neighbourhood around the pixel x, when in the original work is recommended to use $m = 4$. The ROAD statistic provides a measure of how close a pixel value is to its four most similar neighbours, when the unwanted impulses will vary greatly in intensity from most or all of their neighbouring pixels, whereas most pixels composing the actual image should have at least half of their neighbouring pixels of similar intensity, even pixels on an edge [78]. To further improve identification of impulse noise affected pixels, it is proposed to calculate ROAD values for both original image and for median filtered image and subtract results from each other, further followed applying the log function on the result. This leads to suppression of negative structural effect and to amplification of differences between affected pixels with small dissimilarity and non-affected pixels in their neighbourhood.

As noise-affected pixels are subsequently identified those pixels which achieved statistically significant high dissimilarity values:

$$g(x,y) = \begin{cases} 1, & if\ f(x,y) \geq \bar{f} + 2 \cdot \sigma_f \\ 0, & if\ f(x,y) < \bar{f} + 2 \cdot \sigma_f \end{cases} \tag{4-4}$$

where *f(x,y)* is the input log transformed subtraction result of ROAD statistics from original and median filtered data and the threshold value to corresponds to sum of mean value and twice the standard deviation of the input *f* and *g(x,y)* is binary value of output binary image g both at corresponding spatial coordinates x, y. For correction, the detected noise pixels ($g(x, y) = 1$) are replaced by values from median filtered image from corresponding coordinates *x,y*. This replacement strategy is proposed to achieve good computational effectivity.

4.3.3.1 Results

For practical testing of proposed algorithm Lenna test image was used due to its sufficient structural complexity. Random valued impulse noise was added to this image, where its values were generated randomly around borders of used dynamic range and the affected positions were also selected randomly to cover 5 % of all image pixels (see Figure 29). Proposed algorithm was tested and compared to other methods that are in practice used (standard median filter [66], Progressive switching median filter (PSMF) [77] and Noise adaptive fuzzy switching median filter (NAFSM) [76]). Their results were compared in terms of three selected metrics: the peak signal-to-noise ratio (PSNR), mean squared error (MSE) and structural similarity index [173], where the original noise unaffected Lenna test image is considered as reference. From the results, stated in Table 9, it is evident that proposed algorithm achieved best scores compared to other tested methods. For visual evaluation, the results of proposed algorithm are demonstrated in Figure 29 and Figure 30. Especially in Figure 30, the structural preserving capabilities of proposed algorithm are clearly visible compared to standard median filter. [32]

Table 13: Comparison of selected methods for impulse noise reduction using Lenna image. [32]

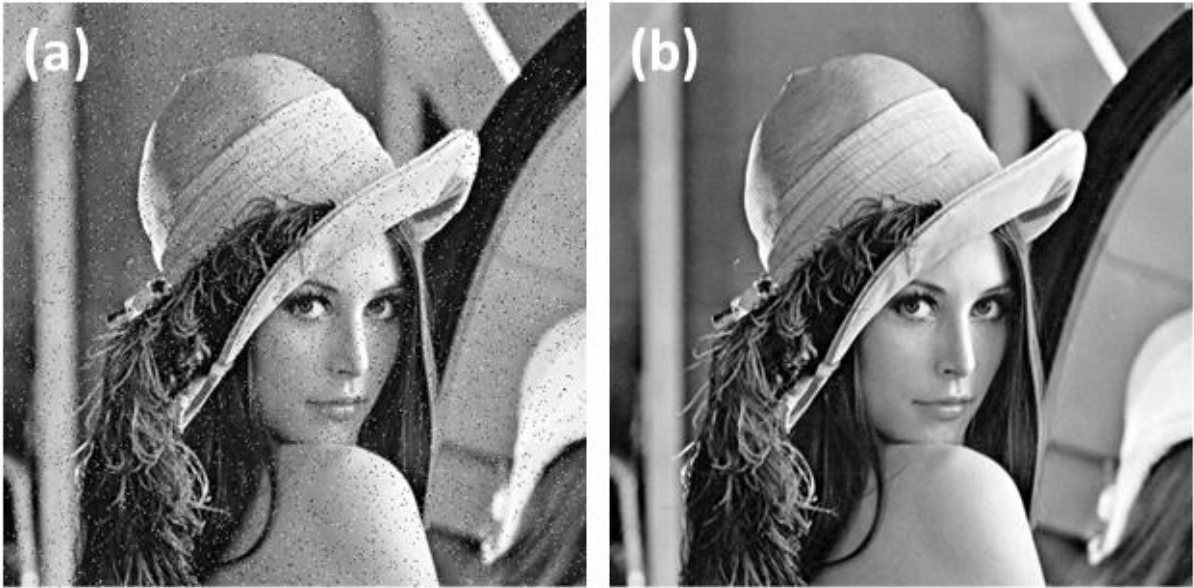| Method	PSNR [dB]	MSE	SSIM
Median	33.750	4.221 e-4	0.907
PSMF	43.736	4.243 e-5	0.995
NAFSM	24.592	0.004	0.645
Proposed	45.547	2.794 e-5	0.996

Figure 29: Results of proposed impulse noise reduction algorithm demonstrated on the Lenna test image: a) input image; b) filtered image.
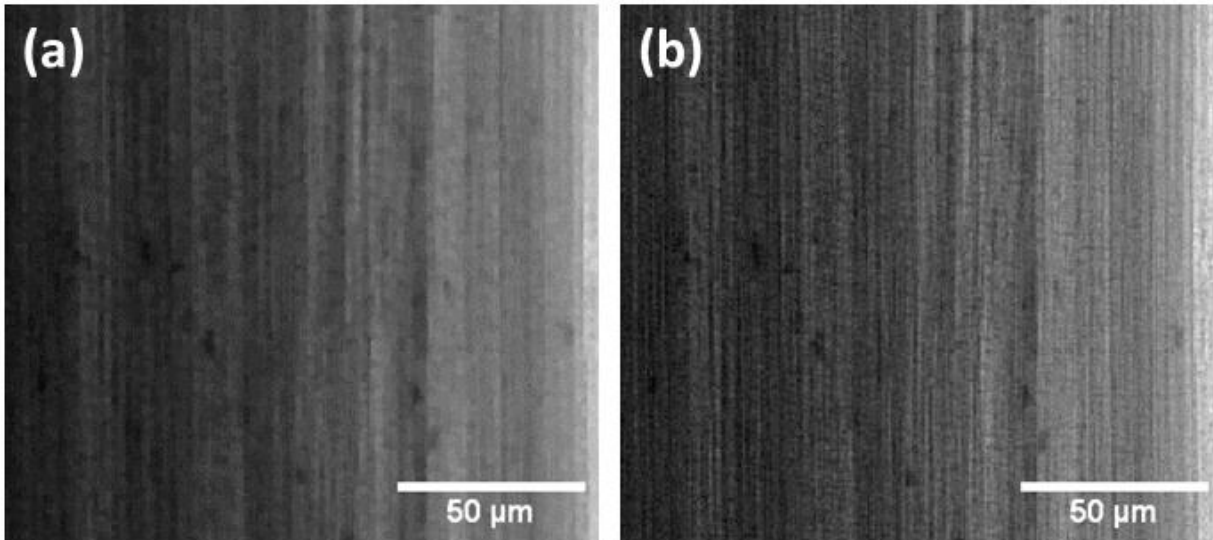

Figure 30: Comparison of impulse noise reduction capabilities on real projection data: a) standard median filter; b) proposed filter. CT system: Rigaku nano3DX; Sample: bamboo stick. [170]

4.3.4 Shot noise reduction

For reduction of shot noise, three algorithms were tested: 3D implementation of Gaussian filter [80], Non-Local-Means (NLM) filter optimized for 3D data [82] and Collaborative approach for enhanced denoising under low-light excitation (CANDLE) [83]. Those methods were specifically selected according to either their low computational cost (Gaussian) or reported superior results (NLM and CANDLE). Methods were tested both in projection and tomogram domain. In projection domain, the JIMA chart resolution pattern was used (data acquisition parameters are specified in Table 6). In tomogram domain, two types of samples were selected: single material sample of ruby ball (Lens unit: L1080, Binning: 2x2, Target: Mo, Exposure: 6 s, voxel size: 2.11 μm) and highly complex sample of Arabidopsis seedpod (Lens unit: L0270, Binning: 2x2, Target: Cu, Exposure: 28 s, voxel size: 0.53 μm). The evaluated CT data were reconstructed using reconstruction settings specified in section 4.1. For quantitative assessment, the achieved spatial resolution and data quality were selected as the evaluation metrics. Spatial resolution was evaluated both in projection and tomogram domain using JIMA RT RC-02B resolution test and MTF analysis (defined in Table 3). As data quality metrics, the SNR and CNR were selected. Specific settings of used methods were tuned according to visual perception of processed data or according to recommendations from original authors.

4.3.4.1 Results

In projection domain, the frame's averaging strategy (10 frames were used) was further incorporated and within the results evaluation considered as reference. Quality of denoising can be visually evaluated in Figure 31, but only minor differences are visible there for all tested methods. Such minor differences are also reflected by the line profile analysis presented in Figure 32 and data quality assessment in Table 14. In the quantitative evaluation (Table 14), the frame's averaging reached the worst results, which might correspond to number of averaged frames. On contrary, the Gaussian filter achieved the best numerical results.

Table 14: Results of data quality analysis in projection domain.

	SNR	CNR
Original	37.73	6.30
Averaging	89.16	16.39
Gaussian	109.47	23.26
NLM	104.72	20.40
CANDLE	103.58	21.52
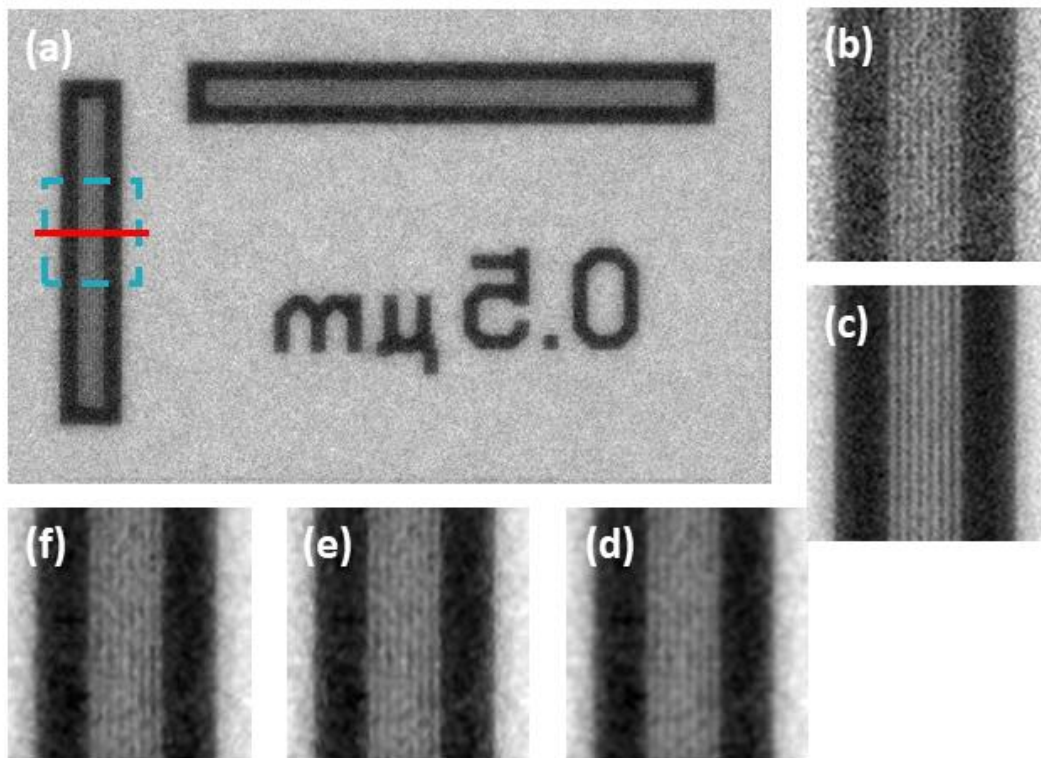
Figure 31: Comparison of tested denoising methods in projection domain on JIMA RT RC-02B chart pattern: a) and b) original data; c) frames averaging; d) CANDLE; e) NLM and f) Gaussian. Red line indicates region assessed by line profile analysis.
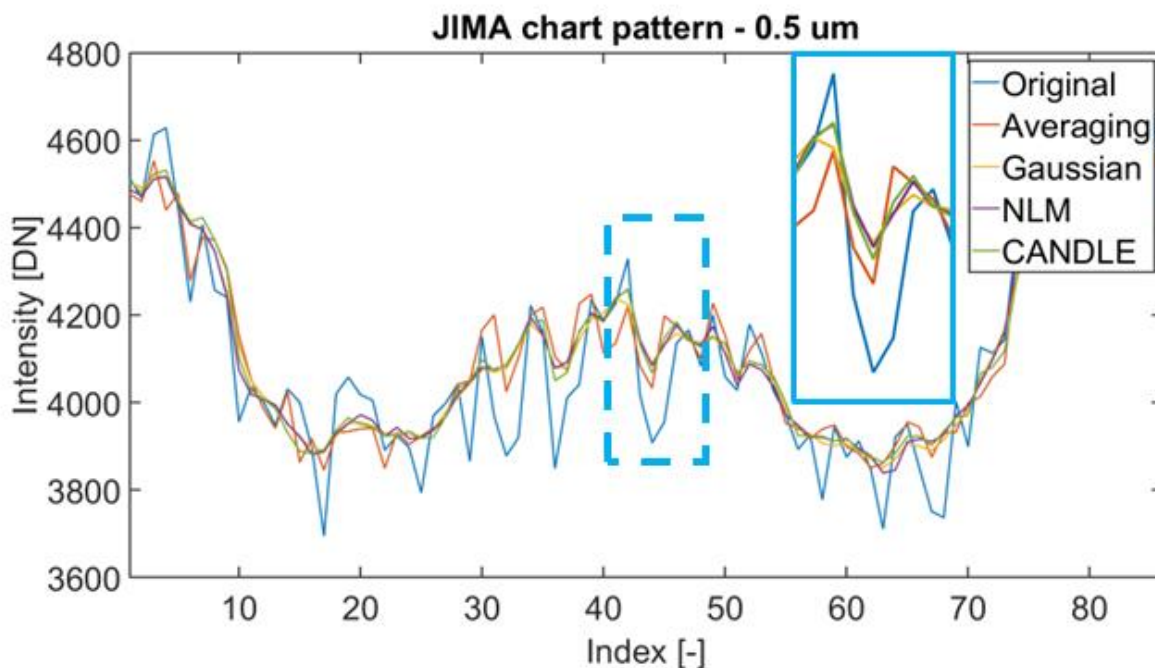
Figure 32: Comparison of tested denoising methods in projection domain using JIMA RT RC-02B resolution test.

In tomogram domain, the CANDLE algorithm achieved the best overall results, corresponding to its local adaptation for noise inhomogeneity and noise stabilization. This algorithm achieved unmatched smoothing and details preservation capabilities independent on sample's complexity (Figure 33 and Figure 34). This is further reflected by quantitative assessment (Table 15 and Table 16), where the spatial resolution preservation can be pointed out (Table 15). However, such high-quality results were balanced by high computational demands (Table 15 and Table 16). Therefore, it was concluded that depending on domain (i.e., projection or tomogram) specific algorithm should be used.
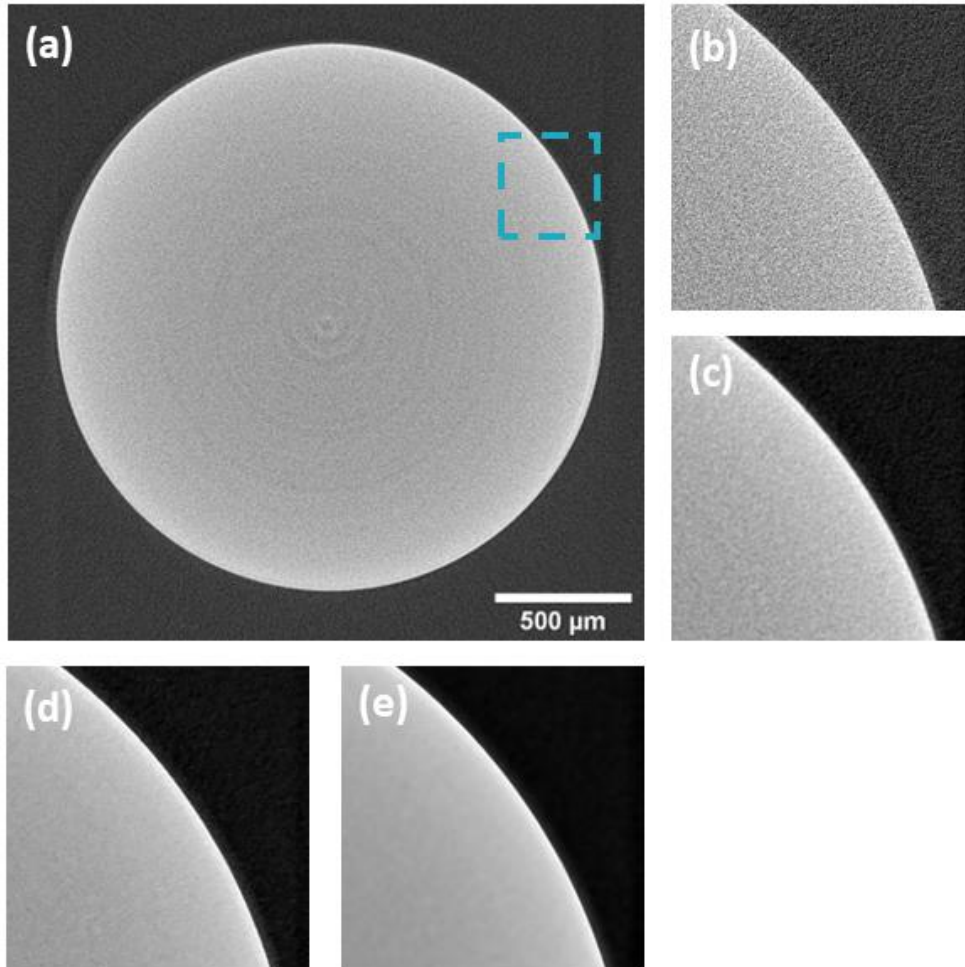
Figure 33: Comparison of tested methods in tomogram domain on single material sample (ruby ball): a) and b) original; c) Gaussian; d) NLM and e) CANDLE.

Table 15: Results of data quality and spatial resolution analysis in tomogram domain for single material sample (ruby ball). The computational time (t) was evaluated for 1000 x 1000 x 11 data and on PC with Intel® Core™ i7-7800x, 3.55 GHz, 128 GB RAM.

	SNR	CNR	SR [µm]	t [s]
Original	7.99	4.97	2.15	-
Gaussian	34.33	21.40	2.79	0.48
NLM	44.37	28.07	2.34	24.40
CANDLE	122.27	63.21	2.13	222.28
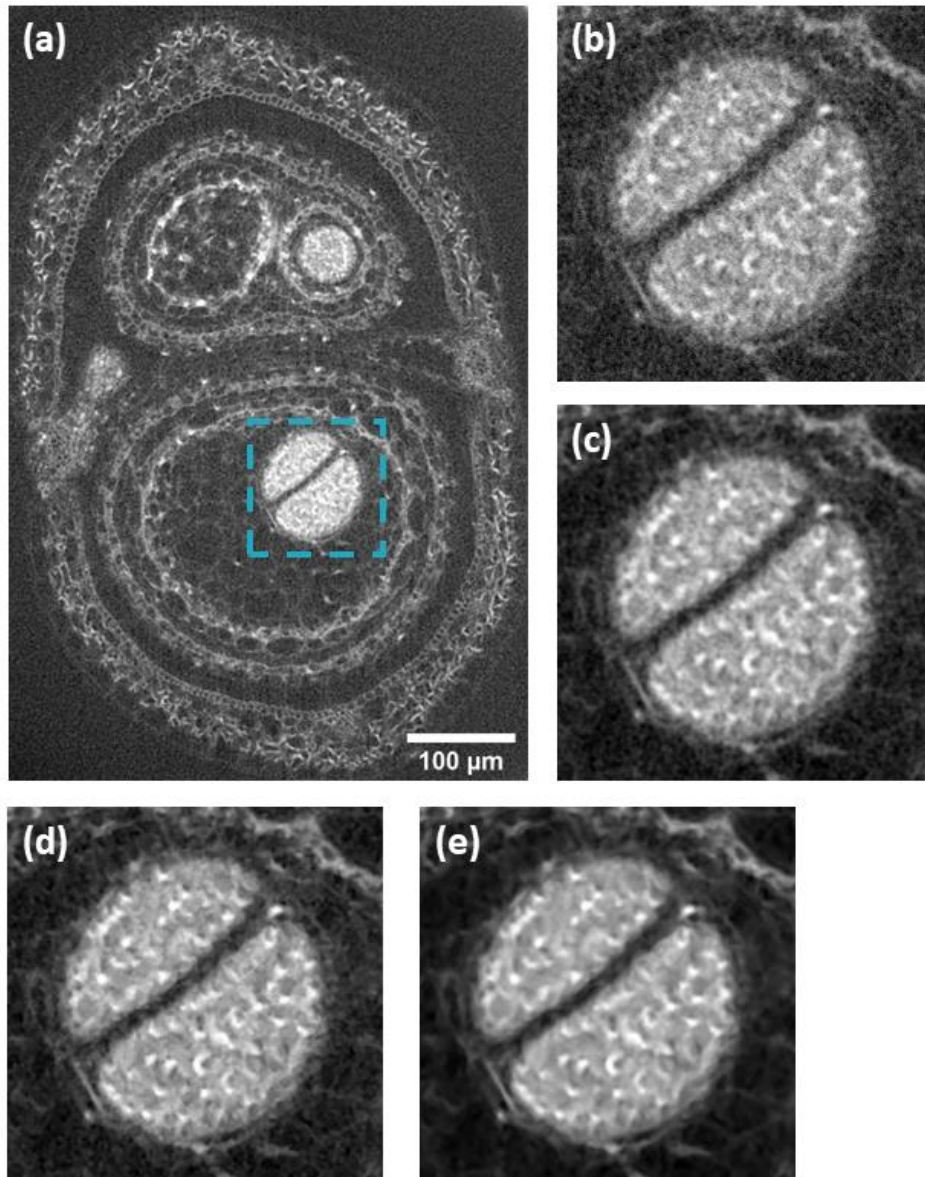
Figure 34: Comparison of tested methods in tomogram domain on complex sample (Arabidopsis seedpod): a) and b) original; c) Gaussian; d) NLM and e) CANDLE.

Table 16: Results of data quality and analysis in tomogram domain for complex sample (Arabidopsis seedpod). The computational time (t) was evaluated for 1341 x 900 x 11 data and on PC with Intel® Core™ i7-7800x, 3.55 GHz, 128 GB RAM.

	SNR	CNR	t [s]
Original	6.82	7.65	-
Gaussian	8.72	14.76	0.44
NLM	8.07	15.44	12.02
CANDLE	9.34	23.80	204.59

4.4 Ring artifacts reduction

As introduced in the section 1.2, CT data are often affected by severe ring arti-facts. They appear as concentric ring-like features superimposed on the imaged scene and are centred on the object's centre of rotation. Ring artifacts are mainly caused by imperfect detector pixels, where a perfect pixel's response should be linearly proportional to the amount of photons incident on the detector. There are many different underlying causes for individual pixels to have imperfect responses. These include defects in the scintillator, the detector itself, and the readout electronics. Moreover, the detector responses may vary due to numerous time-dependent drifts, such as thermal drifts, and also due to changes in the X-ray spectrum. No matter the cause, ring artifacts degrade the resulting image quality. Therefore, it is desirable to remove or at least significantly reduce the presence of ring arti-facts in CT data. However, in the field of submicron CT, the small size of detector pixels used in nano CT devices does not enable an application of any hardware-based method for removing ring artifacts, leaving image-based processing methods as the most promising way for an effective ring artifacts removal. Several approaches from this class exist (see section 1.2), but each with some deficiencies, such as the degradation of data quality and spatial resolution, which is inconsistent with the core purpose of submicron CT. [105]

In the scope of this work, a new two-step ring artifacts reduction scheme was proposed that combines several selected ideas from image-based processing methods into one complex method with a goal to overcome their individual weaknesses and limitations. This procedure was developed for the artifacts' reduction in the sinogram domain and is based on a categorization of ring artifacts into two types. The ring artifacts are categorized based on the observation of responses from different kinds of deficiencies in sinograms and on their specific hardware causes (see Figure 35). In the proposed reduction scheme, each of these classes is then addressed separately using dedicated detection and reduction procedures. The novel iterative schemes based on relative total variations (RTV) [174] were integrated to detect the artifacts. The correction process uses the image inpainting, and the intensity deviations smoothing method. The reduction strategy was optimized for each artifact type separately to preserve the spatial resolution and sample's structural information, which are the most important factors in the field of submicron CT. Practical functionality of the prosed method was verified on both synthetic data and real CT data. It shows a high efficiency of ring artifacts removal, and a robustness to character of input data and used detection system in context of other tested ring artifacts correction techniques. The practical testing demonstrated that the proposed ring artifacts reduction procedure, compared to other methods (see Figure 36), can achieve superior results in the following criteria: artifacts detection accuracy, overall performance, robustness to detection system, and the ability to preserve the spatial resolution. In this section only the main features and results of this procedure are presented, for more details please refer to the published work [105] or Appendix section.
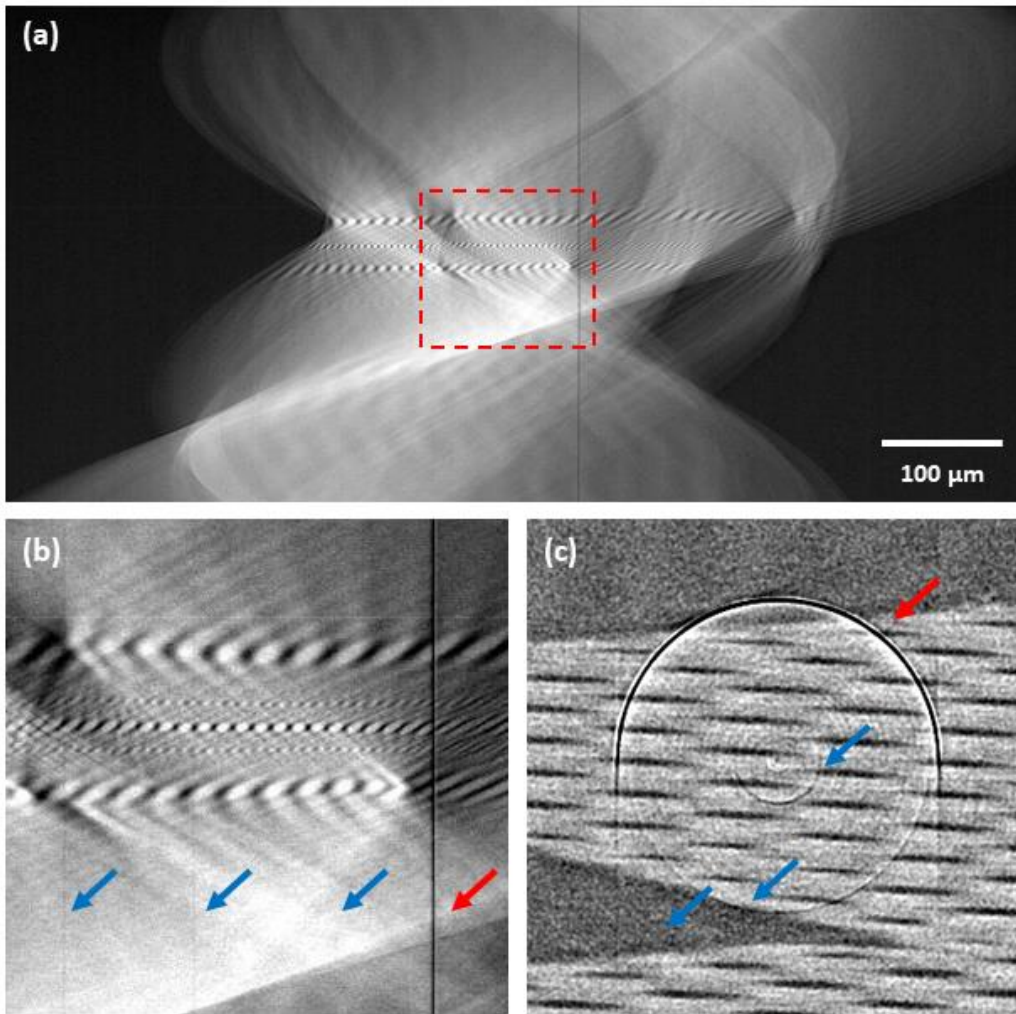
Figure 35: Example of ring artifacts affected data with proposed classification scheme—glass capillary sample acquired with a charge-coupled device (CCD)-based camera: (a) sinogram; (b) detail of sinogram central area; (c) central area of corresponding tomogram. Red arrows indicate the high-level ring artifacts and blue arrows the low-level ring artifacts. [105]
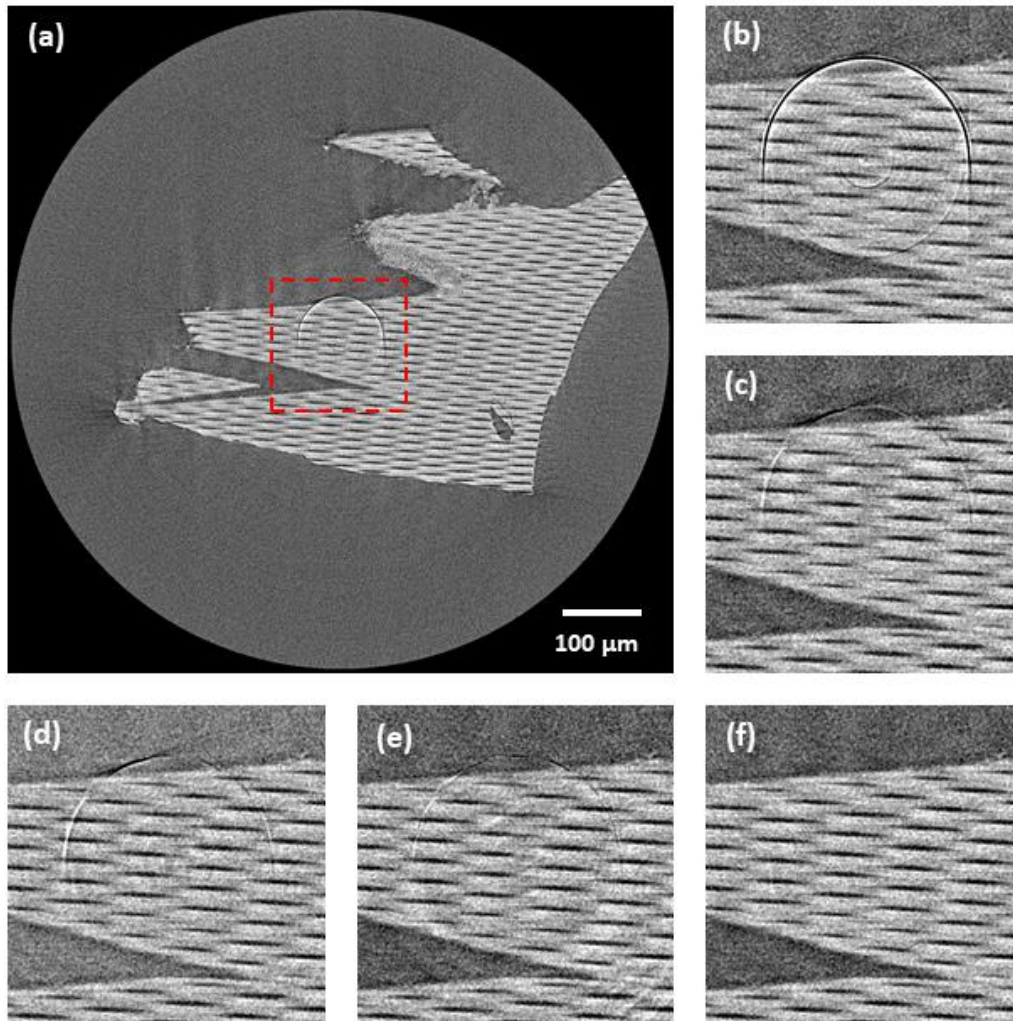
Figure 36: Comparison of tomograms after ring artifacts reduction by tested methods—real computed tomography (CT) data of glass capillary array acquired with a CCD-based camera: (a) original tomogram (without any correction)—red labelled area marks central area visualized in following images; (b) original; (c) Münch [95]; (d) Eldib [97]; (e) Vo [103]; (f) proposed. For visualization, the same contrast setting was used for all the images. [105]

4.5 Assessment and reduction of rotational stages limitations

The application of submicron CT has already proven its applicability and benefits in various fields from R&D to basic research. But the crucial task for every technique used for any metrological assessment is determining measurement uncertainty, which requires analysis of all critical error sources. For high-resolution CT measurements, the geometrical misalignments of system components and their positional instabilities, including vibrations and thermal instability, are one of the most critical. The aim of this work was to study those limitations and develop optimal solution for their reduction. The main outcome of this work is a dedicated sample's holder with reference area (partially developed in the scope of TAČR Zéta grant - TJ02000127) and corresponding methodology for correcting stage instability and imprecision during CT acquisition process. Part of the results was presented at International Conference on Tomography of Materials & Structures (ICTMS 2022, Grenoble, France, title of submission: "Beyond the limits of lab-based submicron CT for metrology").

4.5.1 Analysis of rotational stage stability

In this section, the stability and precision of rotational stage at submicron CT system Rigaku nano3DX is studied. First, thermal dependence of stage positional stability was assessed and then its' overall precision during CT acquisition process was evaluated and put to the context of other laboratory-based CT systems.

4.5.1.1 Thermal stability

In this experiment, evaluation procedure was proposed to study the thermal dependence of rotational stage stability at Rigaku nano3DX system. Because it was not possible to measure this stability with sufficient precision directly, alternative approach was used. This procedure included acquisition of series of projection images (Lens unit: L0270, Binning: 2x2, Target: Cu, Exposure: 30 s, pixel size: 0.54 µm) of static scene (i.e. no intentional stage movement involved) including reference area in the FoV (see Figure 37) – prototype of latter presented sample's holder was used which contained fiducial marker (Ø 25 µm). The total length of the experiment was set to 300 minutes (corresponding to average CT acquisition process this CT system). The Rigaku nano3DX system does not include internal cooling inside measurement chamber, therefore inside's temperature is dependent on the room temperature. Therefore, during the whole experiment temperatures inside the measurement chamber and room temperature was measured using the datalogger ALMENO 2590-4AS (measurement arrangement is shown in Figure 38). The fiducial present in the FoV was automatically detected in each radiogram using processing procedure defined in section 4.5.2 and position of its' centre was evaluated during the experiment, considering the fiducial's position at beginning of the experiment (i.e., first projection) as reference. To avoid any misinterpretation of the results, the used holder with reference area was placed on the rotational stage 2 hours before the experiment to let it properly set.
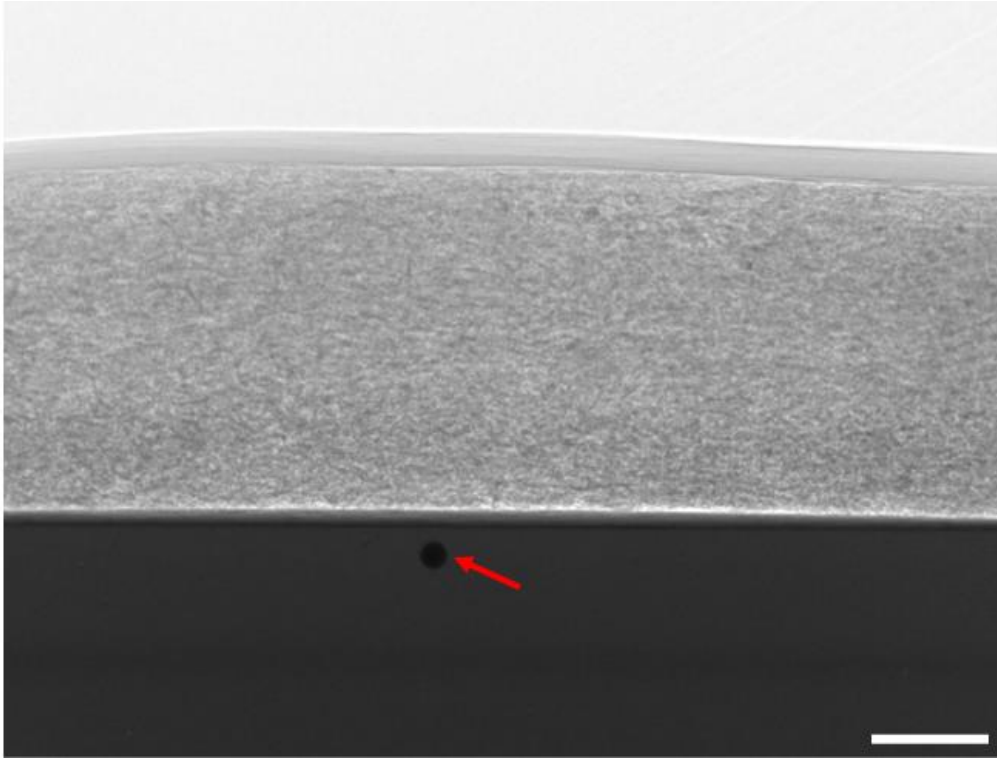
Figure 37: Radiogram of evaluated static scene containing a reference area (marked by red arrow) in the FoV. Scale bar: 100 μm.

Figure 38: Arrangement used within the experiment – red arrow indicates sensor for measuring room temperature and blue arrow indicates sensor used for measuring chamber temperature.

During the experiment, evaluated temperatures were found to be variable: room temperature fluctuated in interval 22.0 °C – 24.4 °C (mean: 22.7 °C, standard deviation: 0.6 °C) and temperature inside measurement chamber varied in interval 23.0 °C – 24.3 °C (mean: 23.6 °C, standard deviation: 0.3 °C). The temperature's fluctuations, considering the temperature in the beginning of experiment as reference, are visualised in the Figure 39. It was found out that this temperature gradient was affecting the detected stage movement (see Figure 40). This movement was more prominent in vertical direction, when the maximum was 2.6 µm compared to reference position (i.e., fiducial's position in the beginning of experiment). The fiducial's movement was found the be correlated with the temperature in the measurement chamber with the Pearson's correlation coefficients -0.74 for horizontal direction and 0.47 for vertical direction. In this experiment, it was found out that it is crucial to keep the temperature in the measurement chamber during the submicron CT acquisition process as stable as possible, when even the fluctuations below 1°C can result in significant instability of rotational stage affecting results of submicron CT data acquisition.
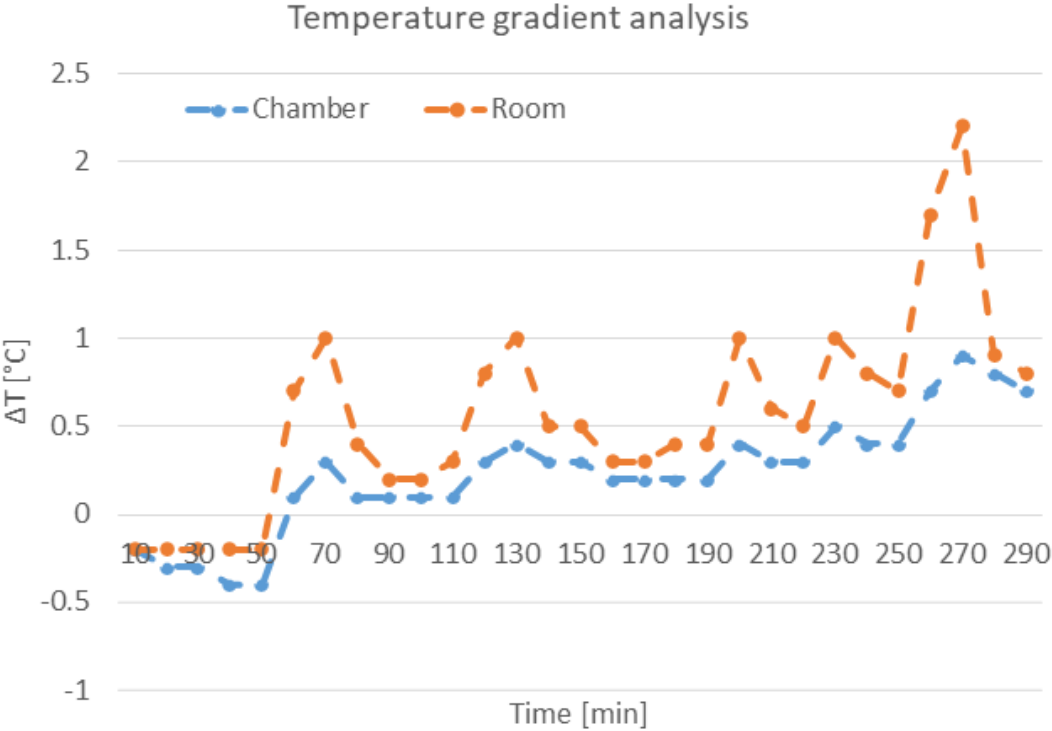
Figure 39: Temperature fluctuations during the experiment: the temperature in the beginning of experiment was considered as reference.
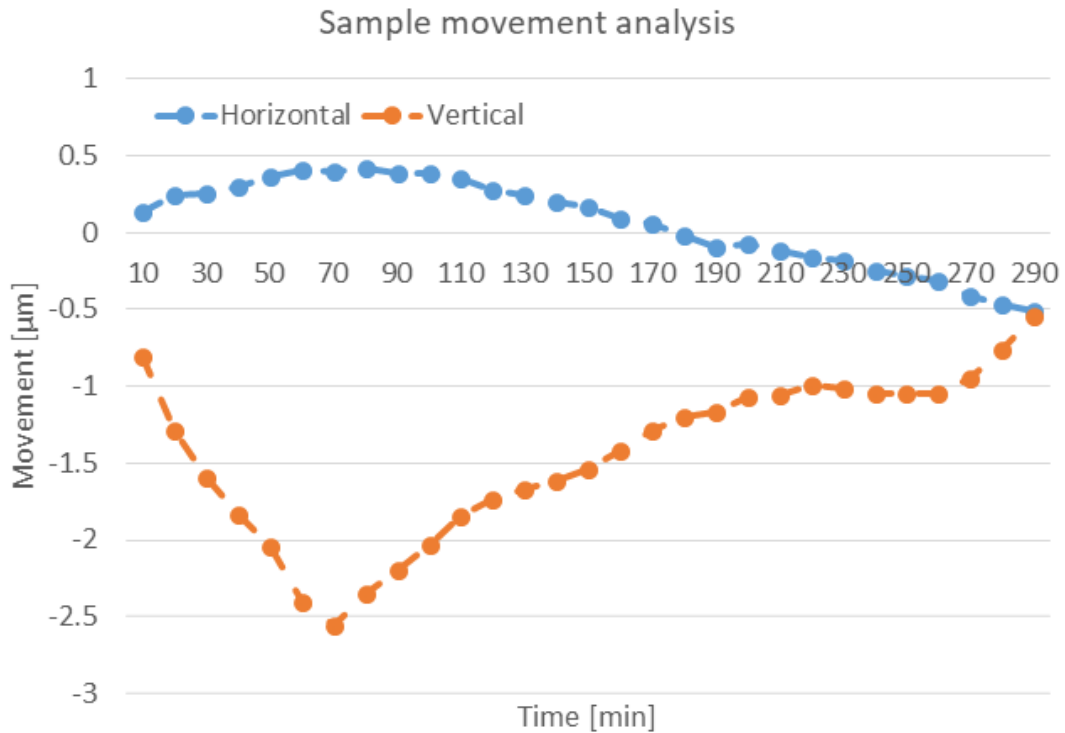
Figure 40: Stage movement during the experiment: visualised as gradient considering the fiducial's position in the beginning of experiment as reference.

4.5.1.2 Assessment of rotation stage stability and precision during CT acquisition

In this part, the main aim was to analyse the rotational stage stability and precision during the CT acquisition process. Practical realization of this task was divided into two separate experiments. Firstly, the assessment was conducted for submicron CT acquisition using Rigaku nano3DX system, using 2 measurement strategies: a) relaxation of a sample on the rotational stage before measurement (i.e., sample mounted on the holder with reference area was placed on the rotational stage 2 hours before the experiment to let it properly set) and b) no relaxation involved (i.e., measurement was started immediately after sample's mounting on the stage). Secondly, the assessment was realized for CT acquisition with voxel resolution above one micron and put in the context of three lab-based CT systems (Rigaku nano3DX, Thermofisher Heliscan and GE phoenix v|tome|x L240), for those measurements no sample's relaxation period before acquisition was employed. Used acquisition parameters of all conducted measurements are summarized in Table 17, specific parameters were set according to standard measurement scenarios and following manufacturer's recommendations to measure given sample with the best possible spatial resolution. In case of GE phoenix v|tome|x L240 two measurement settings were involved, when the hardware-based ring artifacts reduction (i.e., intentional stage movement during CT acquisition) was either on or off. For all the measurements the prototype sample's holder with reference area was used together with processing procedure defined in section 4.5.2

66

Table 17: Acquisition parameters of CT measurements performed within analysis of rotational stage stability during CT acquisition, for all devices circular trajectory was used.

Device	Rigaku nano3DX			Thermofisher Heliscan	GE phoenix v|tome|x L240
Voltage	40 kV	40 kV	40 kV	60 kV	50 kV
Current	30 mA	30 mA	30 mA	120 mA	120 mA
Exposure	16 s	16 s	20 s	4 s	0.4 s
Binning	2x2	2x2	2x2	1x1	1x1
Voxel size	0.53 µm	0.53 µm	1.06 µm	1.19 µm	2.00 µm
Averaging	-	-	-	2	2
Angle range	180°	180°	180°	360°	360°
Projections	800	800	800	3150	2300
Relaxation	Yes	No	No	No	No

Firstly, the effect of sample's relaxation on the rotational stage before submicron CT acquisition was evaluated. According to the results (Figure 41 and Figure 42), it is evident that including the stabilization period was beneficial especially in the initial phase of the CT measurement. In the remaining part of the measurement there were no significant differences, when both measurement scenarios followed similar periodic trend probably corresponding to the temperature fluctuations in the measurement chamber.
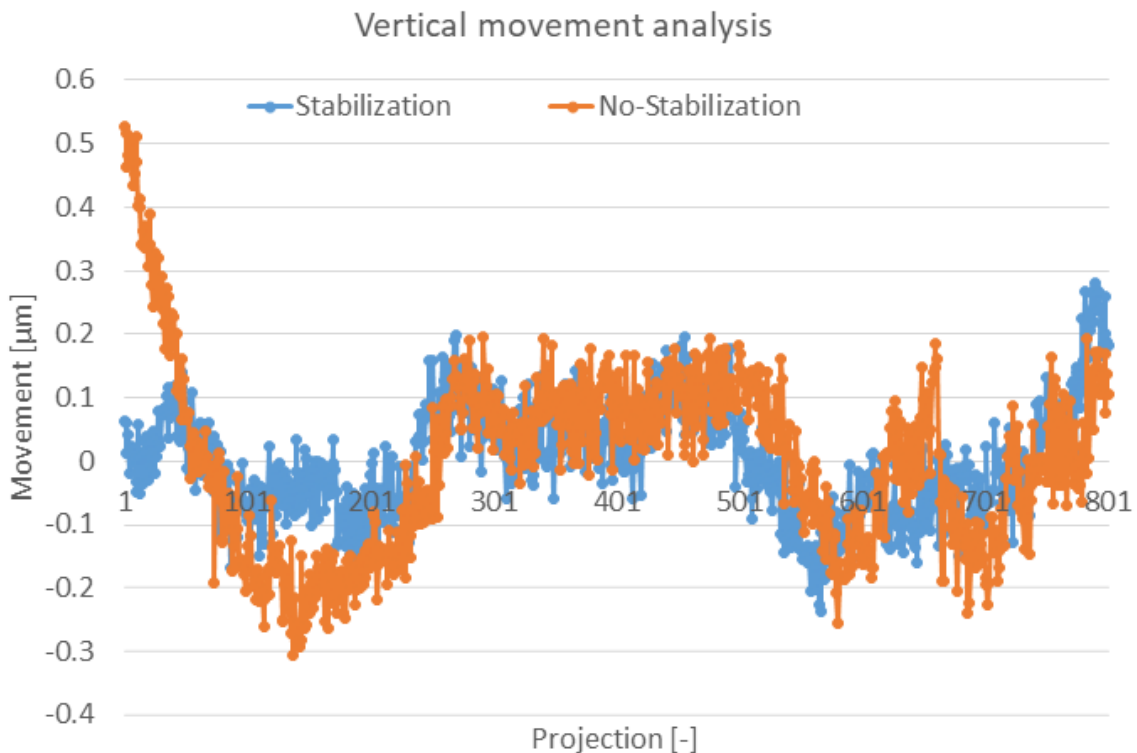
Figure 41: Evaluation of the effect of sample's relaxation on the rotational stage before submicron CT acquisition: vertical movement.
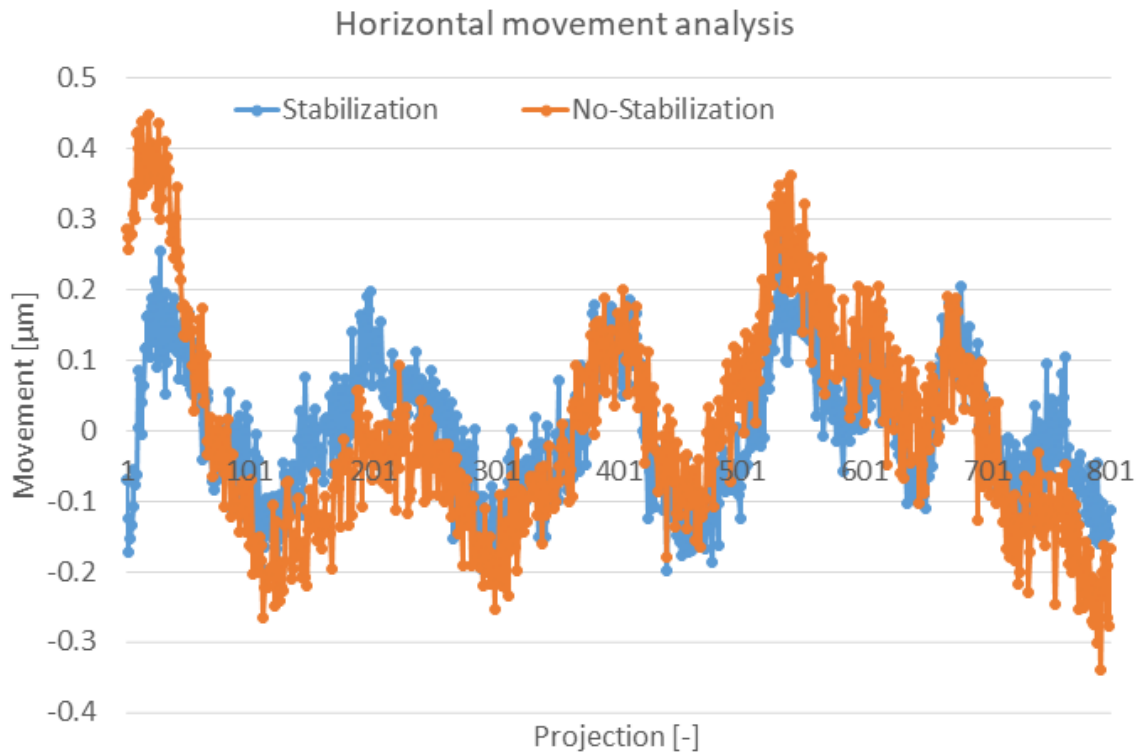
Figure 42: Evaluation of the effect of sample's relaxation on the rotational stage before submicron CT acquisition: horizontal movement.

Secondly, the rotational stage stability and precision assessment was realized for CT acquisition with voxel resolution above one micron and put in the context of three lab-based CT systems. The acquired results are summarised in the Table 18. For both Rigaku and Thermofisher CT systems the observed can be considered as negligible (below the voxel resolution of given measurements). In case of GE phoenix v|tome|x L240 both tested measurement scenarios resulted into significant movement. Especially when the hardware-based ring artifacts reduction was employed, the movement was found to be significant, reaching the maximum values of 25.93 μm in horizontal direction and 4.0 μm in vertical direction, corresponding to low functionality of used procedure in terms of precision of stage movement.

Table 18: Comparison of CT systems in terms of their rotational stage precision during CT acquisition.

Device	Vertical movement [μm]		Horizontal movement [μm]	
	Mean	Maximum	Mean	Maximum
Rigaku Nano3DX	-0.01 ± 0.13	0.35	5.73 e-05 ± 0.11	0.34
Thermofisher Heliscan	-0.03 ± 0.24	0.92	5.62 e-10 ± 0.20	0.85
GE phoenix v|tome|x L240 – RAR* on	-0.07 ± 2.15	4.00	0.00 ± 8.77	25.93
GE phoenix v|tome|x L240 – RAR* off	0.04 ± 0.70	2.25	4.22 e-07 ± 2.26	5.81

* Refers to hardware-based ring artifacts reduction

In summary, it was found out that detectable stability and imprecision of rotational stages was variable among particular CT systems and also dependent on used acquisition parameters such as the voxel resolution or hardware-based ring artifacts reduction. Especially for submicron CT measurements using Rigaku nano3DX system, it was out that for such high-resolution measurements it is beneficial to let the sample relax and set on stage before starting the measurement.

4.5.2 Correction of rotational stage imprecision and instability

In the sphere of high-resolution CT, there are strict requirements on hardware components, when their positional instabilities are one of the most critical error sources (see section 1.2). However, it is technologically almost impossible to achieve precision of those mechanical components that would be substantially smaller than the smallest achievable voxel size for given system. As presented in the previous section (4.5.1), the stability or rotational stage and its precision during submicron CT acquisition can be decreased by various factors. As introduced in the section 1.2, there exist various strategies for correction of rotational stage imprecision during the CT acquisition. Till today the marker-based methods are still the most used having various benefits over the marker-less methods such as low computational demands and robustness to acquired data quality. However, those techniques require mounting selected fiducials (usually golden particles with diameter ranging from nanometres to micrometres) on a sample prior CT acquisition. Especially for submicron CT applications, this is a very challenging task posing high demands on an operator and his skills.

The objective of this work was to create a multi-purpose solution for high-resolution CT applications that would allow to reduce the limits of current technology and overcome limits of existing correction techniques. Inspired by marker-based methods, this resulted into development of an advanced sample's holder containing reference area, therefore, no fiducial manipulation and mounting is required. This project was a follow-up of successful TAČR Zéta grant - TJ02000127: Differentiation of soft tissues using dual-target tomography, where one the outputs was a functional prototype of sample's holder with reference area for alignment of two datasets. Within practical realization of the project TJ02000127, the concept of dedicated sample holder with a reference area was proposed and designed (see Figure 43). This concept was then practically verified by creation of first functional prototype that was then tested in field trials. The concept was confirmed as successful for data registration of CT datasets of biological tissues acquired by dual-target CT practically implemented on Rigaku nano3DX system. Further, this concept was extended to enable not only the CT data registration with sub-pixel precision but to be also applicable for correction of rotational stage inaccuracies to enhance the overall quality and precision of acquired CT data. This was mainly achieved by development of dedicated processing methodology and its implementation.
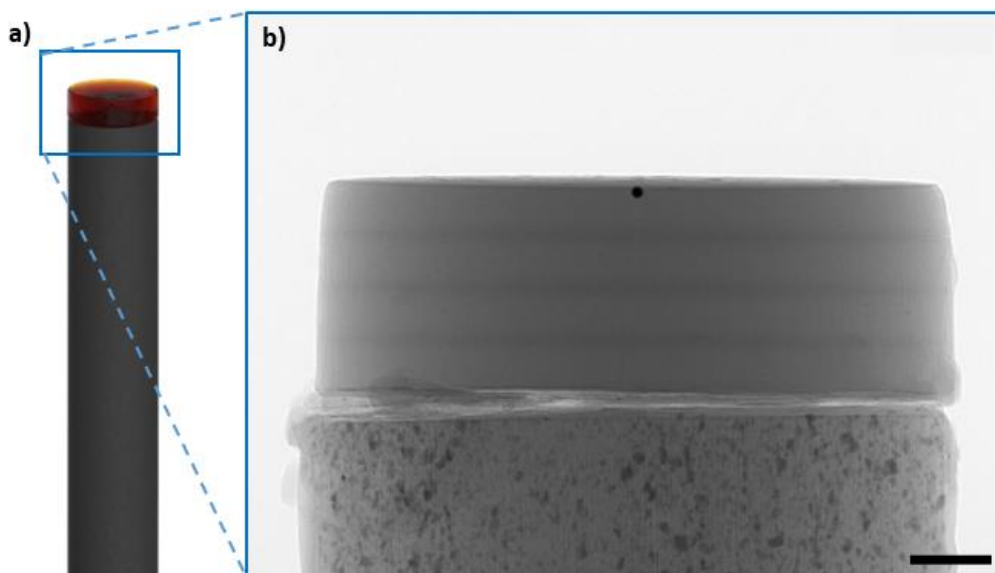

Figure 43: Developed sample's holder with reference area: a) 3D render of technical design; b) Radiogram of the top part with fiducial marker. Scale bar: 100 μm.

4.5.2.1 Proposed methodology for correction of rotational stage imprecision and instability

In this methodology, advantageous features of marker-based and marker-less methods are combined into complex procedure overcoming their individual limits. This procedure combines using developed sample's holder with reference area with dedicated processing procedure to allow for correction of rotational stage inaccuracies (i.e., centre of rotation misalignment and stage instability/movement during CT acquisition). Respectively to order of CT acquisition procedure, the methodology first consists of guidelines for optimal CT acquisition using developed sample's holder:

1. Mounting a sample on the top of a developed holder, the sample should be fixed properly to avoid unrelated movement of the sample and the holder.
2. Mounting the holder with the sample on the rotational stage of a CT device – if recommended by manufacturer of used CT system, allow it to thermally adapt for conditions in the measurement chamber and properly set on the rotational stage before CT measurement.
3. Setting the sample's position in FoV for CT measurement to make sure that the fiducial is visible in every projection image.
4. Setting the acquisition parameters (i.e., accelerating voltage and current, exposure, binning, averaging) according to standard guidelines for your CT device to reach a sufficient level of detected signal.
5. Starting the CT measurement.

Within the proposed data processing procedure, acquired projection data are analysed. For the analysis only bottom part of projection data (containing fiducial) is used to reduce computational demands. The data is further pre-processed by denoising (both impulse noise and shot noise are reduced using methodologies presented in section 4.3). Fiducial is then segmented in each projection image by global thresholding using combination of automatic threshold selection using Otsu's method [175] and local statistics evaluation. To calculate the fiducial's centres, the binary masks are fitted by circles using combination of Taubin [176] and Levenberg-Marquardt [177] methods. Having positions of fiducial's centres, both the rotary axis misalignment and sample's movement can be estimated and corrected. The rotary axis misalignment is estimated by evaluation of the fiducial's centre horizontal coordinates between corresponding projections at 0° and 180°. In ideal case, these two images should be only mirrored, if any horizontal shift between them is detected, its' half corresponds to rotary axis shift. Sample's movement is then estimated separately in vertical and horizontal directions using the coordinates of fiducial's centres. Both coordinates are fitted by ideal trajectories (i.e., sine function in vertical direction and cosine function in horizontal direction) and sample's movement is then calculated as deviation from those trend curves, similarly as in the work of Cheng [137]. For correction of both the rotary axis misalignment and samples movement it is recommended to use the b-spline interpolation method to reach the sub-pixel precision or optimizing the projection geometry within the tomographic reconstruction process.

4.5.2.2 Results

The functionality of proposed methodology for correction of rotational stage imprecision and instability is demonstrated on submicron CT measurement of pharmaceutical sample using Rigaku nano3DX system (Lens unit: L0270, Binning: 2x2, Target: Cu, Exposure: 30 s, voxel size: 0.54 µm). From the results (see Figure 44), it is evident that using proposed procedure the acquired data quality was significantly improved, when all the movement and rotary axis misalignment artifacts were reduced.
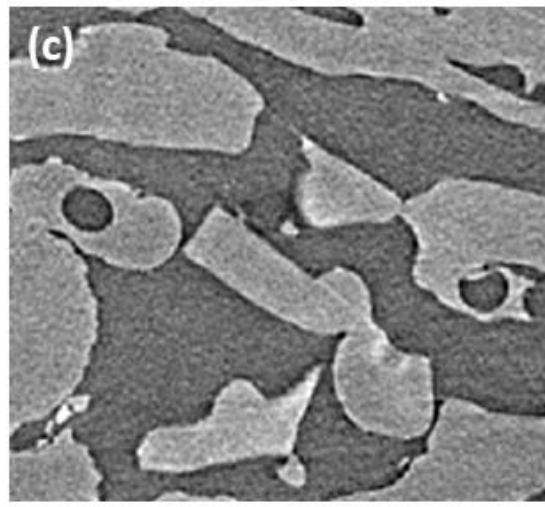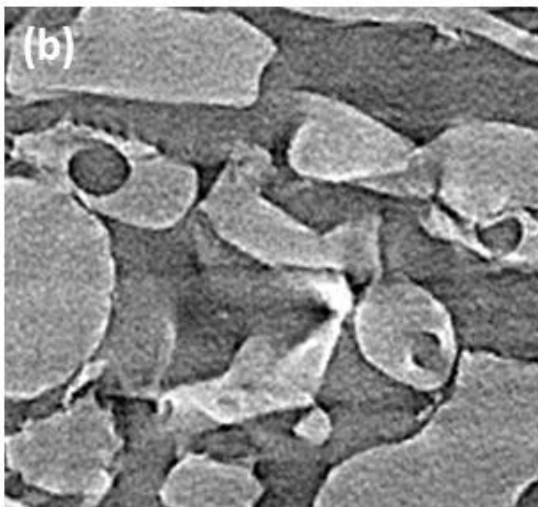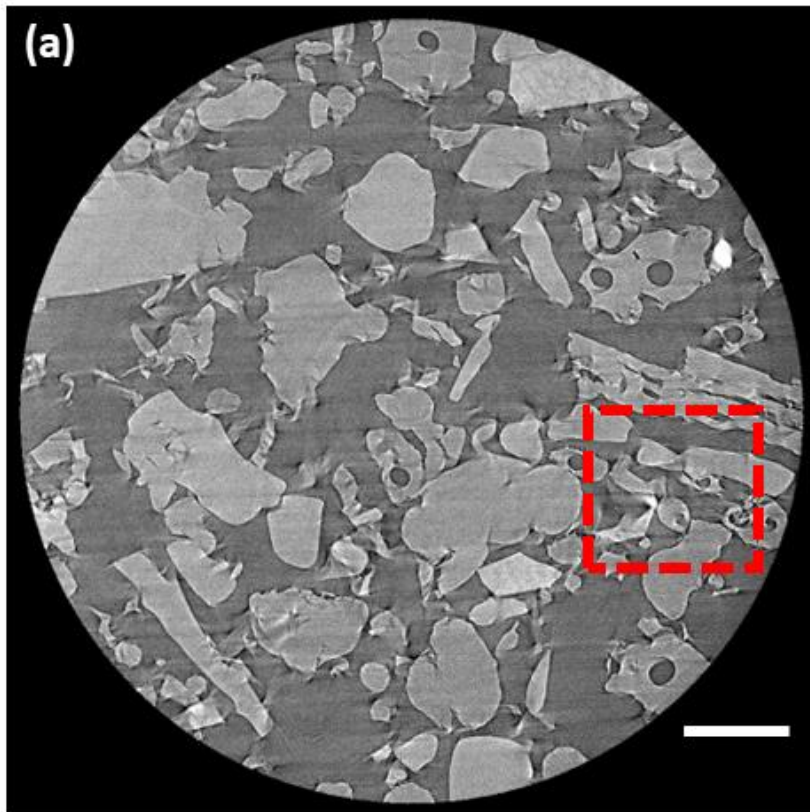
Figure 44: Results of proposed methodology for correction of rotational stage imprecision and instability, demonstrated on pharmaceutical sample: a) and b) original data; c) corrected data. Scale bar: 100 μm.

5 Spectral imaging

As introduced in the section 1.3.1, spectral imaging has in recent years remerged in CT practise, mainly due to technological advances that enabled its' practical implementation. Spectral imaging methods generally aim to increase overall accuracy and quality of CT imaging including methods for tomographic artifacts reduction (section 1.2) and to practical implementation of advanced quantification tools for sample's characterization (section 1.3.2). In terms of practical implementation of spectral CT, two main concepts can be applied, either the detector-based or X-ray source-based. The focus of this work is X-ray source-based Dual-energy CT, which refers to scanning at two energy levels and is a special case of spectral CT. Dedicated CT systems were designed exclusively for DECT, such as the Rigaku nano3DX system. Using this device, not only two energy separate X-ray spectra but also material specific spectra can be achieved during DECT by switching the X-ray source target material. Therefore, this special implementation of DECT is hereafter named as Dual-Target CT (DTCT). However, all the X-ray source-based approaches are practically limited by possible misalignment of acquired data and also by lack of knowledge about practical aspects of setting up DECT measurements. In this work, both these issues are addressed and practically implemented for Rigaku nano3DX device.

5.1 DTCT imaging using Rigaku nano3DX device

The DTCT measurement using the Rigaku nano3DX device consists of two consecutive acquisitions, between which, in addition to the change in the maximum energy of the X-ray radiation, the material of the target of the X-ray source (Cu and Mo), in which the radiation is generated, is changed. Resulting X-ray spectra are not only energetically but also materially different, which helps their separation (see Figure 45). This follows a generally valid rule for DECT, that between both measurements there should be sufficient spectral separation, meaning that the used X-ray spectra should have as small overlap as possible [178].

The sequential character of DTCT data acquisition, requires optimization of acquisition protocol to achieve sufficient data quality for subsequent data processing. In scope of this work, acquisition protocol is proposed to ensure optimal data quality for subsequent processing by optimizing the exposure times for both measurements. This protocol is based on procedure, where Cu target measurement is considered as refence in terms of noise properties and the exposure time for measurement using Mo target is optimized to reach comparable noise properties (for more details see section 5.2). The exposure time for reference measurement is then selected according to the recommendations of Rigaku (i.e., manufacturer of given device). For the DTCT acquisition, it is also proposed to use the developed samples holder with reference area (more details in section 4.5.2), that is utilized both for samples mounting and for the registration of acquired data. In terms of DTCT data processing, it is required that the data are perfectly aligned (i.e., corresponding structures are located on the same positions for both data), however, it is hardly achievable especially for submicron CT measurements mainly due to the rotational stage instability during CT acquisition (see section 4.5) and software-based alignment is therefore necessary. To simplify the task for data registration, it is also recommended to optimize the sample's preparation and mounting to reach sufficient stability and possible eliminations of sample's movement during CT acquisition process.

The proposed DTCT acquisition protocol for the Rigaku nano3DX device is summarized below:

1. Sample's mounting on the developed sample's holder with reference area.
2. CT data acquisition using Cu target (reference measurement):

a. exposure time set according to the manufacturer's recommendations to reach optimal contrast.
3. Switching the target material (Cu → Mo).
4. CT acquisition using Mo target (high energy measurement):
   a. exposure time set according to noise properties in reference measurement – minimizing the difference of total noise standard deviations in bright frames for Cu and Mo measurements (for more details see section 5.2).
5. Projection data processing:
   a. correction of rotational stage instability and imprecision for Cu projection data according to the procedure defined in section 4.5.2.1,
   b. transformation of Mo projection data according to the Cu projection data (for more details see section 5.3).
6. Tomographic reconstruction:
   a. reconstruction of aligned projection datasets using procedure defined in section 4.1.
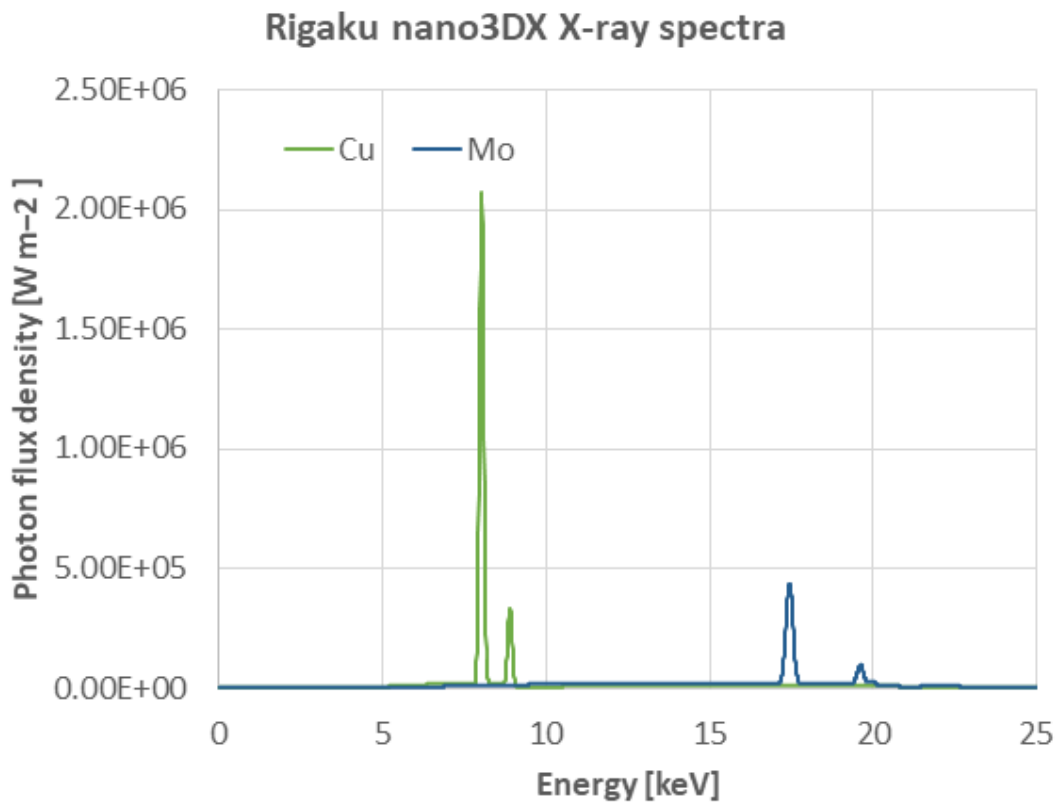
Figure 45: X-ray spectra of Rigaku nano3DX (after 250 mm of air travelling) using both Cu and Mo target materials.

5.2 DTCT acquisition settings

As already mentioned, the sequential character of DTCT data acquisition, requires optimization of acquisition protocol to achieve sufficient data quality for subsequent data processing. However, data acquired using different X-ray spectra mainly differ in terms of noise properties corresponding to different X-ray flux in both measurements, different detector sensitivity to individual X-ray energies and other factors. In the literature, this is usually solved by optimization of used X-ray spectra to achieve the best SNR [179]. However, during practical experiments it was found out that SNR is not ideal metric, because it does not respect the signal generation for different energies levels. Moreover, in case of nano3DX system, the X-ray spectra are unchangeable, and it is, therefore, necessary to optimize the data quality using different approach. Using nano3DX system the only relevant parameter in terms of setting up the parameters of DTCT measurements is the exposure time. Other theoretically relevant parameters affecting the shape of X-ray spectrum, such as accelerating voltage or current, are fixed by the manufacturer to achieve the maximal usage of characteristic part of X-ray spectrum for given target material. Therefore, it was proposed to optimize the exposure times according to noise properties of bright frames before flat-field correction of both Cu and Mo target measurements.

5.2.1 Noise dependence on acquisition parameters

First, noise properties dependence was studied for various acquisition parameters that are relevant within regular CT measurements using Rigaku nano3DX system equipped with CCD-based detector (XSight™ Micron LC X-ray CCD camera [168]). Specifically, we evaluated the effects of binning, sample-detector distance (refers to parameter XD), optical lens unit (i.e., optical magnification) and also used target material and related X-ray beam filtration. The used acquisition parameters are summarized in Table 19. Total noise was quantified from set of bright-field frames by subtraction of an average bright-field frame from intensity stabilized frames and then quantified using standard deviation calculation. This parameter was calculated for central area of original bright-frames (not flat-field corrected), when square-shape ROI with size scaled according to binning (1000 pixels' width for binning 1x1) was evaluated.

Table 19: List of acquisition parameters used within noise dependence study.

Target material:	Cu/ Mo
Beam filtration:	None/ Al plate with 0.1 mm thickness (manufacturer recommendation when measuring high-density samles with Mo target)
XD [mm]:	0.0/ 1.0/ 2.0
Lens unit:	L0270 (FoV: 0.7 × 0.9 mm; minimal pixel size: 0.27 μm)/ L0540 (FoV: 1.4 × 1.8 mm; minimal pixel size: 0.54 μm) / L1080 (FoV: 2.8 × 3.6 mm; minimal pixel size: 1.08 μm)
Binning:	1×1/ 2×2/ 4×4
Exposure time [s]:	From minimal to exposure level for which the signal level in the central area of the FOV is 75% of the saturation level (i.e., around 45 000 DN for 16bit)
Number of projections:	10 per exposure level

5.2.1.1 Effect of binning

According to the acquired results (see Figure 46), the total noise standard deviation was found to be exponentially dependent on exposure and linearly proportional to the used binning factor.
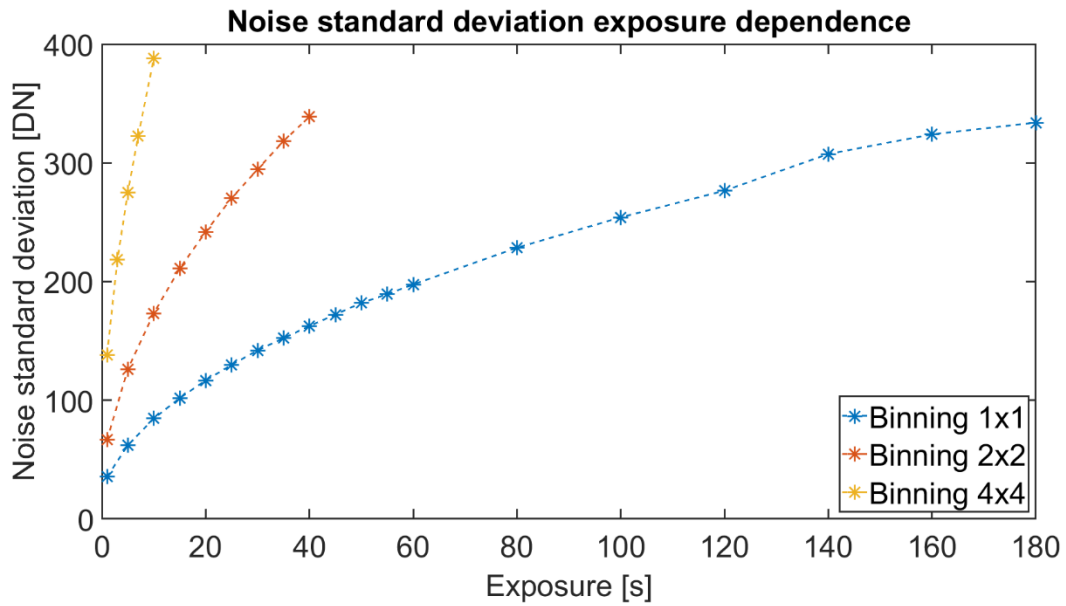
Figure 46: Total noise standard deviation dependence on exposure and binning, evaluated for Cu target.

5.2.1.2 Effect of XD distance

Acquired results (see Figure 47) showed that the effect of XD distance on total noise properties is negligible within the commonly used interval of distances referring to regular CT measurements at used CT system.
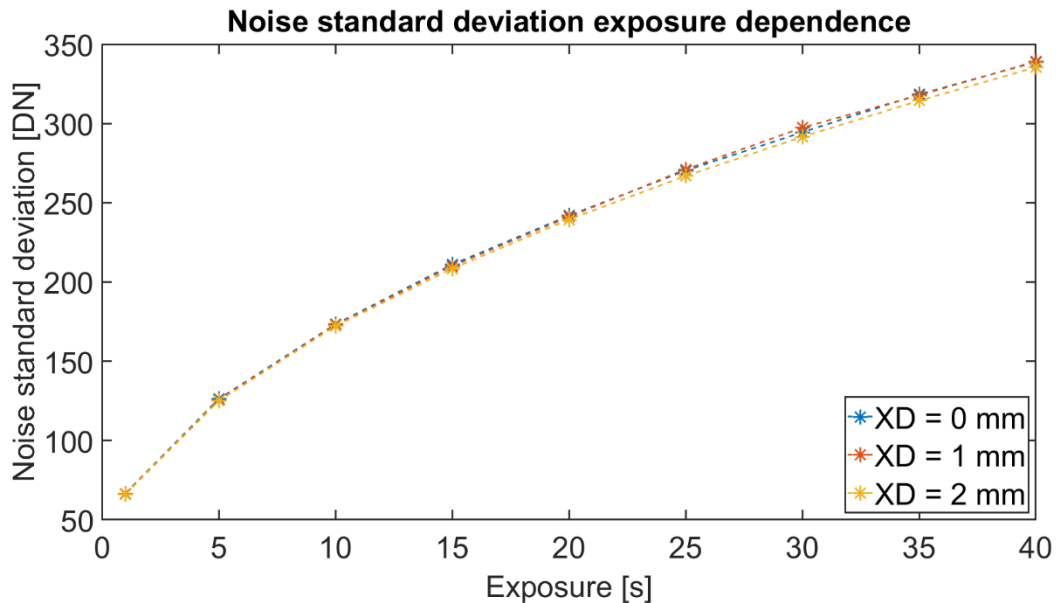
Figure 47: Total noise standard deviation dependence on exposure and XD distance (refers to sample-detector distance), evaluated for Cu target

5.2.1.3   Effect of used target material

According to the acquired results (see Figure 48, Figure 49 and Figure 50), the effect of used target material and beam filtration (aluminium plate with thickness 0.1 mm) was found to be variable within tested optical lens units. Specifically, for L0270 optical lens (Figure 48) the difference between Cu target and Mo target with beam filtration was found to be almost negligible. However, for the other two tested optical lens units, the difference between Cu and Mo targets was more relevant.
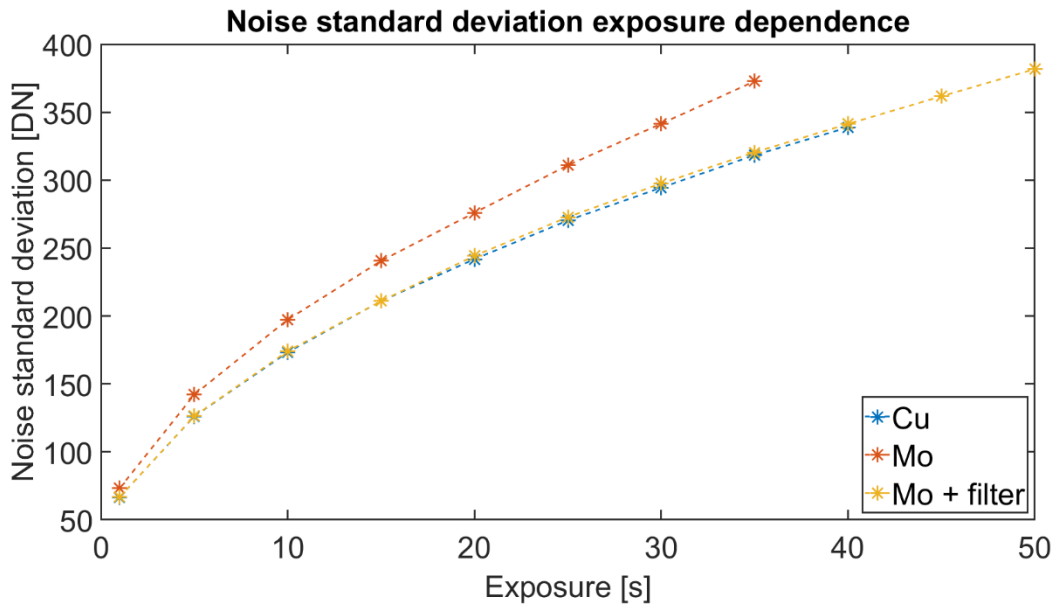
Figure 48: Total noise standard deviation dependence on exposure and used target material, evaluated for optical lens unit L0270, binning 2×2.
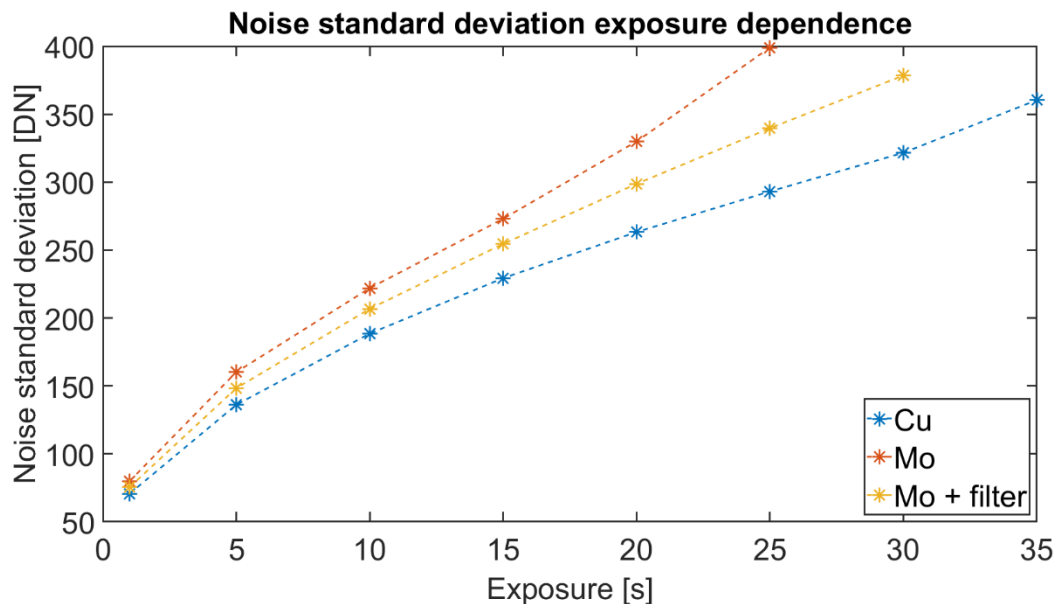
Figure 49: Total noise standard deviation dependence on exposure and used target material, evaluated for optical lens unit L0540, binning 2×2.

76
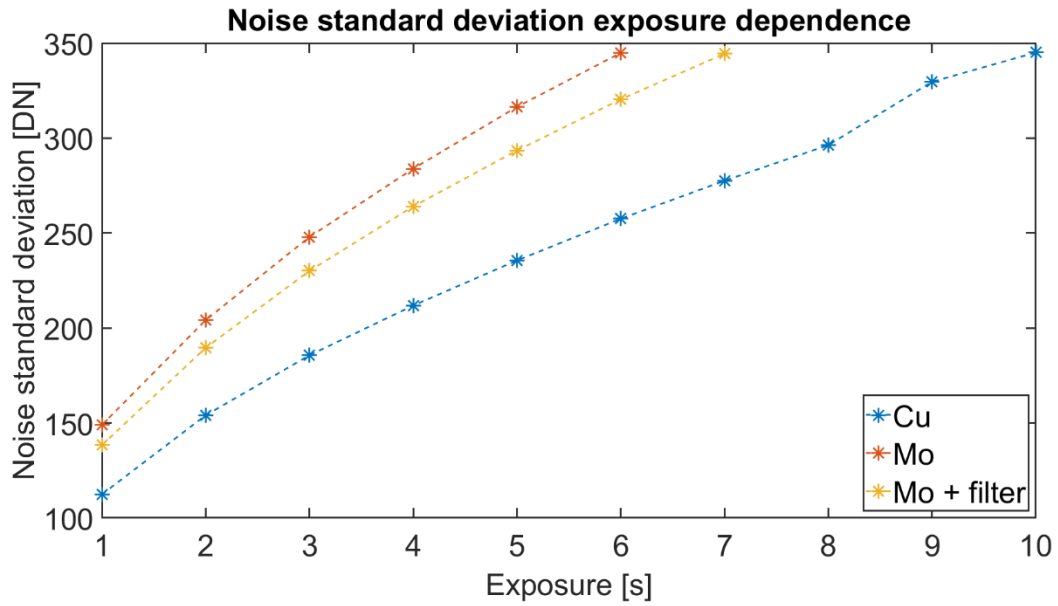
Figure 50: Total noise standard deviation dependence on exposure and used target material, evaluated for optical lens unit L1080, binning 2×2.

5.2.1.4   Effect of used optical lens unit

According to the acquired results (see Figure 51, Figure 52 and Figure 53), the effect of used optical lens unit was found to be almost negligible within tested target materials and beam filtration, but still unique for given optical lens unit.
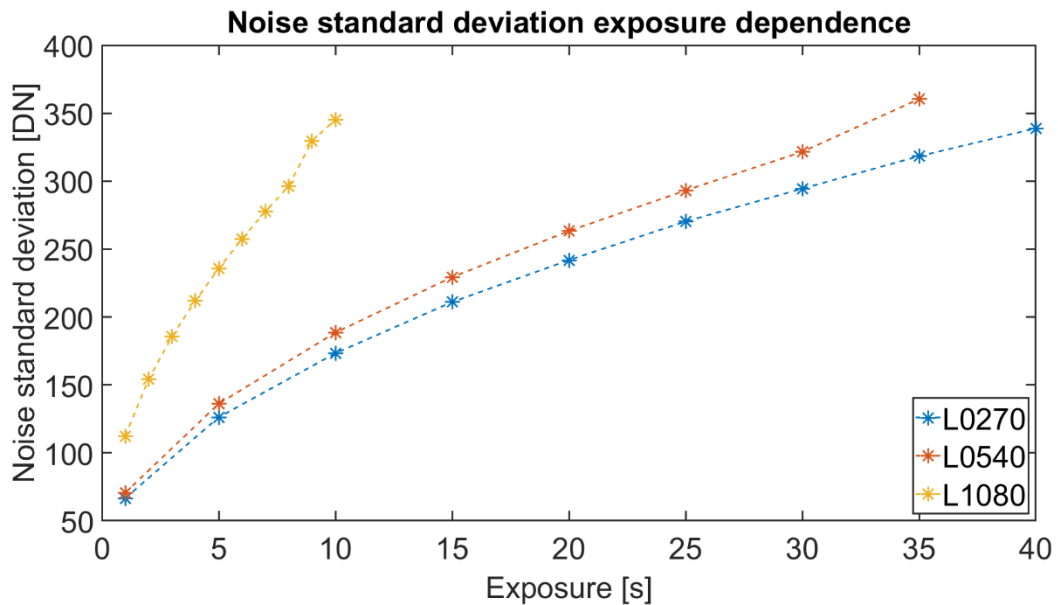
Figure 51: Total noise standard deviation dependence on exposure and used optical lens unit, evaluated for Cu target.
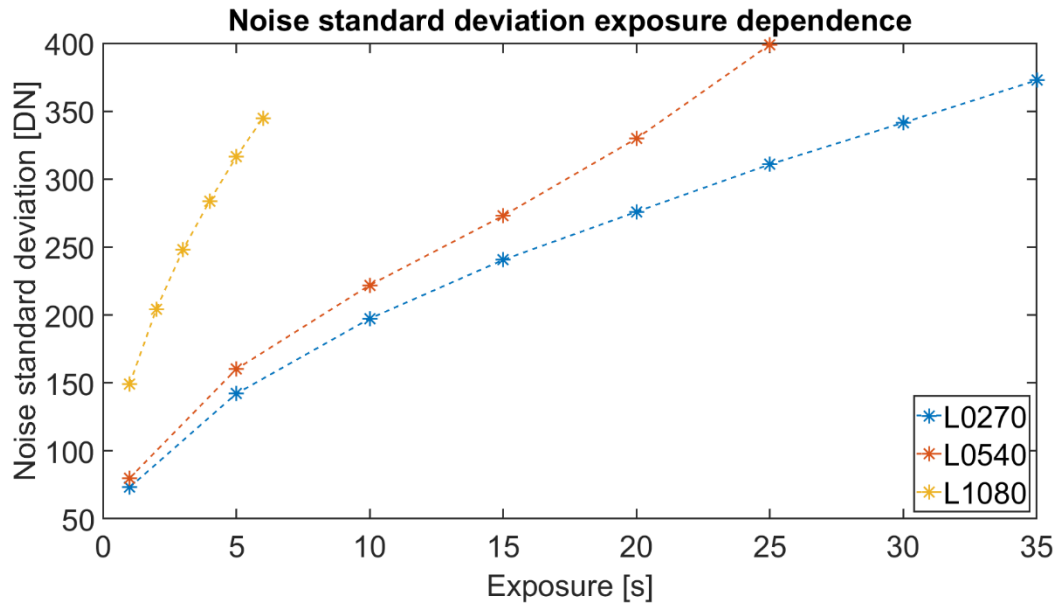
Figure 52: Total noise standard deviation dependence on exposure and used optical lens unit, evaluated for Mo target, binning 2×2.
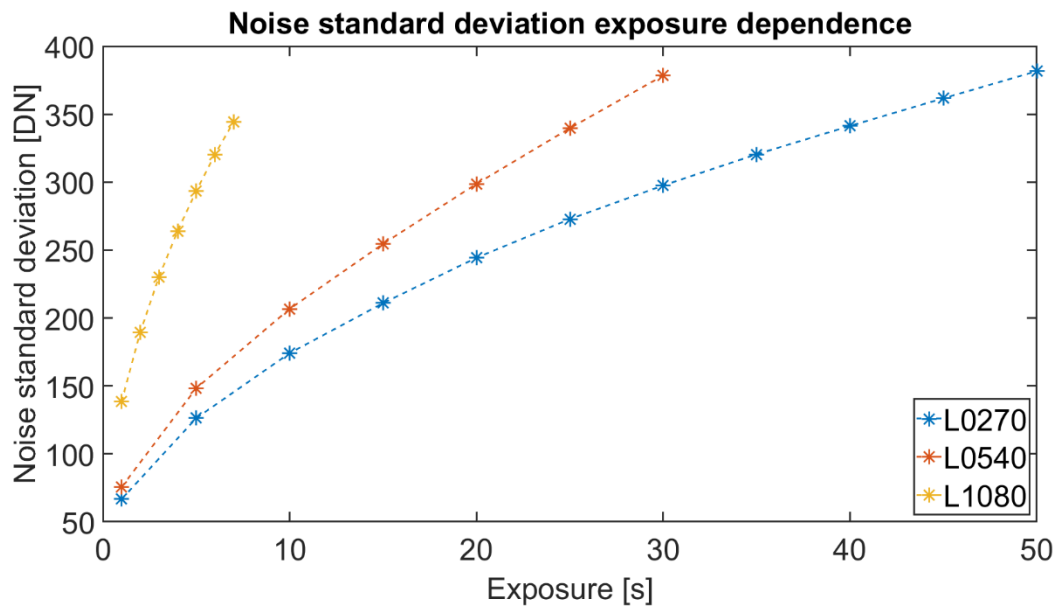
Figure 53: Total noise standard deviation dependence on exposure and used optical lens unit, evaluated for Mo target with beam filtration (aluminium plate with thickness 0.1 mm), binning 2×2.

5.2.2 Proposed strategies for exposure estimation

In scope of this work, it is proposed to use the standard deviation of total noise calculated from bright frames before flat-filed correction as optimization metric to set ideal exposure times for DTCT measurements using Rigaku nano3DX system. Specifically, the noise properties from Cu target measurement are considered as reference and exposure time for Mo target measurement is set to reach minimal difference in this parameter. Using this strategy, robust criteria is achieved that is independent on sample's properties and other factors. Considering the result from the previous section, two approaches are proposed within practical implementation of this strategy and summarized below including their individual advantages and disadvantages:

1. **Utilization of conversion factors:**
   - Multiplying reference exposure (Cu) by corresponding conversion factor (for more details see section 5.2.2.1).
   - Advantage – exposure for second measurement is calculated directly, no further data is required.
   - Disadvantage – calculation of conversion factors must be done for each CT setup, every optical lens unit and target material individually. The models are not constant, because properties of CT system components are not persistent.
2. **Bright frames analysis for each measurement individually:**
   - Bright frames acquisition and analysis before second measurement to set exposure having similar noise standard deviation as reference measurement (bright frames from first measurement are required):
     - i. Acquisition of bright frames for at least 5 exposures around reference exposure (10 frames per exposure) and calculation of total noise standard deviations for given exposure.
     - ii. Regression analysis of calculated noise dependence on exposure levels.
     - iii. Estimating the exposure time with similar total noise standard deviation as for reference measurement.
   - Advantage – generally applicable and robust solution without any requirements for priory information.
   - Disadvantage – additional measurements of bright frames lead to longer acquisition time and significant time gap between the two consecutive CT measurements, when sample movement or structural changes can occur.

5.2.2.1 Optimal exposure estimation according to regression model's analysis

Using the results presented in section 5.2.1, noise dependence models on exposure of Mo target measurements with and without beam filtration were estimated for all tested optical lens units, considering the binning 2×2, which is the preferred settings in terms of given CT system. Those models were calculated using regression analysis, where the dependence of total noise standard deviation on exposure was used as the input. The individual regression models (see Figure 54) were manually optimized to achieve the best possible results in terms of regression (i.e., R-Squared coefficient was maximized). Using those models, noise standard deviation values were estimated for whole considered exposure's interval with step 0.01 s. Real measured Cu target values were then considered as reference and for each of those values the closest values for Mo target with and without filter were found using Euclidean distance metric. For such estimated noise standard deviation values corresponding

exposures were extracted. Conversion coefficients for each measured Cu exposure were estimated as ratio of those exposures and corresponding exposures for Mo target with and without filter (see Figure 55, Figure 56 and Figure 57). For all the evaluated optical lens units, the conversion factor reaches higher values for low exposures compared to remaining exposure interval, which corresponds to dark current and read-out noise components that are predominant for those exposures. In case of L1080 optical lens unit, the drop of conversion factor values at the end of exposure interval corresponds to the proximity of saturation level.
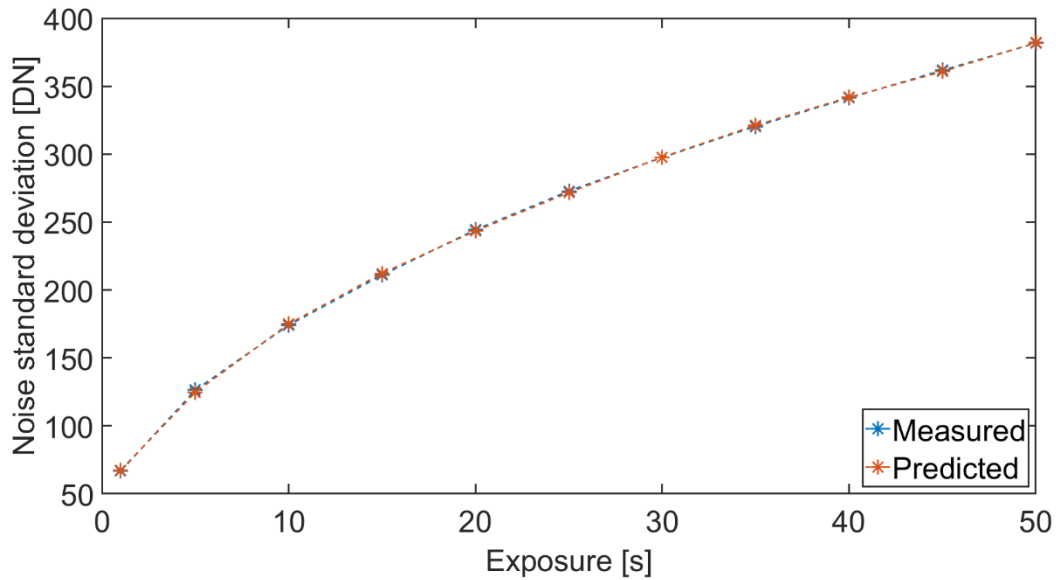
Figure 54: Comparison of real measured data and calculated noise standard deviation regression model for Mo target with beam filtration (0.1 mm Al filter) and L0270 optical lens unit and binning 2×2. Parameters of the model: polynomial: 5; Root Mean Squared Error: 1.35; R-squared: 1.
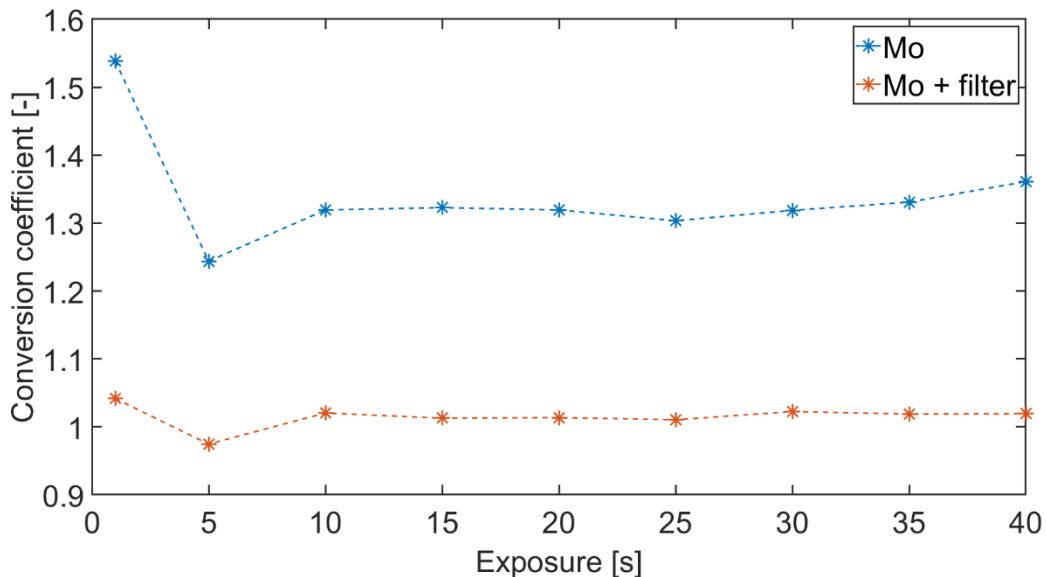
Figure 55:Conversion coefficients calculated for L0270 optical lens unit, binning 2×2.
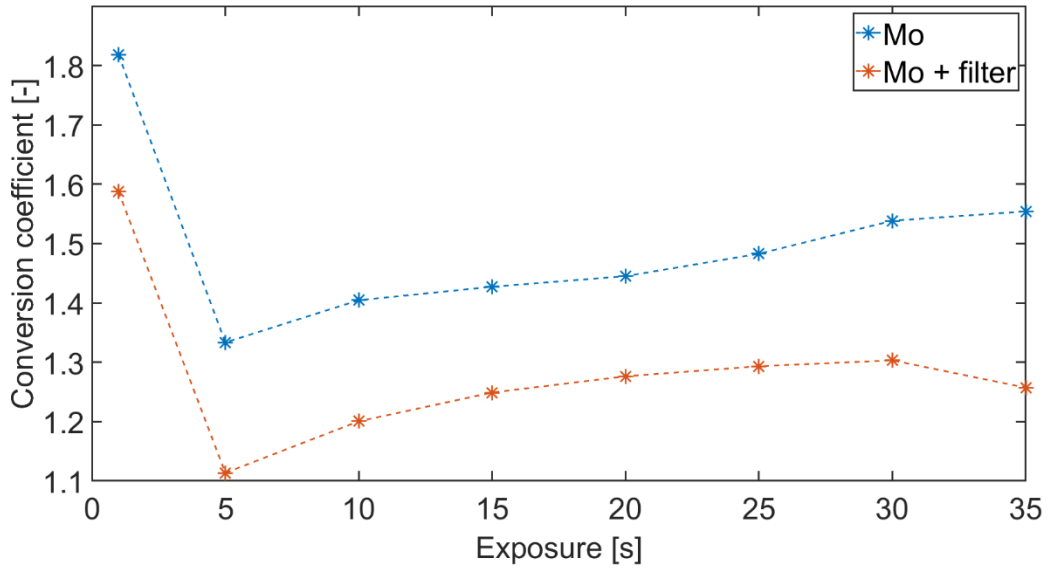
Figure 56:Conversion coefficients calculated for L0540 optical lens unit, binning 2×2.
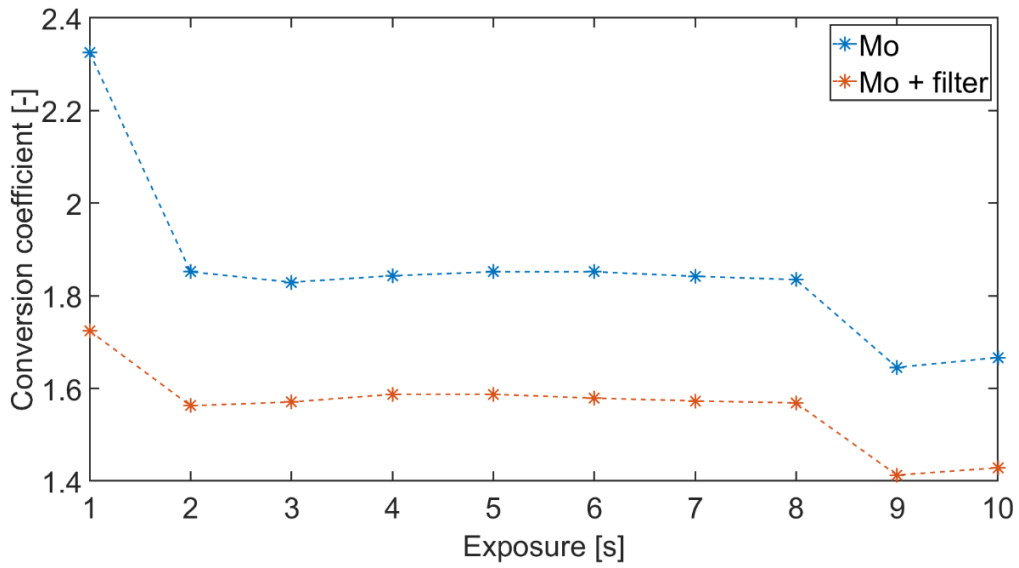
Figure 57:Conversion coefficients calculated for L1080 optical lens unit, binning 2×2

5.3   DTCT data registration

In terms of DTCT data processing, it is required that the data are perfectly aligned (i.e., corresponding structures are located on the same positions for both data). However, due to sequential character of DTCT acquisition using Rigaku nano3DX system, a difference in sample position between the two measurements cannot be ruled out because of various factors such as rotational stage instability (4.5.1) or sample's structural movement. Therefore, DTCT data alignment is necessary before further processing. Image registration is a process of transforming data from different sets of measurements into one coordinate system, which means that corresponding structural information from different times or imaged by different imaging modalities will be on same spatial coordinates. Practically it means that analysed images are aligned and geometrically transformed using a computational method for determining the point-by-point correspondence between those images. Used transformation models can be divided into several classes: rigid, affine, projective and nonrigid transformation when the complexity of the transforms in each transformation is characterised by degrees of freedom. Using such transformation models, an object can be transformed by translation, rotation or scaling. However, the key part of the registration procedure is the actual transformation parameters estimation. For this estimation, there exist many algorithms that can be divided into several classes: intensity-based methods [180], feature extraction based methods [181] or frequency domain methods [182]. However, functionality of those methods is dependent on the quality of input data, mainly in terms of noise and contrast of prominent structures and their overall detectability, which is hardly achievable especially for biological samples.

Therefore, this process is addressed in this work using developed samples holder with the reference area (for more details see section 4.5.2), whose detectability is guaranteed wide range of acquisition parameters due its' high density. This area specifically reduces the problem of volume registration to finding and alignment of a reference point within both acquired data, which increases the accuracy and speed of the whole image registration procedure over standard image registration methods. Within the proposed procedure, projection data are aligned using fully automatic image registration process based on detection of reference area within the developed sample's holder after DTCT acquisition. This procedure was used included in the DTCT workflow due to already mentioned possibility of sample's movement and rotational stage instability during the acquisition process, which cannot be corrected after tomographic reconstruction. Therefore, the registration of projection data prior to tomographic reconstruction enables their better alignment. Following the results from the section 4.5.1, the rotational movement of the stage is considered stable and consistent (perceived only in terms of rotational movement not stage stability), and the tilt of the sample is also considered constant, which reduces the problem of DTCT projection data registration to two parameters – vertical and horizontal displacement. The registration process consist of detecting the centre of reference fiducial in each Cu and Mo data projections, determining the ideal sinusoidal curse of this point within the Cu data acquisition (corresponding to the proposed procedure for rotational stage instability and inaccuracy correction presented in section 4.5.2.1), and then aligning the individual projections of both datasets so they match the estimated ideal course. This is done using b-spline interpolation to reach the sub-pixel precision (see Figure 58).
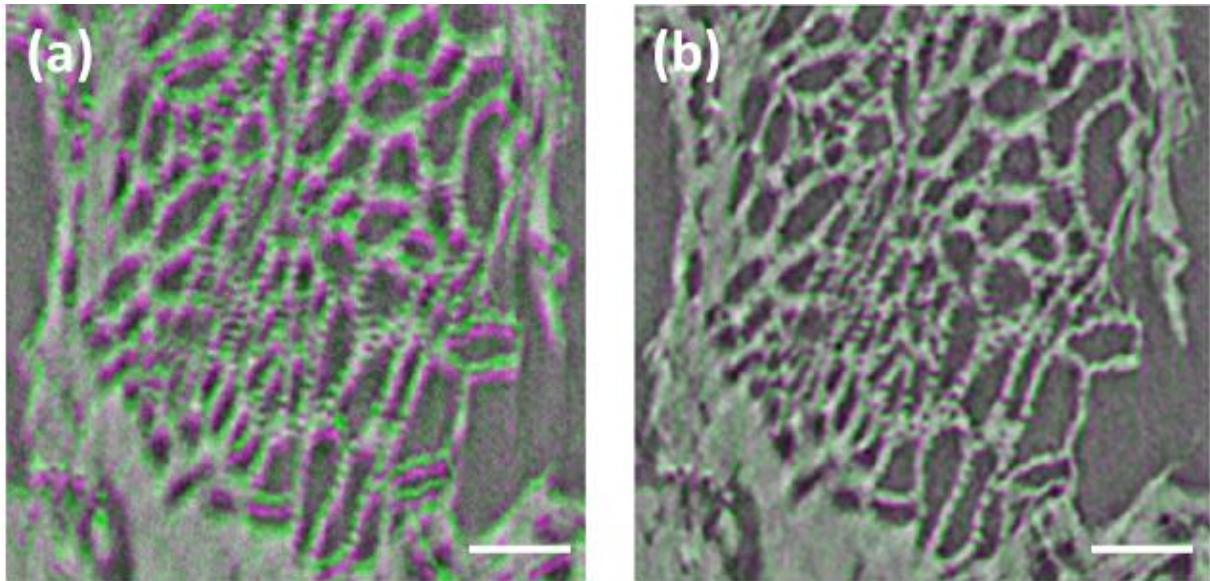
Figure 58: Results of proposed DTCT data registration procedure demonstrated on DTCT data of cumin seed scanned using Rigaku nano3DX device – for visualization purposes CT slices of both Cu and Mo target data were overlapped and presence of green and purple colours indicates level of their misalignment: a) Original data; b) Aligned data. Scale bar: 100 μm.

6 Quantitative analysis of CT data

As introduced in the section 1.3, the most widely used perception of quantitative computed tomography, is related to the quantitative characterization of acquired CT data. In scope of this thesis, two novel quantitative analysis methods were developed and published, and their main features and results relevant in scope of this work, are present in following text. For more details refer to the original works [183] and [184].

6.1 CT analysis of additive manufactured samples

X-ray computed tomography is a common method for non-destructive testing and analysis. One major application of CT is the porosity detection and quantification. This analysis is specifically important for metallic parts made by selective laser melting (SLM) technology, which are evaluated for internal porosity, when the presence of internal defects has a negative effect on their fatigue life and ultimate tensile strength (UTS) [183]. Therefore, one of the major challenges in the SLM production process is minimizing the internal porosity inside the manufactured parts. Currently, there are several possible ways to measure porosity, such as mass measurement, Archimedes method, metallography, and X-ray computed tomography. All these methods are based on different principles and incomparable in terms of getting the absolute value of the porosity for one sample [183]. Metallography is the most frequently used image-based method for the porosity analysis of SLM parts thanks to a high resolution that can be achieved and also to the fact that light or electron microscopes are accessible [183]. The weaknesses of this method are the necessary sample's surface preparation and also the fact that the evaluation of the total porosity (i.e., for the whole sample volume) as a mean value of several surfaces measurements, when the number and selection of the evaluated planar section have the major impact on the final porosity result. In comparison to metallography, CT technique has some undisputed benefits. CT technique enables to visualize the inner structure non-destructively, in three dimensions, and at one measurement process [183].

The porosity analysis using CT data is commonly based on pores segmentation by means of global thresholding, which has a major impact on results of the analysis [185]. Specifically, the threshold selection becomes a critical point influencing the result. In practice, threshold can be determined either automatically or manually by an operation. However, the automatic threshold selection depends on a material inner structure and also quality of input data. But the manual threshold selection is highly subjective and gives variable results depending on the operator's experience, knowledge of the studied sample and even on the way CT data are displayed on an ordinary monitor. This operator related variability brings a significant uncertainty to the porosity measurement in terms of the SLM production quality evaluation and was further studied in our work. These aspects rule out any trustworthy results coming from a comparative porosity measurement of two samples scanned in different laboratories and also of two samples measured in different times within one CT system. [183]

To overcome these issues, a new porosity analysis procedure on CT data was designed. It is based on a correlation with the metallographic image of the sample surface which is obtained with higher resolution and pore contrast than the CT data. For this reason, the metallographic image is used as a reference image for the threshold selection. The procedure respects the given voxel resolution of CT data, and it is objective and reproducible. These properties enable a comparative porosity analysis of samples from separate measurements which are even performed on different CT machines. The proposed procedure was tested on a sample of aluminium alloy including all possible defects related to additive manufacturing. Based on a comparison with manual and standard automatic techniques,

the proposed method showed a reliable determination of pores and a good agreement with the value determined by a group of experienced CT users. [183]

6.1.1 Reproducible porosity analysis (RPA)

The proposed procedure was designed with a respect to the crucial points of tomographic data processing. These aspects are the user independence, correct pores' segmentation, reproducibility, and adaptation for different voxel resolutions. The workflow of proposed procedure is described in Figure 59. The method is based on a correlation between CT data and metallographic data. The characteristics of metallographic analysis using microscopy are high resolution and easy pores segmentation. Therefore, the metallographic analysis complies with the task of the reference and the calibration for the CT porosity analysis. [183]

The correlation of these techniques is based on an alignment of corresponding images, i.e., a light microscopic image of the sample surface (LM image) and a CT top cross-section (CT image). Getting such corresponding images can be guaranteed only when the CT measurement is performed on a sample whose surface was already analysed by metallography. The acquisition of LM and CT images is followed by an image registration which aims to unify both images to the same size and orientation. This is done by a geometric transformation of LM image because the LM reaches higher resolution than micro-CT does. The transformation including the scaling, rotation and translation is determined automatically by the phase correlation [186]. Then the LM image and CT data are trimmed around the sample centre to avoid distorted areas of the image caused by a mechanical preparation of the sample surface. Moreover, removing these edges simplifies the porosity calculation as there is no need to distinguish the background pixels (outer sample space) from the pore's pixels presented by the same grey values. [183]

The threshold selection is implemented on these registered corresponding images. The reference porosity value is determined from LM image using global thresholding with Otsu's automatic threshold selection [175] for pores' segmentation. This method works reliably on LM images because of a high pores/material contrast. The reference porosity value is subsequently used for the selection of an optimal threshold value for CT data. This selection is realized using a brute-force search during the optimization process. In this process, the porosity from CT image is calculated for a series of threshold values (from minimum to maximum CT image intensity value). A criterion function is expressed for each porosity value. This function is defined as Euclidean distance from the reference LM image porosity value and the CT image porosity value for a particular threshold. The optimal threshold for global thresholding of CT data is then selected as a threshold where the criterion function reaches its minimum. This threshold is subsequently applied to the trimmed CT data volume using the global thresholding (see Figure 60) and porosity value is then calculated. [183]
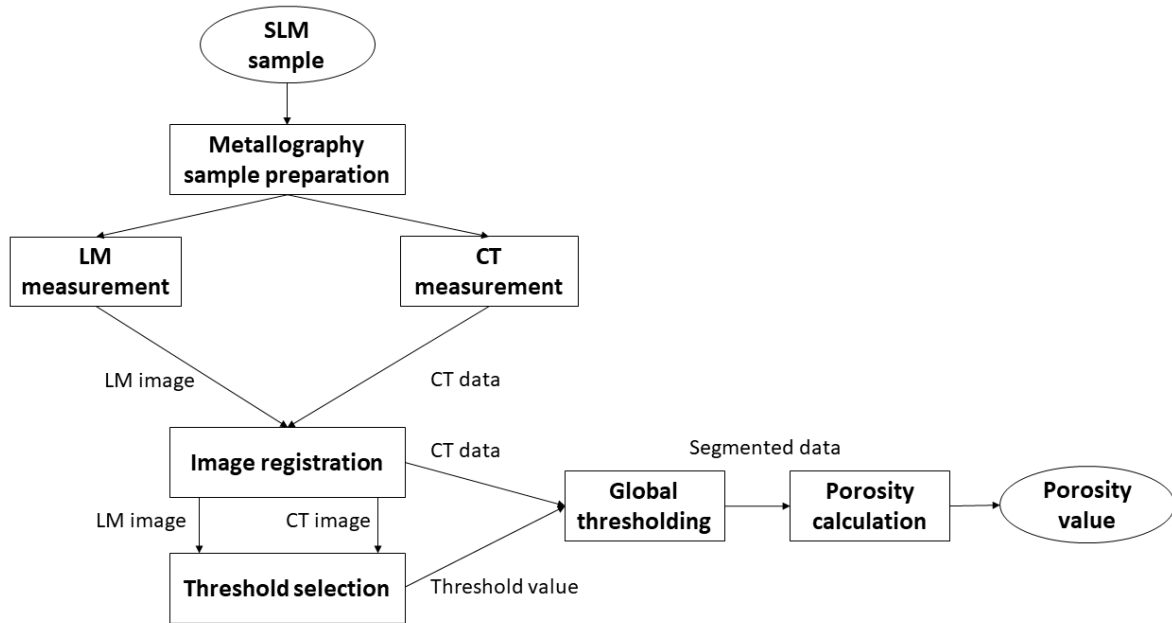
Figure 59: Scheme of proposed reproducible porosity analysis procedure. [183].
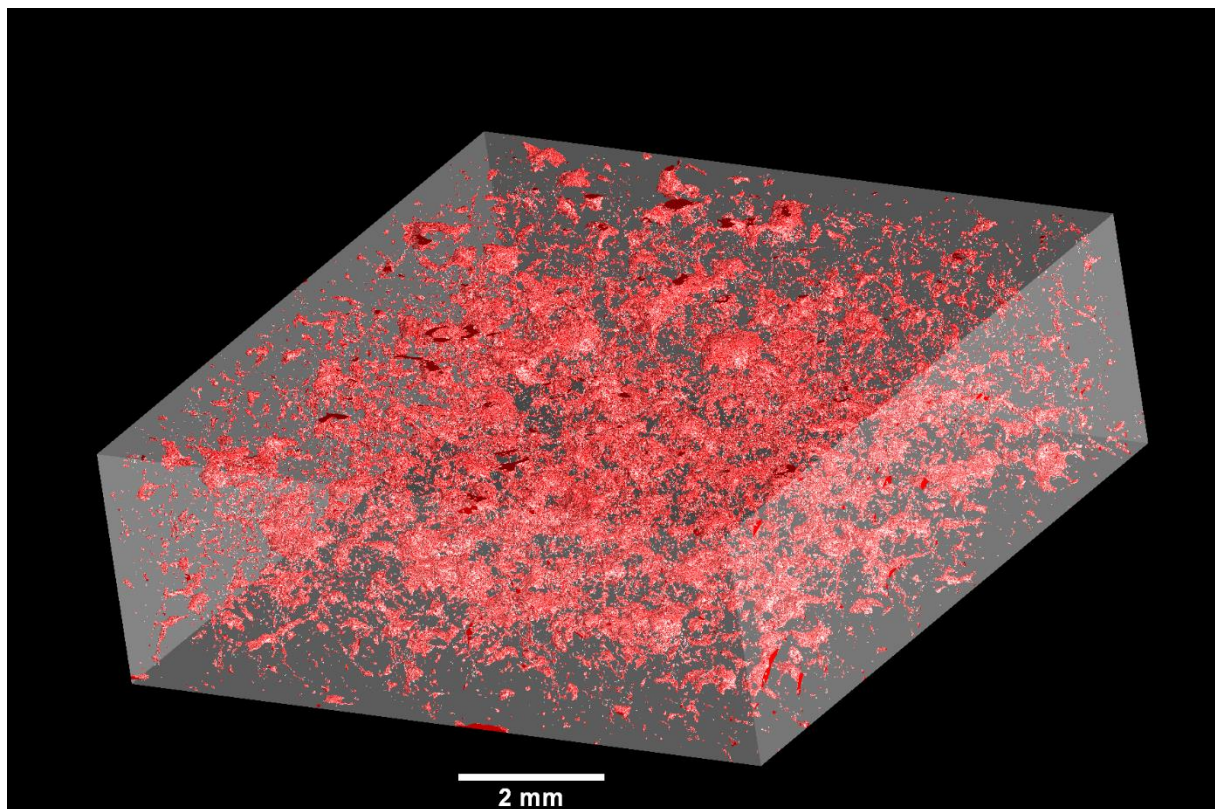
Figure 60: 3D pores distribution in analysed volume of aluminium alloy sample – achieved from CT data with use of proposed porosity analysis procedure. [183]

6.2 CT analysis of a mouse model for Alagille syndrome

The correct three-dimensional (3D) architecture of lumenized structures in our bodies is essential for function and our health [184]. The cardiovascular system, lungs, kidneys, liver, and other organs depend on precisely patterned tubular networks, when several diseases are caused by, or result in, alterations in the 3D architecture of those lumenized structures [184]. Precisely defining 3D architecture of healthy and diseased organs is a fundamental aspect of biology, and improved imaging methods would allow stricter characterization of animal models for human diseases. However, visualization of biological tubes in 3D is very challenging task, which has been until now restricted by a lack of adequate tools. Traditional microscopic imaging of anatomy structures enables only 2D visualization, using slices of tissue. This approach shows the cross-sections of tubes, but not how the ducts connect and interact [184]. An alternative is to use CT technique, which is, however, limited by poor contrast for soft tissues.

To overcome this, a new technique was developed called double resin casting micro computed tomography (DUCT) [184]. The approach involves making casts of biological tube systems using two types of radiopaque resin that show up differently under X-rays. Regarding instrumentation, the DUCT pipeline is not restricted to specific CT systems or acquisitions parameters, therefore samples can be imaged on any CT device with sufficient spatial resolution to study selected samples and their morphology. The new technique was tested on a mouse model of Alagille syndrome [187]. One resin was injected into the bile ducts, and another into the blood vessels, which enabled to reconstruct both trees digitally in 3D by means of CT and subsequent data segmentation (see Figure 61). For more details about developed pipeline for performing double resin casting microCT, please refer to the original work [184] or to the published protocol [188].
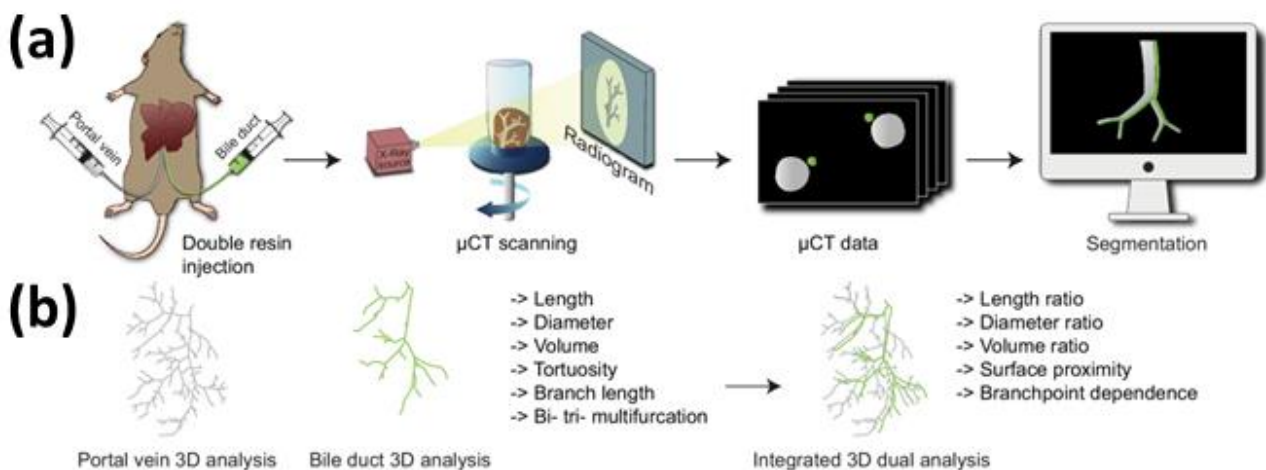
Figure 61: Schematical diagram of: a) DUCT pipeline - resin injection into two systems (portal venous and biliary), microCT of the organ, or individual lobes, and segmentation of CT data into 3D binary masks. b) quantitative analysis pipeline – creating 3D skeletons from the binary masks and quantifying architectural parameters in individual or combined systems. [184]

6.2.1 Quantitative analysis of 3D models of tubular systems

To extend possibilities of the DUCT technique, a new analysis pipeline was developed in scope of this thesis. This pipeline was as well included in the original work [184] and its' purpose was to enable quantitative assessment of 3D models resulting from DUCT procedure. This allowed to study architectural mechanisms of two tubular networks (i.e., revealing their length, volume, branching, and interactions) and together with DUCT could serve as a standard for whole organ analysis in animal models (see Figure 61), and can be further adapted for specific applications. The quantitative analysis pipeline was implemented in Matlab® programming environment and is freely available at: [189].
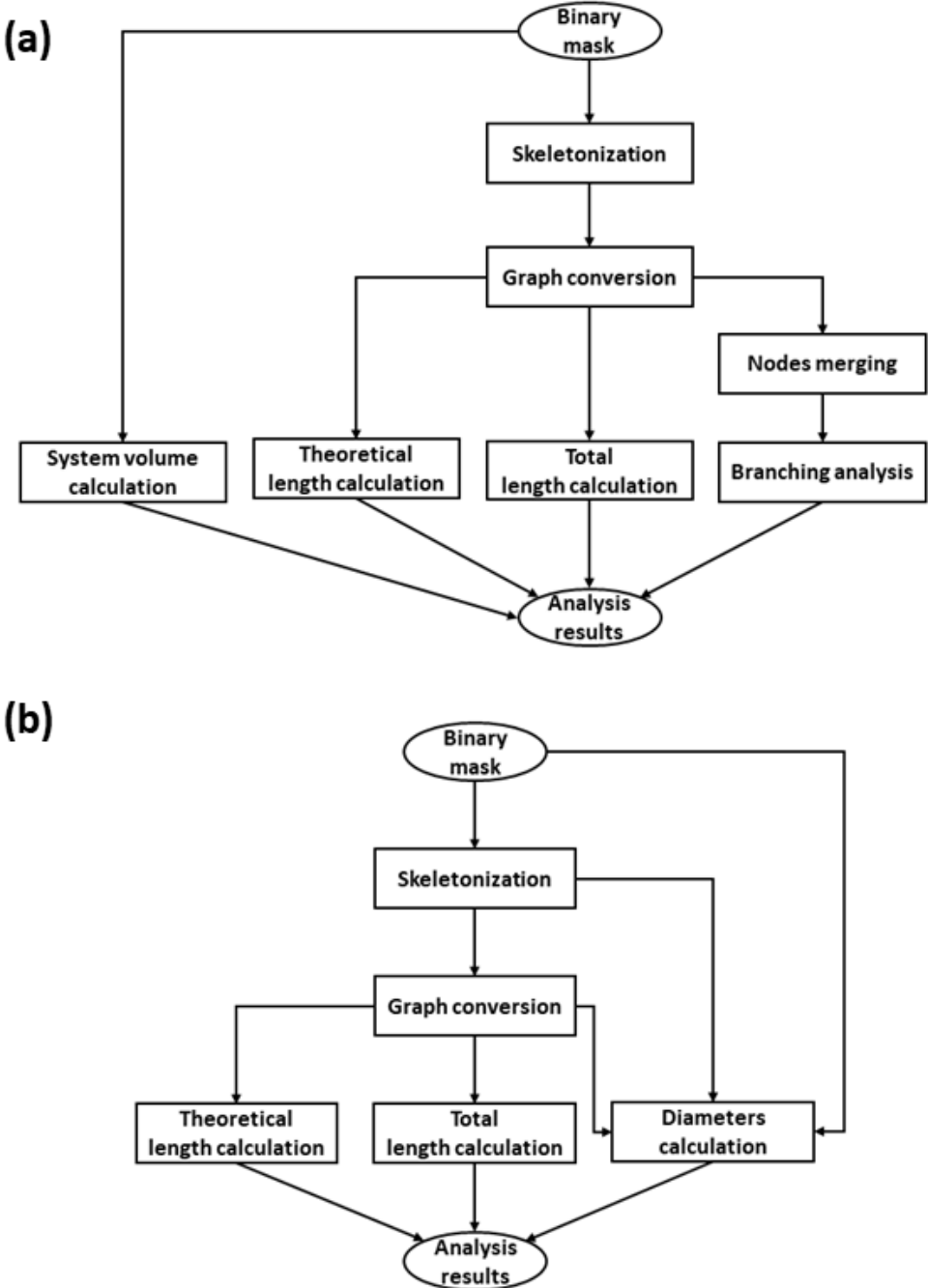
Figure 62: Scheme of proposed algorithms for quantitative analysis of tubular systems: a) Whole system analysis algorithm; b) Main branch analysis algorithm. [184]

Developed algorithm is compatible with 3D binary masks resulting from the DUCT method and was originally designed for morphological analysis of liver tubular system, i.e., bile duct (BD) and portal vein (PV). As result of DUCT, two separate masks of BD and PV system were generated, and the subsequent quantitative analysis was divided in two independent parts. First, the analysis of the entire portal vein and biliary system and second, analysis of the corresponding main branch (i.e., the longest branch) of each system. For detailed analysis and comparison of the whole system versus only the main branch, two algorithms were developed (see Figure 62). They differ in the input data and the evaluated parameters. [184]

However, the first step in both algorithms is to create a 3D skeleton of the input binary mask. The 3D skeleton was derived using the homotopic thinning algorithm originally described in the work by Lee et. al, [190] and subsequently optimized by Kerschnitzki et. al. [191]. Using available Matlab implementation of this algorithm [192], resulting network graph is formed by nodes and links between them, which are subject of further quantitative analysis:

- **Branching analysis**: analysing not only the branching itself but also the distance between BD and PV branching points. This parameter was calculated using 3D Euclidean distances between the BD branching points and the nearest branching point from PV system (see Figure 63). The data is represented as cumulative sum of percentage of BD branching point at a given distances between BD and PV branching points. The number of bi-furcations (i.e., one input and two outputs), tri-furcations (i.e., one input and three outputs) and quadri- and more-furcations (one input and more than three outputs), were assessed based on binary mask skeleton nodes that were divided into endpoints and branching points (see Figure 65). Branching points closer than 0.2 mm (this threshold value was derived based on visual assessment and knowledge of the system) were merged and further represented by one node. [184]
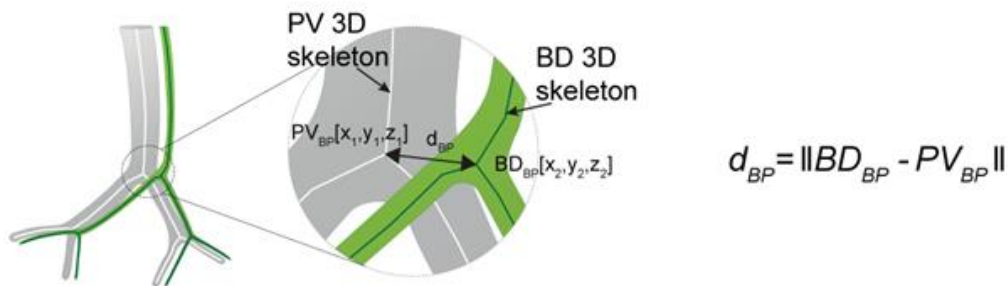
Figure 63: Scheme representing BD to PV branch point analysis. PV_{BD} = PV branch point, BD_{BD} = BD branch point, d_{BP} = Euclidean 3D distance between branch points. [184]

- **Gap analysis between BD and PV**: to evaluate the gap between BD and PV the surface distances were calculated for each BD skeleton point by detecting the nearest PV skeleton point and connecting the two points with a line and measuring the non-resin area on this line (zero area in the input binary masks, see Figure 64). Surface distance was then calculated using 3D Euclidean distance between the detected non-resin voxel coordinates. [184]
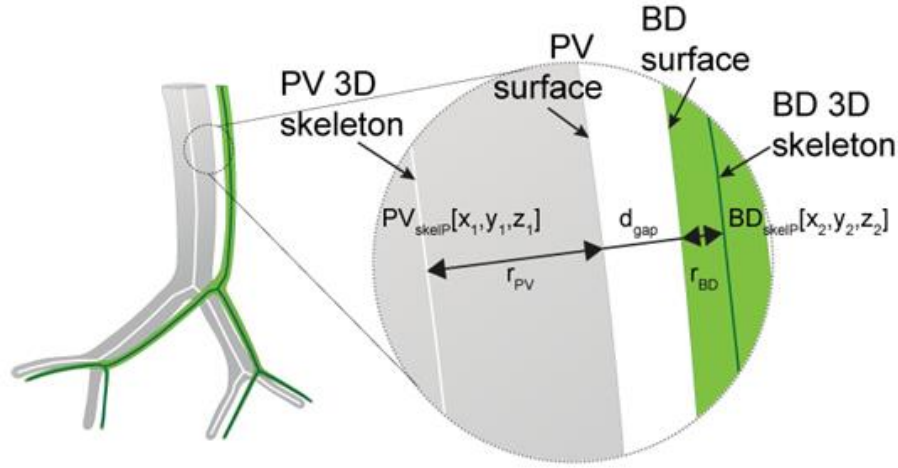
$$d_{gap} = \|BD_{skelP} - PV_{skelP}\| - r_{BD} - r_{PV}$$

Figure 64: Scheme of BD to PV surface distance analysis. PV_{skelP} = single point on PV skeleton, BD_{skelP} = single point on BD skeleton, r_{PV} = radius of PV at PV_{skelP} (i.e., minimal distance from PV_{skelP} to PV surface), r_{BD} = radius of BD at BD_{skelP} (i.e. minimal distance from BD_{skelP} to BD surface), d_{gap} = gap distance, which is derived by subtracting the radii from the skeleton to skeleton distance. [184]

- **Tortuosity measurements: t**o quantify length and tortuosity, total (i.e., curved) and theoretical (i.e., chord) lengths were measured for the whole system length and for the corresponding main branch. The curved length was defined as a cumulative sum of 3D Euclidean distances between neighbouring graph points (i.e., links forming points) multiplied by voxel size. The chord length was defined as cumulative sum of 3D Euclidean distances between neighbouring nodes multiplied by voxel size. The chord length therefore reflects system length where any nodes are connected by links with the shortest possible length. To analyse the relationship between BD and PV a length of the BD was divided by a PV length (curved or chord). Tortuosity was calculated as curved length divided by chord length of the same system and distributed into regions based on the generation number as previously described. Tortuosity was assessed in %, as BD and PV are not straight lines the actual tortuosity measurements were subtracted by 100% (i.e., perfectly straight line). [184]
- **Volume analysis:** total system volume was calculated by multiplying a number of voxels representing PV or BD by volume of one voxel. The relationship between BD and PV volumes was addressed by dividing the BD volume by PV volume. [184]
- **Diameter measurements:** the main branch diameter was calculated every 1.5 mm (this value was derived based on visual assessment and knowledge of the system) along the total length of the main branch. The radius was defined as the minimal distance from the skeleton to the boundary of segmented area in the input binary mask (i.e., border between background and area of interest). This boundary was calculated using a two-step procedure. In the first step, the input map was eroded using a 3D spherical shaped structural element with one pixel radius. Subsequently, the eroded area was subtracted from the original binary mask. This resulted in a binary mask representing the boundary between the background and the area of

90

interest. One radius value at a given skeleton point was then expressed as the minimum distance from that point to the mask boundary. This was calculated, using the minimal value search in the intersection of the boundary mask and the distance map from that point. The distance map from a given skeleton point was calculated as 3D Euclidean distance of the spatial coordinates. Subsequently the diameter value was calculated as the minimum distance to the boundary area multiplied by 2. To avoid any misrepresentation, the one final diameter value at a given point (every 1.5 mm of branch length) was calculated as a mean value of a diameter at that point and diameters at four neighbouring points (two on each side). [184]
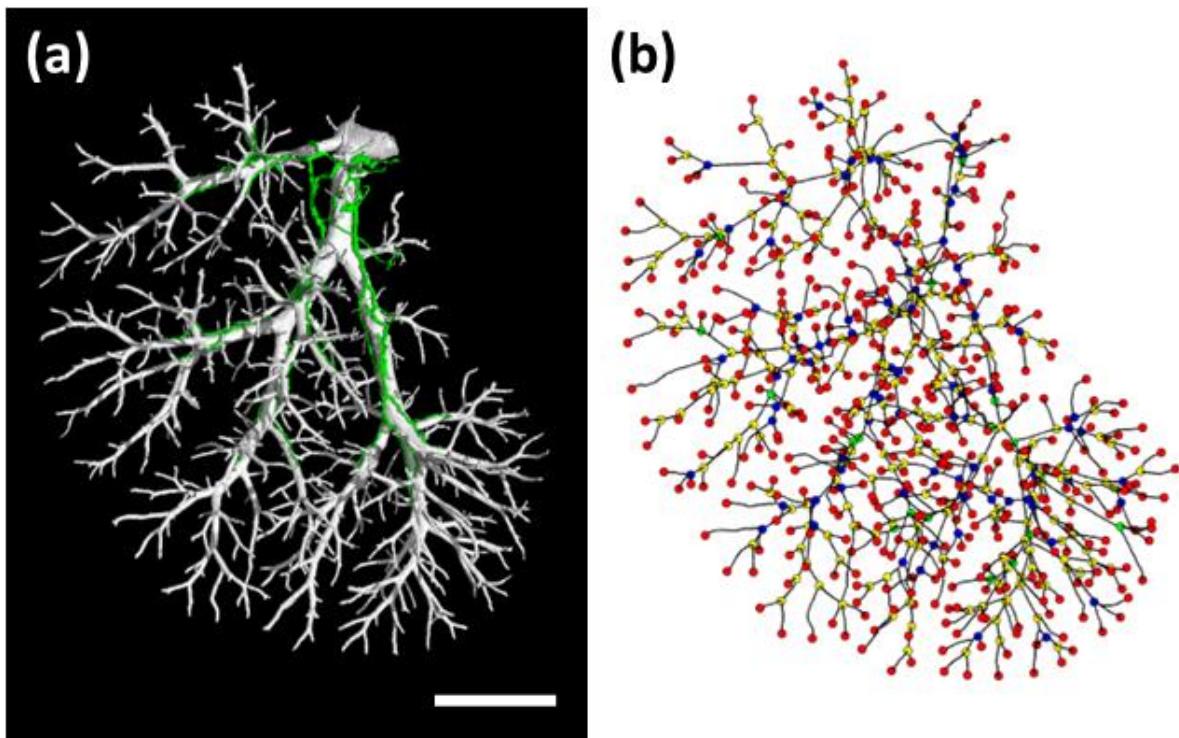
Figure 65: Visual results of DUCT and quantitative analysis pipelines demonstrated on mouse liver sample: a) 3D visualization of segmentation and identification results: bile duct (green area) and portal vein (white area); b)   Visualization of the truncation analysis results for portal vein system; red circles = endpoints, yellow circles = bi-furcations, blue circles = tri-furcations, green circles = quadri- and more- furcations, black lines represent branches between nodes; scale bar: 4 mm.

7 Conclusion

The topic of this thesis reflects the current need of researchers from various R&D fields to have the possibly of utilizing a 3D non-destructive imaging method with sufficient spatial resolution, that will provide them information that would be solely dependent on sample's properties and applicable for further quantitative analysis. X-ray computed tomography can, in general, fulfil all those demands, but especially aiming for higher spatial resolution and implementation of advanced CT techniques (e.g., 4D CT or spectral CT), brings strict requirements for both the hardware and the software. In sphere of submicron CT, the possibility of acquisition of undistorted CT data and its' further quantitative analysis is still highly limited by various technological aspects and lack of dedicated methodologies and correction solutions.

Objectives of this work were dealing with all the aspects of quantitative CT with specific focus on a laboratory-based submicron CT system Rigaku nano3DX. Firstly, the optimal reconstruction process for submicron CT data was found, involving the use of analytical reconstruction method with optimized settings respecting the achievable spatial resolution and data quality. Then the technological limitations of submicron CT acquisition using this device were assessed. Focusing on the technology-based tomographic artifacts, their individual causes and properties were studied, and optimal reduction strategies were proposed. Some of the most prominent artifacts of this class – noise and ring artifacts, are found to be related to the detection system itself. Therefore, three detector types were assessed for the task of submicron CT acquisition and compared in terms of quality and accuracy of acquired data, and the results were further incorporated into proposed reduction procedures. Specifically, novel procedures were developed for ring artifacts reduction and denoising of all the noise types present in Rigaku nano3DX data. The denoising solution, specifically, involves new algorithms for random valued impulse noise reduction and noise absolute deviation estimation, and practically tested state-of-the-art methods for shot noise reduction. Dedicated solution was also developed for the instability and inaccuracy of the rotational stage during submicron CT acquisition. This development involved also studying this instability in terms of thermal dependence and also in context of commercial lab-based CT systems.

Dealing with the spectral imaging and its's implementation for submicron CT data acquisition using Rigaku nano3DX, dedicated acquisition and DTCT data registration methodologies were developed. In terms of the DTCT data acquisition, novel procedure was defined for selecting the optimal acquisition parameters using the noise properties as evaluation metric. For the task of DTCT data registration, developed sample's holder with reference area was utilized resulting into fully automatic, robust, and precise solution. For the quantitative analysis of CT data, two novel methods were developed. One was specifically designed for porosity analysis of additive manufactured samples with a respect to the crucial points of tomographic data processing, making it objective and reproducible. Second method was specifically designed for quantitative assessment of 3D models of biological tubular systems and was practically tested on a mouse model of Alagille syndrome.

Exploiting the results of this work, a multi-purpose solution in form of QCT can be achieved that allows to reduce the limits of current CT technology and to fulfil requirements of R&D and basic research from various fields e.g., materials' development, tissue engineering, pharmacy, and others. In those filed, there is, especially, a need to have the possibility of utilizing a 3D, nondestructive, high-resolution imaging method, that will provide information that is solely dependent on samples' properties and can be used for further quantitative analysis.

References

[1]   MARTZ, Harry E., Clint M. LOGAN, Daniel J. SCHNEBERK a Peter J. SHULL. *X-Ray Imaging: Fundamentals, Industrial Techniques and Applications*. 1st Edition. CRC Press: Boca Raton: Taylor & Francis, 2017. ISBN 9780849397721.

[2]   DE CHIFFRE, L., S. CARMIGNATO, J.-P. KRUTH, R. SCHMITT a A. WECKENMANN. Industrial applications of computed tomography. *CIRP Annals*. 2014, **63**(2), 655-677. ISSN 00078506. Dostupné z: doi:10.1016/j.cirp.2014.05.011

[3]   STOCK, Stuart. *Microcomputed tomography: methodology and applications*. Boca Raton: CRC Press, 2009. ISBN 978-142-0058-765.

[4]   KRAEMER, Alexandra a Gisela LANZA. Assessment of the Measurement Procedure for Dimensional Metrology with X-ray Computed Tomography. *Procedia CIRP*. 2016, **43**, 362-367. ISSN 22128271. Dostupné z: doi:10.1016/j.procir.2016.02.018

[5]   NGUYEN THI, Thanh, Mizuki MORIOKA, Atsushi YOKOYAMA, Senji HAMANAKA, Katsuhisa YAMASHITA a Chisato NONOMURA. Measurement of fiber orientation distribution in injection-molded short-glass-fiber composites using X-ray computed tomography. *Journal of Materials Processing Technology*. 2015, **219**, 1-9. ISSN 09240136. Dostupné z: doi:10.1016/j.jmatprotec.2014.11.048

[6]   DU PLESSIS, Anton, Babatunde OLAWUYI, William BOSHOFF a Stephan LE ROUX. Simple and fast porosity analysis of concrete using X-ray computed tomography. *Materials and Structures*. 2016, **49**(1-2), 553-562. ISSN 1359-5997. Dostupné z: doi:10.1617/s11527-014-0519-9

[7]   CARMIGNATO, Simone, Wim DEWULF a Richard LEACH, ed. *Industrial X-Ray Computed Tomography*. 1 edition. Cham: Springer, 2018. ISBN 9783319595719. Dostupné z: doi:https://doi.org/10.1007/978-3-319-59573-3

[8]   POLUDNIOWSKI, G, G LANDRY, F DEBLOIS, P M EVANS a F VERHAEGEN. SpekCalc: a program to calculate photon spectra from tungsten anode x-ray tubes. *Physics in Medicine and Biology*. 2009, **54**(19), 433-438. ISSN 0031-9155. Dostupné z: doi:10.1088/0031-9155/54/19/N01

[9]   BUSHBERG, J. T., J. A. SEIBERT, E. M.Jr LEIDHOLDT a J. M. BOONE. *The Essential Physics of Medical Imaging:*. Third Edition. Philadelphia, PA, USA,: Lippincott Williams & Wilkins, 2012, 1048 pp. ISBN 9780781780575. Dostupné z: doi:10.1118/1.4811156

[10]   BERGER, M.J., J.H. HUBBELL, S.M SELTZER, J. CHANG, J.S COURSEY, R. SUKUMAR, D.S. ZUCKER a K. OLSEN. XCOM: Photon Cross Sections on a Personal Computer. In: *National Institute of Standards and Technology* [online]. Gaithersburg, MD, 2010 [cit. 2021-03-31]. Dostupné z: http://physics.nist.gov/xcom

[11]   ALLÉ, P, E WENGER, S DAHAOUI, D SCHANIEL a C LECOMTE. Comparison of CCD, CMOS and Hybrid Pixel x-ray detectors: detection principle and data quality. *Physica Scripta*. 2016, **91**(6), 15. ISSN 0031-8949. Dostupné z: doi:10.1088/0031-8949/91/6/063001

[12]   GRUNER, Sol, Mark TATE a Eric EIKENBERRY. Charge-coupled device area x-ray detectors. *Review of Scientific Instruments*. 2002, **73**(8), 2815-2842. ISSN 0034-6748. Dostupné z: doi:10.1063/1.1488674

[13]   MITTONE, Alberto, Ilja MANAKOV, Ludovic BROCHE, Christophe JARNIAS, Paola COAN a Alberto BRAVIN. Characterization of a sCMOS-based high-resolution imaging system. *Journal of Synchrotron Radiation*. 2017, **24**(6), 1226-1236. ISSN 1600-5775. Dostupné z: doi:10.1107/S160057751701222X

[14]   FÖRSTER, Andreas, Stefan BRANDSTETTER a Clemens SCHULZE-BRIESE. Transforming X-ray detection with hybrid photon counting detectors. *Philosophical Transactions of the Royal Society A: Mathematical, Physical and Engineering Sciences*. 2019, **377**(2147). ISSN 1364-503X. Dostupné z: doi:10.1098/rsta.2018.0241

[15]   BALLABRIGA, R., J. ALOZY, F. N. BANDI et al. Photon Counting Detectors for X-Ray Imaging With Emphasis on CT. *IEEE Transactions on Radiation and Plasma Medical Sciences*. 2021, **5**(4), 422-440. ISSN 2469-7311. Dostupné z: doi:10.1109/TRPMS.2020.3002949

[16]   DINAPOLI, Roberto, Anna BERGAMASCHI, Beat HENRICH et al. EIGER: Next generation single photon counting detector for X-ray applications. *Nuclear Instruments and Methods in Physics Research Section A: Accelerators, Spectrometers, Detectors and Associated Equipment*. 2011, **650**(1), 79-83. ISSN 01689002. Dostupné z: doi:10.1016/j.nima.2010.12.005

[17]   CAMPBELL, Michael. 10 years of the Medipix2 Collaboration. *Nuclear Instruments and Methods in Physics Research Section A: Accelerators, Spectrometers, Detectors and Associated Equipment*. 2011, **633**, 1-10. ISSN 01689002. Dostupné z: doi:10.1016/j.nima.2010.06.106

[18]   BALLABRIGA, R., M. CAMPBELL, E. HEIJNE, X. LLOPART, L. TLUSTOS a W. WONG. Medipix3: A 64k pixel detector readout chip working in single photon counting mode with improved spectrometric performance. *Nuclear Instruments and Methods in Physics Research Section A: Accelerators, Spectrometers, Detectors and Associated Equipment*. 2011, **633**, 15-18. ISSN 01689002. Dostupné z: doi:10.1016/j.nima.2010.06.108

[19]   LLOPART, X., R. BALLABRIGA, M. CAMPBELL, L. TLUSTOS a W. WONG. Timepix, a 65k programmable pixel readout chip for arrival time, energy and/or photon counting measurements. *Nuclear Instruments and Methods in Physics Research Section A: Accelerators, Spectrometers, Detectors and Associated Equipment*. 2007, **581**(1-2), 485-494. ISSN 01689002. Dostupné z: doi:10.1016/j.nima.2007.08.079

[20]   BALLABRIGA, R, J ALOZY, G BLAJ et al. The Medipix3RX: a high resolution, zero dead-time pixel detector readout chip allowing spectroscopic imaging. *Journal of Instrumentation*. 2013, **8**(02), 02016-02016. ISSN 1748-0221. Dostupné z: doi:10.1088/1748-0221/8/02/C02016

[21]   VAN NIEUWENHOVE, Vincent, Jan DE BEENHOUWER, Francesco DE CARLO, Lucia MANCINI, Federica MARONE a Jan SIJBERS. Dynamic intensity normalization using eigen flat fields in X-ray imaging. *Optics Express*. 2015, **23**(21), 27975-27989. ISSN 1094-4087. Dostupné z: doi:10.1364/OE.23.027975

[22]   TLUSTOS, L., M. CAMPBELL, E. HEIJNE a X. LLOPART. Signal variations in high granularity Si pixel detectors. In: *2003 IEEE Nuclear Science Symposium. Conference Record (IEEE Cat. No.03CH37515)*. Portland, OR, USA: IEEE, 2003, 1588-1593 Vol.3. ISBN 0-7803-8257-9. ISSN 1082-3654. Dostupné z: doi:10.1109/NSSMIC.2003.1352181

[23]   VåGBERG, William, Jakob LARSSON a Hans HERTZ. Removal of ring artifacts in microtomography by characterization of scintillator variations. *Optics Express*. 2017, **25**(19), 23191-23198. ISSN 1094-4087. Dostupné z: doi:10.1364/OE.25.023191

[24]   CROTON, Linda, Gary RUBEN, Kaye MORGAN, David PAGANIN a Marcus KITCHEN. Ring artifact suppression in X-ray computed tomography using a simple, pixel-wise response correction. *Optics Express*. 2019, **27**(10), 14231-14245. ISSN 1094-4087. Dostupné z: doi:10.1364/OE.27.014231

[25]   PARK, So E., Jae G. KIM, M. A. A. HEGAZY, Min H. CHO a Soo Y. LEE. A flat-field correction method for photon-counting-detector-based micro-CT. *Proc. SPIE 9033: Medical Imaging 2014: Physics of Medical Imaging*. 2014, (90335). Dostupné z: doi:10.1117/12.2043317

[26]   TITARENKO, Sofya, Philip WITHERS a Anatoly YAGOLA. An analytical formula for ring artefact suppression in X-ray tomography. *Applied Mathematics Letters*. 2010, **23**(12), 1489-1495. ISSN 08939659. Dostupné z: doi:10.1016/j.aml.2010.08.022

[27]   LIFTON, Joseph a Tong LIU. Ring artefact reduction via multi-point piecewise linear flat field correction for X-ray computed tomography. *Optics Express*. 2019, **27**(3), 3217-3228. ISSN 1094-4087. Dostupné z: doi:10.1364/OE.27.003217

[28]   PASCHALIS, P, N.D GIOKARIS, A KARABARBOUNIS et al. Tomographic image reconstruction using Artificial Neural Networks. *Nuclear Instruments and Methods in Physics Research Section A: Accelerators, Spectrometers, Detectors and Associated Equipment*. 2004, **527**(1-2), 211-215. ISSN 01689002. Dostupné z: doi:10.1016/j.nima.2004.03.122

[29]   PELT, Daniel a Kees BATENBURG. Fast Tomographic Reconstruction From Limited Data Using Artificial Neural Networks. *IEEE Transactions on Image Processing*. 2013, **22**(12), 5238-5251. ISSN 1057-7149. Dostupné z: doi:10.1109/TIP.2013.2283142

[30]   ARGYROU, Maria, Dimitris MAINTAS, Charalampos TSOUMPAS a Efstathios STILIARIS. Tomographic Image Reconstruction based on Artificial Neural Network (ANN) techniques. In: *2012 IEEE Nuclear Science Symposium and Medical Imaging Conference Record (NSS/MIC)*. IEEE, 2012, s. 3324-3327. ISBN 978-1-4673-2030-6. Dostupné z: doi:10.1109/NSSMIC.2012.6551757

[31]   CHEN, Hu, Yi ZHANG, Weihua ZHANG, Peixi LIAO, Ke LI, Jiliu ZHOU a Ge WANG. ALow-dose CT via convolutional neural network. *Biomedical Optics Express*. 2017, **8**(2), 679-694. ISSN 2156-7085. Dostupné z: doi:10.1364/BOE.8.000679

[32]   ŠALPLACHTA, Jakub. *Kvantitativní počítačová tomografie* [online]. Brno, 2019 [cit. 2021-09-08].
         Dostupné z: https://www.vutbr.cz/studenti/zav-prace/detail/123252. Pojednání. Vysoké učení
         technické v Brně, Středoevropský technologický institut VUT. Vedoucí práce Jozef Kaiser.

[33]   FELDKAMP, L. A., L. C. DAVIS a J. W. KRESS. Practical cone-beam algorithm. *Journal of the Optical
         Society of America A*. 1984, **1**(6), 1-8. ISSN 1084-7529. Dostupné z: doi:10.1364/JOSAA.1.000612

[34]   JAN, Jiří. *Medical image processing, reconstruction and restoration: concepts and methods*. Boca
         Raton: Taylor, 2006. Signal processing and communications, 24. ISBN 08-247-5849-8.

[35]   BEISTER, Marcel, Daniel KOLDITZ a Willi A. KALENDER. Iterative reconstruction methods in X-ray
         CT.   *Physica   Medica*.   2012,   **28**(2),   94-108.   ISSN   11201797.   Dostupné   z:
         doi:10.1016/j.ejmp.2012.01.003

[36]   GORDON, Richard, Robert BENDER a Gabor HERMAN. Algebraic Reconstruction Techniques (ART)
         for three-dimensional electron microscopy and X-ray photography. *Journal of Theoretical Biology*.
         1970, **29**(3), 471-481. ISSN 00225193. Dostupné z: doi:10.1016/0022-5193(70)90109-8

[37]   ANDERSEN, A. Simultaneous Algebraic Reconstruction Technique (SART): A superior
         implementation of the ART algorithm. *Ultrasonic Imaging*. 1984, **6**(1), 81-94. ISSN 01617346.
         Dostupné z: doi:10.1016/0161-7346(84)90008-7

[38]   JI, Dongjiang, Gangrong QU a Baodong LIU. Simultaneous algebraic reconstruction technique
         based on guided image filtering. *Optics Express*. 2016, **24**(14), 15897-15911. ISSN 1094-4087.
         Dostupné z: doi:10.1364/OE.24.015897

[39]   HU, Jingjing, Xing ZHAO a Feng WANG. An extended simultaneous algebraic reconstruction
         technique (E-SART) for X-ray dual spectral computed tomography. *Scanning*. 2016, **38**(6), 599-611.
         ISSN 01610457. Dostupné z: doi:10.1002/sca.21306

[40]   GILBERT, Peter. Iterative methods for the three-dimensional reconstruction of an object from
         projections. *Journal of Theoretical Biology*. 1972, **36**(1), 105-117. ISSN 00225193. Dostupné z:
         doi:10.1016/0022-5193(72)90180-4

[41]   BAPPY, D.M. a Insu JEON. Modified simultaneous iterative reconstruction technique for fast, high-
         quality CT reconstruction. *IET Image Processing*. 2017, **11**(9), 701-708. ISSN 1751-9659. Dostupné
         z: doi:10.1049/iet-ipr.2017.0304

[42]   WOLF, D., A. LUBK a H. LICHTE. Weighted simultaneous iterative reconstruction technique for
         single-axis tomography. *Ultramicroscopy*. 2014, **136**, 15-25. ISSN 03043991. Dostupné z:
         doi:10.1016/j.ultramic.2013.07.016

[43]   SHEPP, L. A. a Y. VARDI. Maximum Likelihood Reconstruction for Emission Tomography. *IEEE
         Transactions on Medical Imaging*. 1982, **1**(2), 113-122. ISSN 0278-0062. Dostupné z:
         doi:10.1109/TMI.1982.4307558

[44]   BOUMAN, C.A. a K. SAUER. A unified approach to statistical tomography using coordinate descent optimization. *IEEE Transactions on Image Processing*. 1996, **5**(3), 480-492. ISSN 1057-7149. Dostupné z: doi:10.1109/83.491321

[45]   THIBAULT, Jean-Baptiste, Ken D. SAUER, Charles A. BOUMAN a Jiang HSIEH. A three-dimensional statistical approach to improved image quality for multislice helical CT. *Medical Physics*. 2007, **34**(11), 4526-4544. ISSN 00942405. Dostupné z: doi:10.1118/1.2789499

[46]   YU, Zhou, Jean-Baptiste THIBAULT, Charles A. BOUMAN, Ken D. SAUER a Jiang HSIEH. Fast Model-Based X-Ray CT Reconstruction Using Spatially Nonhomogeneous ICD Optimization. *IEEE Transactions on Image Processing*. 2011, **20**(1), 161-175. ISSN 1057-7149. Dostupné z: doi:10.1109/TIP.2010.2058811

[47]   DE MAN, B., J. NUYTS, P. DUPONT, G. MARCHAL a P. SUETENS. An iterative maximum-likelihood polychromatic algorithm for CT. *IEEE Transactions on Medical Imaging*. 2001, **20**(10), 999-1008. ISSN 02780062. Dostupné z: doi:10.1109/42.959297

[48]   LAURENT, Gautier, Nicolas VILLANI, Gabriela HOSSU, Aymeric RAUCH, Alain NOËL, Alain BLUM a Pedro Augusto GONDIM TEIXEIRA. Full model-based iterative reconstruction (MBIR) in abdominal CT increases objective image quality, but decreases subjective acceptance. *European Radiology*. 2019, **29**(8), 4016-4025. ISSN 0938-7994. Dostupné z: doi:10.1007/s00330-018-5988-8

[49]   SUN, Jihang, Tong YU, Jinrong LIU, Xiaomin DUAN, Di HU, Yong LIU a Yun PENG. Image quality improvement using model-based iterative reconstruction in low dose chest CT for children with necrotizing pneumonia. *BMC Medical Imaging*. 2017, **17**(1). ISSN 1471-2342. Dostupné z: doi:10.1186/s12880-017-0177-9

[50]   LIU, Lu. Model-based Iterative Reconstruction: A Promising Algorithm for Today's Computed Tomography Imaging. *Journal of Medical Imaging and Radiation Sciences*. 2014, **45**(2), 131-136. ISSN 19398654. Dostupné z: doi:10.1016/j.jmir.2014.02.002

[51]   KAMPSCHULTE, M., A. LANGHEINIRCH, J. SENDER et al. Nano-Computed Tomography: Technique and Applications. *RöFo - Fortschritte auf dem Gebiet der Röntgenstrahlen und der bildgebenden Verfahren*. 2016, **188**(02), 146-154. ISSN 1438-9029. Dostupné z: doi:10.1055/s-0041-106541

[52]   GAMBLE, John F., Mike TOBYN, Shawn ZHANG et al. Characterization of the Morphological Nature of Hollow Spray Dried Dispersion Particles Using X-ray Submicron-Computed Tomography. *AAPS PharmSciTech*. 2022, **23**(1), 1-7. ISSN 1530-9932. Dostupné z: doi:10.1208/s12249-021-02184-7

[53]   ZABLER, Simon, Maximilian ULLHERR, C. FELLA, R. SCHIELEIN a O. FOCKE. *Comparing Image Quality in Phase Contrast subμ X-Ray Tomography - A Round-Robin Study*. 2019, 1-18.

[54]   TOUŠ, Jan, Martin HORVÁTH, Ladislav PÍNA, Karel BLAŽEK a Bruno SOPKO. High-resolution application of YAG:Ce and LuAG:Ce imaging detectors with a CCD X-ray camera. *Nuclear Instruments and Methods in Physics Research Section A: Accelerators, Spectrometers, Detectors and Associated Equipment*. 2008, **591**(1), 264-267. ISSN 01689002. Dostupné z: doi:10.1016/j.nima.2008.03.070

[55]   BARRETT, Julia F. a Nicholas KEAT. Artifacts in CT: Recognition and Avoidance. *RadioGraphics*. 2004, **24**(6), 1679-1691. ISSN 0271-5333. Dostupné z: doi:10.1148/rg.246045065

[56]   HSIEH, Jiang. *Computed Tomography: Principles, Design, Artifacts, and Recent Advances*. Third edition. Bellingham, Washington USA: SPIE Press, 2015. ISBN 9781628418255.

[57]   SCHÜLLER, Sören, Stefan SAWALL, Kai STANNIGEL, Markus HÜLSBUSCH, Johannes ULRICI, Erich HELL a Marc KACHELRIEß. Segmentation-free empirical beam hardening correction for CT. *Medical Physics*. 2015, **42**(2), 794-803. ISSN 00942405. Dostupné z: doi:10.1118/1.4903281

[58]   MCDAVID, William D., Robert G. WAGGENER, William H. PAYNE a Michael J. DENNIS. Correction for spectral artifacts in cross-sectional reconstruction from x rays. *Medical Physics*. 1977, **4**(1), 54-57. ISSN 00942405. Dostupné z: doi:10.1118/1.594302

[59]   PANG, Sing Chin a Sebastian GENNA. Corrections for X-Ray Polychromaticity Effects on Three-Dimensional Reconstruction. *IEEE Transactions on Nuclear Science*. 1976, **23**(1), 623-626. ISSN 0018-9499. Dostupné z: doi:10.1109/TNS.1976.4328316

[60]   HERMAN, G T. Correction for beam hardening in computed tomography. *Physics in Medicine and Biology*. 1979, **24**(1), 81-106. ISSN 00319155. Dostupné z: doi:10.1088/0031-9155/24/1/008

[61]   BROOKS, R A a G Di CHIRO. Beam hardening in X-ray reconstructive tomography. *Physics in Medicine and Biology*. 1976, **21**(3), 390-398. ISSN 00319155. Dostupné z: doi:10.1088/0031-9155/21/3/004

[62]   RÜEGSEGGER, P, Th HANGARTNER, H U KELLER a Th HINDERLING. Standardization of Computed Tomography Images by Means of a Material-Selective Beam Hardening Correction. *Journal of Computer Assisted Tomography*. 1978, **2**(2), 184-188. ISSN 0363-8715. Dostupné z: doi:10.1097/00004728-197804000-00012

[63]   NALCIOGLU, O a R Y LOU. Post-reconstruction method for beam hardening in computerised tomography. *Physics in Medicine and Biology*. 1979, **24**(2), 330-341. ISSN 00319155. Dostupné z: doi:10.1088/0031-9155/24/2/009

[64]   KACHELRIEß, Marc, Katia SOURBELLE a Willi A. KALENDER. Empirical cupping correction: A first-order raw data precorrection for cone-beam computed tomography. *Medical Physics*. 2006, **33**(5), 1269-1274. ISSN 00942405. Dostupné z: doi:10.1118/1.2188076

[65]   KYRIAKOU, Yiannis, Esther MEYER, Daniel PRELL a Marc KACHELRIEß. Empirical beam hardening correction (EBHC) for CT. *Medical Physics*. 2010, **37**(10), 5179-5187. ISSN 00942405. Dostupné z: doi:10.1118/1.3477088

[66]   HUANG, T., G. YANG a G. TANG. A fast two-dimensional median filtering algorithm. *IEEE Transactions on Acoustics, Speech, and Signal Processing*. 1979, **27**(1), 13-18. ISSN 0096-3518. Dostupné z: doi:10.1109/TASSP.1979.1163188

[67]   HWANG, H. a R.A. HADDAD. Adaptive median filters: new algorithms and results. *IEEE Transactions on Image Processing*. 1995, **4**(4), 499-502. ISSN 10577149. Dostupné z: doi:10.1109/83.370679

[68]   VERMA, Kesari, Bikesh Kumar SINGH a A.S. THOKE. An Enhancement in Adaptive Median Filter for Edge Preservation. *Procedia Computer Science*. 2015, **48**, 29-36. ISSN 18770509. Dostupné z: doi:10.1016/j.procs.2015.04.106

[69]   SHRESTHA, Suman. Image Denoising Using New Adaptive Based Median Filter. *Signal & Image Processing : An International Journal (SIPIJ)*. 2014, **5**(4), 1-13. ISSN 22293922. Dostupné z: doi:10.5121/sipij.2014.5401

[70]   LIN YIN, , RUIKANG YANG, M. GABBOUJ a Y. NEUVO. Weighted median filters: a tutorial. *IEEE Transactions on Circuits and Systems II: Analog and Digital Signal Processing*. 1996, **43**(3), 157-192. ISSN 10577130. Dostupné z: doi:10.1109/82.486465

[71]   KHAN, Sajid a Dong-Ho LEE. An adaptive dynamically weighted median filter for impulse noise removal. *EURASIP Journal on Advances in Signal Processing*. 2017, **2017**(1). ISSN 1687-6180. Dostupné z: doi:10.1186/s13634-017-0502-z

[72]   POK, G. a JYH-CHARN LIU. Decision-based median filter improved by predictions. In: *Proceedings 1999 International Conference on Image Processing (Cat. 99CH36348)*. IEEE, 1999, 410-413 vol.2. ISBN 0-7803-5467-2. Dostupné z: doi:10.1109/ICIP.1999.822928

[73]   SAMANTARAY, Aswini Kumar a Priyanka MALLICK. Decision Based Adaptive Neighborhood Median Filter. *Procedia Computer Science*. 2015, **48**, 222-227. ISSN 18770509. Dostupné z: doi:10.1016/j.procs.2015.04.174

[74]   ARAKAWA, Kaoru. Median filter based on fuzzy rules and its application to image restoration. *Fuzzy Sets and Systems*. 1996, **77**(1), 3-13. ISSN 01650114. Dostupné z: doi:10.1016/0165-0114(95)00122-0

[75]   ZHOU, Yan, Quan-hua TANG a Wei-dong JIN. Adaptive Fuzzy Median Filter for Images Corrupted by Impulse Noise. In: *2008 Congress on Image and Signal Processing*. IEEE, 2008, s. 265-269. ISBN 978-0-7695-3119-9. Dostupné z: doi:10.1109/CISP.2008.231

[76]   TOH, K.K.V. a N.A.M. ISA. Noise Adaptive Fuzzy Switching Median Filter for Salt-and-Pepper Noise Reduction. *IEEE Signal Processing Letters*. 2010, **17**(3), 281-284. ISSN 1070-9908. Dostupné z: doi:10.1109/LSP.2009.2038769

[77]   ZHOU WANG, a D. ZHANG. Progressive switching median filter for the removal of impulse noise from highly corrupted images. *IEEE Transactions on Circuits and Systems II: Analog and Digital Signal Processing*. 1999, **46**(1), 78-80. ISSN 10577130. Dostupné z: doi:10.1109/82.749102

[78]   GARNETT, R., T. HUEGERICH, C. CHUI a WENJIE HE. A universal noise removal algorithm with an impulse detector. *IEEE Transactions on Image Processing*. 2005, **14**(11), 1747-1754. ISSN 1057-7149. Dostupné z: doi:10.1109/TIP.2005.857261

[79]   WANG, Gaihua, Dehua LI, Weimin PAN a Zhaoxiang ZANG. Modified switching median filter for impulse noise removal. *Signal Processing*. 2010, **90**(12), 3213-3218. ISSN 01651684. Dostupné z: doi:10.1016/j.sigpro.2010.05.026

[80] HADDAD, R.A. a A.N. AKANSU. A class of fast Gaussian binomial filters for speech and image processing. *IEEE Transactions on Signal Processing*. 1991, **39**(3), 723-727. ISSN 1053587X. Dostupné z: doi:10.1109/78.80892

[81] BUADES, A., B. COLL a J.-M. MOREL. A Non-Local Algorithm for Image Denoising. In: *2005 IEEE Computer Society Conference on Computer Vision and Pattern Recognition (CVPR'05)*. IEEE, 2005, s. 60-65. ISBN 0-7695-2372-2. Dostupné z: doi:10.1109/CVPR.2005.38

[82] COUPE, P., P. YGER, S. PRIMA, P. HELLIER, C. KERVRANN a C. BARILLOT. An Optimized Blockwise Nonlocal Means Denoising Filter for 3-D Magnetic Resonance Images. *IEEE Transactions on Medical Imaging*. 2008, **27**(4), 425-441. ISSN 0278-0062. Dostupné z: doi:10.1109/TMI.2007.906087

[83] COUPÉ, Pierrick, Martin MUNZ, Jose V. MANJÓN, Edward S. RUTHAZER a D. LOUIS COLLINS. A CANDLE for a deeper in vivo insight. *Medical Image Analysis*. 2012, **16**(4), 849-864. ISSN 13618415. Dostupné z: doi:10.1016/j.media.2012.01.002

[84] RUDIN, Leonid, Stanley OSHER a Emad FATEMI. Nonlinear total variation based noise removal algorithms. *Physica D: Nonlinear Phenomena*. 1992, **60**(1-4), 259-268. ISSN 01672789. Dostupné z: doi:10.1016/0167-2789(92)90242-F

[85] GETREUER, Pascal. Rudin-Osher-Fatemi Total Variation Denoising using Split Bregman. *Image Processing On Line*. 2012, **2**, 74-95. ISSN 2105-1232. Dostupné z: doi:10.5201/ipol.2012.g-tvd

[86] CHEN, Qian a Dapeng WU. Image denoising by bounded block matching and 3D filtering. *Signal Processing*. 2010, **90**(9), 2778-2783. ISSN 01651684. Dostupné z: doi:10.1016/j.sigpro.2010.03.016

[87] ZHANG, Shengnan, Lei WANG, Chunhong CHANG, Cong LIU, Longbo ZHANG a Huanqing CUI. An Image Denoising Method Based on BM4D and GAN in 3D Shearlet Domain. *Mathematical Problems in Engineering*. 2020, **2020**, 1-11. ISSN 1024-123X. Dostupné z: doi:10.1155/2020/1730321

[88] KRULL, Alexander, Tim-Oliver BUCHHOLZ a Florian JUG. Noise2Void - Learning Denoising From Single Noisy Images. In: *2019 IEEE/CVF Conference on Computer Vision and Pattern Recognition (CVPR)*. IEEE, 2019, s. 2124-2132. ISBN 978-1-7281-3293-8. Dostupné z: doi:10.1109/CVPR.2019.00223

[89] HENDRIKSEN, Allard Adriaan, Daniel Maria PELT a K. Joost BATENBURG. Noise2Inverse: Self-Supervised Deep Convolutional Denoising for Tomography. *IEEE Transactions on Computational Imaging*. 2020, **6**, 1320-1335. ISSN 2333-9403. Dostupné z: doi:10.1109/TCI.2020.3019647

[90] KIM, Ji, Yongjin CHANG a Jong RA. Denoising of polychromatic CT images based on their own noise properties. *Medical Physics*. 2016, **43**(5), 2251-2260. ISSN 00942405. Dostupné z: doi:10.1118/1.4945022

[91] DAVIS, G.R a J.C ELLIOTT. X-ray microtomography scanner using time-delay integration for elimination of ring artefacts in the reconstructed image. *Nuclear Instruments and Methods in*

Physics Research Section A: Accelerators, Spectrometers, Detectors and Associated Equipment. 1997, **394**(1-2), 157-162. ISSN 01689002. Dostupné z: doi:10.1016/S0168-9002(97)00566-4

[92]   DORAN, Simon, Koen KOERKAMP, Mamdouh BERO, Paul JENNESON, Edward MORTON a Walter GILBOY. A CCD-based optical CT scanner for high-resolution 3D imaging of radiation dose distributions: equipment specifications, optical simulations and preliminary results. *Physics in Medicine and Biology*. 2001, **46**(12), 3191-3213. ISSN 0031-9155. Dostupné z: doi:10.1088/0031-9155/46/12/309

[93]   JENNESON, P.M., W.B. GILBOY, E.J. MORTON a P.J. GREGORY. An X-ray micro-tomography system optimised for the low-dose study of living organisms. *Applied Radiation and Isotopes*. 2003, **58**(2), 177-181. ISSN 09698043. Dostupné z: doi:10.1016/S0969-8043(02)00310-X

[94]   RAVEN, Carsten. Numerical removal of ring artifacts in microtomography. *Review of Scientific Instruments*. 1998, **69**(8), 2978-2980. ISSN 0034-6748. Dostupné z: doi:10.1063/1.1149043

[95]   MÜNCH, Beat, Pavel TRTIK, Federica MARONE a Marco STAMPANONI. Stripe and ring artifact removal with combined wavelet—Fourier filtering. *Optics Express*. 2009, **17**(10), 8567-. ISSN 1094-4087. Dostupné z: doi:10.1364/OE.17.008567

[96]   SADI, Fazle, Soo LEE a Md. HASAN. Removal of ring artifacts in computed tomographic imaging using iterative center weighted median filter. *Computers in Biology and Medicine*. 2010, **40**(1), 109-118. ISSN 00104825. Dostupné z: doi:10.1016/j.compbiomed.2009.11.007

[97]   ELDIB, Mohamed, Mohamed HEGAZY, Yang MUN, Myung CHO, Min CHO a Soo LEE. A Ring Artifact Correction Method: Validation by Micro-CT Imaging with Flat-Panel Detectors and a 2D Photon-Counting Detector. *Sensors*. 2017, **17**(2). ISSN 1424-8220. Dostupné z: doi:10.3390/s17020269

[98]   ANAS, Emran, Soo LEE a Md. KAMRUL HASAN. Classification of ring artifacts for their effective removal using type adaptive correction schemes. *Computers in Biology and Medicine*. 2011, **41**(6), 390-401. ISSN 00104825. Dostupné z: doi:10.1016/j.compbiomed.2011.03.018

[99]   ANAS, Emran, Jae KIM, Soo LEE a Md HASAN. High-quality 3D correction of ring and radiant artifacts in flat panel detector-based cone beam volume CT imaging. *Physics in Medicine and Biology*. 2011, **56**(19), 6495-6519. ISSN 0031-9155. Dostupné z: doi:10.1088/0031-9155/56/19/020

[100]   RASHID, Sabrina, Soo LEE a Md HASAN. An improved method for the removal of ring artifacts in high resolution CT imaging. *EURASIP Journal on Advances in Signal Processing*. 2012, **2012**(1). ISSN 1687-6180. Dostupné z: doi:10.1186/1687-6180-2012-93

[101]   ANAS, Emran, Soo LEE a Md. HASAN. Removal of ring artifacts in CT imaging through detection and correction of stripes in the sinogram. *Physics in Medicine and Biology*. 2010, **55**(22), 6911-6930. ISSN 0031-9155. Dostupné z: doi:10.1088/0031-9155/55/22/020

[102]   ASHRAFUZZAMAN, A., Soo LEE a Md. HASAN. A Self-Adaptive Approach for the Detection and Correction of Stripes in the Sinogram: Suppression of Ring Artifacts in CT Imaging. *EURASIP Journal*

on Advances in Signal Processing. 2011, **2011**(1). ISSN 1687-6180. Dostupné z: doi:10.1155/2011/183547

[103]   VO, Nghia, Robert ATWOOD a Michael DRAKOPOULOS. Superior techniques for eliminating ring artifacts in X-ray micro-tomography. *Optics Express*. 2018, **26**(22), 28396-28412. ISSN 1094-4087. Dostupné z: doi:10.1364/OE.26.028396

[104]   KIM, Younguk, Jongduk BAEK a Dosik HWANG. Ring artifact correction using detector line-ratios in computed tomography. *Optics Express*. 2014, **22**(11), 13380-13392. ISSN 1094-4087. Dostupné z: doi:10.1364/OE.22.013380

[105]   ŠALPLACHTA, Jakub, Tomáš ZIKMUND, Marek ZEMEK, Adam BŘÍNEK, Yoshihiro TAKEDA, Kazuhiko OMOTE a Jozef KAISER. Complete Ring Artifacts Reduction Procedure for Lab-Based X-ray Nano CT Systems. *Sensors*. 2021, **21**(1), 1-20. ISSN 1424-8220. Dostupné z: doi:10.3390/s21010238

[106]   WEI, Zhouping, Sheldon WIEBE a Dean CHAPMAN. Ring artifacts removal from synchrotron CT image slices. *Journal of Instrumentation*. 2013, **8**(06), 06006-06006. ISSN 1748-0221. Dostupné z: doi:10.1088/1748-0221/8/06/C06006

[107]   SIJBERS, Jan a Andrei POSTNOV. Reduction of ring artefacts in high resolution micro-CT reconstructions. *Physics in Medicine and Biology*. 2004, **49**(14), 247-253. ISSN 0031-9155. Dostupné z: doi:10.1088/0031-9155/49/14/N06

[108]   KYRIAKOU, Yiannis, Daniel PRELL a Willi KALENDER. Ring artifact correction for high-resolution micro CT. *Physics in Medicine and Biology*. 2009, **54**(17), 385-391. ISSN 0031-9155. Dostupné z: doi:10.1088/0031-9155/54/17/N02

[109]   LIANG, Xiaokun, Zhicheng ZHANG, Tianye NIU, Shaode YU, Shibin WU, Zhicheng LI, Huailing ZHANG a Yaoqin XIE. Iterative image-domain ring artifact removal in cone-beam CT. *Physics in Medicine & Biology*. 2017, **62**(13), 5276-5292. ISSN 0031-9155. Dostupné z: doi:10.1088/1361-6560/aa7017

[110]   YAN, Luxin, Tao WU, Sheng ZHONG a Qiude ZHANG. A variation-based ring artifact correction method with sparse constraint for flat-detector CT. *Physics in Medicine and Biology*. 2016, **61**(3), 1278-1292. ISSN 0031-9155. Dostupné z: doi:10.1088/0031-9155/61/3/1278

[111]   JI, Dong-Jiang, Gang-Rong QU, Chun-Hong HU, Bao-Dong LIU, Jian-Bo JIAN a Xiao-Kun GUO. Anisotropic total variation minimization approach in in-line phase-contrast tomography and its application to correction of ring artifacts. *Chinese Physics B*. 2017, **26**(6), 1-8. ISSN 1674-1056. Dostupné z: doi:10.1088/1674-1056/26/6/060701

[112]   PALEO, Pierre a Alessandro MIRONE. Ring artifacts correction in compressed sensing tomographic reconstruction. *Journal of Synchrotron Radiation*. 2015, **22**(5), 1268-1278. ISSN 1600-5775. Dostupné z: doi:10.1107/S1600577515010176

[113]   YANG, Haiquan, Meihua LI, Kazuhito KOIZUMI a Hiroyuki KUDO. Exact cone beam reconstruction for a saddle trajectory. *Physics in Medicine and Biology*. 2006, **51**(5), 1157-1172. ISSN 0031-9155. Dostupné z: doi:10.1088/0031-9155/51/5/008

[114]   PACK, Jed D, Frédéric NOO a H KUDO. Investigation of saddle trajectories for cardiac CT imaging in cone-beam geometry. *Physics in Medicine and Biology*. 2004, **49**(11), 2317-2336. ISSN 0031-9155. Dostupné z: doi:10.1088/0031-9155/49/11/014

[115]   KATSEVICH, Alexander. An improved exact filtered backprojection algorithm for spiral computed tomography. *Advances in Applied Mathematics*. 2004, **32**(4), 681-697. ISSN 01968858. Dostupné z: doi:10.1016/S0196-8858(03)00099-X

[116]   BONTUS, Claas, Thomas KÖHLER a Roland PROKSA. A quasiexact reconstruction algorithm for helical CT using a 3-Pi acquisition. *Medical Physics*. 2003, **30**(9), 2493-2502. ISSN 00942405. Dostupné z: doi:10.1118/1.1601913

[117]   GRASS, M, Th KÖHLER a R PROKSA. 3D cone-beam CT reconstruction for circular trajectories. *Physics in Medicine and Biology*. 2000, **45**(2), 329-347. ISSN 0031-9155. Dostupné z: doi:10.1088/0031-9155/45/2/306

[118]   CHEN, Zikuan, Vince D. CALHOUN a Shengjiang CHANG. Compensating the intensity fall-off effect in cone-beam tomography by an empirical weight formula. *Applied Optics*. 2008, **47**(32). ISSN 0003-6935. Dostupné z: doi:10.1364/AO.47.006033

[119]   SHI, Daxin. Successful suppression of cone beam artifacts using iterative reconstruction algorithm. In: *2014 IEEE Nuclear Science Symposium and Medical Imaging Conference (NSS/MIC)*. IEEE, 2014, s. 1-3. ISBN 978-1-4799-6097-2. Dostupné z: doi:10.1109/NSSMIC.2014.7430966

[120]   SIDKY, Emil Y a Xiaochuan PAN. Image reconstruction in circular cone-beam computed tomography by constrained, total-variation minimization. *Physics in Medicine and Biology*. 2008, **53**(17), 4777-4807. ISSN 0031-9155. Dostupné z: doi:10.1088/0031-9155/53/17/021

[121]   CHOI, Shinkook, Jinsung KIM a Jongduk BAEK. A Hybrid Approach to Reduce Cone-Beam Artifacts for a Circular Orbit Cone-Beam CT System. *IEEE Access*. 2018, **6**, 54595-54606. ISSN 2169-3536. Dostupné z: doi:10.1109/ACCESS.2018.2871804

[122]   LIU, Tong. Comparison between four methods for central ray determination with wire phantoms in micro-computed-tomography systems. *Optical Engineering*. 2006, **45**(6). ISSN 0091-3286. Dostupné z: doi:10.1117/1.2214717

[123]   BLEICHRODT, Folkert a K. Joost BATENBURG. Automatic Optimization of Alignment Parameters for Tomography Datasets. In: *Image Analysis*. Berlin, Heidelberg: Springer Berlin Heidelberg, 2013, s. 489-500. Lecture Notes in Computer Science. ISBN 978-3-642-38885-9. Dostupné z: doi:10.1007/978-3-642-38886-6_46

[124]   AZEVEDO, S.G., D.J. SCHNEBERK, J.P. FITCH a H.E. MARTZ. Calculation of the rotational centers in computed tomography sinograms. *IEEE Transactions on Nuclear Science*. 1990, **37**(4), 1525-1540. ISSN 0018-9499. Dostupné z: doi:10.1109/23.55866

[125]   JUN, Kyungtaek a Seokhwan YOON. Alignment Solution for CT Image Reconstruction using Fixed Point and Virtual Rotation Axis. *Scientific Reports*. 2017, **7**(1). ISSN 2045-2322. Dostupné z: doi:10.1038/srep41218

[126] PAN, Yongsheng, Francesco DE CARLO, Xianghui XIAO, Norbert J. PELC, Robert M. NISHIKAWA a Bruce R. WHITING. Automatic detection of rotational centers using GPU from projection data for micro-tomography in synchrotron radiation. In: *Medical Imaging 2012: Physics of Medical Imaging*. 831328. San Diego: SPIE, 2012, s. 831328-. Dostupné z: doi:10.1117/12.911561

[127] YANG, Yimeng, Feifei YANG, Ferdinand F. HINGERL et al. Registration of the rotation axis in X-ray tomography. *Journal of Synchrotron Radiation*. 2015, **22**(2), 452-457. ISSN 1600-5775. Dostupné z: doi:10.1107/S160057751402726X

[128] MIN, Yang, Gao HAIDONG, Li XINGDONG, Meng FANYONG a Wei DONGBO. *A new method to determine the center of rotation shift in 2D-CT scanning system using image cross correlation*. 2012, **46**, 48-54. ISSN 09638695. Dostupné z: doi:10.1016/j.ndteint.2011.09.001

[129] VO, Nghia T., Michael DRAKOPOULOS, Robert C. ATWOOD a Christina REINHARD. Reliable method for calculating the center of rotation in parallel-beam tomography. *Optics Express*. 2014, **22**(16). ISSN 1094-4087. Dostupné z: doi:10.1364/OE.22.019078

[130] LIN, Qiang, Min YANG, Fanyong MENG, Liang SUN a BIN TANG. Calibration method of center of rotation under the displaced detector scanning for industrial CT. *Nuclear Instruments and Methods in Physics Research Section A: Accelerators, Spectrometers, Detectors and Associated Equipment*. 2019, **922**, 326-335. ISSN 01689002. Dostupné z: doi:10.1016/j.nima.2018.11.131

[131] CHENG, Chang-Chieh, Yu-Tai CHING, Pai-Hung KO a Yeukuang HWU. Correction of center of rotation and projection angle in synchrotron X-ray computed tomography. *Scientific Reports*. 2018, **8**(1). ISSN 2045-2322. Dostupné z: doi:10.1038/s41598-018-28149-8

[132] BRUNETTI, Antonio, Ulrich BONSE a Francesco DE CARLO. A robust procedure for determination of center of rotation in tomography. In: *Developments in X-Ray Tomography IV: Optical Science and Technology, the SPIE 49th Annual Meeting,*. 5535. Denver: SPIE, 2004, s. 652-. Dostupné z: doi:10.1117/12.560440

[133] DONATH, Tilman, Felix BECKMANN a Andreas SCHREYER. Automated determination of the center of rotation in tomography data. *Journal of the Optical Society of America A*. 2006, **23**(5). ISSN 1084-7529. Dostupné z: doi:10.1364/JOSAA.23.001048

[134] HOGAN, John P., Robert A. GONSALVES a Allen S. KRIEGER. Micro computed tomography: removal of translational stage backlash. *IEEE Transactions on Nuclear Science*. 1993, **40**(4), 1238-1241. ISSN 0018-9499. Dostupné z: doi:10.1109/TNS.1993.8526784

[135] BRANDT, Sami, Jukka HEIKKONEN a Peter ENGELHARDT. Automatic Alignment of Transmission Electron Microscope Tilt Series without Fiducial Markers. *Journal of Structural Biology*. 2001, **136**(3), 201-213. ISSN 10478477. Dostupné z: doi:10.1006/jsbi.2001.4443

[136] FITCHARD, E E, J S ALDRIDGE, P J RECKWERDT a T R MACKIE. Registration of synthetic tomographic projection data sets using cross-correlation. *Physics in Medicine and Biology*. 1998, **43**(6), 1645-1657. ISSN 0031-9155. Dostupné z: doi:10.1088/0031-9155/43/6/020

[137] CHENG, Chang-Chieh, Chia-Chi CHIEN, Hsiang-Hsin CHEN, Yeukuang HWU, Yu-Tai CHING a Oscar Deniz SUAREZ. Image Alignment for Tomography Reconstruction from Synchrotron X-Ray Microscopic Images. *PLoS ONE*. 2014, **9**(1). ISSN 1932-6203. Dostupné z: doi:10.1371/journal.pone.0084675

[138] VISKOE, A. Computed tomography postacquisition data correction for system alignment errors. *IEEE Transactions on Instrumentation and Measurement*. IEEE, 1999, **48**(5), 972-977. ISSN 00189456. Dostupné z: doi:10.1109/19.799656

[139] SASOV, Alexander, Stuart R. STOCK, Xuan LIU a Phil L. SALMON. Compensation of mechanical inaccuracies in micro-CT and nano-CT. *Developments in X-ray Tomography VI.* SPIE, 2008, **2008**(7078), 401-409. Dostupné z: doi:10.1117/12.793212

[140] GÜRSOY, Doğa, Young P. HONG, Kuan HE et al. Rapid alignment of nanotomography data using joint iterative reconstruction and reprojection. *Scientific Reports*. 2017, **7**(1). ISSN 2045-2322. Dostupné z: doi:10.1038/s41598-017-12141-9

[141] KINGSTON, A., A. SAKELLARIOU, T. VARSLOT, G. MYERS a A. SHEPPARD. Reliable automatic alignment of tomographic projection data by passive auto-focus. *Medical Physics*. 2011, **38**(9), 4934-4945. ISSN 00942405. Dostupné z: doi:10.1118/1.3609096

[142] ADAMS, Judith. Quantitative computed tomography. *European Journal of Radiology*. 2009, **71**(3), 415-424. ISSN 0720048X. Dostupné z: doi:10.1016/j.ejrad.2009.04.074

[143] MAIRE, E. a P. J. WITHERS. Quantitative X-ray tomography. *International Materials Reviews*. 2013, **59**(1), 1-43. ISSN 0950-6608. Dostupné z: doi:10.1179/1743280413Y.0000000023

[144] ALVAREZ, R E a A MACOVSKI. Energy-selective reconstructions in X-ray computerised tomography. *Physics in Medicine and Biology*. 1976, **21**(5), 733-744. ISSN 00319155. Dostupné z: doi:10.1088/0031-9155/21/5/002

[145] GARNETT, Richard. A comprehensive review of dual-energy and multi-spectral computed tomography. *Clinical Imaging*. 2020, **67**(), 160-169. ISSN 08997071. Dostupné z: doi:10.1016/j.clinimag.2020.07.030

[146] SO, Aaron a Savvas NICOLAOU. Spectral Computed Tomography: Fundamental Principles and Recent Developments. *Korean Journal of Radiology*. 2021, **22**(1). ISSN 1229-6929. Dostupné z: doi:10.3348/kjr.2020.0144

[147] BHAYANA, Rajesh, Anushri PARAKH a Avinash KAMBADAKONE. Material decomposition with dual- and multi-energy computed tomography. *MRS Communications*. 2020, **10**(4), 558-565. ISSN 2159-6859. Dostupné z: doi:10.1557/mrc.2020.86

[148] RIT, Simon, Cyril MORY a Peter B. NOËL. Image Formation in Spectral Computed Tomography. In: *Spectral, Photon Counting Computed Tomography*. 1st Edition. Boca Raton: 1st Edition, 2020, s. 18. ISBN 9780367490119.

[149] CAI, Caifang, All MOHAMMAD-DJAFARI, Samuel LEGOUPIL a Thomas RODET. Bayesian data fusion and inversion in X-ray multi-energy computed tomography. In: *2011 18th IEEE International Conference on Image Processing*. Brussels, Belgium: IEEE, 2011, s. 1377-1380. ISBN 978-1-4577-1303-3. Dostupné z: doi:10.1109/ICIP.2011.6115694

[150] PESSIS, Eric, Jean-Michel SVERZUT, Raphaël CAMPAGNA, Henri GUERINI, Antoine FEYDY a Jean-Luc DRAPÉ. Reduction of Metal Artifact with Dual-Energy CT: Virtual Monospectral Imaging with Fast Kilovoltage Switching and Metal Artifact Reduction Software. *Seminars in Musculoskeletal Radiology*. 2015, **19**(05), 446-455. ISSN 1089-7860. Dostupné z: doi:10.1055/s-0035-1569256

[151] D'ANGELO, Tommaso, Giuseppe CICERO, Silvio MAZZIOTTI et al. Dual energy computed tomography virtual monoenergetic imaging: technique and clinical applications. *The British Journal of Radiology*. 2019, **92**(1098). ISSN 0007-1285. Dostupné z: doi:10.1259/bjr.20180546

[152] JOHNSON, Thorsten R. C. Dual-Energy CT: General Principles. *American Journal of Roentgenology*. 2012, **199**(5), 3-8. ISSN 0361-803X. Dostupné z: doi:10.2214/AJR.12.9116

[153] MCCOLLOUGH, Cynthia H., Shuai LENG, Lifeng YU a Joel G. FLETCHER. Dual- and Multi-Energy CT: Principles, Technical Approaches, and Clinical Applications. *Radiology*. 2015, **276**(3), 637-653. ISSN 0033-8419. Dostupné z: doi:10.1148/radiol.2015142631

[154] LONG, Yong a Jeffrey A. FESSLER. Multi-Material Decomposition Using Statistical Image Reconstruction for Spectral CT. *IEEE Transactions on Medical Imaging*. 2014, **33**(8), 1614-1626. ISSN 0278-0062. Dostupné z: doi:10.1109/TMI.2014.2320284

[155] JOONKI NOH, J.A. FESSLER a P.E. KINAHAN. Statistical Sinogram Restoration in Dual-Energy CT for PET Attenuation Correction. *IEEE Transactions on Medical Imaging*. 2009, **28**(11), 1688-1702. ISSN 0278-0062. Dostupné z: doi:10.1109/TMI.2009.2018283

[156] XUE, Yi, Ruoshui RUAN, Xiuhua HU, Yu KUANG, Jing WANG, Yong LONG a Tianye NIU. Statistical image-domain multimaterial decomposition for dual-energy CT. *Medical Physics*. 2017, **44**(3), 886-901. ISSN 00942405. Dostupné z: doi:10.1002/mp.12096

[157] LI, Zhipeng, Saiprasad RAVISHANKAR, Yong LONG a Jeffrey A. FESSLER. DECT-MULTRA: Dual-Energy CT Image Decomposition With Learned Mixed Material Models and Efficient Clustering. *IEEE Transactions on Medical Imaging*. 2020, **39**(4), 1223-1234. ISSN 0278-0062. Dostupné z: doi:10.1109/TMI.2019.2946177

[158] NIU, Tianye, Xue DONG, Michael PETRONGOLO a Lei ZHU. Iterative image-domain decomposition for dual-energy CT. *Medical Physics*. 2014, **41**(4). ISSN 00942405. Dostupné z: doi:10.1118/1.4866386

[159] *Rigaku Corporation: Compact two-dimensional CC detector* [online]. [cit. 2019-08-21]. Dostupné z: https://www.rigaku.com/en/products/detectors/micron,

[160] *Rigaku Corporation: Compact two-dimensional sCMOS detector* [online]. [cit. 2019-08-21]. Dostupné z: https://www.rigaku.com/en/products/detectors/micron-cmos

[161] *Phoenix v|tome|x L – versatile and flexible CT system*. Germany, 2019. Dostupné také z: https://www.industrial.ai/sites/g/files/cozyhq596/files/acquiadam_assets/geit_31205_flyer_vto mex_l_en_1213.pdf

[162] KINGSTON, Andrew M., Glenn R. MYERS, Shane J. LATHAM, Benoit RECUR, Heyang LI a Adrian P. SHEPPARD. Space-Filling X-Ray Source Trajectories for Efficient Scanning in Large-Angle Cone-Beam Computed Tomography. *IEEE Transactions on Computational Imaging*. 2018, **4**(3), 447-458. ISSN 2333-9403. Dostupné z: doi:10.1109/TCI.2018.2841202

[163] RUEDEN, Curtis T., Johannes SCHINDELIN, Mark C. HINER, Barry E. DEZONIA, Alison E. WALTER, Ellen T. ARENA a Kevin W. ELICEIRI. ImageJ2: ImageJ for the next generation of scientific image data. *BMC Bioinformatics*. 2017, **18**(1). ISSN 1471-2105. Dostupné z: doi:10.1186/s12859-017-1934-z

[164] VAN AARLE, Wim, Willem PALENSTIJN, Jeroen CANT et al. Fast and flexible X-ray tomography using the ASTRA toolbox. *Optics Express*. 2016, **24**(22), 25129-25147. ISSN 1094-4087. Dostupné z: doi:10.1364/OE.24.025129

[165] ŠALPLACHTA, Jakub, Tomáš ZIKMUND, Martin HORVÁTH, Yoshihiro TAKEDA, Kazuhiko OMOTE, Ladislav PÍNA a Jozef KAISER. CCD and scientific-CMOS detectors for submicron laboratory based X-ray Computed tomography. In: *9th Conference on Industrial Computed Tomography (iCT) 2019, 13-15 Feb, Padova, Italy (iCT 2019)*. The e-Journal of Nondestructive Testing, 2019. ISSN 1435-4934.

[166] *IEC 62220-1:2003(E): Medical electrical equipment – Characteristics of digital X-ray imaging devices – Part 1: Determination of the detective quantum efficiency*. Switzerland: International Electrotechnical Commission, 2003.

[167] *ASTM E1695-95: Standard Test Method for Measurement of Computed Tomography (CT) System Performance*. West Conshohocken, PA,: ASTM International, 2013.

[168] KRAEMER, Alexandra, Ekaterina KOVACHEVA a Gisela LANZA. *Projection based evaluation of CT image quality in dimensional metrology*. In: . Digital Industrial Radiology and Computed Tomography (DIR 2015). Belgium, Ghent, 2015.

[169] WANG, Z., A.C. BOVIK, H.R. SHEIKH a E.P. SIMONCELLI. Image Quality Assessment: From Error Visibility to Structural Similarity. *IEEE Transactions on Image Processing*. 2004, **13**(4), 600-612. ISSN 1057-7149. Dostupné z: doi:10.1109/TIP.2003.819861

[170] SALPLACHTA, Jakub, Tomas ZIKMUND a Jozef KAISER. DENOISING APPROACH FOR HIGH-RESOLUTION COMPUTED TOMOGRAPHY DATA. In: *IADIS International Conference Computer Graphics, Visualization, Computer Vision and Image Processing 2018 (part of MCCSIS 2018)*. Spain: IADIS, 2018, s. 439-441. ISBN 978-989-8533-79-1.

[171] IMMERKæR, John. Fast Noise Variance Estimation. *Computer Vision and Image Understanding*. 1996, **64**(2), 300-302. ISSN 10773142. Dostupné z: doi:10.1006/cviu.1996.0060

[172] SHEN-CHUAN TAI, a SHIH-MING YANG. A fast method for image noise estimation using Laplacian operator and adaptive edge detection. In: *2008 3rd International Symposium on Communications, Control and Signal Processing*. IEEE, 2008, s. 1077-1081. ISBN 978-1-4244-1687-5. Dostupné z: doi:10.1109/ISCCSP.2008.4537384

[173] WANG, Z., A.C. BOVIK, H.R. SHEIKH a E.P. SIMONCELLI. Image Quality Assessment: From Error Visibility to Structural Similarity. *IEEE Transactions on Image Processing*. 2004, **13**(4), 600-612. ISSN 1057-7149. Dostupné z: doi:10.1109/TIP.2003.819861

[174] JIMA RT RC-02B Resolution test. In: *X-RAY WorX* [online]. [cit. 2019-08-29]. Dostupné z: https://www.x-ray-worx.com/x-ray-worx/index.php/en/microfocus-x-ray-tubes-overview/jima-resolution-test/jima-rt-rc-02b-resolution-test,

[175] YU, Jonathan, Francisco IMAI, Nitin SAMPAT, David COLLINS, Alireza YASAN, Feng XIAO, Sanghoon BAE a Shri RAMASWAMI. Hot pixel reduction in CMOS image sensor pixels. *Proc. SPIE 7537: Digital Photography VI*. **2010**(753704). Dostupné z: doi:10.1117/12.839118

[176] XU, Li, Qiong YAN, Yang XIA a Jiaya JIA. Structure extraction from texture via relative total variation. *ACM Transactions on Graphics*. 2012, **31**(6). ISSN 07300301. Dostupné z: doi:10.1145/2366145.2366158

[177] SAVITZKY, Abraham. a M. GOLAY. Smoothing and Differentiation of Data by Simplified Least Squares Procedures. *Analytical Chemistry*. 1964, **36**(8), 1627-1639. ISSN 0003-2700. Dostupné z: doi:10.1021/ac60214a047

[178] BOIN, Mirko a Astrid HAIBEL. Compensation of ring artefacts in synchrotron tomographic images. *Optics Express*. 2006, **14**(25), 12071-12075. ISSN 1094-4087. Dostupné z: doi:10.1364/OE.14.012071

[179] MÜNCH, Beat, Pavel TRTIK, Federica MARONE a Marco STAMPANONI. Stripe and ring artifact removal with combined wavelet—Fourier filtering. *Optics Express*. 2009, **17**(10), 8567-8591. ISSN 1094-4087. Dostupné z: doi:10.1364/OE.17.008567

[180] ZIKMUND, Tomáš, Jakub ŠALPLACHTA, Aneta ZATOČILOVÁ et al. Computed tomography based procedure for reproducible porosity measurement of additive manufactured samples. *NDT & E International*. 2019, **103**, 111-118. ISSN 09638695. Dostupné z: doi:10.1016/j.ndteint.2019.02.008

[181] REDDY, B.S. a B.N. CHATTERJI. An FFT-based technique for translation, rotation, and scale-invariant image registration. *IEEE Transactions on Image Processing*. 1996, **5**(8), 1266-1271. ISSN 10577149. Dostupné z: doi:10.1109/83.506761

List of symbols and shortcuts

1D	One-Dimensional
2D	Two-Dimensional
3D	Three-Dimensional
4D	Four-Dimensional
A	System matrix
ART	Algebraic Reconstruction Technique
b	Absorption
B	Bright-field image
BD	Bile Duct
BP	Back Projection
c	Speed of light ($2.998 \cdot 10^8$ ms^{-1})
C	Local contrast
CANDLE	Collaborative Approach For Enhanced Denoising Under Low-Light Excitation
CCD	Charged-Coupled Device
CERN	Conseil Européen pour la Recherche Nucléaire
CNR	Contrast-to-Noise Ratio
CoM	Centre-of-Mass
CoR	Centre-of-Rotation
CT	Computed Tomography
δ	Dirac delta function
D	Dark-field image
DECT	Dual-Energy-CT
DN	Digital Number
DUCT	DoUble resin Casting micro Computed Tomography
DTCT	Dual-Target CT

E	Energy
E_b	Binding energy
E_k	Kinetic energy
E_p	Photon energy
EMCCD	Electron Multiplying CCD
ERF	Edge Response Function
f	Frequency
f	Object function
f_s	Sampling frequency
F_1	1D Fourier Transform
F_1^{-1}	Inverse 1D Fourier Transform
FBP	Filtered Back Projection
FT	Fourier Transform
FFT	Fast Fourier Transform
FoV	Field-of-View
FPN	Fixed Pattern Noise
G	Gain
GPU	Graphical Processor Unit
h	Plank's constant ($6.626 \cdot 10^{-24}\ J \cdot s$)
HPD	Hybrid Pixel Detectors
HPCD	Hybrid Photon Counting Detector
HRA	High-level Ring Artifacts
I	X-ray intensity after sample's passing
I_0	Incident X-ray intensity
I_c	Flat-field corrected image
I_R	Acquired raw data
IR	Iterative reconstruction

JNB	Just Noticeable Blur
lp	Line pair
L	Path
LM	Light microscopy
LRA	Low-level Ring Artifacts
M	Geometric magnification
MOS	Metal Oxide Silicon
MSE	Mean Squared Error
MTF	Modulation Transfer Function
NAFSM	Noise Adaptive Fuzzy Switching Median Filter
NDE	Non-Destructive Evaluation
NLM	Non-Local-Means
NNPS	Normalized Noise Power Spectrum
Nq	Nyquist frequency
OPR	Opposite projection registration
OS	Ordered Subsets
p	Pixel size
p	Radon transform
PCA	Principle Component Analysis
PCD	Photon Counting Detector
PSF	Point Spread Function
PSMF	Progressive Switching Median Filter
PSI	Paul Scherrer Insitut
PSNR	Peak Signal-to-Noise Ration
PV	Portal Vein
QCT	Quantitative Computed Tomography
r	Distance from projection centre

RE	Reconstruction Evaluation
ROAD	Rank-Ordered Absolute Differences
RMSE	Root Mean Square Error
RTV	Relative Total Variations
SART	Simultaneous algebraic technique
sCMOS	Scientific-Complementary-Metal-Oxide-Semiconductor
SDD	Source-to-Detector Distance
SIRT	Simultaneous iterative reconstruction technique
SLM	Selective Laser Melting
SML	Sum of Modified Laplacians
SNR	Signal-to-Noise Ratio
SR	Spatial Resolution
SSD	Source-to-Sample Distance
SSE	Sinogram Symmetry Evaluation
SSIM	Structural Similarity Index
TFT	Thin Film Transistor
μ	Linear attenuation coefficient
μ_{CS}	Linear attenuation coefficient due to the Compton scattering
μ_{PE}	Linear attenuation coefficient due to the Photoelectric effect
μ_{PP}	Linear attenuation coefficient due to the pair production
μ_{RS}	Linear attenuation coefficient due to the Rayleigh scattering
θ	Acquisition angle
IωI	Impulse characteristics of used high pass filter
VAR	Variance
vx	Voxel size
XD	Sample detector distance – notation used in Rigaku software
Z	Atomic number

Author's publications and other outputs
Publications
First-author

ŠALPLACHTA, J.; ZIKMUND, T.; ZEMEK, M.; BŘÍNEK, A.; TAKEDA, Y.; OMOTE, K.; KAISER, J. Complete Ring Artifacts Reduction Procedure for Lab-Based X-ray Nano CT Systems. *SENSORS,* 2021, vol. 21, no. 1, p. 1-20. ISSN: 1424-8220.

Shared first-author

HANKEOVÁ, S.; ŠALPLACHTA, J.; VAN HUL, N.; KAVKOVÁ, M.; IQBAL, A.; ZIKMUND, T.; KAISER, J.; ANDERSSON, E. DUCT: Double Resin Casting followed by Micro-Computed Tomography for 3D Liver Analysis. *Journal of visualized experiments : JoVE,* 2021, vol. 175, no. e62941, p. 1-19. ISSN: 1940-087X.

HANKEOVÁ, S.; ŠALPLACHTA, J.; ZIKMUND, T.; KAVKOVÁ, M.; VAN HUL, N.; BŘÍNEK, A.; SMÉKALOVÁ, V.; LÁZŇOVSKÝ, J.; DAWIT, F.; JAROŠ, J.; BRYJA, V.; LENDAHL, U.; ELLIS, E.; NEMETH, A.; FISCHLER, B.; HANNESO, E.; KAISER, J.; ANDERSSON, E. DUCT reveals architectural mechanisms contributing to bile duct recovery in a mouse model for Alagille syndrome. *eLife,* 2021, no. 10, p. 1-29. ISSN: 2050-084X.

Co-author

CASTALDO, R.; AVOLIO, R.; COCCA, M.; ERRICO, M.; LAVORGNA, M**.; ŠALPLACHTA, J**.; SANTILLO, CH.; GENTILE, G. p Hierarchically porous hydrogels and aerogels based on reduced graphene oxide, montmorillonite and hyper-crosslinked resins for water and air remediation. *CHEMICAL ENGINEERING JOURNAL,* 2022, vol. 430, no. 4, p. 1-10. ISSN: 1385-8947.

MATULA, J.; POLÁKOVÁ, V.; **ŠALPLACHTA, J.;** TESAŘOVÁ, M.; ZIKMUND, T.; KAUCKÁ, M.; ADAMEYKO, I.; KAISER, J. Resolving complex cartilage structures in developmental biology via deep learning-based automatic segmentation of X-ray computed microtomography images. *Scientific Reports,* 2022, vol. 12, no. 1, p. 1-13. ISSN: 2045-2322.

KAVKOVÁ, M.; ZIKMUND, T.; KALA, A.; **ŠALPLACHTA, J.;** LISSETTE PROSKAUER PENA, S.; KAISER, J.; JEŽEK, K. Contrast enhanced X-ray computed tomography imaging of amyloid plaques in Alzheimer disease rat model on lab based micro CT system. *Scientific Reports,* 2021, vol. 11, no. 1, p. 1-10. ISSN: 2045-2322.

JAQUES, V.; DU PLESSIS, A.; ZEMEK, M.; **ŠALPLACHTA, J.;** ŠTUBIANOVÁ, Z.; ZIKMUND, T.; KAISER, J. Review of porosity uncertainty estimation methods in computed tomography dataset. *Measurement Science and Technology,* 2021, vol. 32, no. 8, p. 1-17. ISSN: 0957-0233.

OLIVER, C.; IBAÑEZ, R.; FLORES-MERINO, M.; VOJTOVÁ, L.; **ŠALPLACHTA, J.;** ČELKO, L.; KAISER, J.; MONTUFAR JIMENEZ, E. Lyophilized Polyvinylpyrrolidone Hydrogel for Culture of Human Oral Mucosa Stem Cells. *Materials,* 2021, vol. 14, no. 1, p. 1-14. ISSN: 1996-1944.

113

GAMBLE, J.; TOBYN, M.; ZHANG, S.; ZHU, A.; **ŠALPLACHTA, J.**; MATULA, J.; ZIKMUND, T.; KAISER, J.; OBERTA, P. Characterization of the Morphological Nature of Hollow Spray Dried Dispersion Particles Using X-ray Submicron-Computed Tomography. *AAPS PHARMSCITECH,* 2021, vol. 23, no. 1, p. 1-7. ISSN: 1530-9932.

KUNISHIMA, N.; TAKEDA, Y.; HIROSE, R.; KALASOVÁ, D.; **ŠALPLACHTA, J.**, OMOTE, K. Visualization of internal 3D structure of small live seed on germination by laboratory-based X-ray microscopy with phase contrast computed tomography. *PLANT METHODS,* 2020, vol. 16, no. 1, p. 1-10. ISSN: 1746-4811.

ZIKMUND, T.; **ŠALPLACHTA, J.**; ZATOČILOVÁ, A.; BŘÍNEK, A.; PANTĚLEJEV, L.; ŠTĚPÁNEK, R.; KOUTNÝ, D.; PALOUŠEK, D.; KAISER, J. Computed tomography based procedure for reproducible porosity measurement of additive manufactured samples. *NDT & E INTERNATIONAL,* 2019, vol. 103, no. 1, p. 111-118. ISSN: 1879-1174.

VOJTOVÁ, L.; ZIKMUND, T.; PAVLIŇÁKOVÁ, V.; **ŠALPLACHTA, J.**; KALASOVÁ, D.; PROSECKÁ, E.; BRTNÍKOVÁ, J.; ŽÍDEK, J.; PAVLIŇÁK, D.; KAISER, J. The 3D imaging of mesenchymal stem cells on porous scaffolds using high-contrasted x-ray computed nanotomography. *Journal of Microscopy,* 2019, vol. 273, no. 3, p. 169-177. ISSN: 1365-2818.

PROCHAZKA, D.; ZIKMUND, T.; POŘÍZKA, P.; BŘÍNEK, A.; KLUS, J.; **ŠALPLACHTA, J.**; NOVOTNÝ, J.; KAISER, J. Joint utilization of double-pulse laser-induced breakdown spectroscopy and X-ray computed tomography for volumetric information of geological samples. *Journal of Analalytical Atomic Spectrometry,* 2018, no. 9, p. 1-7. ISSN: 0267-9477.

Products

KALASOVÁ, D.; **ŠALPLACHTA, J.**; PAVLIŇÁKOVÁ, V.; ZIKMUND, T.; KAISER, J.: Sample's holder nanoCT – SEM. (functional sample)

ŠALPLACHTA, J.; TESAŘOVÁ, M.; ZEMEK, M.; KAISER, J.: Sample's holder with reference area. (functional sample)

Grants

March 2020	**CEITEC Specific research programme** – main solver
– February 2021	**Project name:** 3D visualization of Lithium-ion batteries internal structures by X-ray microscope Rigaku nano3DX.
May 2019	**TAČR programme ZETA** – member of participating team
– April 2021	**Project name:** Differentiation of soft tissues using dual-target tomography.
	Role in team: Software and algorithms development for CT data registration and tomographic reconstruction. Development and optimization of sample holder with reference area for data registration.

January 2018	**TAČR programme ZETA** – member of participating team
– December 2019	**Project name:** Advanced techniques for biological samples imaging using X-ray computed nanotomography.
	Role in team: Software and algorithms development for CT data analysis and post-processing.

March 2019	**CEITEC Specific research programme** – main solver
– February 2020	**Project name:** Data registration for Dual-Target X-ray nano Computed tomography

March 2018	**CEITEC Specific research programme** – main solver
– February 2019	**Project name:** Quantitative nano computed tomography

Conferences

5th International Conference on Tomography of Materials and Structures (ICTMS 2020)

27.6. – 1. 7. 2022, Grenoble, France

Oral presentation: Beyond the limits of lab-based submicron CT for metrology

9th Conference on Industrial Computed Tomography (ICT 2019)

13. – 15. 2. 2019, Padova, Italy

Poster: CCD and scientific-CMOS detectors for submicron laboratory- based X-ray Computed Tomography

12th International Conference on Computer Graphics, Visualization, Computer Vision and Image Processing (CGVCVIP 2018)

18 – 20 July 2018, Madrid, Spain

Poster: Denoising approach for high-resolution computed tomography data

Appendix

Full texts of first-author [105] and shared-first author publications [184; 188], and extended abstract published at proceedings of ICT 2019 conference are listed here.

Complete Ring Artifacts Reduction Procedure for Lab-Based X-ray Nano CT Systems

Jakub Šalplachta [1] , **Tomáš Zikmund** [1] , **Marek Zemek** [1] , **Adam Břínek** [1] , **Yoshihiro Takeda** [2] , **Kazuhiko Omote** [2] and **Jozef Kaiser** [1,*]

1 CEITEC—Central European Institute of Technology, Brno University of Technology, Purkyňova 656/123, 612 00 Brno, Czech Republic; jakub.salplachta@ceitec.vutbr.cz (J.Š.); tomas.zikmund@ceitec.vutbr.cz (T.Z.); marek.zemek@ceitec.vutbr.cz (M.Z.); adam.brinek@ceitec.vutbr.cz (A.B.)

2 Rigaku Corporation, 3-9-12, Matsubara-cho, Akishima-shi, Tokyo 196-8666, Japan; y-takeda@rigaku.co.jp (Y.T.); omote@rigaku.co.jp (K.O.)

* Correspondence: jozef.kaiser@ceitec.vutbr.cz

Abstract: In this article, we introduce a new ring artifacts reduction procedure that combines several ideas from existing methods into one complex and robust approach with a goal to overcome their individual weaknesses and limitations. The procedure differentiates two types of ring artifacts according to their cause and character in computed tomography (CT) data. Each type is then addressed separately in the sinogram domain. The novel iterative schemes based on relative total variations (RTV) were integrated to detect the artifacts. The correction process uses the image inpainting, and the intensity deviations smoothing method. The procedure was implemented in scope of lab-based X-ray nano CT with detection systems based on charge-coupled device (CCD) and scientific complementary metal-oxide-semiconductor (sCMOS) technologies. The procedure was then further tested and optimized on the simulated data and the real CT data of selected samples with different compositions. The performance of the procedure was quantitatively evaluated in terms of the artifacts' detection accuracy, the comparison with existing methods, and the ability to preserve spatial resolution. The results show a high efficiency of ring removal and the preservation of the original sample's structure.

Keywords: ring artifacts reduction; CCD detector; sCMOS detector; high-resolution X-ray computed tomography; relative total variation

1. Introduction

In the field of high-resolution X-ray computed tomography (CT) with a micron and submicron spatial resolution, reconstructed CT data are often affected by severe ring artifacts. They appear as concentric ring-like features superimposed on the imaged scene and are centered on the object's center of rotation creating either full rings (full scan over 360°) or half rings (half scan over 180°) [1]. Ring artifacts are mainly caused by imperfect detector pixels, where a perfect pixel's response should be linearly proportional to the amount of photons incident on the detector. There are many different underlying causes for individual pixels to have imperfect responses. These include defects in the scintillator, the detector itself, and the readout electronics [2]. Moreover, the detector responses may vary due to numerous time-dependent drifts, such as thermal drifts, and also due to changes in the X-ray spectrum [2]. No matter the cause, ring artifacts degrade the resulting image quality. Therefore, it is desirable to remove or at least significantly reduce the presence of ring artifacts in CT data.

Ring artifacts reduction methods can be divided into three approaches. The first is based on a flat-field correction of a detector [3]. The proper flat-field correction should ideally remove all the detector sensitivity variations [4]. However, ring artifacts may persist after this correction due to the detector pixels intensity dependencies and non-linear

response functions, or due to time-dependent non-uniformities of the incident beam [5]. To overcome these issues, advanced flat-field correction approaches were proposed in several recent works [2,4,6,7]. However, such sophisticated flat-field methods are not easily applicable in practice, because they require specific CT acquisition scenarios, and precise knowledge of used detection system is needed.

Second approach is the hardware-based ring artifacts reduction method. This method is based on moving the detector system in defined horizontal steps during the CT acquisition so that the object is projected on different regions of the detector during a CT scan [8]. Through this, the effect of non-uniform detector responses is suppressed. Although the practical functionality of this method was reported in [9] and [10], this procedure's disadvantage is reducing the spatial resolution of the CT data if the detector shifts are not accurately known [2] or the movement precision is worse than the used detector pixel size. In general, this method is hardly applicable in nano CT systems due to such demanding requirements on the movement precision.

The third approach for the ring artifacts reduction are the image-based processing methods. These methods can be further divided, based on the domain of processed data, to sinogram-based (sinogram pre-processing) and tomogram-based (CT data post-processing) methods [11]. Sinogram-based methods work directly with the sinogram data, where the ring artifacts appear as straight lines in a vertical direction and are therefore easier to detect and to process. Some of these methods assume the presence of a specific high-frequency component that is directly related to the ring artifacts. Therefore, they aim to filter out the artifacts using low pass filters [12–15]. Most of these, however, fail to remove the strong artifacts related to dead detector elements or damaged areas on the scintillator, in which case they create an extra band around the original ring [10]. To overcome this, other methods first detect the ring artifacts elements and then correct them using various approaches: image inpainting [1,16–18] moving average and weighted moving average filters [19–21], sensitivity equalization [22]. However, even these methods have their limitations. Most of these methods are only suitable for suppressing a certain type of stripe. Moreover, they are generally difficult to use in practice due to many parameters needing to be adjusted when a wrong selection of parameters significantly affects the resulting quality. However, the work of Anas [16] can be pointed out because it introduced a novel idea for classifying rings based on their statistical properties and for addressing each type separately.

On the contrary, the tomogram post-processing methods work with CT data after the tomographic reconstruction. These methods often use a conversion of the data from Cartesian to the polar coordinate system. After this conversion, the ring artifacts appear as stripes that can be further processed using similar assumptions and strategies as for sinogram-based methods [23–27]. One method from these can be pointed out, Liang [26] proposed a novel ring artifacts reduction approach integrating benefits of an efficient iterative framework together with relative total variations (RTV) algorithm for the texture extraction. However, this method uses a simple mean values analysis to detect and correct the artifacts, which is insufficient in the case of dead detector elements or damaged areas on the scintillator. Moreover, tomogram-based methods are, in general, strongly dependent on the quality of the used tomographic reconstruction because some extra artifacts might be created [20]. Therefore, a novel class of methods lying between sinogram-based and tomogram-based approaches has been recently developed. The ring artifacts reduction is addressed directly during the reconstruction process using specific forms of regularizations (e.g., [11,28,29]). Such regularizations can, however, be highly computationally demanding, which limits the practical applicability of those methods.

In this article, we present a new ring artifacts reduction procedure that combines several selected ideas from image-based processing methods into one complex sinogram-based method with a goal to overcome all previously mentioned limitations. The ring artifacts are classified into two types based on their cause and actual appearance in the CT data. We prefer to separate the detection and correction schemes for each type of artifact

for their effective removal. We propose a two-step iterative correction scheme that deals with all the artifact types in the sinogram domain. Consequently, a significant influence of tomographic reconstruction on the efficiency of artifacts reduction is avoided. The reduction strategy was optimized for each artifact type separately to preserve the spatial resolution and sample's structural information, which are the most important factors in the field of nano-tomography. Practical functionality of the prosed method was verified on both synthetic data and real CT data. It shows a high efficiency of ring artifacts removal, and a robustness to character of input data and used detection system in context of other tested ring artifacts correction techniques.

2. Materials and Methods

In this article, a two-step ring artifacts reduction scheme is proposed. This scheme was developed for the artifacts' reduction in the sinogram domain and is based on a categorization of ring artifacts into two types. The ring artifacts are categorized based on the observation of responses from different kinds of deficiencies in sinograms and on their specific hardware causes (see Figure 1). In the proposed reduction scheme, each of these classes is then addressed separately using dedicated detection and reduction procedures. In the first step, the most prominent ring artifacts (high-level artifacts) are corrected, and subsequently weak artifacts (low-level artifacts) are corrected in the second step.
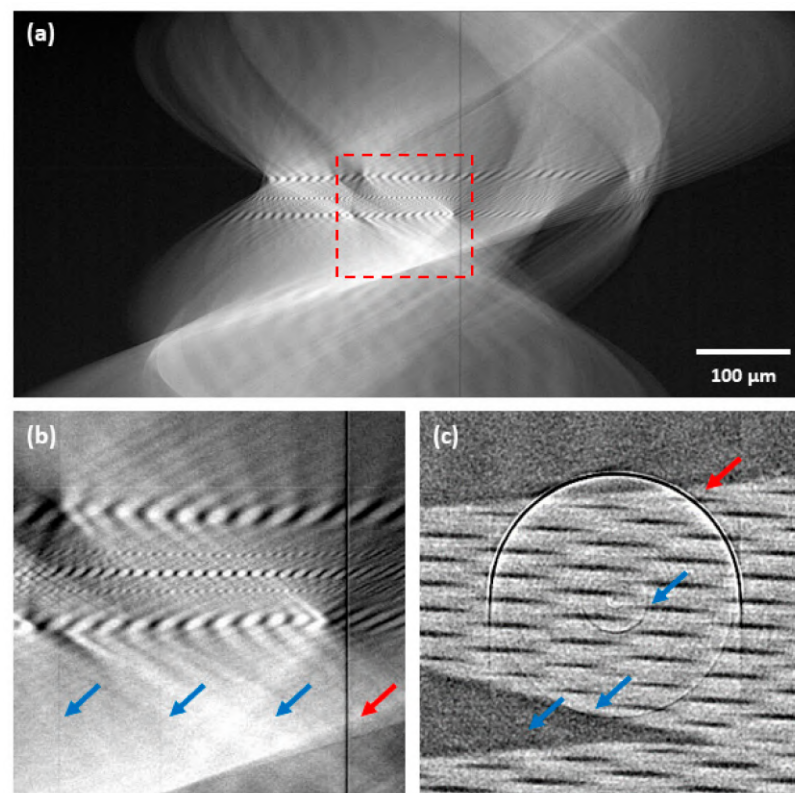

Figure 1. Example of ring artifacts affected data—glass capillary sample acquired with a charge-coupled device (CCD)-based camera: (**a**) sinogram; (**b**) detail of sinogram central area; (**c**) central area of corresponding tomogram. Red arrows indicate the high-level ring artifacts and blue arrows the low-level ring artifacts.

2.1. High-Level Ring Artifacts

The class of high-level ring artifacts (HRA) is represented by the most prominent stripes in the sinograms (see Figure 1). The actual cause of such artifacts is two-fold. One cause originates from entirely dead detector pixels or damaged areas on the scintillator. The behavior of these pixels then does not follow the pattern of responses of adjacent

non-defective elements. Their responses are close or equal to the saturation level of the detector (maximum of the dynamic range) or the minimum of the dynamic range. The second cause is related to so-called "hot pixels", which may be considered as a type of fixed pattern noise [30]. They are defined as pixels with the dark current values significantly above the average. They follow the responses of the adjacent non-defective pixels but with significant deviations that do not vary in time. In the sinograms, they appear as prominent stripes, but they do not reach the extremes of the dynamic range.

High-Level Ring Artifacts Removal

The reduction in high-level ring artifacts is divided into two parts: first, the artifacts' positions are detected, and second, the input sinogram is corrected at these positions. For the artifacts' detection, an iterative detection scheme was designed. This detection procedure consists of 5 steps (see Figure 2) that are iteratively repeated until any of 4 stopping conditions is fulfilled. These steps are:
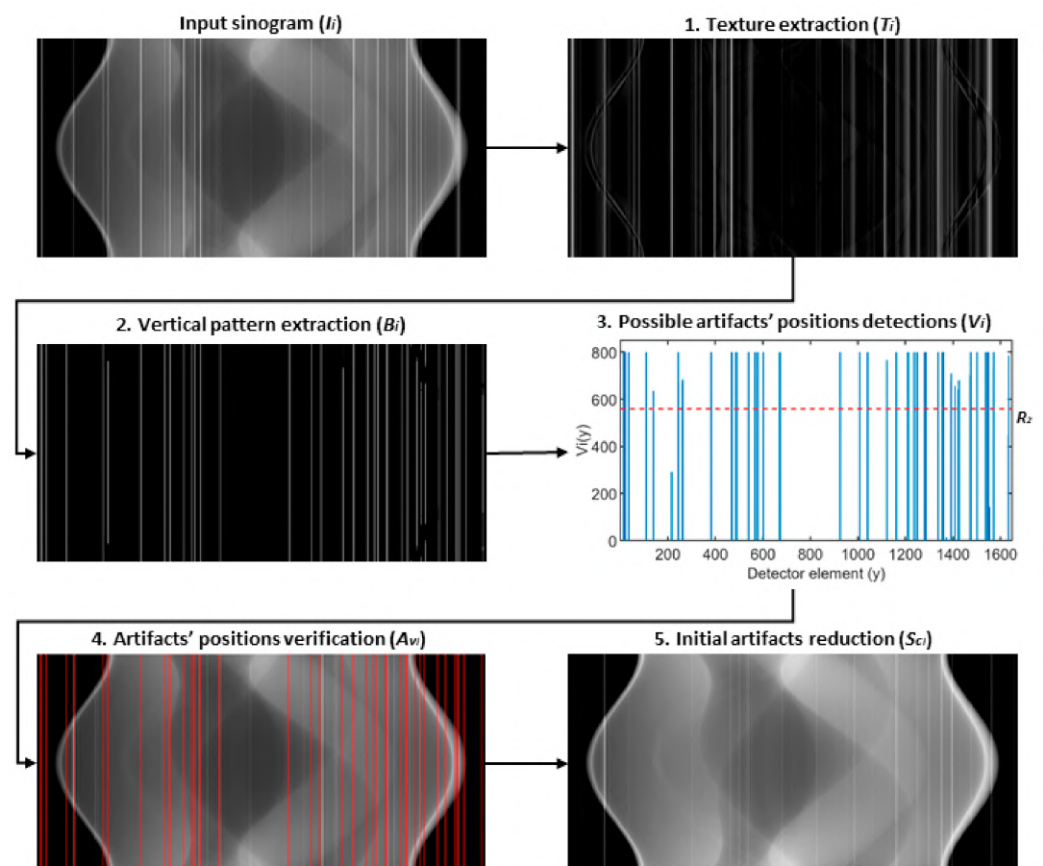
1. Texture extraction

Figure 2. Illustrative scheme of proposed high-level ring artifacts detection scheme—as example images, the outputs from the first iteration are shown.

Ring artifacts, together with the structural details, are considered as a texture of sinogram. Therefore, textural information is first extracted using the subtraction of input sinogram and its smoothened version (i.e., image after texture removal):

$$T_i = I_i - S_{s_i}, \tag{1}$$

where T_i is extracted texture image in the current iteration i, I_i is input sinogram in the current iteration i and $S_{s,i}$ is input sinogram after the texture removal. For texture removal, an algorithm based on relative total variation (RTV) is used (for more details see the

Appendix A section). After the texture extraction in the current iteration, the first stopping condition (SC 1) is evaluated:

$$\frac{\|T_i - T_{i-1}\|_2}{\|T_1\|_2} \leq R_1, \tag{2}$$

where T_i is extracted texture image in the current iteration i, T_{i-1} is extracted texture image in the previous iteration, T_1 is extracted texture image in the first iteration, and R_1 is a selected threshold value. Using this stopping condition, the iteration is stopped when the normalized L2 norm of the difference between two sequential extracted textures is equal or lower than the set value R_1.

2. Vertical pattern extraction

The extracted texture image from the previous step is further convolved:

$$P_i = T_i * k, \tag{3}$$

with a convolution kernel k that corresponds to one-dimensional (1D) vertical mean filter with the length l. This is done to highlight a vertical stripe pattern (e.g., ring artifacts) and to blur remaining non-vertical structures. Then, the first derivative is approximated by finite differences in the horizontal direction, and the result is binarized row-by-row by thresholding with a threshold value set to a double of the calculated standard deviation of a given row:

$$B_i(x,y) = \begin{cases} 1, & if \ \Delta_x P_{ix}(y) > 2 \cdot \sigma_{\Delta_x P_{ix}} \\ 0, & otherwise \end{cases}, \tag{4}$$

where $B_{i(x,y)}$ corresponds to the value of resulting binary mask in the current iteration i at coordinates x,y and σ is used notation for standard deviation.

3. Possible artifacts' positions detections

The binary mask is then summed in the column direction:

$$V_i(y) = \sum_{x=1}^{M} B_i(x,y), \tag{5}$$

where $V_{i(y)}$ refers to value of the resulting vector at position y and M refers to number of rows in the binary mask B_i, x and y refer to vertical and horizontal indices, respectively. In the resulting vector, only elements with values above threshold R_2 are considered as possible candidates for positions of ring artifacts A_p:

$$A_{pi}(y) = \begin{cases} 1, & if \ V_i(y) > R_2. \\ 0, & otherwise \end{cases} \tag{6}$$

However, the inevitable RTV smoothing errors may negatively affect this detection. To avoid this, the distances between possible detected artifacts are also analyzed. When the distance between two neighboring possible artifacts' positions is below threshold R_3, the intermediate positions are also considered as the possible artifacts' positions. In this step, the second stopping condition (SC 2) is evaluated, the iteration is stopped when no possible artifacts' positions are detected.

4. Artifacts' positions verification

Verification of detected possible artifacts' positions A_p is achieved by the analysis of mean column vector L_{Ti} of extracted textural information T_i in the current iteration i. Possible artifact positions A_p are considered as verified A_v, if they meet the following condition:

$$A_{vi}(y) = \begin{cases} 1, & if \ |L_{T_i}(A_{pi}(y)) - L_{T_i}(A_{pi}(y_x))| > 2 \cdot \sigma_{\Delta L_{T_i}}, \\ 0, & otherwise \end{cases} \tag{7}$$

where $A_{pi}(y_x)$ is the nearest artifact-free position to analyzed possible artifacts' position $A_{pi}(y)$ and the threshold value corresponds to twice the standard deviation value of the first derivative of L_{Ti}, which is approximated by finite differences. If no possible artifacts' positions are considered as verified, the iteration is stopped (the third stopping condition—SC 3). On the other hand, when certain positions are verified in the current iteration i, they are then compared to the verified positions from previous iterations and if no new verified artifacts' position is detected, the iteration is stopped (the fourth stopping condition—SC 4).

5.　Initial artifacts reduction

In each iteration, the sinogram is corrected at new verified artifacts' positions. This is achieved by filling the sinogram at artifacts' positions by means of image inpainting. In our work, this is completed by using a partial differential equation (PDE)-based approach, where Laplace equation is solved with the Dirichlet boundary condition:

$$S_{C_i} = \begin{cases} \nabla^2 u = 0, & for\ A_{vi} \\ u(x,y) = I_i\,(x,y), & on\ \partial A_{vi} \end{cases}, \tag{8}$$

where *Sc* corresponds to corrected sinogram in the current iteration *i*.

After the termination of the detection procedure, the final artifacts reduction is conducted. In this step, the previously described inpainting scheme is used again, and the input sinogram is corrected at the detected ring artifacts' positions A_v. The implementation details and used parameters can be found in Appendix C (Table A3).

2.2. Low-Level Ring Artifacts

Low-level ring artifacts (LRA) are caused by miscalibrated detector pixels. Their sensitivity deviations result from higher or lower dark current values compared to the non-defected pixels. They follow the responses of the adjacent non-defective pixels but with certain deviations. In the sinogram (see Figure 1), their presence is not distinct from the non-defective pixels as the HRA, but they still negatively affect the data quality.

Low-Level Ring Artifacts Removal

The main idea of the proposed algorithm for LRA removal is that column-wise neighboring homogenous areas (i.e., areas at same vertical positions of two adjacent columns) from extracted texture should ideally (without any artifact) have the same average values. To achieve this, an iterative procedure was proposed (see Figure 3), consisting of these steps:

1.　Texture extraction

For the texture extraction, the same procedure as in high-level ring artifacts removal (Equation (1)) is used with the same stopping condition (Equation (2)) set to the threshold value R_1. To reduce the presence of noise and its negative effect on the subsequent analysis, the extracted texture is further filtered with a 1D pixel-wise adaptive low-pass Wiener filter in column-wise direction:

$$T_{f_i} = T_i * w, \tag{9}$$

where T_i is extracted texture in current iteration i, w is kernel of 1D Wiener filter with the length l and T_{fi} is the noise reduced texture, which is used only within steps 2 and 3.

2.　Homogenous areas detection

Homogenous texture areas are detected column-wise using the following formula:

$$H_i(x,y) = \begin{cases} 1, & if\ T_{f_i}(x,y) \leq \overline{T_{fi}(1:M,y)} \\ 0, & otherwise \end{cases}, \tag{10}$$

where *y* is the coordinate of analyzed column, $H_i(x,y)$ corresponds to the value of resulting binary mask in the current iteration *i* at coordinates *x,y* and *M* is the number of sinogram rows.
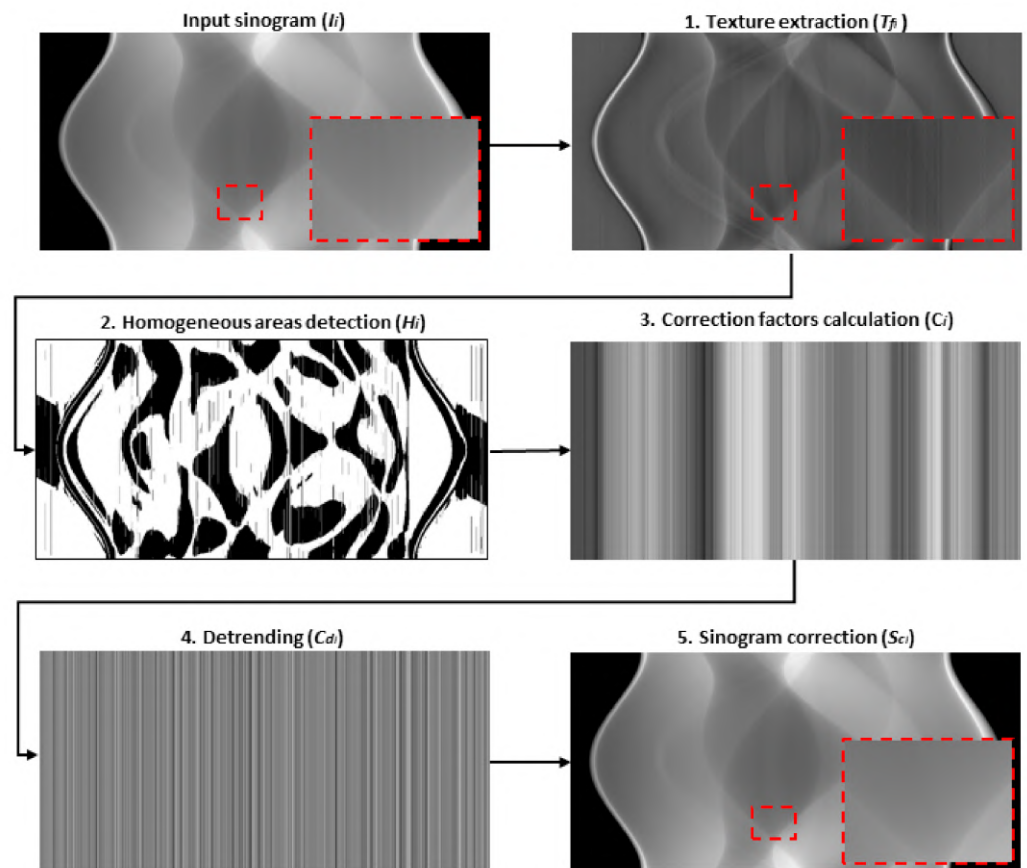
Figure 3. Illustrative scheme of the proposed low-level ring artifacts removal procedure—the outputs from the first iteration are shown as examples.

3.   Correction factors calculation

Correction factors for sinogram columns are calculated from extracted texture T_{f_i} by comparing two neighboring columns in terms of average intensity values of their neighboring homogenous areas. The column with smaller index is always taken as a reference, and other column is then corrected using the following equation:

$$T_{f_i}(1:M,y) = T_{f_i}(1:M,y) + C_i(y), \tag{11}$$

where $C_i(y)$ is a correction factor for column y in the current iteration i:

$$C_i(y) = \left(\frac{\sum_{j=1}^{N_h} T_{f_i}(h, y-1)}{N_h} - \frac{\sum_{j=1}^{N_h} T_{f_i}(h, y)}{N_h} \right), \tag{12}$$

where h is x coordinates of neighboring homogenous areas in analyzed columns (at coordinates y and $y-1$), h is those coordinates where $H_y = 1 \wedge H_{y-1} = 1$, and N_h is the number of those positions. If $N_h = 0$, the correction factor for the previous column (C_{y-1}) is used.

4.   Detrending

Calculated correction factors in the previous step can successfully reduce the artifacts, but the overall structural trend of the extracted texture is also lost. To avoid this, the Savitzky-Golay filter [31] is used to extract this trend from the calculated correction factor values:

$$t = C_i * s, \tag{13}$$

where s is the 1D kernel of the Savitzky-Golay filter with polynomial order r and frame length f. The value of this parameter f is decreasing with each iteration by power of two—by this the over-smoothing effect is avoided. Subsequently, this trend is subtracted from the calculated correction factors:

$$C_{d_i} = C_i - t, \tag{14}$$

to ensure that only the artifacts are reduced while the overall structural pattern of the textural information is preserved.

5.   Sinogram correction

In each iteration i, the corrected sinogram S_C is calculated as the sum of the smoothened sinogram S_s (i.e., sinogram after texture removal) and the extracted texture after an artifact reduction:

$$S_{C_i} = S_{s_i} + \left(T_i + C_{d_i}\right). \tag{15}$$

These steps are repeated until the stopping condition described by Equation (2) is fulfilled. The implementation details and used parameters can be found in Appendix C (Table A4).

2.3. Real CT Data Acquisition

A laboratory-based CT system Rigaku nano3DX [32] was used for CT measurements. For purposes of our study, this CT system was equipped with a Rigaku's scientific X-ray CDD camera (XSight™ Micron LC X-ray CCD camera [33]) and a scientific X-ray scientific complementary metal-oxide-semiconductor (sCMOS) camera (XSight™ Micron LC X-ray sCMOS camera [34]), nominal parameters of used cameras are stated in Table A2 in Appendix B. As it was shown in our previous study [35], radiographic data acquired by tested charge-coupled device (CCD) and sCMOS cameras mainly differ in projection domain in terms of the population of hot pixels that mostly correspond to high-level ring artifacts. As samples, a glass capillary array (pores diameter: 3 µm) and a ruby ball (diameter: 300 µm) were selected. They were scanned using circular trajectory with an angular range from 0 to 180 degrees with an acquisition of 800 projection images for one CT scan. Molybdenum rotatory target was used (50 kV and 24 mA) for all the measurements. Exposure times for X-ray projection data were selected following the manufacturer's recommendations (based on the level of detected signal). Specifically, the exposure times for glass capillary array measurements were 16 s (CCD) and 6 s (sCMOS), and they were 13 s (CCD) and 4.5 s (sCMOS) for ruby ball measurements. Acquired projection data were only flat-field corrected before the ring artifacts reduction was applied. Subsequently, CT data were reconstructed using ASTRA toolbox [36]—filtered back projection (FBP) reconstruction with cosine filter. Then, all the data were normalized so that the minimum and maximum values were 0 and 1 arbitrary units, respectively. The achieved linear voxel size values for binning 2×2 were 0.53 µm and 0.63 µm for the CCD and sCMOS cameras, respectively.

2.4. Synthetic Data Creation

Three synthetic images were used in this work, representing various levels of data complexity—a ball phantom (single material sample), a Shepp-Logan phantom (multi material sample) and a Siemens star phantom (highly complex sample). Phantom images were generated in tomogram domain (see Figure 4) and then transformed by Radon transform to sinogram domain, using the ASTRA Tomography Toolbox [36]. The sinograms were simulated to have similar parameters as those acquired by nano3DX device equipped with a CCD camera, specifically to have a linear voxel size of 0.53 µm, a detector width of 1648 pixels and to follow the acquisition of 800 projection angles from an angular range of 0° to 180°. Gaussian distributed noise with a standard deviation of 0.01 (reflects noise properties of real projection data) was also added to generated sinograms.

The ring artifacts were simulated (see Figure 5) and added to the sinograms (see Figure 6). In total, 25% of detector elements were affected by artifacts: 5% HRA and

20% LRA. The artifacts' positions were generated randomly without any recurrences. As for high-level artifacts, one fifth of affected positions was assigned the intensity value (referring to detector response) equal to the maximum of used dynamic range (16bit), which corresponds to dead, unresponsive detector pixels. The remaining high-level artifacts' positions were assigned the intensity deviations generated as uniformly distributed random numbers from the interval from 10% to 60% of maximum sinogram intensity value. The intensity deviations of low-level artifacts were generated similarly but from the interval $\pm$ 1% of maximum sinogram intensity value. Such deviations were then added to the original responses at given artifacts' positions. Using such parameters, an extreme case of ring artifacts presence in sinogram was simulated.

Figure 4. Synthetic data used for testing and validation of all tested methods: (**a**) ball phantom; (**b**) Shepp-Logan phantom; (**c**) Siemens star phantom.
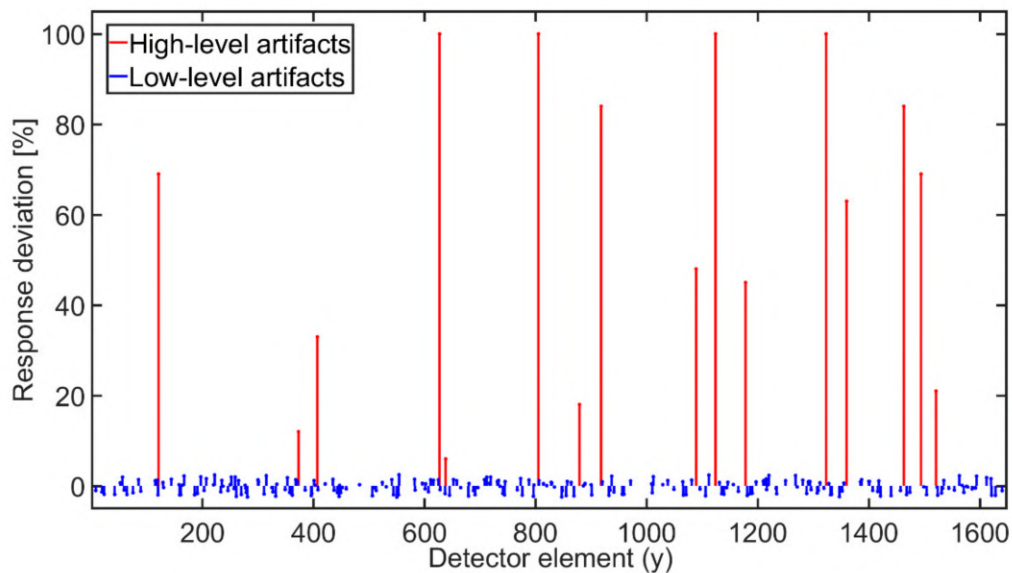

Figure 5. Example of simulated response deviations of detector elements representing the ring artifacts.
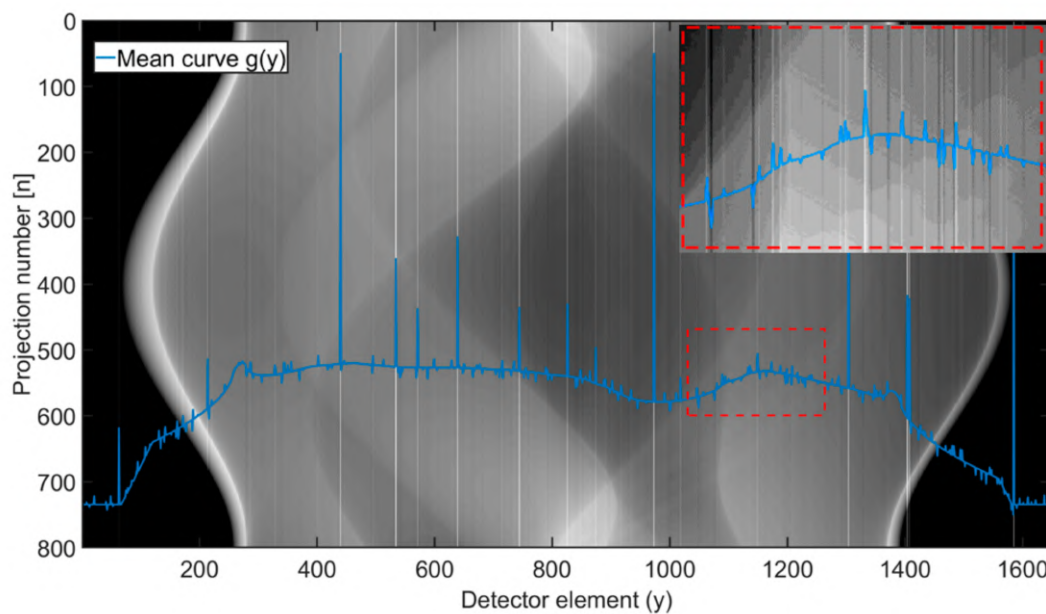
Figure 6. Shepp-Logan phantom sinogram affected by simulated ring artifacts presented in Figure 5. Blue curve shows mean column values—the highest peaks belong to high-level ring artifacts (HRA). In the red labelled image, the magnified area affected by low-level ring artifacts (LRA) is shown.

2.5. Other Methods

The performance of the proposed method was compared to three other selected approaches from the class of sinogram-based methods: the wavelet-Fourier-transform-based method by Münch [13], correction vector-based method by Eldib [15] and complex correction technique by Vo [21]. For notational simplicity, these methods are further called M1, M2 and M3, respectively. Since the performance of all the methods is highly dependent on specific settings, the optimal parameters for each method were selected to ensure a relevant and fair comparison. This was completed based on the suggestions in the original works and also based on the practical testing on synthetic data using a combination of both qualitative and quantitative evaluation (brute-force search with structural similarity index (SSIM) [37] as a validation metric). To test the consistency of these parameters within various test samples, only one specific setting was used for each of the methods (see Table A5).

2.6. Evaluated Criteria and Metrics

The proposed method was tested on both synthetic and real high-resolution CT data. Three criteria were considered for the evaluation. First, the proposed method was tested in terms of artifacts detection accuracy focused on the HRA detection. For this evaluation, three statistical metrics were used: true positive rate (TPR—ratio of correctly detected artifacts' positions to all positions labelled as artifacts) [38], positive predictive value—precision (PPV—percentage of artifacts' positions that were correctly detected) [39] and Dice similarity coefficient (DSC) [40].

Then, the overall performance of the proposed method was evaluated in context of other ring artifacts correction methods. This was completed both quantitatively using synthetic data with ground truth images and qualitatively on real CT data. For the quantitative performance evaluation, two metrics were used: the peak signal-to-noise ratio (PSNR), and structural similarity index (SSIM) [37]. These were calculated between the corrected tomogram (tomogram reconstructed from the ring artifacts corrected sinogram) and the ground truth tomogram (tomogram reconstructed from the corresponding sinogram without ring artifacts). The resulting tomogram data were first standardized to Z-scores, i.e., mean value was subtracted from the data and the result was divided by the corresponding standard deviation. This was completed so that the possible effect of intensity shifts on

corrected data could be eliminated. It was possible to precisely evaluate the functionality of ring artifacts reduction and also the effect of distortion on the data.

The lastly considered criterion focused on the robustness of the proposed ring artifacts reduction procedure to the used detection system, and on its effect on achieved spatial resolution. For the spatial resolution calculation, the modulation transfer function (MTF) analysis [41] was used following the procedure defined in ASTM E1695-95(2013) standard [42]. CT data of the ruby ball sample, acquired by both CCD- and sCMOS- based cameras, were used for this analysis.

3. Results

3.1. HRA Detection Accuracy of Proposed HRA Detection Scheme

The accuracy of the proposed HRA detection scheme was evaluated on the synthetic data with known artifacts' positions. The results are stated in Table 1. For all the phantom images, the proposed method was able to classify all the artifacts' positions with a precision above 95%. However, a certain amount of artifacts' positions, out of total 82 artifacts' positions, was not detected in all the cases: two artifacts' positions for Shepp-Logan and Siemens star phantoms, and three positions in the case of ball phantom. For Siemens star phantom, a higher number of falsely classified artifacts' positions led to a PPV score of 84.21% and DSC of 90.40%. On the contrary, for Shepp-Logan phantom, all the positions classified as artifacts were correct (PPV = 100%).

Table 1. Proposed HRA detection scheme accuracy—evaluated for synthetic data.

|	Ball	Shepp-Logan	Siemens Star
TPR [%]	96.34	97.56	97.56
PPV [%]	96.34	100.0	84.21
DSC [%]	96.34	98.77	90.40

We further evaluated the effect of noise level in the data on the detection accuracy of proposed HRA detection scheme (tested on Shepp-Logan phantom). Results of this analysis are shown in Figure 7. The precision of artifacts' detection was found almost independent of the noise presence, reaching values above 95% for all tested cases. However, a direct proportion was found between the noise level and the number of artifacts' positions that were not detected. This tendency is expressed by both the TPR and DSC metrics. Despite this tendency, the proposed HRA detection scheme resulted in scores of both metrics above 80% even for cases with a severe noise presence.

3.2. Overall Performance Evaluation in Context of Other Tested Methods

A high ring artifacts presence in the synthetic data made their correction very challenging, which is reflected by the poor results of the tested methods (Table 2). Apart from the proposed method, all the tested methods failed to successfully reduce the artifacts, especially the population of HRA, and to preserve the structural information (see Figure 8). The overall worst results were achieved by the M2 method. Especially in case of the ball phantom, the M2 method failed to distinguish the artifacts and sample structure. It led to an almost complete suppression of structural information (see Figure 9), which is further represented by a negative SSIM value (Table 2). In the case of the M1 method, a poor correction led to wide rings and blurring the overall image structures (see Figure 8). The M3 method results were visually good, and most of the artifacts were successfully reduced (see Figure 8). However, the quantitative evaluation (Table 2) revealed a poor input data preservation in terms of structural information and intensity values. This effect is further demonstrated in Figure 10 by histogram analysis of the Shepp-Logan phantom tomogram. Unlike the proposed method, the M3 method led to a significant transformation of histogram shape and Z-score range compared to the reference data. Compared to all other methods, the proposed method obtained the best results, as all the artifacts were reduced, and the sample structure was fully preserved (see Figures 8–10).

Table 2. Quantitative performance evaluation of tested methods.

	Ball		Shepp-Logan		Siemens-Star	
	PSNR [dB]	**SSIM**	**PSNR [dB]**	**SSIM**	**PSNR [dB]**	**SSIM**
M1	7.59	0.39	3.95	0.29	3.66	0.22
M2	1.03	−0.03	1.81	0.27	3.21	0.21
M3	11.39	0.47	1.91	0.22	3.30	0.20
Proposed	27.48	0.97	28.45	0.97	11.17	0.72
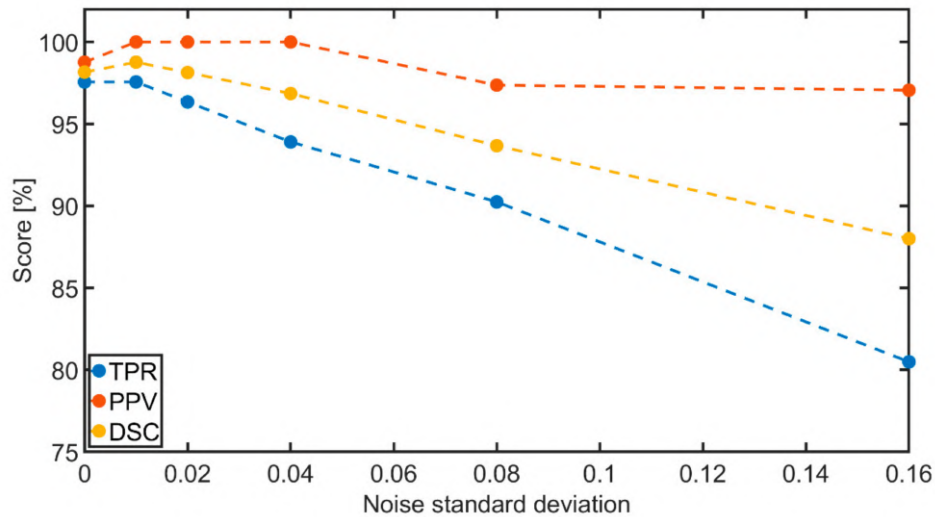
Figure 7. Dependence of the accuracy of the proposed HRA detection scheme on the noise level—evaluated for Shepp-Logan phantom.
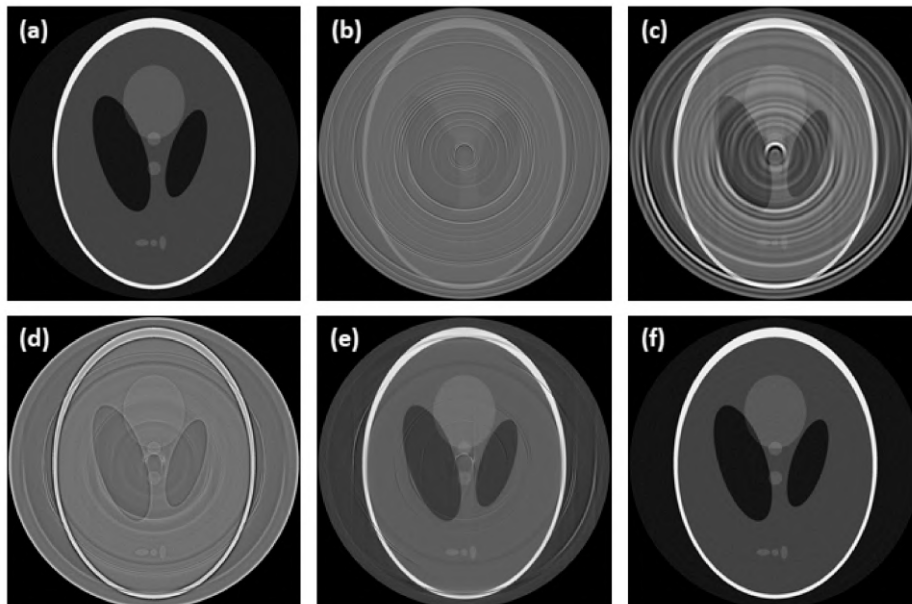
Figure 8. Comparison of tomograms after ring artifacts reduction by tested methods—simulated data of Shepp-Logan phantom: (**a**) reference; (**b**) original (without any correction); (**c**) M1; (**d**) M2; (**e**) M3; (**f**) proposed. For visualization, the same contrast setting was used for all the images.
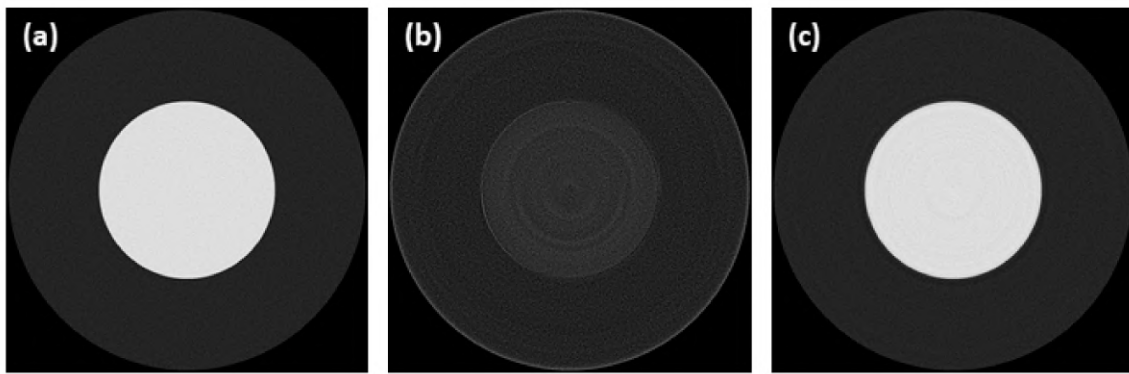
Figure 9. Comparison of data distortion between the proposed method and M2 method—tomograms of ball phantom: (**a**) reference; (**b**) M2 method; (**c**) proposed. For visualization, the same contrast setting was used for all the images.
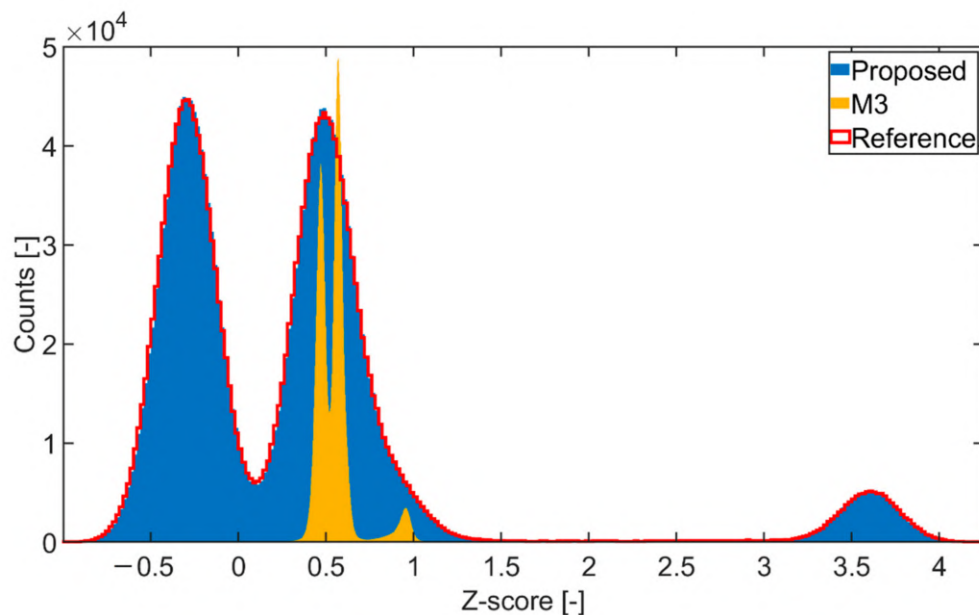

Figure 10. Comparison of data distortion between the proposed method and M3 method—histogram analysis of standardized tomogram values.

The overall performance of the tested methods was further evaluated on real CT data. From the resulting tomograms, the effectiveness of the tested methods was evaluated qualitatively using visual perception. For visualization purposes, the glass capillary array data acquired by a CCD camera were selected due to the presence of prominent HRA in the central area (see Figure 11). Apart from the proposed method, the other methods only reduced the HRA to a certain degree, leaving the artifacts still detectable after the correction. Moreover, in the case of the M3, some extra artifacts were created during the correction (see Figure 11e).
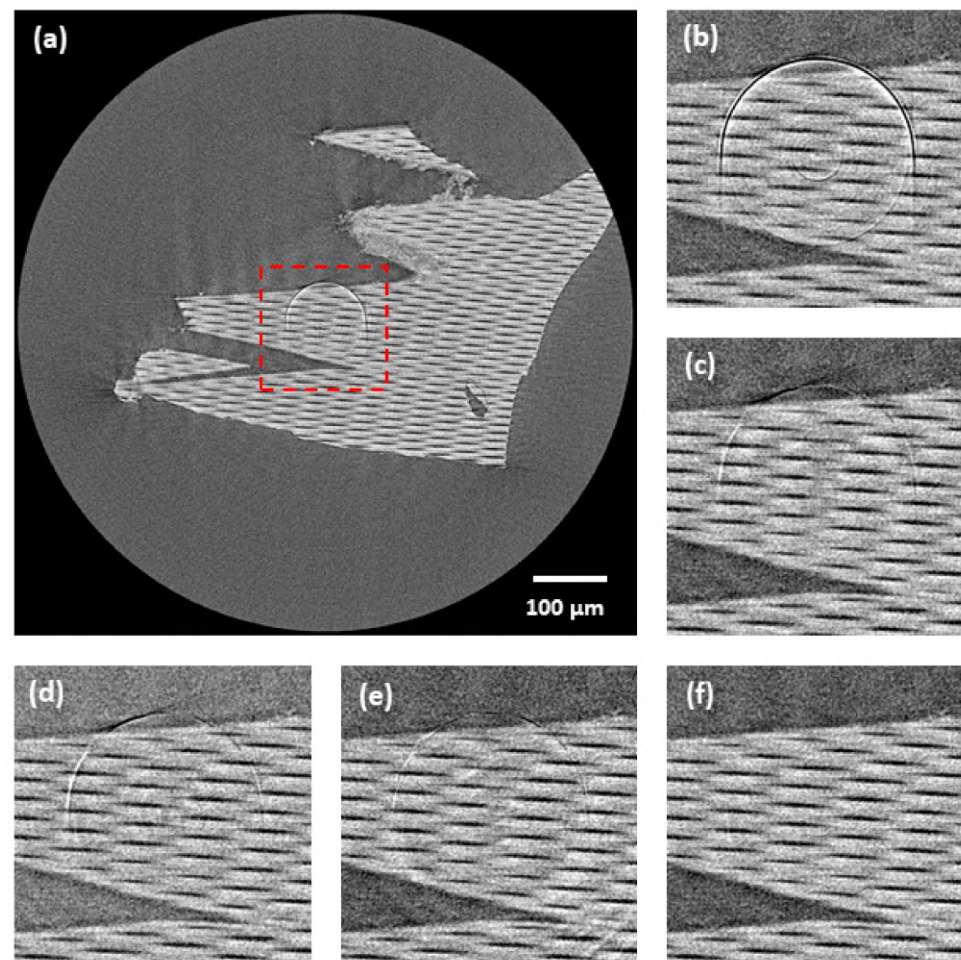
Figure 11. Comparison of tomograms after ring artifacts reduction by tested methods—real computed tomography (CT) data of glass capillary array acquired with a CCD-based camera: (**a**) original tomogram (without any correction)—red labelled area marks central area visualized in following images; (**b**) original; (**c**) M1; (**d**) M2; (**e**) M3; (**f**) proposed. For visualization, the same contrast setting was used for all the images.

3.3. Spatial Resolution Preservation and Robustness to Used Detection System

The results of the spatial resolution evaluation are stated in Table 3. The proposed method was able to preserve the spatial resolution within the accuracy limit of the used standard for both used detection systems. The robustness is further visually demonstrated in Figure 12. The proposed method in this example reduced all the ring artifacts without any negative effect or distortion on the data regardless of the used detection system.

Table 3. Results of spatial resolution evaluation.

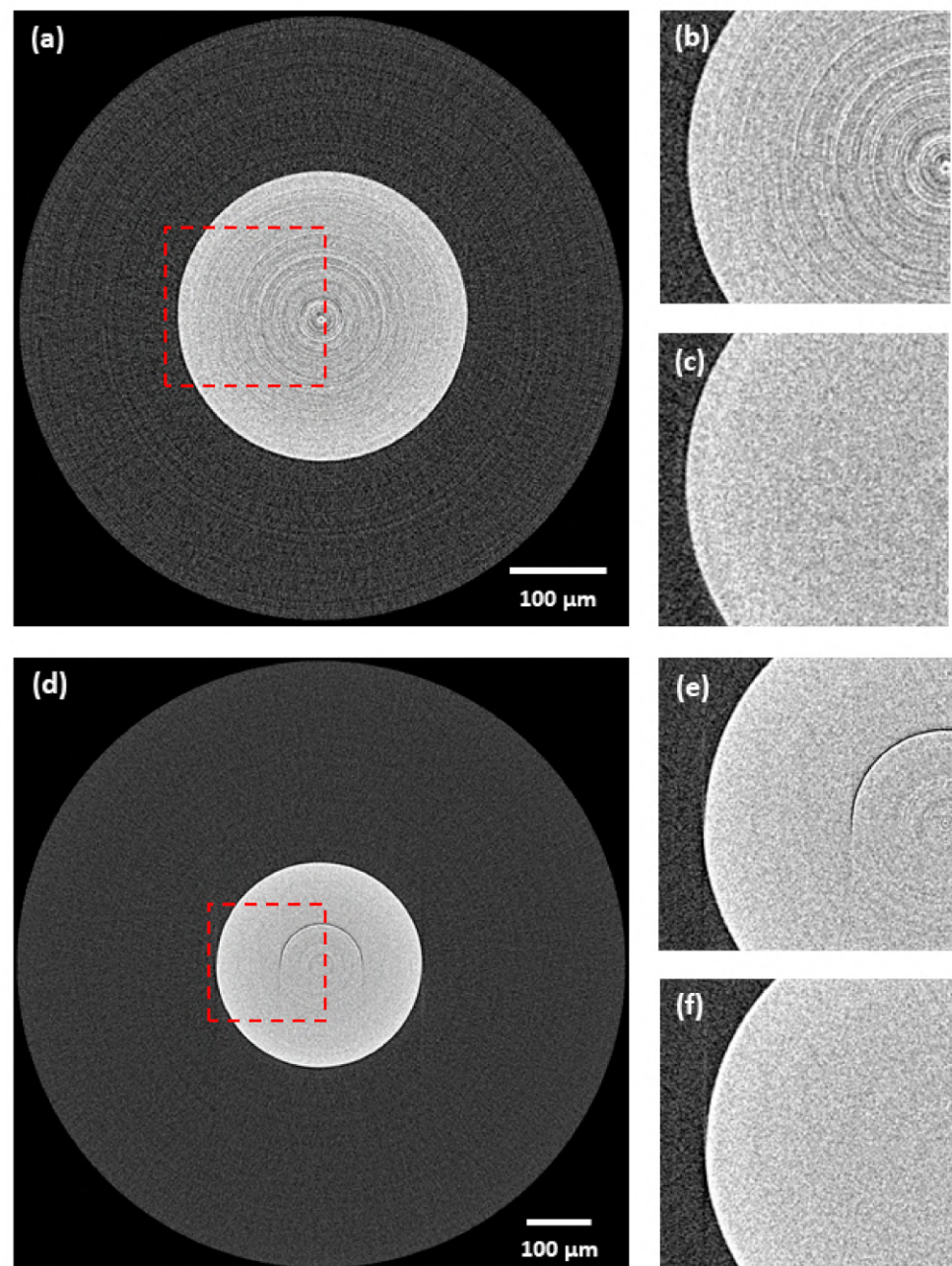|	CCD	sCMOS
Original	$0.62 \, \mu m \pm 0.03 \, \mu m$	$0.85 \, \mu m \pm 0.04 \, \mu m$
Proposed	$0.62 \, \mu m \pm 0.03 \, \mu m$	$0.82 \, \mu m \pm 0.04 \, \mu m$

Figure 12. Demonstration of robustness of the proposed method to the used detection system—real CT data of ruby ball: (**a**) original tomogram (scientific complementary metal-oxide-semiconductor (sCMOS), without any correction)—red labelled area marks the central area visualized in following images; (**b**) detail (sCMOS)—original; (**c**) detail (sCMOS)—corrected by proposed method; (**d**) original tomogram (CCD, without any correction)—red labelled area marks the central area visualized in following images; (**e**) detail (CCD)—original; (**f**) detail (CCD)—corrected by proposed method. For visualization, the same contrast setting was used for all the images.

4. Discussion

The practical testing demonstrated that the proposed ring artifacts reduction procedure, compared to other methods, can achieve superior results in the following criteria: artifacts detection accuracy, overall performance, robustness to detection system, and the ability to preserve the spatial resolution. First, the method was tested in terms of HRA detection accuracy. It was found that for all the tested data, the proposed HRA detection scheme achieved a precision higher than 95% (see Table 1), even for the increasing noise

level present in the data (see Figure 7). However, for all data, a certain amount of artifacts' positions was not detected. Moreover, a direct proportion was found between the number of HRA positions that were not detected and the noise level. However, this amount was found to be negligible in terms of the total number of artifacts' positions, as both the TPR and DSC metrics scored above 80% even for cases with a severe noise presence.

Although the proposed method did not detect all the HRA positions, the overall quantitative and qualitative results were superior to other tested methods. This was achieved by the proposed two-step correction scheme, when the HRA reduction algorithm and LRA reduction algorithm are working in tandem reducing all the artifacts effectively. A high ring artifacts presence in the case of the synthetic data made their correction very challenging, which was reflected by poor results of the M1, M2 and M3 methods (see Table 2). As for the M1 method, residual rings persisted after the correction for all the tested data resulting in unusable data for further analysis. However, the worst overall results were achieved with the M2 method, as it failed to reduce all the artifacts and preserve the structural information of the input data. Specifically, in the case of ball phantom, the method failed to distinguish the artifacts and sample structure leading to an almost complete suppression of structural information (see Figure 9), which is further represented by a negative SSIM value (Table 2). The M3 method achieved visually acceptable results, but the quantitative evaluation on synthetic data revealed that the method had led to a poor preservation of structural information and intensity range of the input data (see Figure 10). All these findings were further confirmed by testing on the real CT data. The acquired results corresponded to those from testing on the synthetic data. Compared to all other methods, the proposed method obtained the best results, as all the artifacts were reduced, and the sample structures were fully preserved.

The lastly considered criterion focused on the robustness of the proposed ring artifacts reduction procedure to the used detection system and its effect on the spatial resolution. In this analysis, the proposed method proved itself to preserve the spatial resolution within the accuracy limit of the regular standard for both detection systems (see Table 3). Moreover, the proposed method was functional regardless of the detection system without the need for any settings' optimization.

All the beforehand discussed aspects restrict the application of the M1, M2 and M3 methods in nano-tomography, where preservation of quality and structural information of input data are of key importance. Moreover, these methods were found highly dependent on the used parameters and the character of input data. Even following the original authors' recommendations and optimization, the methods did not achieve acceptable results with one setting for all the tested data. This showed a limited robustness and applicability of these methods in practice. Only the proposed method achieved acceptable results for all the conducted tests and showed a high robustness to the character of input data in terms of structure complexity and also the used detection system.

5. Conclusions

The small size of detector pixels used in nano CT devices does not enable an application of any hardware-based method for removing ring artifacts, leaving image-based processing methods as the most promising way for an effective ring artifacts removal. Several approaches from this class exist but each with some deficiencies, such as the degradation of data quality and spatial resolution, which is inconsistent with the core purpose of nano-tomography. The procedure presented in this paper is based on a smart implementation of several ideas from existing methods and utilization of their advantages.

The ring artifacts are classified into two types based on their cause and actual appearance in the CT data. Each artifact class is then handled separately since it is impossible for a single approach to remove all of them. In our procedure, we applied novel iterative RTV-based algorithms in the sinogram domain to avoid any negative influence of tomographic reconstruction. The proposed procedure was optimized and tested on different types of data, cameras, and samples as well.

In confrontation with other advanced ring artifacts reduction methods, it proved its supremacy during practical tests, being robust regarding the character of input data and used detection system. Moreover, the method was able to fully preserve the input data, structural information and spatial resolution. Such features show a high potential of the proposed procedure for practical use in the field of synchrotron- or lab-based nano CT systems.

Institutional Review Board Statement: Not applicable.

Informed Consent Statement: Not applicable.

Data Availability Statement: The data and the code used for the manuscript are available for researchers on request from the corresponding author.

Conflicts of Interest: The authors declare no conflict of interest.

Appendix A

In this work, a relative total variation (RTV)-based algorithm proposed by Xu et al. [43] is used for the texture extraction. Objective function of this algorithm can be expressed as:

$$\operatorname*{argmin}_{S} \sum_{p} \left(S_p - I_p\right)^2 + \lambda \cdot \left(\frac{D_x(p)}{L_x(p) + \varepsilon} + \frac{D_y(p)}{L_y(p) + \varepsilon} \right). \tag{A1}$$

The data term $\left(S_p - I_p\right)^2$ makes the input I and result S not extensively deviate, where p corresponds to pixel indices. The second part of the objective function, $\lambda \cdot ((Dx\,(p))/(Lx\,(p) + \varepsilon) + (Dy\,(p))/(Ly\,(p) + \varepsilon))$, corresponds to the RTV measure, where λ is a weight controlling the degree of smoothing, and ε is a small positive number to avoid division by zero and also controlling the sharpness of the image S. $D_x(p)$ and $D_y(p)$ are windowed total variations in the x and y directions for pixel p:

$$D_x(p) = \sum_{q \in R(p)} g_{p,q} \cdot \left| (\partial_x S)_q \right|, \tag{A2}$$

$$D_y(p) = \sum_{q \in R(p)} g_{p,q} \cdot \left| (\partial_y S)_q \right|, \tag{A3}$$

which count the absolute spatial difference within the rectangular window $R(p)$ centered at pixel p. Pixel q belongs to $R(p)$. The term $g_{p,q}$ refers to a weighting function defined according to spatial affinity:

$$g_{p,q} \propto \exp\left(-\frac{\left(x_p - x_q\right)^2 + \left(y_p - y_q\right)^2}{2\sigma^2} \right), \tag{A4}$$

where σ controls the spatial scale of the window corresponding to the size of textural elements. To help distinguish the prominent structures from the texture elements, the RTV

measure also contains windowed inherent variations $L_x(p)$ and $L_y(p)$ in the directions x and y, defined as:

$$L_x(p) = \left| \sum_{q \in R(p)} g_{p,q} \cdot (\partial_x S)_q \right|, \tag{A5}$$

$$L_y(p) = \left| \sum_{q \in R(p)} g_{p,q} \cdot (\partial_y S)_q \right|. \tag{A6}$$

The objective function defined in Equation (A1) is non-convex and can be solved using the linear optimization process with the penalty of quadratic measure proposed by Xu et al. [43]. For a practical implementation, the available Matlab® code by Xu et al. [43] was used with the settings stated in Table A1. These settings were selected by an extensive practical testing where the overall functionality of both HRA and LRA removal algorithms was evaluated and optimized using described synthetic data by a combination of both qualitative and quantitative evaluation (brute-force search with SSIM [37] as a validation metric).

Table A1. Relative total variation (RTV) texture extraction settings used within HRA and LRA removal algorithms.

Parameter	HRA Removal	LRA Removal
Λ	0.005	0.050
E	0.020	0.030
Σ	6	1

Appendix B

Table A2. Nominal parameters of both used cameras without a lens unit.

Technical Features	CCD Camera	sCMOS Camera
Array size	3320(H) × 2500(V)	2048(H) × 2048(V)
Pixel size	5.4 μm	6.5 μm
Sensor diagonal	22.5 mm	18.8 mm
Nonlinearity	<1%	0.2%
Dynamic range	2300: 1	21,400: 1
Acquisition gain	0.45 e-/ADU	0.52 e-/ADU
Readout noise	11 e-rms	1.4 e-rms
Readout rate	8 Mpix./s (approx. 1 fps)	40 fps (@ 16 bit)
Dark current	0.001 e-/pix./s −35 °C	0.14 e-/pix./s @ 0 °C
Binning	Independent on-chip binning in x, y	2 × 2, 3 × 3, 4 × 4, 8 × 8
Peak quantum efficiency	56% @ 540 nm	82% @ 550 nm
Shutter type	Electromechanical	Rolling shutter
Data interface	USB 2.0	USB 3.0

Appendix C

Appendix C.1. Proposed Method—Used Settings

These settings were selected by an extensive practical testing where the overall functionality of the algorithms was evaluated and optimized using synthetic data by a combination of both qualitative and quantitative evaluation (brute-force search with SSIM [37] as a validation metric).

Table A3. HRA removal algorithm settings.

Parameter	Value
L	10% of sinogram rows
R_1	0.05
R_2	70% of sinogram rows
R_3	0.25% of sinogram columns

Table A4. LRA removal algorithm settings.

Parameter	Value
F	129
L	10% of sinogram rows
R_1	0.02
R	6

Appendix C.2. Other Methods—Used Settings

Table A5. List of the other methods and used settings (notations of the parameters are adopted from the original works).

Method	Notation	Settings
Münch [13]	M1	Wavelet: DB7; Decomposition level: 4; Damping factor: 1.3
Eldib [15]	M2	Filter size: 15; Standard deviation: 10
Vo [21]	M3	Algorithms sequence: 6, 5, 3; $R = 7$; Filter size for algorithms 5 and 6: 81; Filter size for algorithm 3: 31

References

1. Yousuf, M.; Asaduzzaman, M. An Efficient Ring Artifact Reduction Method Based on Projection Data for Micro-CT Images. *J. Sci. Res.* **2009**, *2*, 37–45. [CrossRef]
2. Lifton, J.; Liu, T. Ring artefact reduction via multi-point piecewise linear flat field correction for X-ray computed tomography. *Opt. Express* **2019**, *27*, 3217–3228. [CrossRef] [PubMed]
3. Seibert, J.; Dobbins, J., III; Boone, J.; Boone, J.; Lindfors, K. Flat-field correction technique for digital detectors. In *Medical Imaging 1998: Physics of Medical Imaging, Proceedings of the SPIE, San Diego, CA, USA, 21–26 February 1998*; International Society for Optics and Photonics: Bellingham, WA, USA, 1998; Volume 1998, pp. 348–354.
4. Vågberg, W.; Larsson, J.; Hertz, H. Removal of ring artifacts in microtomography by characterization of scintillator variations. *Opt. Express* **2017**, *25*, 23191–23198. [CrossRef] [PubMed]
5. Boin, M.; Haibel, A. Compensation of ring artefacts in synchrotron tomographic images. *Opt. Express* **2006**, *14*, 12071–12075. [CrossRef]
6. Croton, L.; Ruben, G.; Morgan, K.; Paganin, D.; Kitchen, M. Ring artifact suppression in X-ray computed tomography using a simple, pixel-wise response correction. *Opt. Express* **2019**, *27*, 14231–14245. [CrossRef]
7. Van Nieuwenhove, V.; De Beenhouwer, J.; De Carlo, F.; Mancini, L.; Marone, F.; Sijbers, J. Dynamic intensity normalization using eigen flat fields in X-ray imaging. *Opt. Express* **2015**, *23*, 27975–27989. [CrossRef]
8. Davis, G.; Elliott, J. X-ray microtomography scanner using time-delay integration for elimination of ring artefacts in the reconstructed image. *Nucl. Instrum. Methods Phys. Res. Sect. A Accel. Spectrom. Detect. Assoc. Equip.* **1997**, *394*, 157–162. [CrossRef]
9. Doran, S.; Koerkamp, K.; Bero, M.; Jenneson, P.; Morton, E.; Gilboy, W. A CCD-based optical CT scanner for high-resolution 3D imaging of radiation dose distributions: Equipment specifications, optical simulations and preliminary results. *Phys. Med. Biol.* **2001**, *46*, 3191–3213. [CrossRef]
10. Jenneson, P.; Gilboy, W.; Morton, E.; Gregory, P. An X-ray micro-tomography system optimised for the low-dose study of living organisms. *Appl. Radiat. Isot.* **2003**, *58*, 177–181. [CrossRef]
11. Ji, D.; Qu, G.; Hu, C.; Liu, B.; Jian, J.; Guo, X. Anisotropic total variation minimization approach in in-line phase-contrast tomography and its application to correction of ring artifacts. *Chin. Phys. B* **2017**, *26*, 060701. [CrossRef]
12. Raven, C. Numerical removal of ring artifacts in microtomography. *Rev. Sci. Instrum.* **1998**, *69*, 2978–2980. [CrossRef]
13. Münch, B.; Trtik, P.; Marone, F.; Stampanoni, M. Stripe and ring artifact removal with combined wavelet—Fourier filtering. *Opt. Express* **2009**, *17*, 8567–8591. [CrossRef] [PubMed]
14. Sadi, F.; Lee, S.; Hasan, M. Removal of ring artifacts in computed tomographic imaging using iterative center weighted median filter. *Comput. Biol. Med.* **2010**, *40*, 109–118. [CrossRef] [PubMed]

15. Eldib, M.; Hegazy, M.; Mun, Y.; Cho, M.; Cho, M.; Lee, S. A Ring Artifact Correction Method: Validation by Micro-CT Imaging with Flat-Panel Detectors and a 2D Photon-Counting Detector. *Sensors* **2017**, *17*, 269. [CrossRef]

16. Anas, E.; Lee, S.; Kamrul Hasan, M. Classification of ring artifacts for their effective removal using type adaptive correction schemes. *Comput. Biol. Med.* **2011**, *41*, 390–401. [CrossRef]

17. Anas, E.; Kim, J.; Lee, S.; Hasan, M. High-quality 3D correction of ring and radiant artifacts in flat panel detector-based cone beam volume CT imaging. *Phys. Med. Biol.* **2011**, *56*, 6495–6519. [CrossRef]

18. Rashid, S.; Lee, S.; Hasan, M. An improved method for the removal of ring artifacts in high resolution CT imaging. *EURASIP J. Adv. Signal Process.* **2012**, *2012*, 93. [CrossRef]

19. Anas, E.; Lee, S.; Hasan, M. Removal of ring artifacts in CT imaging through detection and correction of stripes in the sinogram. *Phys. Med. Biol.* **2010**, *55*, 6911–6930. [CrossRef]

20. Ashrafuzzaman, A.; Lee, S.; Hasan, M. A Self-Adaptive Approach for the Detection and Correction of Stripes in the Sinogram: Suppression of Ring Artifacts in CT Imaging. *EURASIP J. Adv. Signal Process.* **2011**, *2011*, 1–8. [CrossRef]

21. Vo, N.; Atwood, R.; Drakopoulos, M. Superior techniques for eliminating ring artifacts in X-ray micro-tomography. *Opt. Express* **2018**, *26*, 28396–28412. [CrossRef]

22. Kim, Y.; Baek, J.; Hwang, D. Ring artifact correction using detector line-ratios in computed tomography. *Opt. Express* **2014**, *22*, 13380–13392. [CrossRef] [PubMed]

23. Wei, Z.; Wiebe, S.; Chapman, D. Ring artifacts removal from synchrotron CT image slices. *J. Instrum.* **2013**, *8*, C06006. [CrossRef]

24. Sijbers, J.; Postnov, A. Reduction of ring artefacts in high resolution micro-CT reconstructions. *Phys. Med. Biol.* **2004**, *49*, N247–N253. [CrossRef] [PubMed]

25. Kyriakou, Y.; Prell, D.; Kalender, W. Ring artifact correction for high-resolution micro CT. *Phys. Med. Biol.* **2009**, *54*, N385–N391. [CrossRef]

26. Liang, X.; Zhang, Z.; Niu, T.; Yu, S.; Wu, S.; Li, Z.; Zhang, H.; Xie, Y. Iterative image-domain ring artifact removal in cone-beam CT. *Phys. Med. Biol.* **2017**, *62*, 5276–5292. [CrossRef]

27. Yan, L.; Wu, T.; Zhong, S.; Zhang, Q. A variation-based ring artifact correction method with sparse constraint for flat-detector CT. *Phys. Med. Biol.* **2016**, *61*, 1278–1292. [CrossRef]

28. Paleo, P.; Mirone, A. Ring artifacts correction in compressed sensing tomographic reconstruction. *J. Synchrotron Radiat.* **2015**, *22*, 1268–1278. [CrossRef]

29. Titarenko, S.; Withers, P.; Yagola, A. An analytical formula for ring artefact suppression in X-ray tomography. *Appl. Math. Lett.* **2010**, *23*, 1489–1495. [CrossRef]

30. Yu, J.; Imai, F.; Sampat, N.; Collins, D.; Yasan, A.; Xiao, F.; Bae, S.; Ramaswami, S. Hot pixel reduction in CMOS image sensor pixels. In Proceedings of the SPIE 7537: Digital Photography VI 2010, San Jose, CA, USA, 18–19 January 2010.

31. Savitzky, A.; Golay, M. Smoothing and Differentiation of Data by Simplified Least Squares Procedures. *Anal. Chem.* **1964**, *36*, 1627–1639. [CrossRef]

32. Rigaku Corporation: Nano3DX—X-ray Microscope. Available online: https://www.rigaku.com/en/products/xrm/nano3dx (accessed on 21 August 2019).

33. Rigaku Corporation: Compact Two-Dimensional CC Detector. Available online: https://www.rigaku.com/en/products/detectors/micron (accessed on 21 August 2019).

34. Rigaku Corporation: Compact Two-Dimensional sCMOS Detector. Available online: https://www.rigaku.com/en/products/detectors/micron-cmos (accessed on 21 August 2019).

35. Šalplachta, J.; Zikmund, T.; Horváth, M.; Takeda, Y.; Omote, K.; Pína, L.; Kaiser, J. CCD and scientific-CMOS detectors for submicron laboratory based X-ray Computed tomography. In Proceedings of the 9th Conference on Industrial Computed Tomography (iCT), Padova, Italy, 13–15 February 2019.

36. Van Aarle, W.; Palenstijn, W.; Cant, J.; Janssens, E.; Bleichrodt, F.; Dabravolski, A.; De Beenhouwer, J.; Joost Batenburg, K.; Sijbers, J. Fast and flexible X-ray tomography using the ASTRA toolbox. *Opt. Express* **2016**, *24*, 25129–25147. [CrossRef]

37. Wang, Z.; Bovik, A.; Sheikh, H.; Simoncelli, E. Image Quality Assessment: From Error Visibility to Structural Similarity. *IEEE Trans. Image Process.* **2004**, *13*, 600–612. [CrossRef] [PubMed]

38. Altman, D.; Bland, J. Statistics Notes: Diagnostic tests 1. *BMJ* **1994**, *308*, 1552. [CrossRef] [PubMed]

39. Altman, D.; Bland, J. Statistics Notes: Diagnostic tests 2. *BMJ* **1994**, *309*, 102. [CrossRef] [PubMed]

40. Zou, K.; Warfield, S.; Bharatha, A.; Tempany, C.; Kaus, M.; Haker, S.; Wells, W.; Jolesz, F.; Kikinis, R. Statistical validation of image segmentation quality based on a spatial overlap index1. *Acad. Radiol.* **2004**, *11*, 178–189. [CrossRef]

41. Friedman, S.; Fung, G.; Siewerdsen, J.; Tsui, B. A simple approach to measure computed tomography (CT) modulation transfer function (MTF) and noise-power spectrum (NPS) using the American College of Radiology (ACR) accreditation phantom. *Med. Phys.* **2013**, *40*, 051907. [CrossRef]

42. ASTM E1695-95: Standard Test Method for Measurement of Computed Tomography (CT) System Performance 2013. Available online: https://compass.astm.org/Standards/HISTORICAL/E1695-95R13.htm (accessed on 1 December 2020).

43. Xu, L.; Yan, Q.; Xia, Y.; Jia, J. Structure extraction from texture via relative total variation. *ACM Trans. Graph.* **2012**, *31*, 1–10. [CrossRef]

DUCT reveals architectural mechanisms contributing to bile duct recovery in a mouse model for Alagille syndrome

Simona Hankeova[1,2†], Jakub Salplachta[3†], Tomas Zikmund[3‡], Michaela Kavkova[3‡], Noémi Van Hul[1‡], Adam Brinek[3], Veronika Smekalova[3], Jakub Laznovsky[3], Feven Dawit[4], Josef Jaros[5], Vítězslav Bryja[2], Urban Lendahl[6], Ewa Ellis[4], Antal Nemeth[7], Björn Fischler[4], Edouard Hannezo[8], Jozef Kaiser[3*], Emma Rachel Andersson[1,6*]

[1]Department of Biosciences and Nutrition, Karolinska Institutet, Solna, Sweden; [2]Department of Experimental Biology, Masaryk University, Brno, Czech Republic; [3]CEITEC – Central European Institute of Technology, Brno University of Technology, Brno, Czech Republic; [4]Department of Pediatrics, Clinical Science, Intervention and Technology (CLINTEC), Karolinska Institutet and Karolinska University Hospital, Solna, Sweden; [5]Department of Histology and Embryology, Masaryk University, Brno, Czech Republic; [6]Department of Cell and Molecular Biology, Karolinska Institutet, Solna, Sweden; [7]Department of Laboratory Medicine, Karolinska Institutet, Solna, Sweden; [8]Institute of Science and Technology, Klosterneuburg, Austria

*For correspondence:
Jozef.Kaiser@ceitec.vutbr.cz (JK);
emma.andersson@ki.se (ERA)

†These authors contributed equally to this work
‡These authors also contributed equally to this work

Abstract Organ function depends on tissues adopting the correct architecture. However, insights into organ architecture are currently hampered by an absence of standardized quantitative 3D analysis. We aimed to develop a robust technology to visualize, digitalize, and segment the architecture of two tubular systems in 3D: *double resin casting micro computed tomography* (DUCT). As proof of principle, we applied DUCT to a mouse model for Alagille syndrome (*Jag1Ndr/Ndr* mice), characterized by intrahepatic bile duct paucity, that can spontaneously generate a biliary system in adulthood. DUCT identified increased central biliary branching and peripheral bile duct tortuosity as two compensatory processes occurring in distinct regions of *Jag1Ndr/Ndr* liver, leading to full reconstitution of wild-type biliary volume and phenotypic recovery. DUCT is thus a powerful new technology for 3D analysis, which can reveal novel phenotypes and provide a standardized method of defining liver architecture in mouse models.

Introduction

The correct three-dimensional (3D) architecture of lumenized structures in our bodies is essential for function and health. The cardiovascular system, lungs, kidneys, liver, and other organs depend on precisely patterned tubular networks. Several diseases are caused by, or result in, alterations in the 3D architecture of lumenized structures. Vascular architecture defects contribute to Alzheimer's disease (*Klohs et al., 2014*), opportunistic infections cause narrowing of bile ducts in liver (*De Angelis et al., 2009*), and branching morphogenesis defects in the renal urinary system cause hypertension (*Short and Smyth, 2016*). In some pathologies, several lumenized structures are affected at once. Visualizing multiple tubular systems in tandem in 3D, in animal disease models, is necessary to allow investigation of how these systems interact in vivo in development, homeostasis, and disease.

eLife digest Many essential parts of the body contain tubes: the liver for example, contains bile ducts and blood vessels. These tubes develop right next to each other, like entwined trees. To do their jobs, these ducts must communicate and collaborate, but they do not always grow properly. For example, babies with Alagille syndrome are born with few or no bile ducts, resulting in serious liver disease. Understanding the architecture of the tubes in their livers could explain why some children with this syndrome improve with time, but many others need a liver transplant.

Visualising biological tubes in three dimensions is challenging. One major roadblock is the difficulty in seeing several tubular structures at once. Traditional microscopic imaging of anatomy is in two dimensions, using slices of tissue. This approach shows the cross-sections of tubes, but not how the ducts connect and interact. An alternative is to use micro computed tomography scans, which use X-rays to examine structures in three dimensions. The challenge with this approach is that soft tissues, which tubes in the body are made of, do not show up well on X-ray. One way to solve this is to fill the ducts with X-ray absorbing resins, making a cast of the entire tree structure. The question is, can two closely connected tree structures be distinguished if they are cast at the same time?

To address this question, Hankeova, Salplachta et al. developed a technique called double resin casting micro computed tomography, or DUCT for short. The approach involved making casts of tube systems using two types of resin that show up differently under X-rays. The new technique was tested on a mouse model of Alagille syndrome. One resin was injected into the bile ducts, and another into the blood vessels. This allowed Hankeova, Salplachta et al. to reconstruction both trees digitally, revealing their length, volume, branching, and interactions. In healthy mice, the bile ducts were straight with uniform branches, but in mice with Alagille syndrome ducts were wiggly, and had extra branches in the centre of the liver.

This new imaging technique could improve the understanding of tube systems in animal models of diseases, both in the liver and in other organs with tubes, such as the lungs or the kidneys. Hankeova, Salplachta et al. also lay a foundation for a deeper understanding of bile duct recovery in Alagille syndrome. In the future, DUCT could help researchers to see how mouse bile ducts change in response to experimental therapies.

2D histological sections remain the standard practice for all types of tissues. Recent advances in tissue clearing (*Chung et al., 2013*; *Susaki et al., 2014*; *Renier et al., 2016*) carbon ink injections (*Kaneko et al., 2015*) and high-end microscopy begin to address the need for, and benefits of, whole organ analysis. Importantly, organ systems often interact with one another and almost always are connected to blood supply. In order to study tissue spatial organization in development, disease, and regeneration, a 3D analysis of multiple networks is indispensable. A lack of markers, suitable antibodies, tissue autofluorescence and/or organ size often preclude the possibility for whole organ analysis. Radiopaque resin casting is an alternative approach that enables micro computed tomography (μCT) scanning, digitalization with full rotation and the possibility for both qualitative and quantitative analyses compatible with multiple imaging softwares.

In this study, we focused on establishing a simple, robust, antibody-free and inexpensive method for whole organ visualization of lumenized structures. We built on previous work to image a single network using resin (*Masyuk et al., 2003*; *Kline et al., 2011*; *Walter et al., 2012*) and imaging with μCT. First, in order to visualize multiple structures, we tested different radiopaque substances to enhance the resin contrast, resulting in mixing of two MICROFIL resins with distinctive radiopacity. As proof of principle, we focused on studying the hepatic vascular and biliary systems of wild type and *Jagged1* Nodder (*Jag1^{Ndr/Ndr}*) (*Andersson et al., 2018*) mice, which are challenging to image by other methods due to liver size and autofluorescence (*Renier et al., 2016*). We devised *double resin-casting micro computed tomography* (DUCT) to inject, image and digitalize two systems in tandem in 3D to gain a deeper insight into the organ recovery process. The subsequent analysis is performed using a custom-written MATLAB pipeline (available and deposited in https://github.com/JakubSalplachta/DUCT; *Hankeova, 2021* copy archived at swh:1:rev:6b0b0eb88bbaf9bfc4f8ee42ca-fa4c122866fbba) as well as with ImageJ.

Alagille syndrome (ALGS) is a congenital disorder affecting multiple organs, including the hepatic and cardiovascular systems (*Spinner et al., 1993*; *Mašek and Andersson, 2017*). The disease is usually caused by mutations in the Notch ligand *JAGGED1* (*JAG1*, OMIM: ALGS1 [*Oda et al., 1997*; *Li et al., 1997*; *Gilbert et al., 2019*]) or, less frequently, in the receptor *NOTCH2* (OMIM: ALGS2 [*Spinner et al., 1993*; *McDaniell et al., 2006*]), and is chiefly characterized by intrahepatic peripheral bile duct paucity (*Alagille et al., 1975*; *Riely et al., 1979*). Importantly, bile duct development is regulated by portal vein mesenchyme (*Hofmann et al., 2010*), implying that the architectural relationship between liver cells and the vasculature affects opportunities for signaling cross-talk between these systems in liver. Some patients with ALGS spontaneously recover a biliary system (*Riely et al., 1979*; *Fujisawa et al., 1994*). Ductular reaction, aberrant biliary growth and/or trans-differentiation from hepatocytes can contribute to biliary recovery in ALGS and other cholestatic disorders (*Schaub et al., 2018*; *Fabris et al., 2007*). Furthermore, it has been reported that liver vascular architecture is affected in ALGS (previously also known as arteriohepatic dysplasia or syndromic paucity of bile ducts [*Hadchouel et al., 1978*]). It is thus clear that understanding and defining both biliary and vascular intrahepatic defects is essential for ALGS.

DUCT is a versatile, reliable tool allowing standardized architecture analysis and definition of multiple lumenized trees on a whole organ level, facilitating systems insights. We demonstrated the applicability of DUCT by revealing the distinct morphological features that allow the de novo generated $Jag1^{Ndr/Ndr}$ adult biliary system to achieve wild-type biliary volume: (1) an increase in the number of central low generation branches and (2) profound tortuosity in the liver periphery. We confirmed these 3D findings in 2D sections from $Jag1^{Ndr/Ndr}$ mice and patients with ALGS, demonstrating that the new phenotypes identified with DUCT in the mouse model are representative of patient pathology. Using DUCT we also discovered novel phenotypes such as bile duct bridging between two portal veins, which would be misinterpreted as bile duct proliferation in 2D histological sections. Hence, 2D histological sections are not sufficient to understand the structural abnormalities of tubular networks.

Results

DUCT revealed that $Jag1^{Ndr/Ndr}$ adult mice generate a full-volume biliary system

In order to define and quantify the adaptive process resulting in a de novo generated biliary system in adult $Jag1^{Ndr/Ndr}$ mice, we investigated the spatial relationship of portal venous and biliary systems in normal and diseased liver in 3D. First, we compared double carbon ink injection (*Kaneko et al., 2015*) and whole mount immunofluorescence staining combined with tissue clearing using iDISCO+ (*Renier et al., 2016*) to assess the 3D architecture of the liver (*Figure 1—figure supplement 1A and B*). Neither carbon ink injection nor iDISCO+ (due to poor labeling of vascular network) were suitable for dual 3D analysis of vascular and biliary networks. We therefore developed an alternative approach for 3D analysis: DUCT (*Figure 1A*, *Figure 1—figure supplement 1C*) followed by semi-automated segmentation generating 3D binary masks of these two systems. The binary masks were used directly for DUCT data volume analysis. For further quantification of the architectural parameters the binary masks were skeletonized and analyzed (*Figure 1B*) using a custom-written MATLAB pipeline, ImageJ, or qualitative visual assessment.

DUCT outperformed ink injection and immunofluorescence in most aspects (*Figure 1—figure supplement 1D*), from 3D analysis (not possible with ink) to analysis of lumenization (not possible with immunofluorescence). One limitation, however, is that DUCT cannot visualize lumens smaller than 5 μm. Finally, to test whether DUCT can be applied to other organ systems, we visualized lung architecture by injecting the airways (via the trachea) and the vasculature (via the pulmonary artery) and 3D reconstructed the respiratory and vascular systems (*Figure 1—figure supplement 1E*). In lungs, as in liver, the two lumenized systems can be clearly distinguished using DUCT. In all the DUCT liver experiments in this manuscript, we applied DUCT to the right medial lobe, and used the other lobes for sample-matched quality control (*Figure 1—figure supplement 2*).

Our previous work revealed that $Jag1^{Ndr/Ndr}$ bi-potential hepatoblasts did not differentiate into cholangiocytes during embryonic development. Newborn $Jag1^{Ndr/Ndr}$ mice were jaundiced and displayed intrahepatic bile duct paucity. However, by adulthood $Jag1^{Ndr/Ndr}$ livers exhibited mature
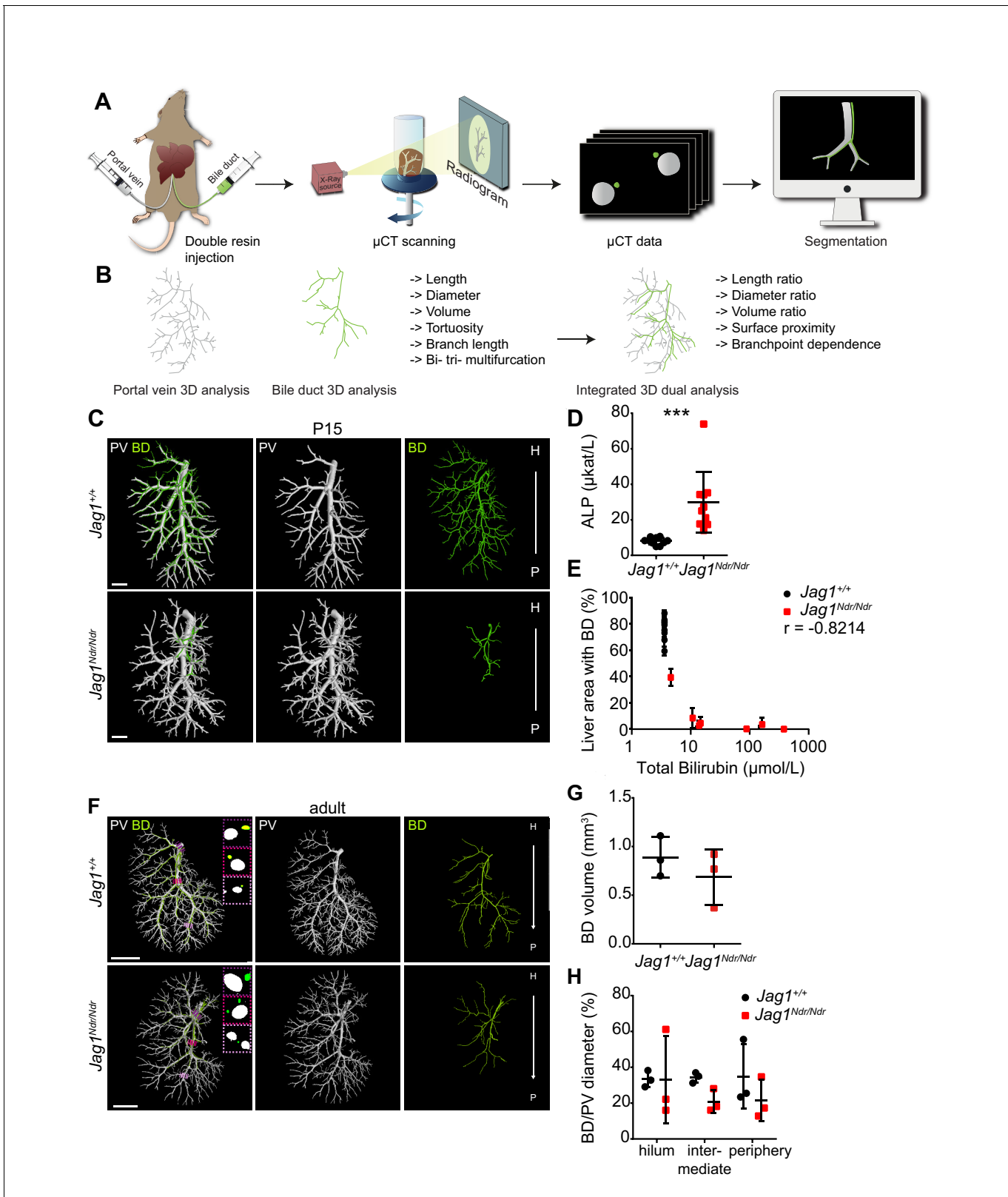
Figure 1. DUCT revealed that *Jag1[Ndr/Ndr]* bile ducts recover a full-volume biliary system. (**A**) The DUCT pipeline encompasses resin injection into two systems (portal venous and biliary), micro computed tomography (μCT) scanning of the organ, or individual lobes, and segmentation of μCT data (tomographs) into 3D binary masks. (**B**) The image analysis pipeline creates 3D skeletons from the binary masks, to quantify architectural parameters in individual or combined systems. (**C**) 3D rendering of BD and PV structures using DUCT in postnatal day 15 (P15) *Jag1^{+/+}* (top panel) and *Jag1[Ndr/Ndr]*

Figure 1 continued on next page

Figure 1 continued

livers (bottom panel). Scale bar = 1 mm. (**D**) Alkaline phosphatase (ALP) serum levels at P15. Each dot represents one animal; lines show mean value ± standard deviation. Statistical test – unpaired *t*-test, p=0.0008. (**E**) Correlation analysis between total bilirubin levels and liver area with resin-injected BD. Each dot represents one animal; lines show mean value ± standard deviation (measured in right medial and left lateral lobe). Statistical test – non-parametric Spearman correlation, p=0.0341, r = −0.8214. (**F**) 3D rendering of BD and PV structures using DUCT in adult (4.5–6.5 months old) *Jag1+/+* (top panel) and adult de novo generated *Jag1Ndr/Ndr* livers (bottom panel). Boxed regions highlight 2D sections of hilar, intermediate and peripheral regions identified with dotted lines in matched colors. Scale bar = 4 mm. (**G**) BD system volume is similar in adult *Jag1+/+* and *Jag1Ndr/Ndr* mice. Each dot represents one animal; lines show mean value ± standard deviation, unpaired *t*-test, p=0.3730 (**H**) BD/PV diameter ratio in *Jag1+/+* and *Jag1Ndr/Ndr* mice in hilar, intermediate and peripheral regions. Each dot represents one animal; lines show mean value ± standard deviation. Two-way ANOVA, p=0.2496. 3D, three dimensional; ALP, alkaline phosphatase; BD, bile duct; DUCT, double resin casting micro computed tomography; H, hilar; P, peripheral. PV, portal vein.

The online version of this article includes the following source data and figure supplement(s) for figure 1:

Figure supplement 1. DUCT outperforms other state of the art techniques to visualize mouse liver in 3D.

Figure supplement 2. Resin injection quality control of the left lateral lobe.

Figure supplement 3. Liver cast of P15 *Jag1+/+* showing bile duct (green) and portal vein (white) together (top panel) or separately (bottom panels).

Figure supplement 3—source data 1. 3D interactive liver cast shown in *Figure 1—figure supplement 3*.

Figure supplement 4. Liver cast of P15 *Jag1Ndr/Ndr* showing bile duct (green) and portal vein (white) together (top panel) or separately (bottom panels).

Figure supplement 4—source data 1. 3D interactive liver cast shown in *Figure 1—figure supplement 4* .

Figure supplement 5. *Jag1Ndr/Ndr* bile ducts displayed heterogeneous de novo growth.

Figure supplement 6. Liver cast of adult *Jag1+/+* showing bile duct (green) and portal vein (white) together (top panel) or separately (bottom panels).

Figure supplement 6—source data 1. 3D interactive liver cast shown in *Figure 1—figure supplement 6*.

Figure supplement 7. Liver cast of adult *Jag1+/+* showing bile duct (green) and portal vein (white) together (top panel) or separately (bottom panels).

Figure supplement 7—source data 1. 3D interactive liver cast shown in *Figure 1—figure supplement 7*.

Figure supplement 8. Liver cast of adult *Jag1+/+* showing bile duct (green) and portal vein (white) together (top panel) or separately (bottom panels).

Figure supplement 8—source data 1. 3D interactive liver cast shown in *Figure 1—figure supplement 8*.

Figure supplement 9. Liver cast of adult *Jag1Ndr/Ndr* showing bile duct (green) and portal vein (white) together (top panel) or separately (bottom panels).

Figure supplement 9—source data 1. 3D interactive liver cast shown in *Figure 1—figure supplement 9*.

Figure supplement 10. Liver cast of adult *Jag1Ndr/Ndr* showing bile duct (green) and portal vein (white) together (top panel) or separately (bottom panels).

Figure supplement 10—source data 1. 3D interactive liver cast shown in *Figure 1—figure supplement 10*.

Figure supplement 11. Liver cast of adult *Jag1Ndr/Ndr* showing bile duct (green) and portal vein (white) together (top panel) or separately (bottom panels).

Figure supplement 11—source data 1. 3D interactive liver cast shown in *Figure 1—figure supplement 11*.

Figure supplement 12. Overview of 3D reconstructed bile duct and portal vein systems, their branching skeletons and volume.

bile ducts, but with abnormal apical polarity (*Andersson et al., 2018*). Using DUCT, we first investigated to what degree *Jag1Ndr/Ndr* mice can grow a biliary tree by postnatal day 15 (P15). We examined the biliary system in 7 *Jag1Ndr/Ndr* P15 pups and discovered a rudimentary or absent biliary tree in *Jag1Ndr/Ndr* pups, while there was a fully developed biliary tree in *Jag1+/+* mice (*Figure 1C*). The 3D reconstruction of both systems can be explored in separate channels or in tandem with rotation (interactive PDFs, *Figure 1—figure supplements 3* and *4*). We noted high variability in biliary outgrowth between the right medial lobe (RML) and the left lateral lobe (LLL) in *Jag1Ndr/Ndr* livers (illustration of liver lobes *Figure 1—figure supplement 5A*). In the RML of five *Jag1Ndr/Ndr* pups, the biliary tree covered >5% of liver area, whereas in LLL only 1 *Jag1Ndr/Ndr* pup displayed >5% biliary tree coverage, while four *Jag1Ndr/Ndr* pups had no lumenized bile ducts. In *Jag1+/+* pups the biliary network covered on average 75% of the liver area in both RML and LLL (*Figure 1—figure supplement 5B and C*). The P15 *Jag1Ndr/Ndr* pups were cholestatic, and manifested increased levels of alkaline phosphatase (ALP) (*Figure 1D*), aspartate aminotransferase (AST), alanine aminotransferase (ALT) and decreased levels of albumin (*Figure 1—figure supplement 5D*). Interestingly, two different groups were noted in *Jag1Ndr/Ndr* pups with regard to the total bilirubin levels, that is, 50% of the animals had highly increased and 50% had mildly increased total bilirubin (p=0.0079), while all *Jag1+/+* mice displayed bilirubin levels below detection limits (*Figure 1—figure supplement 5D*). We correlated the total bilirubin amount with the liver area covered by lumenized bile ducts and detected a strong negative correlation between these two factors (*Figure 1E*, r = −0.8214). We further sectioned the resin injected P15 liver and stained for the early biliary marker SOX9 (SRY-Box

transcription factor 9) (note remaining resin in some portal veins). In *Jag1^{+/+}* central liver, lumenized bile ducts were clearly detected, whereas in all four *Jag1^{Ndr/Ndr}* central livers no lumenized bile ducts were visible and the number of SOX9 positive cells varied between animals, poorly reflecting the total bilirubin levels (*Figure 1—figure supplement 5E*).

Next, we aimed to characterize and quantify the biliary architecture of the *Jag1^{Ndr/Ndr}* de novo generated biliary system in adult mice (*Figure 1F*). The 3D reconstruction of both systems can be explored in separate channels or in tandem (interactive PDFs, *Figure 1—figure supplement 6–11*). While *Jag1^{+/+}* mice demonstrated a stereotyped vascular and biliary architecture (*Figure 1—figure supplement 12A, B and C*), *Jag1^{Ndr/Ndr}* livers exhibited greater architectural variability (*Figure 1—figure supplement 12D, E and F*). To quantify the degree of de novo biliary formation, we extracted the volume (using the binary masks) and diameters of the portal venous and biliary systems (using the binary masks and skeletons). The total volume of the vascular and biliary trees was similar in *Jag1^{Ndr/Ndr}* and *Jag1^{+/+}* mice (*Figure 1G*, *Figure 1—figure supplement 12H*). There was a tendency toward a larger portal venous volume and smaller biliary volume in *Jag1^{Ndr/Ndr}* mice, resulting in a trend toward a reduced BD:PV (bile duct, portal vein) volume ratio in *Jag1^{Ndr/Ndr}* mice (*Figure 1—figure supplement 12H*, p=0.0594). Next, we investigated portal vein and bile duct diameters along the main branch. There was a tendency to an increase in the *Jag1^{Ndr/Ndr}* portal vein diameter and a decrease in biliary diameter as a function of distance compared with *Jag1^{+/+}* mice (*Figure 1—figure supplement 12I*). However, there was high variability in venous and bile duct diameter in the *Jag1^{Ndr/Ndr}* hilar region. In *Jag1^{+/+}* liver, the BD:PV diameter ratio was consistently 1:3 in hilar and intermediate regions (*Figure 1H*). This BD:PV diameter ratio was not preserved in the *Jag1^{Ndr/Ndr}* livers (*Figure 1H*).

DUCT enabled 3D visualization of postnatal and adult biliary and vascular trees. The biliary network in *Jag1^{Ndr/Ndr}* mice appeared postnatally, but with high heterogeneity between liver lobes and animals. Moreover, the liver area with lumenized bile ducts correlated with total bilirubin levels and disease severity at P15. The adult segmented µCT data were analyzed for volume and inner diameter of two injected systems. Comparisons of the portal vein and bile duct diameters demonstrated a conserved portal vein – bile duct architectural relationship with a stereotype BD:PV 1:3 diameter ratio in *Jag1^{+/+}* liver. The adult *Jag1^{Ndr/Ndr}* mice displayed a heterogeneous phenotype that nevertheless resulted in full restoration of biliary function (*Andersson et al., 2018*) via recovery of a wild-type biliary volume.

Alagille syndrome human and murine bile ducts end abruptly

The intrahepatic biliary tree forms by a tubulogenic process in which a heterogeneous, hierarchical fine mesh of connected cholangiocytes is refined to single larger conduits of bile ducts, resembling a branching tree (*Ober and Lemaigre, 2018*; *Tanimizu et al., 2016*). In *Jag1^{+/+}* liver, the qualitative analysis of network connectivity revealed that the biliary system formed a continuous tree, branching outwards toward the periphery as expected (*Figures 1C, F* and *2A* left panel). In contrast, the *Jag1^{Ndr/Ndr}* biliary system displayed some branches oriented from peripheral to hilar, with abrupt endings (*Figure 2A* right panels, blue arrowheads, on average one abruptly ending BD per lobe). We confirmed the abruptly ending bile ducts in *Jag1^{Ndr/Ndr}* livers in serial liver sections (*Figure 2B*, bottom panels). The black arrowhead labels a well-formed bile duct, that ended bluntly in the following section (+5 µm, blue arrowhead), and disappeared completely in the next section (+10 µm).

To determine whether the *Jag1^{Ndr/Ndr}* biliary abnormalities were representative of pathology in patients with Alagille syndrome, we evaluated liver serial sections from whole liver explants (patients with severe Alagille syndrome (S-ALGS) that underwent transplantation) and biopsies obtained for clinical reasons in non-transplanted patients (patients with mild Alagille syndrome (M-ALGS)).The liver function tests for individual patients are reported in *Table 1* and representative liver sections are presented in *Figure 2—figure supplement 1*. One patient (M_ALGS-5) had been biopsied at multiple time points revealing paucity of bile duct at 2.5 months, a regenerating phase with hepatocytes expressing CK7 at 1.3 years and bile duct recovery at 4.7 years (*Figure 2—figure supplement 1D*).

We evaluated liver sections from patients with severe (top panel) and mild (bottom panel) Alagille syndrome for the presence of abruptly terminating bile ducts. A black arrowhead labels a well-formed bile duct that terminated in the subsequent section (+5 µm, blue arrowhead), (*Figure 2C*). In conclusion, DUCT facilitated qualitative assessments of the tubular networks, including connectivity
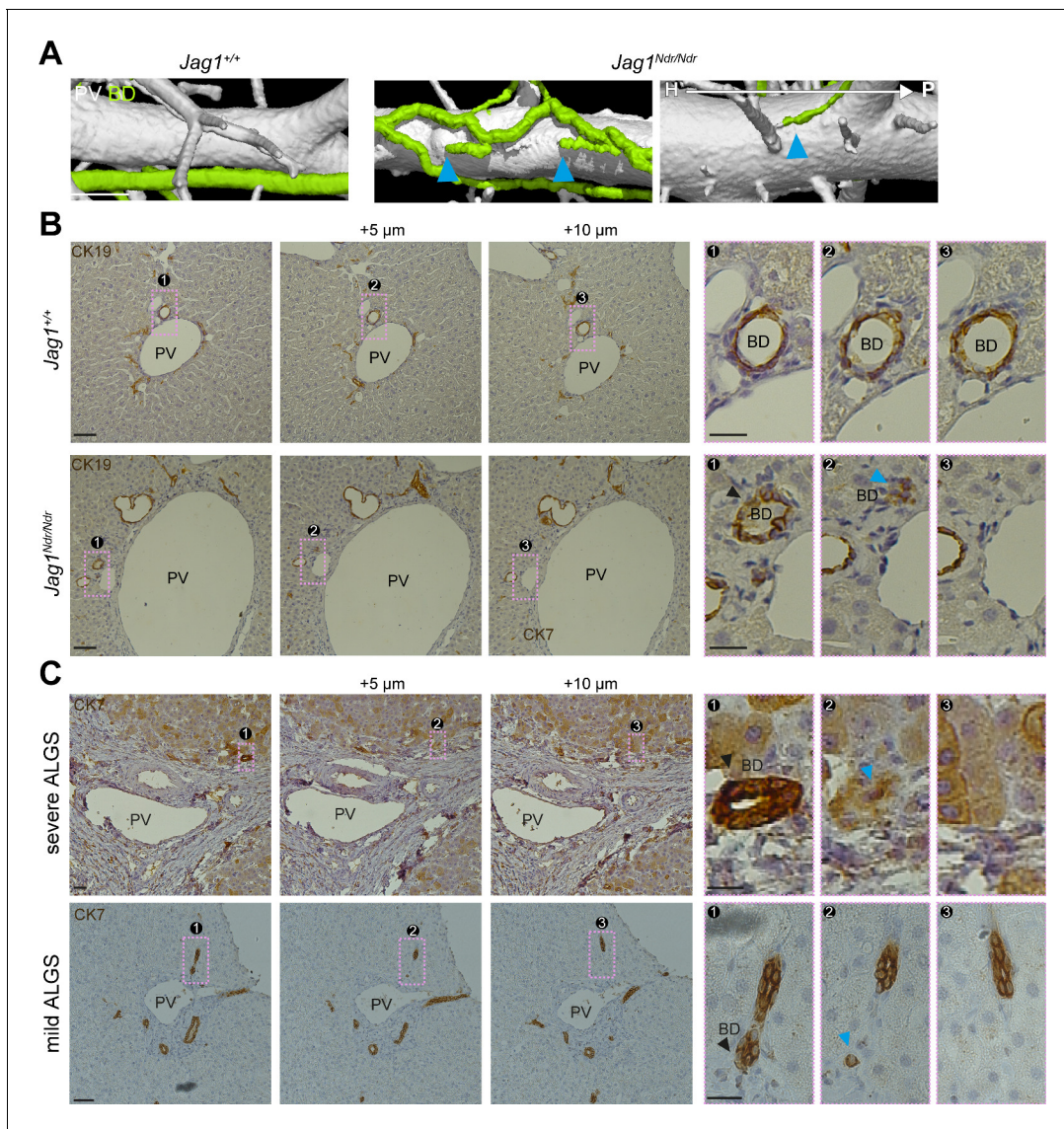
Figure 2. Alagille syndrome human and murine bile ducts end abruptly. (**A**) *Jag1^Ndr/Ndr* BDs (right panel) terminated randomly and facing toward the hilum (blue arrowheads). (**B**) 2D histological consecutive liver sections confirmed abruptly terminating BDs in *Jag1^Ndr/Ndr* liver. Black arrowhead depicts lumenized well-formed BD that ended in the following sections (blue arrowhead). (**C**) BDs in patients with severe ALGS (top panel) or mild ALGS (bottom panel) terminate abruptly (blue arrowhead) in consecutive liver histological sections. Scale bars (**A**) 500 μm, (**B** left panels), (**C**) 50 μm, (**B** boxed region) 20 μm. ALGS, Alagille syndrome; BD, bile duct; CK, cytokeratin; H, hilar; P, peripheral. PV, portal vein.

The online version of this article includes the following figure supplement(s) for figure 2:

Figure supplement 1. Overview of liver samples from patients with Alagille syndrome stained for CK7.

and perfusion. Both the *Jag1^Ndr/Ndr* and Alagille syndrome biliary systems displayed abruptly ending bile ducts, which may affect bile flow and shear stress.

Alagille syndrome human and murine de novo generated bile ducts are further from portal veins

During embryonic development, cholangiocytes differentiate from hepatoblasts that are in contact with portal vein mesenchyme expressing *Jag1* (*Ober and Lemaigre, 2018*). Whether postnatally de novo generated bile ducts arise adjacent to the portal vein, or whether they are less dependent on portal vein proximity has not yet been explored. We therefore analyzed the distance between the biliary and portal venous systems by calculating the surface distances using the MATLAB pipeline.

Table 1. Liver function test overview for patients with Alagille syndrome.
M-ALGS stands for patients with mild Alagille syndrome. S-ALGS stands for patients with severe Alagille syndrome.

ID	Age (years)	ALT (μkat/L)	AST (μkat/L)	ALP (μkat/L)	GT (μkat/L)	Bil Tot (μmol/L)	BilD (μmol/L)	Bile acids (μmol/L)	Sample
Reference value		<0.76	<1	<7.6	<0.76	<22	<4	<10	
S-ALGS_1	1.2	3.29	2.87	23.4	21.8	308	272	665	Explant
S-ALGS_2	1.5	3.09	-	10.8	13.5	274	246	473	Explant
S-ALGS_3	4	4.41	-	9.9	7.5	238	215	246	Explant
S-ALGS_4	6	3.9	-	9.4	8.1	220	193	244	Explant
M-ALGS_1	0.6	1.09	-	4.6	1.2	7	2	-	Biopsy
M-ALGS_2	1.4	0.78	0.96	6.6	1.2	3	<2	33	Biopsy
M-ALGS_3	2.5	1.46	1.44	13.6	7.4	10	6	106	Biopsy
M-ALGS_4	3.4	0.68	0.92	5.2	1.5	14	4	31	Biopsy
M-ALGS_5_1	0.2	1.44	1.77	-	-	46	39	175	Biopsy
M-ALGS_5_2	1.2	1.59	1.8	-	-	3	2	-	Biopsy
M-ALGS_5_3	4.7	0.79	0.93	3.5	0.52	9	<2	2	Biopsy
M-ALGS_6	6.4	1.18	1.44	6.4	3	6	<2	1	Biopsy

Specifically, the surface distance was defined as the shortest length from biliary skeleton to the portal venous skeleton, minus radiuses of these systems at the defined points (*Figure 3A*). $Jag1^{+/+}$ bile ducts maintained a uniform distance to adjacent portal veins throughout the liver (*Figure 3B* top panel, asterisk, 3C, 3D 100% of BDs within 0.5 mm of a PV). In contrast, $Jag1^{Ndr/Ndr}$ bile ducts did not maintain a uniform distance to the nearest portal vein (*Figure 3B* bottom panel, double arrow, 3C, 3D 1.5% of BD are placed 0.5–1.26 mm away from a PV) and sometimes traversed the parenchyma to join another portal vein branch (*Figure 3B* bottom right panel, *Figure 1—figure supplement 2* empty arrowheads). Both the increased BD-PV distance and parenchymal bile ducts were validated in histological sections, in which $Jag1^{+/+}$ bile ducts were in close proximity to, or embedded in portal vein mesenchyme (*Figure 3E* left panel, asterisk). In contrast, $Jag1^{Ndr/Ndr}$ bile ducts were confirmed to be present outside of the portal vein mesenchyme area (*Figure 3E* middle panel, double arrow) or even in the liver parenchyma close to the edge of the liver (*Figure 3E* right panel). This phenotype, visualized in 2D sections, could resemble biliary proliferation, or ductular reaction, rather than a bridging structure, highlighting the importance of 3D imaging. Parenchymal bile ducts were also detected in liver samples from patients with severe and mild Alagille syndrome (*Figure 3F*) but not in control human liver. In sum, DUCT pipeline together with the MATLAB algorithm, measured the gap between surfaces of two resin injected systems to address the spatial relationship between them. Our data showing biliary cells in the parenchyma and bile ducts far from portal veins in $Jag1^{Ndr/Ndr}$ liver and liver from patients with Alagille syndrome thus suggest that postnatal bile duct formation does not rely on close proximity to portal vein mesenchyme and may occur independent of signals from portal vein mesenchyme.

Alagille syndrome human and murine de novo generated bile ducts display branching independent of portal vein branching

Portal vascular and biliary systems are ductal tree-like structures with numerous branches, which function to maximize the area of exchange between the tissue and its lumen. We evaluated portal venous and biliary branching using the DUCT pipeline and the MATLAB script to quantify the total number of vascular or biliary branch points. Branch points were identified using the 3D skeletons of each system, and categorized based on the number of incoming/outgoing branches (classifying as bifurcations, trifurcations, or nodes with more than three branches) (*Figure 1—figure supplement 12D and G*). We did not identify any differences in the absolute numbers of branch points in $Jag1^{+/+}$ and $Jag1^{Ndr/Ndr}$ systems, again suggesting that de novo biliary growth generally reconstituted a full-volume, well-branched biliary tree (*Figure 4—figure supplement 1*).
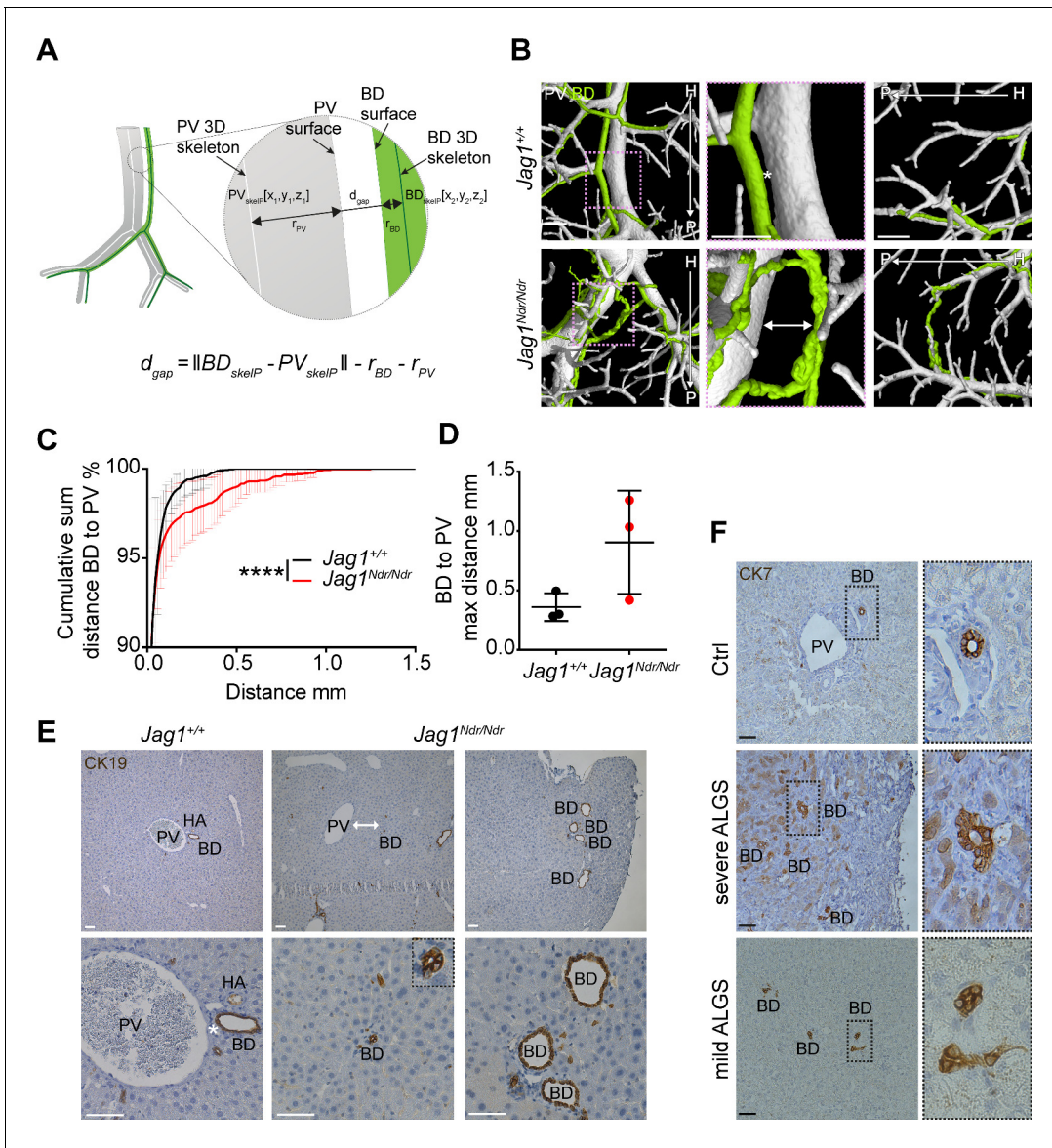
Figure 3. Alagille syndrome human and murine de novo generated bile ducts are further from portal veins. (A) Scheme of BD to PV surface distance analysis. PV_{skelP} = single point on PV skeleton, BD_{skelP} = single point on BD skeleton, r_{PV} = radius of PV at PV_{skelP} (i.e. minimal distance from PV_{skelP} to PV surface), r_{BD} = radius of BD at BD_{skelP} (i.e. minimal distance from BD_{skelP} to BD surface), d_{gap} = gap distance, which is derived by subtracting the radii from the skeleton to skeleton distance. (B) 3D rendering shows homogenous distance between a BD and PV in $Jag1^{+/+}$ livers (asterisk), but a large heterogeneous distance in $Jag1^{Ndr/Ndr}$ liver (double-headed arrow). Right panel shows a parenchymal bile duct traversing between two PVs at the $Jag1^{Ndr/Ndr}$ liver edge. Scale bar 500 µm. (C) Cumulative sum of percentage of BDs at a given distance from the nearest PV. 3 $Jag1^{+/+}$ and 3 $Jag1^{Ndr/Ndr}$ mice were used. Bars represent mean ± standard deviation, Kolmogorov - Smirnov test (on raw data), p<0.0001, (****). For individual data points see *Figure 3—source data 1*. (D) Maximum distance between BD and PV. Each dot represents one animal, bars are mean ± standard deviation, unpaired *t*-test, p=0.1041, not significant. (E) BD – PV distances confirmed in 2D histological sections. Overview in top panel and magnification in bottom panel. $Jag1^{Ndr/Ndr}$ PVs can be present in the parenchyma far from (middle panels), or independent of (right panels), the nearest PV. Scale bars 50 µm. (F) Healthy human liver with BD close to PV (top panel). Parenchymal CK7+ BDs in histological liver sections from a patient with severe ALGS (middle panel) and distant BDs in a patient with mild ALGS (bottom panel). Magnification shows lumenization of BDs. Scale bar 50 µm. ALGS, Alagille syndrome, BD, bile duct; CK, cytokeratin; H, hilar; HA, hepatic artery; P, peripheral; PV, portal vein.

The online version of this article includes the following source data for figure 3:

Source data 1. Raw data measuring the distance from the surface of bile duct to a portal vein surface.

During embryonic development, the biliary system is established alongside the portal venous system. This is reflected in the final architecture of the system, with bile ducts in close proximity to portal veins (*Figure 3*). A prediction based on this embryonic process and BD/PV dependency is therefore that bile ducts should invariably branch where portal veins branch. We extracted the coordinates for branch points in the biliary and portal venous systems from the corresponding 3D skeletonized data and calculated 3D Euclidean distances between biliary branch points and their nearest neighboring portal vein branch point (*Figure 4A*). Indeed, $Jag1^{+/+}$ bile ducts (*Figure 4B* left panel, blue arrowhead) branched adjacent to portal vein branch points (magenta arrowhead, defined as within 0.5 mm). In contrast, $Jag1^{Ndr/Ndr}$ bile ducts (*Figure 4B* middle panel, blue arrowhead) branched further from portal vein branch points (magenta arrowhead), or independent of portal vein branch points (blue arrow in *Figure 4B*, and data in 4C; independence defined as distance >0.54 mm). On average, 1.3% of $Jag1^{+/+}$ bile ducts branch points and 8.6% of $Jag1^{Ndr/Ndr}$ bile duct branch points were further than 0.5 mm from the nearest portal vein branch point (*Figure 4C*). We analyzed consecutive histological liver sections to confirm branching morphology defects discovered using DUCT. $Jag1^{+/+}$ bile ducts (*Figure 4D* top panel, blue arrowhead) indeed branched at the same point as portal veins branch (magenta arrowhead). In contrast, in $Jag1^{Ndr/Ndr}$ liver bile ducts might bifurcate in the absence of portal vein branching (*Figure 4D* bottom panel, blue arrow).

We next asked whether similar branching phenotypes were present in healthy human liver or in patients with mild or severe Alagille syndrome. In normal human liver, biliary branching occurred close to portal vein bifurcation (*Figure 4E* top panel, blue arrowheads, PV branching within 25 µm in this example, branching not shown). In patients with severe Alagille syndrome, biliary branching could be seen independent of portal vein branching (*Figure 4E* middle panel, blue arrows), the nearest portal vein branch point for this bile duct was 13 sections hilar (circa 65 µm earlier). We also detected independent bile duct branching in patients with mild Alagille syndrome (*Figure 4E* bottom panel, blue arrows). In conclusion, DUCT revealed dual system 3D architectural phenotypes: (1) similar numbers of branch points in $Jag1^{+/+}$ and $Jag1^{Ndr/Ndr}$ livers but (2) a greater distance between portal vein and bile duct branch points in $Jag1^{Ndr/Ndr}$ livers. Bile ducts in patients with Alagille syndrome displayed similar branching abnormalities, corroborating the architectural independence from portal vein patterning.

Strahler analysis of resin casts reveal excess central branching in the $Jag1^{Ndr/Ndr}$ de novo generated biliary system

Whether de novo bile duct formation occurs evenly throughout the liver or is more extensive in certain regions has not yet been quantitatively defined. One of the mechanisms by which the biliary system can regenerate is via abundant branching of the network (*Vartak et al., 2016*; *Masyuk et al., 2001*). We therefore employed the DUCT pipeline and ImageJ to perform a Strahler analysis (3D branching analysis based on generation number from the origin, see Material and methods section 'Branching analysis' for details on generation number calculation) to address the branch length, number and distribution in specific liver areas. In order to define anatomy correctly for differently sized livers, the liver lobe data were separated into three equivalent regions using portal vein branch generation number and lengths as a proxy for hilum/intermediate/periphery. These regions were denoted region 1 (R1 enriched for hilar region), 2 (R2, intermediate), and 3 (R3, peripheral-enriched) (*Figure 5A*). The average branch length of the portal vein was shorter in $Jag1^{Ndr/Ndr}$ livers, resulting in significantly smaller portal vein region sizes (*Figure 5B* middle panel), reflecting the overall smaller size of the mice and livers. Using the regions defined by the portal venous system, biliary region size was similar in the 1 st and 2nd region of wild type and $Jag1^{Ndr/Ndr}$ mice, while region three was smaller in both animal groups due to resin not penetrating ducts < 5 µm (*Figure 5B* right panel, *Figure 5—figure supplement 1*). Two out of three $Jag1^{Ndr/Ndr}$ mice had a marked reduction in biliary region size in R3, while one had an increase, reflecting the somewhat variable phenotype manifested by both the patients and the mouse model.

Branching trees in biological systems have a stereotype structure in which branch lengths shorten with each branching generation from start (R1) to end (periphery, R3) (*Masyuk et al., 2001*; *Hannezo et al., 2017*). We analyzed the portal vein and biliary branch lengths within each region and found that portal vein segments shortened as expected with each generation in both $Jag1^{+/+}$ and $Jag1^{Ndr/Ndr}$ livers (*Figure 5C* middle panel). $Jag1^{+/+}$ bile ducts followed the same stereotype branching principle, but $Jag1^{Ndr/Ndr}$ bile ducts branch lengths were significantly shorter in regions 1
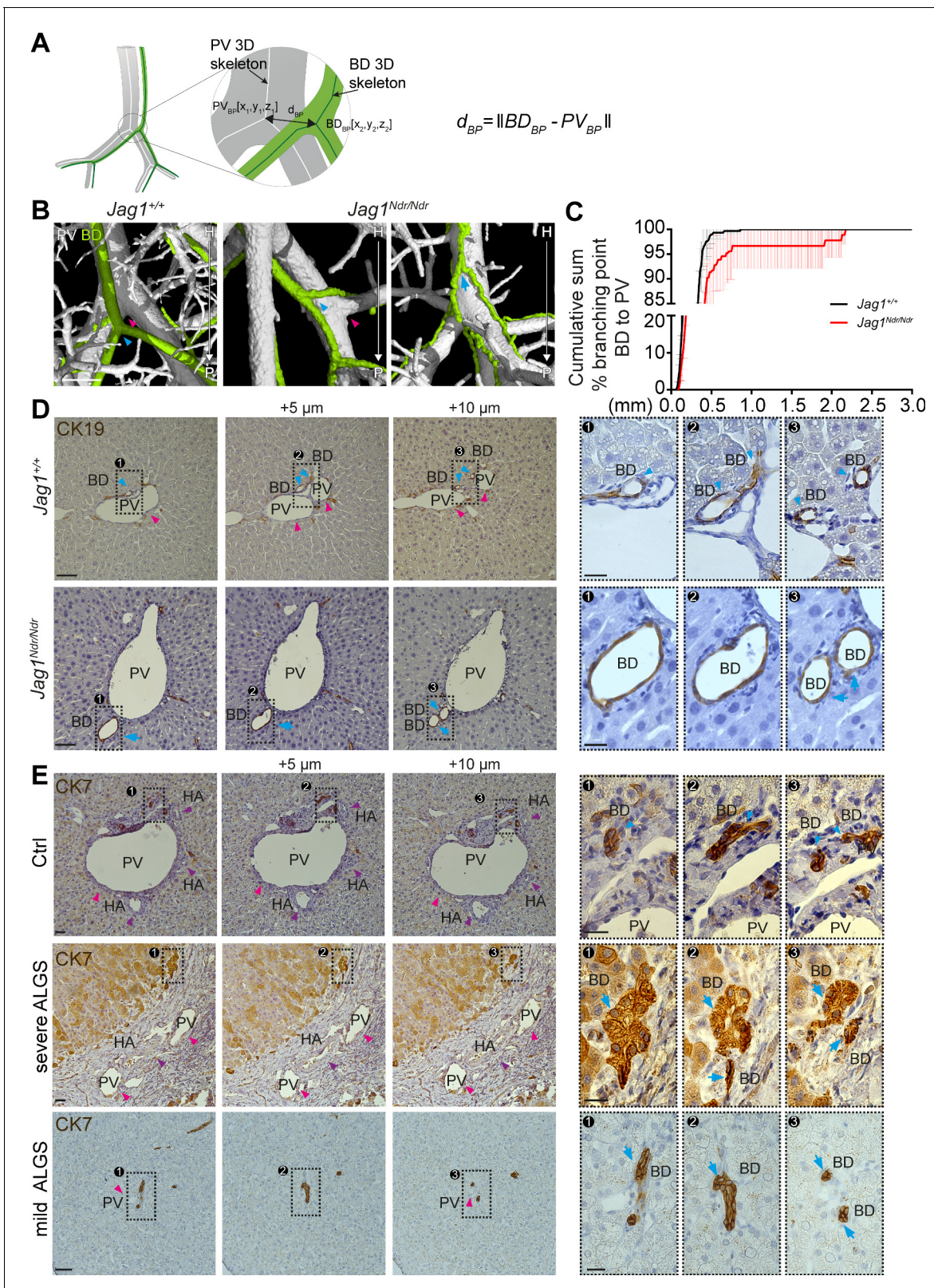
Figure 4. Alagille syndrome human and murine de novo generated bile ducts display branching independent of portal vein branching. (A) Scheme representing BD to PV branch point analysis. PV_{BD} = PV branch point, BD_{BD} = BD branch point, d_{BP} = Euclidean 3D distance between branch points. (B) Branching pattern in $Jag1^{+/+}$ (left panel) and $Jag1^{Ndr/Ndr}$ liver (middle and right panel). PV branch points (pink arrowheads) were near BD branch points (blue arrowheads) in wild type mice, but further away in $Jag1^{Ndr/Ndr}$ mice. BD branch points in $Jag1^{Ndr/Ndr}$ mice also occurred in the absence of

Figure 4 continued on next page

Figure 4 continued

PV branching (blue arrow). Scale bar 500 µm. (C) Cumulative sum of BD branching point percentage at a given distance to the nearest PV branching point. 3 *Jag1*$^{+/+}$ and 3 *Jag1*$^{Ndr/Ndr}$ mice were used. 100% of *Jag1*$^{+/+}$ bile duct branchpoints were within 1 mm of a PV branchpoint, but only 95% of *Jag1*$^{Ndr/Ndr}$ branchpoints were within 1 mm. Bars represent mean ± standard deviation, Kolmogorov-Smirnov test (on raw data, p=0.9985, not significant). For individual data points see *Figure 4—source data 1* (D) Branching analysis in 2D histological consecutive *Jag1*$^{+/+}$ and *Jag1*$^{Ndr/Ndr}$ liver sections. PV branching (pink arrowheads) was present near BD branching (blue arrowheads) in wild type mice (top panels). In *Jag1*$^{Ndr/Ndr}$ mice, BDs branched ectopically in the absence of PV branching (bottom panel). Boxed regions magnified in panels at right. Scale bar 50 µm, boxed region 20 µm. (E) Branching pattern in consecutive human liver histological sections shows BD branching in association with PV (pink arrowhead) branching in controls (top panel), but BD branching in the absence of PV branching in patients with severe ALGS (middle panel) and patients with mild ALGS (bottom panel). Scale bar 50 µm, boxed region 20 µm. ALGS, Alagille syndrome; BD, bile duct; CK, cytokeratin; HA, hepatic artery; H, hilar; P, peripheral; PV, portal vein.

The online version of this article includes the following source data and figure supplement(s) for figure 4:

Source data 1. Raw data measuring the distance from the bile duct branching point to a portal vein branching point.

Figure supplement 1. De novo grown bile ducts did not show significant differences in the numbers of bifurcations, trifurcations or nodes > 3 branches when normalized to system size.

and 2, and uniform across the hierarchy of branches (*Figure 5C* right panel). We further analyzed the distribution of number of branches in the three regions and discovered that, on average, 9% of *Jag1*$^{+/+}$ portal vein branches fell into R1, 66% into R2% and 25% into R3, with a similar distribution in *Jag1*$^{Ndr/Ndr}$ livers (*Figure 5D* middle panel). Based on biological tree structure, we would expect fewest biliary branches in R1, an intermediate number in R2, and most branches in R3. However, resin penetration and lumen diameter precluded filling of all terminal portal vein branches in R3. Mirroring the wild type portal venous branch distribution, *Jag1*$^{+/+}$ biliary branch distribution was, on average, 16% in R1, 66% in R2% and 18% in R3. *Jag1*$^{Ndr/Ndr}$ biliary branch distribution was shifted, with 44% in R1, 44% in R2% and 12% in R3 (*Figure 5D* right panel). The distribution of biliary branches number was highly heterogeneous among the different *Jag1*$^{Ndr/Ndr}$ mice. DUCT pipeline is compatible with multiple image analysis software programs. Here, we used ImageJ to address the branching length over branching generations, and our data collectively indicated that low-generation number biliary segments were shorter and more numerous than expected, suggesting that ectopic regenerative branching and/or incorporation of de novo generated biliary cells, occurs in region 1. However, peripheral branching, which may be undetectable if biliary diameters are under 5 µm, cannot be excluded.

Alagille syndrome human and murine de novo generated bile ducts are tortuous

The biliary system can adapt to excessive amounts of bile by increasing its diameter or length (*Vartak et al., 2016*; *Slott et al., 1990*). One means of enlarging length is by duct convolution. We therefore investigated the length and tortuosity of the biliary and portal vascular trees using the DUCT pipeline in combination with the MATLAB algorithm (whole system and main branch quantification) and ImageJ (R1, R2 and R3 analysis). 3D reconstruction of portal vein vasculature and the biliary network revealed straight *Jag1*$^{+/+}$ bile ducts (*Figure 6A* top panel), whereas *Jag1*$^{Ndr/Ndr}$ bile ducts were tortuous (*Figure 6A* bottom panel), especially in the liver periphery. We confirmed in histological liver sections that the *Jag1*$^{Ndr/Ndr}$ BDs were tortuous (*Figure 6B*). We further assessed biliary tortuosity in patients with mild Alagille syndrome and found several tortuous bile ducts (*Figure 6C*); however, we did not detect any tortuous bile ducts in patients with severe Alagille syndrome (data not shown). In order to quantify tortuosity, we calculated the actual (curved) length and theoretical (chord) length (scheme *Figure 6D*). The curved and chord lengths of the entire system, and the main branch alone did not differ for portal venous or biliary systems in *Jag1*$^{+/+}$ and *Jag1*$^{Ndr/Ndr}$ mice (*Figure 6—figure supplement 1A–G*). The BD:PV ratio was not significantly different for curved (*Figure 6—figure supplement 1H*) or chord length (*Figure 6—figure supplement 1I*). However, there was a 6% increase in overall portal venous tortuosity in *Jag1*$^{Ndr/Ndr}$ mice when the entire system was taken into account (*Figure 6E*) and biliary tortuosity was increased by 50%. Biliary tortuosity was greatest in the *Jag1*$^{Ndr/Ndr}$ liver periphery, with a 140% increase in R3 (*Figure 6E*). The tortuosity of the main portal vein or main bile ducts branch analyzed alone was not significantly different (*Figure 6—figure supplement 1J and K*), highlighting the importance of analyzing the
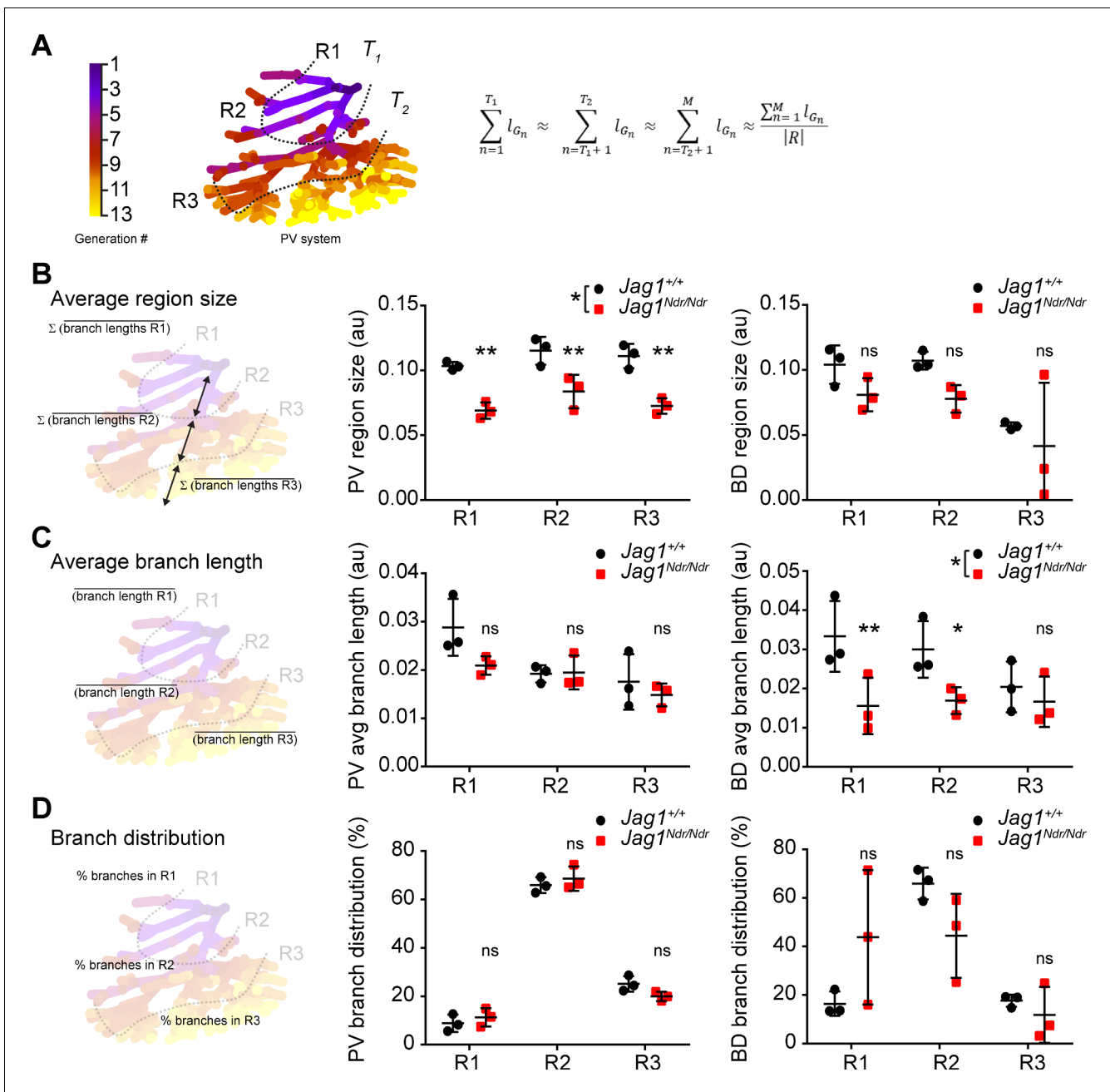
Figure 5. Strahler analysis of resin casts reveal excess central branching in the *Jag1^{Ndr/Ndr}* de novo generated biliary system. (**A**) 3D branching analysis based on Strahler number. The branching generations were divided into three equal regions: R1, R2 and R3 based on portal vein average branch length and generation number. Formula: R = {R1, R2, R3}; n ∈ [1, M] ⊂ ℕ; T₁, T₂⊂ n; R, region; G, branch generation; M, maximal branch generation number; l_Gn, average branch length of nth generation; T₁, T₂, borders between regions (specific generation number). (**B**) Schematic representation of region size calculation, deriving the sum of the average branch lengths within a given region (left). Liver region size for PV (middle panel) and BD (right panel). (**C**) Schematic representation of average branch length calculation within a region (left panel). Average branch length analysis for PV (middle panel) and BD (right panel) system. (**D**) Schematic representation of branch distribution, deriving the percentage of branches belonging to each region (left panel). Percentage of branches in each liver region in PV (middle panel) and BD (right panel) systems. Each dot represents one animal, bars represent mean ± standard deviation. Two-way ANOVA, (**B**) middle panel p = 0.0289, right panel p = 0.2029; (**C**) middle panel p = 0.1177, right panel p = 0.0367; (**D**) middle panel p = 0.4226, right panel p = 0.8845; followed by Sidak's multiple comparisons test, p < 0.05 (*), p < 0.01 (**), ns not significant. au, arbitrary units; BD, bile duct; PV, portal vein.

The online version of this article includes the following figure supplement(s) for figure 5:

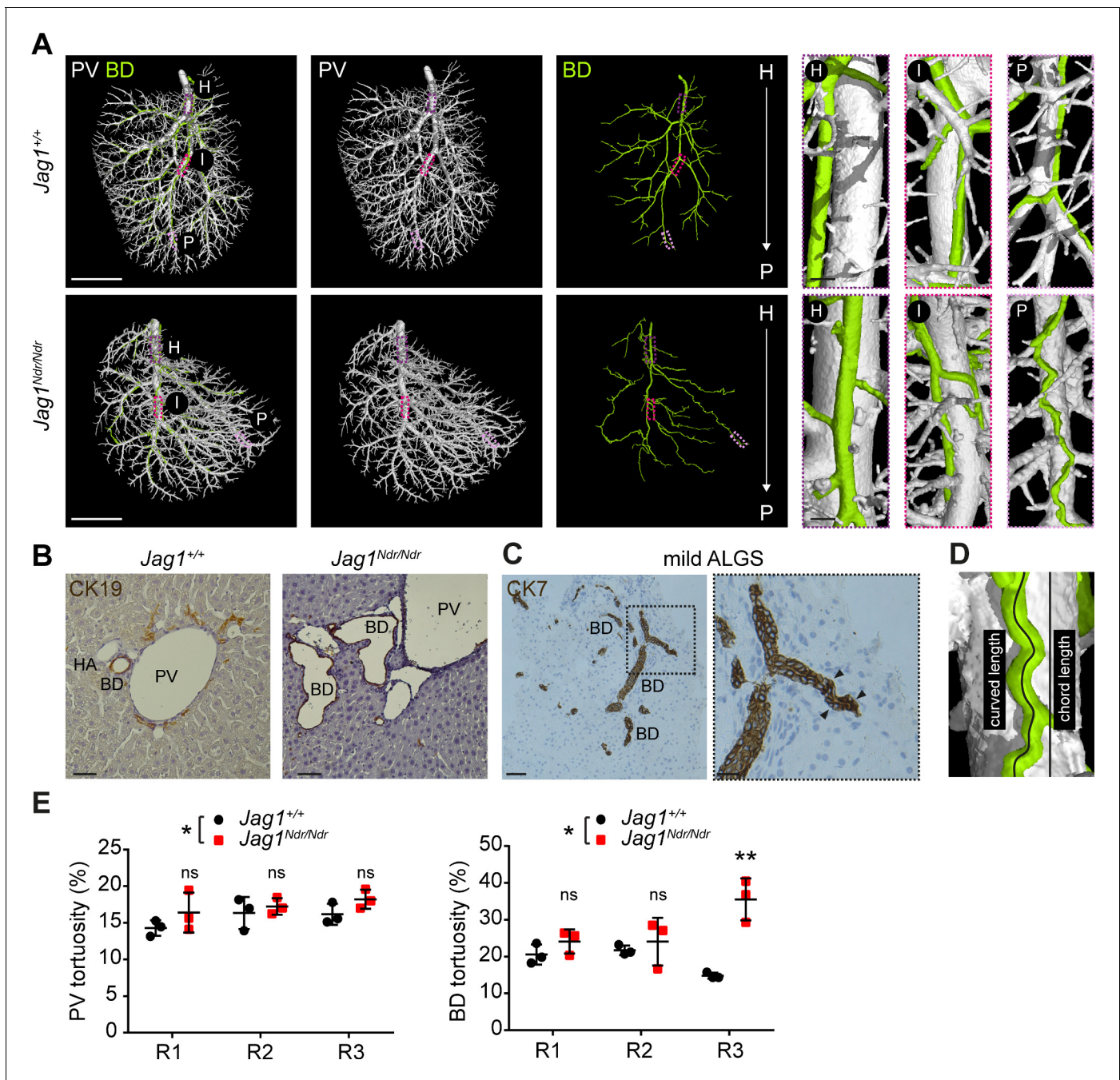**Figure supplement 1.** Bile duct branch distribution per region.

Figure 6. Alagille syndrome human and murine de novo generated bile ducts are tortuous. (**A**) DUCT 3D rendering of BD and PV structures in *Jag1*$^{+/+}$ (top panels) and *Jag1*$^{Ndr/Ndr}$ liver (bottom panels). Boxed areas magnify the hilar (**H**), intermediate (**I**) and peripheral (**P**) regions. Scale bars left 4 mm, boxed regions 250 μm. (**B**) 2D histological liver sections, show well-formed round CK19+ BDs in *Jag1*$^{+/+}$ liver, but aberrantly formed BDs in *Jag1*$^{Ndr/Ndr}$ liver. Scale bar 50 μm. (**C**) 2D liver section from patient with mild ALGS revealed tortuous misshaped BDs. Scale bar 50 μm, boxed region 20 μm. (**D**) Schematic representing length measurements. Percentage tortuosity was calculated by dividing curved (actual) length by chord (theoretical) length, and subtracting 100% (final value of 0% = not tortuous, perfectly straight). (**E**) The overall *Jag1*$^{Ndr/Ndr}$ PV (left graph) and BD (right graph) systems are more tortuous than wild types, and the *Jag1*$^{Ndr/Ndr}$ BD system is particularly tortuous in Region 3 (periphery). Each dot represents one animal, lines show mean value ± standard deviation. Statistical test: two-way ANOVA, left panel p=0.0141, right panel p=0.0251; followed by Sidak's multiple comparisons test; p<0.05 (*), p<0.01 (**). ALGS, Alagille syndrome; BD, bile duct; CK, cytokeratin; DUCT, double resin casting micro computed tomography, H, hilar; HA, hepatic artery, I, intermediate P, peripheral; PV, portal vein.

The online version of this article includes the following figure supplement(s) for figure 6:

Figure supplement 1. The adult de novo formed *Jag1*$^{Ndr/Ndr}$ and *Jag1*$^{+/+}$ biliary systems are similar in length.

entire tree to obtain comprehensive and accurate results. In summary, DUCT allowed analysis of curved and chord length measurements for the entire or defined regions of the injected trees. $Jag1^{Ndr/Ndr}$ bile ducts recovered wild-type lengths postnatally, with a pronounced increase in peripheral tortuosity.

Discussion

Precisely defining the three-dimensional (3D) architecture of healthy and diseased organs is a fundamental aspect of biology, and improved imaging methods would allow stricter characterization of animal models for human diseases. Until now, 3D liver analysis has been restricted by a lack of adequate tools and high auto-fluorescence of the tissue. Carbon ink injection is robust, but imaging is 2D, precluding 3D analysis of the architecture. In contrast, immunostaining and clearing allows 3D analysis, but success is variable and highly dependent on tissue fixation, antibody quality, penetrance and tissue autofluorescence. Here, we further advanced organ resin casting, which was previously used to analyze one system at a time (*Masyuk et al., 2003*; *Kline et al., 2011*; *Walter et al., 2012*). We developed a simple, robust and inexpensive method (DUCT) for simultaneous visualization and digitalization of two lumenized systems in mouse to analyze organ architecture. DUCT is completely independent of antibody staining, endogenous fluorescent proteins and is not sensitive to tissue fixation. Unlike whole mount immunohistochemistry techniques, DUCT provides information about the lumen, internal diameter, perfusion and connectivity of the injected tree. The most important limitation of DUCT is that it cannot visualize structures with a diameter under 5 µm, due to resin viscosity. We showed that resin casting, segmentation and 3D representation can be used as input for further investigation by visual qualitative assessment, and for in depth analysis by imaging softwares such as ImageJ or custom written MATLAB scripts. The pipeline for imaging and segmentation followed by detailed customized quantification of cellular and architectural mechanisms of two tubular networks could serve as a standard for whole organ analysis in animal models, and can be further adapted for a specific applications.

DUCT is based on radiopaque resin injection into multiple lumenized systems. First, identifying resins with sufficient contrast and low viscosity is crucial for scanning using computed tomography. Combining multiple resins with distinct contrasts can upscale the analysis to several networks simultaneously. In our study, it was imperative to use two fresh MICROFIL resins to obtain sufficiently distinct contrast to separate the two injected systems. Prolonged storage (~>3 months) of the MICROFIL resin leads to resin precipitation and a significant decrease in the resin radiopacity (for details see materials and methods). Future efforts to identify or develop differentially radiopaque substances would further accelerate the analysis pipeline. Second, in order to achieve a successful injection, an appropriate resin injection site for each system must be identified, and a suitable amount of pressure must be applied while avoiding bubble formation. Third, resin segmentation of the scanned sample is straightforward in well-injected, well-contrasted samples, but in samples with bubbles or poor contrast segmentation requires time-consuming manual correction and careful tracing of the resin throughout the whole organ to ensure a coherent network. Minor resin leakage can be digitally excluded during the image segmentation, but artefacts such as air bubbles in resin, non-homogenous resin contrast (in our set up caused by mixing of blue and yellow MICROFIL) and resin leakage due to lumen rupture (probably caused by high pressure during injection) slow down the analyses substantially (*Figure 7B*). Thus, a well-chosen and well-injected resin are a prerequisite for efficient downstream analyses.

Regarding instrumentation, the DUCT pipeline is not restricted to specific CT systems or acquisitions parameters, therefore samples can be imaged on any CT device with sufficient spatial resolution to study selected samples and their morphology. For further qualitative and quantitative analysis of the DUCT µCT data, robust computational power is necessary – and dedicated workstations with sufficient RAM memory (>64 MB RAM) are recommended, dependent on the volume of acquired data.

Our study describes a complex spatial adaptation of the biliary tree to postnatal BD paucity in a mouse model for Alagille syndrome (ALGS), with validation in samples from patients with ALGS. Based on our data and reported case studies, we propose a model in which *Jag1* mutant intrahepatic bile ducts (IHBDs) did not form during embryonic development (*Andersson et al., 2018*; *Alessandro et al., 2007*) but in some animals (and some patients, *Figure 2—figure supplement*

1D), bile ducts grew after birth (*Dahms et al., 1982*). The lumenized bile ducts formed from hilar to peripheral regions with different timings in the different liver lobes and in individual animals. The fully remodeled biliary system was tortuous, exhibited abrupt ends, and was hyper-branched in region 1 (summarized in *Figure 8*).

Our findings in the mice, using DUCT, may help to explain the poor prognostic value of biopsies in patients with ALGS. Our results suggest that the lack of predictive value between peripheral bile duct paucity, observed in diagnostic biopsies, and phenotype severity in patients with ALGS (*Mouzaki et al., 2016*) may reflect differences in bile duct growth and presence/absence in hilar versus peripheral regions (*Figure 1C*, *Figure 1—figure supplement 5B,C,E*). Mouzaki et al, showed that bile duct density was not predictive of outcome, instead, bilirubin levels, fibrosis, and cholestasis were correlated with disease presentation. In line with this, in the *Jag1^{Ndr/Ndr}* pups the total bilirubin levels correlated well with 3D postnatal bile duct growth, which was apparent from 3D resin-injected whole lobe analysis, but did not correlate with bile duct paucity in 2D sections of central

Figure 7. Schematic of *Jag1^{Ndr/Ndr}* biliary abnormalities in de novo generated bile ducts. Left panel depicts a simplified wild type or healthy human spatial arrangement of portal veins and bile ducts in three liver regions (R1, R2 and R3). Right panel illustrates a simplified adult *Jag1^{Ndr/Ndr}* regenerated biliary system displaying morphological abnormalities including (1) increased branching in region 1, (2) branching independent of the portal vein, (3) increased distance from portal vein, (4) abrupt/blunt endings facing the hilum, (5) peripheral tortuosity and (6) bridging between two portal veins. Independently branching, abruptly ending, parenchymal and tortuous bile ducts were confirmed in liver from patients with Alagille syndrome.
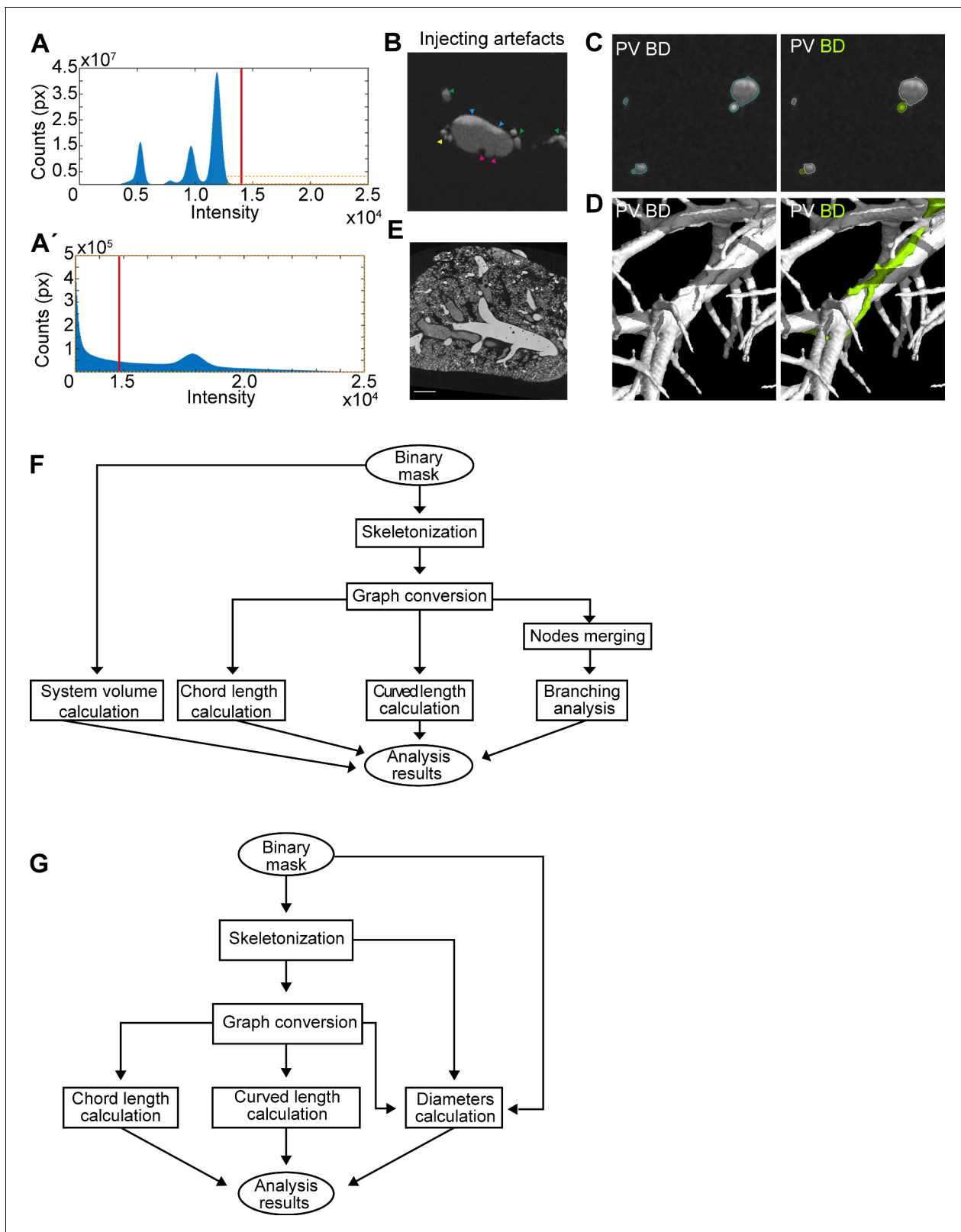
Figure 8. Micro computed tomography image processing. (**A**) µCT scan thresholding. Orange box in (**A**), magnified in (**A′**), shows MICROFIL intensity levels. (**B**) Resin injection artefacts including inadequate mixing of MICROFIL resin (blue arrowheads), bubbles in the resin which require manual correction (magenta arrowheads), and leakage due to excessive injection pressure or vessel/duct weakness (yellow arrowhead). Green arrowheads represent side branches. (**C**) Global thresholding separates old MICROFIL injected ducts and vessels from background tissue. BD and PV are identified

Figure 8 continued on next page

Figure 8 continued

manually. (**D**) 3D visualization of BD and PV after first segmentation (left panel) and after the systems separation. (**E**) Global thresholding separates fresh MICROFIL injected airways and vessels from each other and the background tissue. (**F**) Quantification pipeline schematic for the whole lobe (**G**) or only the main branch analysis.

liver. A 40% regrowth of lumenized bile ducts in *Jag1*$^{Ndr/Ndr}$ pup was sufficient to reduce cholestatic burden to almost wild type levels, while not leading to a normal density of bile ducts in the periphery - emphasizing the importance of whole-liver architecture analyses.

Identifying and quantifying architectural defects such as branch length differences, stochastic branching, tortuosity, differences in portal-biliary distance and blunt end bile ducts is very challenging in sections (compare histology and 3D imaging in *Figures 2–6*). We demonstrated here that DUCT is a powerful method for visualization and semi-automated quantitative analysis of two lumenized biological systems in vivo. DUCT could be applied to other tubular networks including blood vessels and bronchi in lung (*Figure 1—figure supplement 1E*) or blood vessels and urinary ducts in kidney (*Wagner et al., 2011*; *Wei et al., 2006*). DUCT has multiple advantages over ink injections and iDISCO+, as 3D imaging with µCT avoids the drawbacks of tissue autofluorescence or poor antibody penetration. By injecting two resins into a single animal, it is possible to study the relation between these biological systems, which has not been previously reported. While experts in the field are careful to discriminate hilar and peripheral regions of the liver, carefully tracing organ structures for hundreds of micrometers in tissue sections is not standard practice and is a demanding endeavor. DUCT would be a suitable readout for testing drug compounds in mouse models for liver cholestatic diseases. With DUCT, it is now possible to map and quantify architecture of two networks in mouse models, setting the stage for an in depth understanding of how systems interact in health, disease, and regenerative processes.

Materials and methods

Key resources table

Reagent type (species) or resource	Designation	Source or reference	Identifiers	Additional information
Antibody	Anti-Cytokeratin 7 (rabbit monoclonal)	Abcam	Cat # ab181598 RRID:AB_2783822	iDISCO+ (1:1000)
Antibody	Anti-Cytokeratin 7 (mouse monoclonal)	Invitrogen/ThermoFisher Scientific	Cat # MA5-11986, clone: OV-TL 12/30 RRID:AB_10989596	IHC (1:200)
Antibody	Anti-Cytokeratin 7 (mouse monoclonal)	Sigma - Aldrich	Cat # C6198 RRID:AB_476856	iDISCO+ (1:2000)
Antibody	Anti-Cytokeratin 19 (rat monoclonal)	DSHB	Cat # TROMA-III RRID:AB_2133570	IHC (1:50)
Antibody	Anti-human SOX9 (goat polyclonal)	RnD Systems	Cat # AF3075 RRID:AB_2194160	IHC (1:100)
Commercial assay or kit	MICROFIL	Flow Tech Inc	Cat # MV120, MV-122	DUCT
Software, algorithm	MATLAB	Mathworks	RRID:SCR_001622	codes available: https://github.com/JakubSalplachta/DUCT

Experimental mice

All animal experiments were performed in accordance with Stockholm's Norra Djurförsöksetiska nämnd (Stockholm animal research ethics board, ethics approval numbers: N150/14, N61/16, N5253/19, N2987/20) regulations. Animals were maintained with standard day/night cycles, provided with food and water ad libitum, and were housed in cages with enrichment. For postnatal day 15 (P15) experiments, 10 wild type (*Jag1*$^{+/+}$) (eight males and two females) and 10 *Jagged1* Nodder (*Jag1*$^{Ndr/Ndr}$) littermate pups (five males and five females) were used for serum analysis. Within this group, nine *Jag1*$^{+/+}$ and seven *Jag1*$^{Ndr/Ndr}$ mice were injected with resin. All 16 animals were analyzed in 3D, revealing extensive heterogeneity that would necessitate performing DUCT on a large

number of animals to obtain significant quantitative data, while the bile duct paucity was obvious. 1 *Jag1*$^{+/+}$ and 1 *Jag1*$^{Ndr/Ndr}$ pair was therefore scanned and rendered in 3D. From this group, four *Jag1*$^{+/+}$ and four *Jag1*$^{Ndr/Ndr}$ left medial lobes were used for 2D liver sections and staining.

Adult animals were between 4.5 and 6.5 months old. In total, 18 *Jag1*$^{+/+}$ and 6 *Jag1*$^{Ndr/Ndr}$ animals were injected with resin for μCT. Quality control of injections (*Figure 1—figure supplement 2*) was performed on all livers during method development until surgery and injection technique resulted in well-injected livers. Three *Jag1*$^{+/+}$ and three *Jag1*$^{Ndr/Ndr}$ animals were used for the DUCT quantifications in adulthood. For liver histology, two *Jag1*$^{+/+}$ and three *Jag1*$^{Ndr/Ndr}$ mice were used. For ink injections, nine *Jag1*$^{+/+}$ mice were used (four males and five females) and for iDISCO+ four *Jag1*$^{+/+}$ and four *Jag1*$^{Ndr/Ndr}$ mice were used (six males and two females). For lung 3D resin casting five *Jag1*$^{+/+}$ mice were used (two males and three females). Samples were not blinded for investigation since the phenotype is overt and the genotype is therefore obvious to the experimenter. The animals were maintained on a mixed C57bl6J/C3HeN background. *Jag1*$^{Ndr/+}$ (Nodder) mice were bred and genotyped as previously described (*Andersson et al., 2018*).

Patient samples

Collection of liver samples and clinical data from patients or donors was approved by the Swedish Ethical Review Authority (2017/269-31, 2017/1394–31). Samples from patients with severe Alagille syndrome (four) were obtained at time of liver transplant from extirpated liver. Samples were obtained with a consent to be used for research according to ethical permit 2017/269–31. Samples were dissociated for primary cell culture e.g. organoids (data not shown), and a matching sample was formalin fixed or fresh-frozen for comparative analyses. Liver tissue samples from patients with mild Alagille syndrome (six) were obtained for clinical follow-up purposes and were retrospectively analyzed. The liver material was obtained within the framework of clinical patient care can be analyzed retrospectively without the need for consent according to ethical permit 2017/1394–31. Healthy controls (two) were left-over donor material, or from organ donation post-mortem. The liver function tests were obtained during routine biochemical analyses.

MICROFIL injections

MICROFIL (Flow Tech Inc) was prepared as follows. Yellow MICROFIL (Y) cat. #MV-122 was diluted with clear MICROFIL (C) cat. # MV-Diluent in 3:1 (Y:C). Blue MICROFIL (B) cat. #MV-120 was diluted 1:1 (B:C) with clear MICROFIL. Diluted yellow MICROFIL was mixed with diluted blue MICROFIL 1:1 creating a green MICROFIL. Yellow MICROFIL was injected into common bile duct (CBD) or pulmonary artery (PA). Green MICROFIL was injected into portal vein (PV) or trachea (TA). 1 ml of diluted MICROFIL is mixed with 50 μl of hardener (supplied by Flow Tech Inc) prior injection.

Postnatal day 15 (P15) mice were sacrificed by decapitation and perfused through the heart with 3 ml of Hanks' Balanced Salt solution (HBSS) (Life Technologies cat. # 14025092). Adult mice were sacrificed by CO$_2$ inhalation and perfused through the heart with HBSS for 3 min (perfusion rate 5 ml / 1 min). For liver resin injections, the mice were perfused trough the left ventricle, for lung resin injections the mice were perfused though the right ventricle.

Injection into CBD

A small transversal incision was made in inferior vena cava with spring scissor to release the liver vascular pressure. CBD was exposed by moving aside the liver and intestine and cleaned from surrounding tissue in area about 5 mm long. Silk suture (Agnthos AB cat. #14757) was loosely wrapped around the cleaned CBD. A longitudinal CBD incision was made at the spot where CBD enters the pancreas next to sphincter of Oddi by spring scissor. The tubing (PE10, BD Biosciences cat. # 427401) ~15 cm long was prepared by stretching one side of the tube until the diameter becomes thin enough to fit into CBD. Diagonal cut is made at the tip of the tubing while the other side contains needle (27G) connected to the syringe filled with MICROFIL. The tubing connected to a syringe and filled with a yellow MICROFIL was inserted into the CBD, the suture around the CBD can be tighten to secure the tubing in place. Yellow MICROFIL was injected into the CBD until resistance was met or MICROFIL spots were visible on the liver surface. Massaging the liver with cotton swab while injecting helped to disperse the MICROFIL. The tubing was removed and silk suture was tightened around the CBD to prevent leakage.

Injection into PV

PV was cleaned from surrounded tissue. A small incision was made in PV using spring scissor. Silk suture was loosely wrapped around the cleaned PV above the incision. Tubing (PE10) ~15 cm long connected to (27G) needle was inserted into the PV incision and secured with silk suture. Green MICROFIL was injected into the PV until blood vessels on the surface were filled or resistance was met. Massaging the liver with a cotton swab while injecting helped to introduce the MICROFIL. The tubing was removed and silk suture was tightened around the PV to prevent leakage.

Liver was dissected out and placed at 4°C overnight (ON) for MICROFIL to solidify. The next day the liver was fixed with 3.7% formaldehyde solution (FA) (Sigma-Aldrich cat. #F1635) diluted in Dulbecco's phosphate-buffered saline (DPBS) (Life Technologies cat. # 14190144). After 24 hr, liver was washed and kept in DPBS. Liver was separated into lobes. The left lateral lobe was placed in 50% methanol (Sigma-Aldrich, cat. # 322415) for 4 hr and into 100% methanol ON. Further, the lobe was placed in benzyl alcohol (Sigma-Aldrich, cat. #402834) and benzyl benzoate (Sigma-Aldrich, cat. #B6630) (BA:BB 1:2) solution until transparent. The right medial lobe (only FA fixed) was used for μCT scanning. Liver lobe images of right medial lobe (P15) and left lateral lobe (P15 and adult) were taken using a stereomicroscope Stemi 305 (Carl Zeiss Microscopy) with a PowerShot S3 IS camera (Canon) or iPhone6 connected to a LabCam adapter.

Injection into lung

The mouse heart was pulled toward the liver to expose the pulmonary artery (PA) and pinned down through the heart apex with a 1 ml empty syringe connected with a needle. A silk suture was wrapped loosely around the PA as close to the heart as possible. A small incision was made in the right ventricle with spring scissors. Tubing (PE50, BD bioscience, cat #427411) ~15 cm long (stretched at the tip) connected to (23G) needle was inserted into the PA through the incision in the right ventricle and tightened with the suture. A total of 1 ml of DPBS was injected into the lung via PA to remove all the remaining blood. Afterwards, to expand the collapsed lung, the trachea was exposed and cleaned from surrounding tissue. A silk suture was loosely wrapped around the trachea and a small incision was made into the trachea with spring scissors. Tubing (PE50) ~15 cm long connected to (23G) needle was inserted into the trachea and tightened with the suture. One ml of DPBS was injected into the lungs via trachea – this inflates the collapsed lungs. A 1 ml syringe filled with yellow MICROFIL was connected to the tubing inserted into the PA, and MICROFIL was injected into the PA vasculature until all the blood vessels were filled. Massaging the lung with a cotton swab while injecting helped to disperse the MICROFIL. After the vasculature was completely filled, the tubing was removed and the suture around the PA tightened to prevent MICROFIL leakage. For airways injection, a 1 ml syringe filled with green MICROFIL was connected to the tubing inserted into the trachea, and MICROFIL was injected into the trachea until the lung was entirely filled with MICROFIL. Massaging the lung with cotton swab while injecting again helped to disperse the MICROFIL. After the lung was completely filled, the tubing was removed and the suture around the trachea tightened to prevent MICROFIL leakage.

Lungs were dissected out and placed at 4°C ON to allow the MICROFIL to solidify. The next day the lung was fixed with 3.7% FA diluted in DPBS. After 24 hr, lungs were washed and kept in DPBS. Lungs were separated into lobes and the right superior lobe was used for μCT scanning.

Ink injections

Mice were sacrificed by CO_2 inhalation and transcardially perfused with HBSS for 3 min (perfusion rate 5 ml/1 min).

Injection into CBD and PV. CBD and PV were accessed in the same way as described for MICROFIL injections. When injecting with ink, there is no need to tighten the CBD with silk suture as the ink is not leaking out. Black ink (Higgins cat. #44032) was injected into the CBD until BDs on the surface were filled or resistance was met. White ink (Higgins cat. #44032) was injected using PE50 tubing into the PV until blood vessels on the surface were filled or resistance was met. Liver was dissected out and separated into lobes. All lobes were cleared in BABB as described above. Liver ink images of right medial lobe were taken under stereomicroscope Stemi 305 (Carl Zeiss Microscopy) using PowerShot S3 IS camera (Canon).

Whole mount immunohistochemistry

Mice were anesthetized by isoflurane inhalation (~2%) and transcardially perfused with HBSS for 3 min (perfusion rate 5 ml/1 min) and 10% neutral buffered formalin (NBF) for 5 min. Liver was dissected out and further immersion fixed with 10% NBF ON at 4°C. The next day liver was washed and kept in DPBS and separated into lobes. Right medial lobe was stained and cleared following the iDISCO+ protocol and imaged by light sheet microscope by Gubra (Denmark).

Fixed and washed samples were dehydrated in methanol/H_2O gradient: 20%, 40%, 60%, 80% and 2 × 100% methanol, each step 1 hr at room temperature (RT). The samples were bleached in cooled fresh 5% H_2O_2 in methanol ON at 4°C. The samples were subsequently rehydrated in methanol/PBS series: 80%, 60%, 40%, 20%, with 0.2% Triton X-100, 1 hr each at RT. They were washed in PBS with 0.2% Triton X-100 (PTx.2) for 2 × 1 hr at RT.

Whole organ immunolabeling (iDISCO+)

Samples were incubated in permeabilization solution at 37°C for 3 days. Blocking is carried out in blocking solution at 37°C for 2 days. The samples were incubated with primary antibody in PTwH/5% DMSO/3% donkey serum at 37°C for 7 days. They were washed in PTwH for 1 × 10 min, 1 × 20 min, 1 × 30 min, 1 × 1 hr, 1 × 2 hr and 1 × 2 days. Samples were incubated with secondary antibody in PTwH/3% donkey serum at 37°C for 7 days, followed by washes in PTwH: 1 × 10 min, 1 × 20 min, 1 × 30 min, 1 × 1 hr, 1 × 2 hr and 1 × 3 days. All steps were performed in tightly closed tubes to minimize evaporation and oxidation.

Solutions for iDISCO

PTx.2 (1L): 100 ml PBS 10x, 2 ml TritonX-100
PTwH (1L): 100 PBS 10x, 2 ml Tween-20, 1 ml of 10 mg/ml heparin stock solution
Permeabilization solution (500 ml): 400 ml PTx.2, 11.5 g glycine, 100 ml DMSO
Blocking solution (50 ml): 42 ml PTx.2, 3 ml donkey serum, 5 ml DMSO
Secondary antibody: Alexa Fluor 488 (dilution 1:1000, Life technologies)

Tissue clearing

Tissue was cleared in methanol/H_2O series: 20%, 40%, 60%, 80%, and 100% for 1 hr each at RT. Samples were incubated for 3 hr (with shaking) in 66%DCM (Dichloromethane)/33% methanol at RT and in 100% DCM 15 min 2x (with shaking) to remove traces of methanol. They were incubated in DiBenzyl Ether (DBE) (without shaking).

Light sheet microscopy

Tissue samples were imaged using a light sheet microscope (UltramicroscopeII, Miltenyi). DBE was used as clearing agent during data acquisition. Data was collected at room temperature using Lavision ultramicroscope system and MV PLAPO 2X C/0.5 objective with dry lens, RI correction collar using Andor Zyla 4.2 Plus sCMOS camera. CK7 staining was detected with AF790 (Alexa Fluor, Life Technologies). The acquisition software used was ImSpector (LaVision biotech).

Liver immunohistochemistry

5 μm FFPE-liver (mouse and human) sections were deparafinized and rehydrated through consecutive baths of xylene (cat. #28975.325, VWR) and isopropanol (cat. #K50655934838, Merck). Endogenous peroxidase was blocked by immersion of the slides in methanol (cat. #322415, Sigma-Aldrich) containing 0,3% H_2O_2 (cat. #H1009, Sigma-Aldrich) for 15 min and rehydration was finalized by rinsing the slides in tap water. Heat-induced epitope retrieval was done using citrate buffer (PH 6.0) for 20 min in a pressure cooker. After blocking of the sections with 2% BSA (cat. #A7906, Sigma-Aldrich) for 20 min, slides were incubated for 1 hr at 37°C with primary antibody (antibodies used are listed in Key resources table). Anti-mouse (cat. #G21040, dilution: 1/1000, Invitrogen) or anti-goat (Impress, cat. #MP7405, Vector), respectively, HRP-coupled secondary antibody was applied for 30 min at 37°C and revealed with DAB for 30 s (cat. #K3468, Dako). After counterstaining with hematoxylin (cat. #HX86014349, diluted 1/5, Merck), the sections were dehydrated in consecutive baths of ethanol (cat. #20821.310, VWR), isopropanol (cat. #K50655934838, Merck), and xylene

(cat. #28975.325, VWR) to finally be mounted with hardening medium (Eukitt, cat. #03989, Sigma-Aldrich).

Liver section image acquisition

Chromogenic stained images were taken with AxioImager (Carl Zeiss) microscope, Axiocam 503 color camera using Plan-Apochromat 5x/0.16, Plan-Apochromat 10x/0.45 M27, Plan-Apochromat 20x/0.8 M27 and Plan-Apochromat 40x/1.4 Oil DIC (UV) VIS-IR M27 objectives at room temperature. The acquisition software used was Zen Blue (Carl Zeiss).

Image processing

Whole mount liver images cleared with iDISCO+ were initially processed in ImageJ for maximum z-projection and segmentation. The images were filtered using the unsharp mask and integral image filter function. Images were next processed in Amira. In Amira images were filtered using the Gaussian filter and background detection correlation. Images were manually segmented. The manual segmentation was further traced using the autoskeleton function. The skeletons were further analyzed in Amira for length, volume and branching.

Images of ink injected liver were proceeds for filament tracing. Bile duct and portal vein filament tracing was performed using Amira. The images were filtered using the unsharp mask and mean filter. The signal was manually segmented to remove artificial signal. The manual segmentation was further traced using the autoskeleton function. The skeletons were analyzed in Amira for length, volume and branching. For double ink injection (*Figure 1—figure supplement 1A*) the background was changed for esthetic purposes using the lasso tool in Adobe Photoshop.

DUCT 2D slices were exported from MyVGL (Volumegraphics) and processed in ImageJ for maximum contrast and brightness.

Liver sections IHC were processed in ImageJ for contrast and brightness

P15 MICROFIL injected and BABB-cleared left lateral and right medial lobe were analyzed in ImageJ. The total liver area was measured followed by the measurement of the liver area covered by MICRO-FIL injected bile ducts. The percentage of liver containing bile ducts was calculated.

Blood serum collection and analysis

Blood from P15 pups was collected from the trunk after decapitation into 1.5 ml tubes. The serum was allowed to clot at room temperature. The blood was centrifuged for 15 min at 17,000 g at room temperature. The serum was stored at −80℃ until analyzed. Serum was sent to the Swedish University of Agricultural Sciences for analysis of alanine aminotransferase (ALT), alkaline phosphatase (ALP), aspartate aminotransferase (AST), albumin (Alb), and total bilirubin.

MicroCT measurement

The system GE Phoenix v|tome|x L 240 (GE Sensing and Inspection Technologies GmbH, Germany) equipped with nanofocus X-ray tube (180 kV/15 W) was used for the tomographic measurements that were carried out in the air-conditioned cabinet (fixed temperature 21℃). The samples were adapted for this temperature before the measurement to prevent any thermal expansion effect. To prevent any sample motion during the scanning, the samples were placed in 15 ml Falcon tube, filled with 1% agarose gel. The tomographic reconstruction of acquired data was performed using GE phoenix datos|x 2.0 software. The voxel resolution was fixed for all the adult liver samples at 12 µm, except one (sample #2401, 8 µm). For all the P15 liver samples the voxel resolution was fixed at 6.5 µm and for the lung lobe sample at 8 µm. Detailed overview of used acquisition parameters is stated in *Table 2*.

MicroCT data segmentation

The identification and segmentation of both tubular systems (e.g. bile duct (BD) and portal vein (PV) for liver samples and pulmonary artery and airways for lung samples) in each CT cross-section was necessary for further analysis of each system. The segmentation was based on differential contrast between the resin and the soft tissue. Two different resins were used to identify the individual

tubular systems. The differential contrast for system identification was highly dependent on the freshness of the MICROFIL.

The resin segmentation was performed by global thresholding in VG Studio MAX 3.3 (Volume Graphics GmbH, Germany) software together with manual corrections where necessary. The threshold value was determined based on the histogram shape and visual evaluation of a selected cross-section (*Figure 8A,A'*). The resin cast, especially when using an old MICROFIL, could contain artefacts caused by poor contrast, insufficient filling or high injection pressure. These artefacts include air bubbles in resin, non-homogenous resin contrast (caused by mixing of blue and yellow MICROFIL) and resin leakage due to lumen rupture (probably caused by high pressure during injection), (*Figure 8B*). Therefore, the thresholding step was supplemented with manual corrections to create smooth, continuous and solid canal masks. Furthermore, the cut-off for the smallest distal canal included in the mask is considered an area of at least four voxels.

Next, the individual tubular systems were identified in the segmented resin mask (*Figure 1—figure supplement 12D and G*). When fresh MICROFIL was used, it was possible to identify each system by global thresholding with threshold value determined based on histogram shape and visual evaluation of CT data. However, in case of the old MICROFIL (used for adult liver samples) the resin absorption properties were not distinguishable in CT data. In most regions, both tubular systems blended with each other in one continuous region (*Figure 8C, D* left panel). Manual segmentation was therefore necessary to ensure the correct identification of both systems (*Figure 8C, D* right panel). The manual segmentation was performed by outlining the BD regions in every slice of the CT data. VG Studio automatically creates 3D render based on the regions outlined in CT sections.

MicroCT data analysis

The adult liver was analyzed using a custom-written algorithm and freely available Matlab codes (Version R2017a, The MathWorks Inc, Natick, MA). The algorithm was designed to analyze morphological parameters of the BD and PV systems, and is compatible with the 3D binary masks. Two separate masks of BD and PV system were generated and the analysis was divided in two independent parts. First, the analysis of the entire portal vein and biliary system and second, analysis of the corresponding main branch (=the longest branch) of each system (*Figure 6—figure supplement 1A*). For detailed analysis and comparison of the whole system versus only the main branch, two algorithms, described by the diagrams in *Figure 8F, G*, were developed. They differ in the input data and the evaluated parameters. For both algorithms, the first step is to create a 3D skeleton of the input binary mask.

Skeletonization of binary masks

The 3D skeleton was derived using the homotopic thinning algorithm described in *Lee et al., 1994* specifically optimized for Matlab implementation by Kollmannsberger (*Kerschnitzki et al., 2013*), (online source: https://www.mathworks.com/matlabcentral/fileexchange/43400-skeleton3d).

Table 2. Settings parameters of the GE Phoenix v|tome|x L 240 system.

Sample	Voxel size	Acceleration voltage	X-ray tube current	Exposition time	Number of projections
2401	8 μm	80 kV	160 μA	600 ms*	2500*
2404	12 μm	80 kV	160 μA	600 ms*	2500*
2405	12 μm	80 kV	160 μA	600 ms*	2500*
2431	12 μm	80 kV	160 μA	600 ms*	2500*
2713	12 μm	80 kV	160 μA	334 ms[†]	1900[†]
2714	12 μm	80 kV	160 μA	334 ms[†]	1900[†]
N864	6.5 μm	80 kV	160 μA	400 ms[†]	1800[†]
N865	6.5 μm	80 kV	160 μA	400 ms[†]	1800[†]
$Jag1^{+/+}$ lung	8 μm	80 kV	160 μA	400 ms[†]	2000[†]

*Flat panel DXR250 (2048 px ×2048 px, pixel size 200 μm).

[†]Flat panel dynamic 41|100 (4048 px ×4048 px, pixel size 100 μm with binning 2).

Calculated 3D medial axis skeleton was subsequently converted to a network graph, using algorithm described in *Kerschnitzki et al., 2013* (online source: https://www.mathworks.com/matlabcentral/fileexchange/43527-skel2graph-3d). Resulting network graph is formed by nodes and links between them (*Figure 1—figure supplement 12D and G*).

Liver region subdivision

Liver was separated into three regions: R1 (approximately hilum), R2 (approx. intermediate) and R3 (approx. periphery). The optimal region size was calculated as a summary of average PV branch lengths per generation and divided by three (detailed branching generation subdivision *Table 3* for PV and *Table 4* for BD). Subsequently the branching generations were assigned to a region by matching the summary of branch length per generation to optimal region size. The same region was applied for both PV and BD analysis with the exception of one $Jag1^{Ndr/Ndr}$ sample (#1 or 2714) where the bile duct optimal region size was greater than portal vein.

Regions were assigned in order that total average lengths of each generation within each region yielded an equal size of R1, R2, and R3. Each sub-column represents one animal.

The distribution of BD branches within each region were quantified based on regions defined by the PV system (*Table 4*). Each sub-column represents one animal.

Branching analysis

Branching points analysis was programmed in Matlab to analyze the distance between BD and PV branching point. This parameter was calculated using 3D Euclidean distances between the BD branching points and the nearest branching point from PV system. The data is represented as cumulative sum of percentage of BD branching point at a given distances between BD and PV branching points (from 0.015 mm to 3 mm).

For branch length analysis the structure of BD and PV trees were first reconstructed in 3D, using the Analyze Skeleton toolbox in ImageJ, which provided the three-dimensional coordinates of all branch points for both BD and PV, as well as the connectivity of the graph. Next, we computed for each branch the length along its path to the Euclidean distance between its extremities (branch points). To calculate the generation number of branches (both for the PV and BD structures), we manually defined the origin of the ducts and vessels as generation 1, and computed generation number as the number of generation branches separating a given branch from the origin. To distinguish side branching events, we calculated the angle between a branch and its 'parent' by computing the dot product p of both their unit vectors. A branch with p>0.95 with its parent branch was considered to belong to the same generation. We then computed distributions of length for the BD and PV structures as a function of generation number. Each generation was assigned to a region R1, R2, or R3.

The branch distribution in each region was calculated as a summary of number of branches per generation in a given region. The sum of branch numbers of each region is displayed as a proportion of the total number of branches per sample.

The number of bi-furcations (i.e. one input and two outputs), tri-furcations (i.e. one input and three outputs) and quadri- and more-furcations (one input and more than three outputs), were assessed in Matlab based on binary mask skeleton nodes that were divided into endpoints and branching points. Branching points closer than 0.2 mm (this threshold value was derived based on visual assessment and knowledge of the system) were merged together and further represented by one node.

Table 3. PV branching generation distribution into liver regions.

PV generation #	$Jag1^{+/+}$ (3 animals)			$Jag1^{Ndr/Ndr}$ (3 animals)		
R1	1–4	1–3	1–4	1–4	1–3	1–3
R2	5–10	4–9	5–10	5–8	4–7	4–7
R3	11–18	10–14	11–17	9–15	8–12	8–11

Table 4. BD branching generation distribution into liver regions.

BD generation #	Jag1⁺/⁺(3 animals)			Jag1^{Ndr/Ndr} (3 animals)		
R1	1–4	1–4	1–2	1–4	1–6	1–6
R2	5–7	5–7	3–5	5–9	7–10	7–10
R3	8–12	8–11	6–7	10–16	11	11–12

Gap analysis between bile duct and portal vein

To evaluate the gap between BD and PV the surface distances were calculated in Matlab for each BD skeleton point by detecting the nearest PV skeleton point and connecting the two points with a line and measuring the non-resin area on this line (zero area in the input binary masks). Surface distance was then calculated using 3D Euclidean distance between the detected non-resin voxel coordinates. The data is represented as cumulative sum of percentage of BD at a given distance from PV (from 0.015 mm to 1.5 mm). The maximum distance between BD and PV for each liver sample was depicted in a separate graph.

Tortuosity measurements

To quantify length and tortuosity, total (curved) and theoretical (chord) lengths were measured in Matlab for the whole system length and for the corresponding main branch. The curved length was defined as a cumulative sum of 3D Euclidean distances between neighboring graph points (i.e. links forming points) multiplied by voxel size. The chord length was defined as cumulative sum of 3D Euclidean distances between neighboring nodes multiplied by voxel size. The chord length therefore reflects system length where any nodes are connected by links with the shortest possible length. To analyze the relationship between BD and PV a length of the BD was divided by a PV length (curved or chord). Tortuosity was calculated as curved length divided by chord length of the same system and distributed into regions based on the generation number as previously described. Tortuosity was assessed in %, as BD and PV are not straight lines the actual tortuosity measurements were subtracted by 100% (perfectly straight line).

Volume analysis

Total system volume was calculated in Matlab by multiplying a number of voxels representing PV or BD by volume of one voxel. The relationship between BD and PV volumes was addressed by dividing the BD volume by PV volume.

Diameter measurements

The main branch diameter was calculated in Matlab every 1.5 mm along the total length of the main branch. The radius was defined as the minimal distance from the skeleton to the segmented area boundary in the input binary mask (i.e. border between background and area of interest). This boundary was calculated using a two-step procedure. In the first step, the input map was eroded using a 3D spherical shaped structural element with one pixel radius. Subsequently, the eroded area was subtracted from the original binary mask. This resulted in a binary mask representing the boundary between the background and the area of interest. One radius value at a given skeleton point was then expressed as the minimum distance from that point to the mask boundary. This was calculated, using the minimal value search in the intersection of the boundary mask and the distance map from that point. The distance map from a given skeleton point was calculated as 3D Euclidean distance of the spatial coordinates. Subsequently the diameter value was calculated as the minimum distance to the boundary area multiplied by 2. To avoid any misrepresentation, the one final diameter value at a given point (every 1.5 mm of branch length) was calculated as a mean value of a diameter at that point and diameters at four neighboring points (two on each side). PV and BD diameters were divided into three areas: hilum, intermediate and periphery. Hilar region represents distance from 0 to 1.5 (sample #2401) or 0–3 mm (other samples), Intermediate region is from 3 to 6 mm (sample #2401) or 4.5 mm – 9 mm (other samples), Periphery is from 7.5 mm – 9 mm (sample #2401) or 10.5–13.5 mm (other samples). BD to PV diameter ratio was calculated by dividing BD diameter at a given region by PV dimeter of the same region.

Statistical analysis

Jag1$^{+/+}$ and *Jag1*$^{Ndr/Ndr}$ data were tested for significant differences using multiple tests based on the type of experiment and data distribution. Student's *t*-test (*Figures 1D, G* and *3D*, *Figure 1—figure supplement 12H*, *Figure 6—figure supplement 1B–E, H–K*). Kolmogorov-Smirnov test (on raw data, graph depicts cumulative sum) (*Figures 3C* and *4C*). Mann-Whitney test (*Figure 4—figure supplement 1*). Wilcoxon test (*Figure 1—figure supplement 5D*). Two-way ANOVA (*Figures 1H* and *5B–D*, *6E*, *Figure 1—figure supplements 5C* and *12I*, *Figure 6—figure supplement 1F and G*) followed by Sidak's multiple comparisons test. Spearman correlation (*Figure 1E*). A p value below 0.05 was considered statistically significant. The statistical analysis was done in Prism 9 (GraphPad).

Acknowledgements

Additional information

Author contributions

Simona Hankeova, Conceptualization, Data curation, Formal analysis, Validation, Investigation, Visualization, Methodology, Writing - original draft; Jakub Salplachta, Conceptualization, Software, Formal analysis, Investigation, Visualization, Methodology, Writing - original draft; Tomas Zikmund, Conceptualization, Software, Formal analysis, Supervision, Investigation, Visualization, Methodology, Writing - review and editing; Michaela Kavkova, Formal analysis, Investigation, Visualization, Methodology, Writing - review and editing; Noémi Van Hul, Formal analysis, Validation, Investigation, Visualization, Writing - original draft; Adam Brinek, Jakub Laznovsky, Software, Visualization, Writing - review and editing; Veronika Smekalova, Visualization, Writing - review and editing; Feven Dawit, Investigation; Josef Jaros, Validation, Writing - review and editing; Vítězslav Bryja, Urban Lendahl, Funding acquisition, Writing - review and editing; Ewa Ellis, Resources, Writing - review and editing; Antal Nemeth, Björn Fischler, Data curation; Edouard Hannezo, Conceptualization, Investigation, Writing - review and editing; Jozef Kaiser, Conceptualization, Resources, Funding acquisition, Project administration, Writing - review and editing; Emma Rachel Andersson, Conceptualization, Resources, Data curation, Formal analysis, Supervision, Funding acquisition, Methodology, Writing - original draft, Project administration

Author ORCIDs

Simona Hankeova (ID) https://orcid.org/0000-0002-7797-3818
Jakub Salplachta (ID) https://orcid.org/0000-0002-0149-7843
Noémi Van Hul (ID) https://orcid.org/0000-0003-1410-8808
Vítězslav Bryja (ID) http://orcid.org/0000-0002-9136-5085
Ewa Ellis (ID) http://orcid.org/0000-0002-3057-5337
Edouard Hannezo (ID) http://orcid.org/0000-0001-6005-1561
Emma Rachel Andersson (ID) https://orcid.org/0000-0002-8608-625X

Ethics

Human subjects: Collection of liver samples from patients or donors was approved by the Swedish Ethical Review Authority (2017/269-31, 2017/1394-31). Samples were obtained with a consent to be used for research according to ethical permit 2017/269-31.

Animal experimentation: All animal experiments were performed in accordance with Stockholm's Norra Djurförsöksetiska nämnd (Stockholm animal research ethics board, ethics approval numbers: N150/14, N61/16, N5253/19, N2987/20) regulations.

Decision letter and Author response

Decision letter https://doi.org/10.7554/eLife.60916.sa1
Author response https://doi.org/10.7554/eLife.60916.sa2

Additional files

Supplementary files

• Transparent reporting form

Data availability

Our MATLAB pipeline is deposited in Github: https://github.com/JakubSalplachta/DUCT. Copy archived at https://archive.softwareheritage.org/swh:1:rev:6b0b0eb88bbaf9bfc4f8ee42ca-fa4c122866fbba/. All data generated or analysed during this study are included in the manuscript and supporting files. Source data files have been provided for Figures 3 and 4.

References

Alagille D, Odièvre M, Gautier M, Dommergues JP. 1975. Hepatic ductular hypoplasia associated with characteristic facies, vertebral malformations, retarded physical, mental, and sexual development, and cardiac murmur. *The Journal of Pediatrics* **86**:63–71. DOI: https://doi.org/10.1016/S0022-3476(75)80706-2, PMID: 803282

Alessandro G, Incerti M, Andreani M. 2007. Alagille syndrome: prenatal sonographic findings. *Journal of Clinical Ultrasound : JCU* **35**:156–158. DOI: https://doi.org/10.1002/jcu.20292, PMID: 17295271

Andersson ER, Chivukula IV, Hankeova S, Sjöqvist M, Tsoi YL, Ramsköld D, Masek J, Elmansuri A, Hoogendoorn A, Vazquez E, Storvall H, Netušilová J, Huch M, Fischler B, Ellis E, Contreras A, Nemeth A, Chien KC, Clevers H, Sandberg R, et al. 2018. Mouse model of alagille syndrome and mechanisms of Jagged1 missense mutations. *Gastroenterology* **154**:1080–1095. DOI: https://doi.org/10.1053/j.gastro.2017.11.002, PMID: 29162437

Chung K, Wallace J, Kim SY, Kalyanasundaram S, Andalman AS, Davidson TJ, Mirzabekov JJ, Zalocusky KA, Mattis J, Denisin AK, Pak S, Bernstein H, Ramakrishnan C, Grosenick L, Gradinaru V, Deisseroth K. 2013. Structural and molecular interrogation of intact biological systems. *Nature* **497**:332–337. DOI: https://doi.org/10.1038/nature12107, PMID: 23575631

Dahms BB, Petrelli M, Wyllie R, Henoch MS, Halpin TC, Morrison S, Park MC, Tavill AS. 1982. Arteriohepatic dysplasia in infancy and childhood: a longitudinal study of six patients. *Hepatology* **2**:350–358. DOI: https://doi.org/10.1002/hep.1840020311, PMID: 7076119

De Angelis C, Mangone M, Bianchi M, Saracco G, Repici A, Rizzetto M, Pellicano R. 2009. An update on AIDS-related cholangiopathy. *Minerva Gastroenterologica E Dietologica* **55**:79–82. PMID: 19212310

Fabris L, Cadamuro M, Guido M, Spirli C, Fiorotto R, Colledan M, Torre G, Alberti D, Sonzogni A, Okolicsanyi L, Strazzabosco M. 2007. Analysis of liver repair mechanisms in alagille syndrome and biliary atresia reveals a role for notch signaling. *The American Journal of Pathology* **171**:641–653. DOI: https://doi.org/10.2353/ajpath.2007.070073, PMID: 17600123

Fujisawa T, Kage M, Ushijima K, Kimura A, Ono E, Kato H. 1994. Alagille syndrome with a spontaneous appearance of the interlobular bile ducts. *Pediatrics International* **36**:506–509. DOI: https://doi.org/10.1111/j.1442-200X.1994.tb03235.x, PMID: 7825452

Gilbert MA, Bauer RC, Rajagopalan R, Grochowski CM, Chao G, McEldrew D, Nassur JA, Rand EB, Krock BL, Kamath BM, Krantz ID, Piccoli DA, Loomes KM, Spinner NB. 2019. Alagille syndrome mutation update: comprehensive overview of JAG1 and NOTCH2 mutation frequencies and insight into missense variant classification. *Human Mutation* **40**:2197–2220. DOI: https://doi.org/10.1002/humu.23879, PMID: 31343788

Hadchouel M, Hugon RN, Gautier M. 1978. Reduced ratio of portal tracts to paucity of intrahepatic bile ducts. *Archives of Pathology & Laboratory Medicine* **102**:402. PMID: 580878

Hankeova S. 2021. DUCT. *Software Heritage*. swh:1:rev:6b0b0eb88bbaf9bfc4f8ee42cafa4c122866fbba. https://archive.softwareheritage.org/swh:1:dir:afbad9c713d7371c41db68b434647c147709600c;origin=https://github.com/JakubSalplachta/DUCT;visit=swh:1:snp:078f3064f3631c5a2055016f6184b774fccacba4;anchor=swh:1:rev:6b0b0eb88bbaf9bfc4f8ee42cafa4c122866fbba/

Hannezo E, Scheele C, Moad M, Drogo N, Heer R, Sampogna RV, van Rheenen J, Simons BD. 2017. A unifying theory of branching morphogenesis. *Cell* **171**:242–255. DOI: https://doi.org/10.1016/j.cell.2017.08.026, PMID: 28938116

Hofmann JJ, Zovein AC, Koh H, Radtke F, Weinmaster G, Iruela-Arispe ML. 2010. Jagged1 in the portal vein mesenchyme regulates intrahepatic bile duct development: insights into alagille syndrome. *Development* **137**:4061–4072. DOI: https://doi.org/10.1242/dev.052118, PMID: 21062863

Kaneko K, Kamimoto K, Miyajima A, Itoh T. 2015. Adaptive remodeling of the biliary architecture underlies liver homeostasis. *Hepatology* **61**:2056–2066. DOI: https://doi.org/10.1002/hep.27685, PMID: 25572923

Kerschnitzki M, Kollmannsberger P, Burghammer M, Duda GN, Weinkamer R, Wagermaier W, Fratzl P. 2013. Architecture of the osteocyte network correlates with bone material quality. *Journal of Bone and Mineral Research* **28**:1837–1845. DOI: https://doi.org/10.1002/jbmr.1927, PMID: 23494896

Kline TL, Zamir M, Ritman EL. 2011. Relating function to branching geometry: a micro-CT study of the hepatic artery, portal vein, and biliary tree. *Cells Tissues Organs* **194**:431–442. DOI: https://doi.org/10.1159/000323482, PMID: 21494011

Klohs J, Rudin M, Shimshek DR, Beckmann N. 2014. Imaging of cerebrovascular pathology in animal models of Alzheimer's disease. *Frontiers in Aging Neuroscience* **6**:1–30. DOI: https://doi.org/10.3389/fnagi.2014.00032, PMID: 24659966

Lee TC, Kashyap RL, Chu CN. 1994. Building skeleton models via 3-D medial surface Axis thinning algorithms. *CVGIP: Graphical Models and Image Processing* **56**:462–478. DOI: https://doi.org/10.1006/cgip.1994.1042

Li L, Krantz ID, Deng Y, Genin A, Banta AB, Collins CC, Qi M, Trask BJ, Kuo WL, Cochran J, Costa T, Pierpont ME, Rand EB, Piccoli DA, Hood L, Spinner NB. 1997. Alagille syndrome is caused by mutations in human Jagged1, which encodes a ligand for Notch1. *Nature Genetics* **16**:243–251. DOI: https://doi.org/10.1038/ng0797-243, PMID: 9207788

Mašek J, Andersson ER. 2017. The developmental biology of genetic Notch disorders. *Development* **144**:1743–1763. DOI: https://doi.org/10.1242/dev.148007, PMID: 28512196

Masyuk TV, Ritman EL, LaRusso NF. 2001. Quantitative assessment of the rat intrahepatic biliary system by three-dimensional reconstruction. *The American Journal of Pathology* **158**:2079–2088. DOI: https://doi.org/10.1016/S0002-9440(10)64679-2, PMID: 11395385

Masyuk TV, Ritman EL, LaRusso NF. 2003. Hepatic artery and portal vein remodeling in rat liver: vascular response to selective cholangiocyte proliferation. *The American Journal of Pathology* **162**:1175–1182. DOI: https://doi.org/10.1016/S0002-9440(10)63913-2, PMID: 12651609

McDaniell R, Warthen DM, Sanchez-Lara PA, Pai A, Krantz ID, Piccoli DA, Spinner NB. 2006. NOTCH2 mutations cause alagille syndrome, a heterogeneous disorder of the notch signaling pathway. *The American Journal of Human Genetics* **79**:169–173. DOI: https://doi.org/10.1086/505332, PMID: 16773578

Mouzaki M, Bass LM, Sokol RJ, Piccoli DA, Quammie C, Loomes KM, Heubi JE, Hertel PM, Scheenstra R, Furuya K, Kutsch E, Spinner NB, Robbins KN, Venkat V, Rosenthal P, Beyene J, Baker A, Kamath BM. 2016. Early life predictive markers of liver disease outcome in an international, multicentre cohort of children with alagille syndrome. *Liver International* **36**:755–760. DOI: https://doi.org/10.1111/liv.12920, PMID: 26201540

Ober EA, Lemaigre FP. 2018. Development of the liver: insights into organ and tissue morphogenesis. *Journal of Hepatology* **68**:1049–1062. DOI: https://doi.org/10.1016/j.jhep.2018.01.005, PMID: 29339113

Oda T, Elkahloun AG, Pike BL, Okajima K, Krantz ID, Genin A, Piccoli DA, Meltzer PS, Spinner NB, Collins FS, Chandrasekharappa SC. 1997. Mutations in the human Jagged1 gene are responsible for alagille syndrome. *Nature Genetics* **16**:235–242. DOI: https://doi.org/10.1038/ng0797-235, PMID: 9207787

Renier N, Adams EL, Kirst C, Wu Z, Azevedo R, Kohl J, Autry AE, Kadiri L, Umadevi Venkataraju K, Zhou Y, Wang VX, Tang CY, Olsen O, Dulac C, Osten P, Tessier-Lavigne M. 2016. Mapping of brain activity by automated volume analysis of immediate early genes. *Cell* **165**:1789–1802. DOI: https://doi.org/10.1016/j.cell.2016.05.007, PMID: 27238021

Riely CA, Cotlier E, Jensen PS, Klatskin G. 1979. Arteriohepatic dysplasia: a benign syndrome of intrahepatic cholestasis with multiple organ involvement. *Annals of Internal Medicine* **91**:520–527. DOI: https://doi.org/10.7326/0003-4819-91-4-520, PMID: 484950

Schaub JR, Huppert KA, Kurial SNT, Hsu BY, Cast AE, Donnelly B, Karns RA, Chen F, Rezvani M, Luu HY, Mattis AN, Rougemont AL, Rosenthal P, Huppert SS, Willenbring H. 2018. De novo formation of the biliary system by TGFβ-mediated hepatocyte transdifferentiation. *Nature* **557**:247–251. DOI: https://doi.org/10.1038/s41586-018-0075-5, PMID: 29720662

Short KM, Smyth IM. 2016. The contribution of branching morphogenesis to kidney development and disease. *Nature Reviews Nephrology* **12**:754–767. DOI: https://doi.org/10.1038/nrneph.2016.157, PMID: 27818506

Slott PA, Liu MH, Tavoloni N. 1990. Origin, pattern, and mechanism of bile duct proliferation following biliary obstruction in the rat. *Gastroenterology* **99**:466–477. DOI: https://doi.org/10.1016/0016-5085(90)91030-A, PMID: 1694804

Spinner NB, Leonard LD, Krantz ID. 1993. *Alagille Syndrome*: GeneReviews(R).

Susaki EA, Tainaka K, Perrin D, Kishino F, Tawara T, Watanabe TM, Yokoyama C, Onoe H, Eguchi M, Yamaguchi S, Abe T, Kiyonari H, Shimizu Y, Miyawaki A, Yokota H, Ueda HR. 2014. Whole-brain imaging with single-cell resolution using chemical cocktails and computational analysis. *Cell* **157**:726–739. DOI: https://doi.org/10.1016/j.cell.2014.03.042, PMID: 24746791

Tanimizu N, Kaneko K, Itoh T, Ichinohe N, Ishii M, Mizuguchi T, Hirata K, Miyajima A, Mitaka T. 2016. Intrahepatic bile ducts are developed through formation of homogeneous continuous luminal network and its dynamic rearrangement in mice. *Hepatology* **64**:175–188. DOI: https://doi.org/10.1002/hep.28521, PMID: 26926046

Vartak N, Damle-Vartak A, Richter B, Dirsch O, Dahmen U, Hammad S, Hengstler JG. 2016. Cholestasis-induced adaptive remodeling of interlobular bile ducts. *Hepatology* **63**:951–964. DOI: https://doi.org/10.1002/hep.28373, PMID: 26610202

Wagner R, Van Loo D, Hossler F, Czymmek K, Pauwels E, Van Hoorebeke L. 2011. High-resolution imaging of kidney vascular corrosion casts with Nano-CT. *Microscopy and Microanalysis* **17**:215–219. DOI: https://doi.org/10.1017/S1431927610094201, PMID: 21122193

Walter TJ, Sparks EE, Huppert SS. 2012. 3-Dimensional resin casting and imaging of mouse portal vein or intrahepatic bile duct system. *Journal of Visualized Experiments* **1**:e4272. DOI: https://doi.org/10.3791/4272

Wei W, Popov V, Walocha JA, Wen J, Bello-Reuss E. 2006. Evidence of angiogenesis and microvascular regression in autosomal-dominant polycystic kidney disease kidneys: a corrosion cast study. *Kidney International* **70**:1261–1268. DOI: https://doi.org/10.1038/sj.ki.5001725, PMID: 16883324

jove

DUCT: Double Resin Casting followed by Micro-Computed Tomography for 3D Liver Analysis

Simona Hankeova[*,1], **Jakub Salplachta**[*,2], **Noemi Van Hul**[1], **Michaela Kavkova**[2], **Afshan Iqbal**[1], **Tomas Zikmund**[2], **Jozef Kaiser**[2], **Emma R. Andersson**[1]

[1] Karolinska Institutet [2] Central European Institute of Technology

[*] These authors contributed equally

Corresponding Authors

Jozef Kaiser
jozef.kaiser@ceitec.vutbr.cz

Emma R. Andersson
emma.andersson@ki.se

Abstract

The liver is the biggest internal organ in humans and mice, and high auto-fluorescence presents a significant challenge for assessing the three-dimensional (3D) architecture of the organ at the whole-organ level. Liver architecture is characterized by multiple branching lumenized structures, which can be filled with resin, including vascular and biliary trees, establishing a highly stereotyped pattern in the otherwise hepatocyte-rich parenchyma. This protocol describes the pipeline for performing double resin casting micro-computed tomography, or "DUCT". DUCT entails injecting the portal vein and common bile duct with two different radiopaque synthetic resins, followed by tissue fixation. Quality control by clearing one lobe, or the entire liver, with an optical clearing agent, allows for pre-screening of suitably injected samples. In the second part of the DUCT pipeline, a lobe or the whole liver can be used for micro-computed tomography (microCT) scanning, (semi-)automated segmentation, and 3D rendering of the portal venous and biliary networks. MicroCT results in 3D coordinate data for the two resins allowing for qualitative as well as quantitative analysis of the two systems and their spatial relationship. DUCT can be applied to postnatal and adult mouse liver and can be further extended to other tubular networks, for example, vascular networks and airways in the lungs.

Introduction

Organ resin casting is a technique that dates back to the 17th century[1]. One of the first examples of modern resin casting was performed on the human liver from an autopsy. Intrahepatic bile ducts were filled with a contrast agent mixed with gelatin, followed by imaging with an x-ray CT scan[2].

The aim of the DUCT technique is to visualize, digitalize and analyze two tubular resin-casted networks, in tandem, in 3D.

DUCT is based on the extensive existing knowledge of single-system liver resin casting[3,4,5,6,7,8] and extends to simultaneous 3D visualization and analysis of two systems[9].

DUCT advanced single resin casting to double resin casting by mixing two radiopaque resins of different contrast and injecting these resins into two different networks, specifically the common bile duct and portal vein. DUCT can be applied to young postnatal mice with reproducible results as early as postnatal day 15 (P15). Compared to microscopy-based imaging techniques, the main advantage is that DUCT is faster, antibody-free, and liver tissue autofluorescence does not interfere with imaging. Further, DUCT provides quantitative data describing lumenization status, internal diameter, network connectivity, and perfusion. Differentiating between the presence of lumen-forming cells and their de facto morphogenesis into tubes is essential for analyzing organs in which ductular cells are present but do not form tubes, as can be the case in Alagille syndrome[10]. The main disadvantage of DUCT is the limited penetration of the resin, which is viscous and does not enter tubes with a small caliber (<5 μm). DUCT can be applied for any tubular structure after determining the injection entry point, such as the arterial and venous circulatory systems, airways, the extrahepatic bile duct, or lymphatic vessels. It could thus facilitate whole organ architecture analysis of other tissues such as lungs and pancreas.

MicroCT segmented images can be processed using commercially available imaging software, such as ImageJ, or custom-written pipelines (e.g., MATLAB). The resin-injected liver can be analyzed qualitatively for network expansion and connectivity or quantitatively for volume, length, branching, tortuosity of a single system, and the interaction between two systems such as the distance between two systems, or branchpoint dependence (does system 1 branch in proximity to system 2 branching?). The DUCT pipeline encompassing resin injection, microCT scanning, and CT data segmentation, combined with detailed quantitative analysis of architectural

mechanisms of two tubular systems, could provide a standard for whole liver analysis in animal models.

Protocol

The protocol described in this study was approved and follows the animal welfare rules and regulations of the Stockholms Norra Djurförsöksetiska nämnd (Stockholm animal research ethics board). The animals used in this study were wild type or homozygous Jag1H268Q mutant mice on a mixed C3H/N and C57bl6J background. Both males and females were included in the study. The animals were used at postnatal day 15 or as adults between 3 - 8 months.

1. Double resin injections

1. Preparation

   1. Prepare resin solution. For double system resin injections, prepare both yellow and green resins as described in the steps 1.1.2-1.1.4.

   2. Prepare 1 mL aliquots of diluted resin per mouse.

   3. Yellow Resin: Dilute yellow silicone rubber (high radiopacity) with the clear diluent in a 3:1 dilution to prepare yellow resin for injection.

   4. Green Resin: Mix blue silicone rubber (undetectable radiopacity) with the clear diluent in a 1:1 dilution to prepare blue resin. To generate green resin, mix the diluted blue resin with the diluted yellow resin at a ratio of 1:1. Vortex the green resin thoroughly until the color is homogeneous.

      NOTE: Blue resin has very low radiopacity that is not detectable with microCT, which therefore necessitates dilution with yellow resin to create two resins with different radiopacities.

CAUTION: Resin may contain lead chromate, which is a carcinogen. It produces poisonous gases in a fire. Handle with care and dispose of the resin as hazardous waste.

5. Prepare two injection sets (injection set #1 and injection set #2) with tubing as described in the steps 1.1.6-1.1.11.

   NOTE: For adult mice (>P30 (postnatal day 30) = P30 - 2 years), use injection set #1 (PE10 tubing with 0.6 mm outer diameter) for common bile duct injection and injection set #2 (PE50 tubing with 0.96 mm outer diameter) for portal vein injection. For young postnatal mice (up to P30), prepare two #1 injection sets, one for bile duct and one for portal vein injection (no injection set #2 as the portal vein is too narrow to accommodate PE50 tubing).

6. To prepare injection set #1, cut 30 cm of PE10 tubing and stretch one end of the tubing by hand by pulling it until it becomes as thin as possible (**Figure 1A,B**, approximately 0.15 mm diameter, non-stretched PE10 tubing is 0.6 mm diameter).

7. Cut the tip of the stretched PE10 tubing diagonally to create a beveled tip (**Figure 1B**).

8. Connect the non-stretched end of the PE10 tubing to a 30 G needle (**Figure 1A**, Injection set #1).

9. To prepare injection set #2, cut 30 cm of PE50 tubing and stretch one end of the tubing by hand by pulling it until it becomes thin enough to fit into the portal vein (**Figure 1A,B**, approximately 0.7 mm, non-stretched PE50 tubing is 0.96 mm diameter).

10. Cut the tip of the stretched PE50 tubing diagonally to create a beveled tip (**Figure 1B**).

11. Connect the non-stretched end of the PE50 tubing to a 23 G needle (**Figure 1A**, injection set #2).

    NOTE: Each injection set can only be used for one injection since the resin will harden in the syringe and tubing. Adjust the size of the stretched and beveled tip based on the size of the common bile duct and portal vein of the mouse, depending on its age, genotype, and phenotype. When unsure about the size and fit of the tubing, insert the tubing in the appropriate duct or vessel after the incision and before the tubing is filled with resin. If the tubing is too wide to fit in the duct/vessel, stretch it further.

12. Anesthetize the animal by isoflurane inhalation (first 4% in the induction chamber and ~2% using the nose cone).

13. Place the mouse on a ventilated bench on a dissection pad while the mouse is breathing isoflurane through the nose cone. Verify that the animal is unconscious by an institute/IRB-recommended method, e.g., by pinching one of the paws.

    CAUTION: Isoflurane may cause drowsiness or dizziness upon inhalation and may cause damage to the cardiovascular system and central nervous system through prolonged or repeated exposure. Do not inhale it. Handle the substance on a ventilated bench and in well-ventilated areas.

    NOTE: It is possible to use another anesthetizing method, as long as it is compatible with cardiac perfusion.

14. Once the animal is unconscious, spray the ventral side with 70% ethanol to prevent interference from fur.

15. Using skin scissors, cut the skin, fascia, and muscle layer starting at the midline of the abdominal cavity and cut through to the thoracic cavity to expose the internal organs.

16. Grab the xiphoid process with forceps to lift the sternum and cut the diaphragm and rib cage on both sides to expose the heart and lungs.

17. Remove the rib cage by cutting through the ribs on the left and right sides of the ribcage with scissors. Take extra care not to damage the liver as this will result in leakage of the resin.

18. Using straight forceps, pull the heart towards the liver and cut away the right atrium.

19. Insert a butterfly needle (23 G), connected to a peristaltic perfusion pump, into the left ventricle. Perfuse the mouse transcardially with Hanks balanced salt solution (HBSS) and heparin (1 U/g of mouse body weight). Perfuse for 3 min with a perfusion rate of 5 mL/min.
    NOTE: If the mouse is being perfused correctly, the internal organs will become pale, especially the liver. If, instead, the lungs are turning white, the needle is inserted into the right ventricle and should be repositioned. After perfusion, the mouse is exsanguinated and can be removed from the nose cone and isoflurane.

20. Turn off the isoflurane pump.

2. Resin injection - Biliary system resin casting

   1. Move the mouse to the dissection microscope, abdomen up, tail towards the experimenter, and head away from the experimenter. The anatomical landmarks of interest are depicted in **Figure 2A**.

   2. Locate the inferior vena cava (**Figure 2A**) by moving the intestine to the side. Use spring scissors to make a small transversal incision in the inferior vena cava to allow the release of hepatic vascular pressure (**Figure 2Bi**).

   3. Expose the common bile duct and portal vein as described in steps 1.2.4- 1.2.6.

   4. Move the intestine and pancreas to the right side (of the experimenter) using a phosphate-buffered saline (PBS)-wetted cotton swab.

   5. Flip the ventral side of the liver towards the heart using the PBS-wetted cotton swab to expose the visceral surface and the hilar region.

   6. Locate the common bile duct that runs from the hilar region across the pancreas and into the intestine at the sphincter of Oddi (**Figure 2Bii**, common bile duct outlined with the yellow dotted line, black arrowheads point to Sphincter of Oddi).
      NOTE: Make sure the liver is moist throughout the procedure by sprinkling it with PBS.

   7. Clear surrounding tissue (area ~ 5 mm) from the common bile duct using straight forceps. Place silk suture thread (size 4-0, 0.17 mm, 3 - 5 cm long) under the common bile duct (**Figure 2Bii**) and tie a loose overhand knot around the common bile duct (**Figure 2Biii**).
      NOTE: Choose an area for the knot halfway between the hilar region and the sphincter of Oddi and at some distance from the portal vein so that after the suture is tightened around the common bile duct, it will not interfere with the portal vein injection.

   8. Hold the spring scissors flat against the common bile duct to make an oblique incision to the common bile

jove.com   September 2021 · 175 · e62941 · Page 4 of 19

duct at the spot where the common bile duct enters the pancreas and intestine next to the sphincter of Oddi. (**Figure 2Biv**), yellow dotted line outlines the sphincter of Oddi region, emphasized by black arrowheads).

NOTE: This is a crucial step. Make an oblique and not a transversal cut, and make an incision; do not sever the bile duct. Cutting through the entire bile duct makes insertion of the tubing very challenging.

9. Just before use, mix 1 mL of the yellow resin with 50 µL of the curing agent (by filling and emptying the 1 mL syringe) and fill a 1 mL Luer syringe with the resin - curing agent mixture.

10. Connect the filled syringe with the tubing (set #1). Press the plunger to fill the tubing completely. Ensure that the resin/curing agent mix drips from the tip of the tubing.

NOTE: Avoid and remove bubbles in the syringe and tubing for best results.

11. Using forceps, straighten the area around the common bile duct incision and insert the tubing into the opening in the common bile duct (**Figure 2Bv**), with the longest edge of the beveled tip downwards towards the dorsal side of the bile duct. This orientation ensures that resin can exit the tubing opening, which is facing upwards, into the duct (**Figure 2Bv**).

12. Tighten the silk thread knot to secure the tubing inside the common bile duct (**Figure 2Bvi**).

13. Inject the resin into the common bile duct. Observe the gall bladder and the individual liver lobes.

14. Massage the liver with a PBS-wetted cotton swab to help spread the resin equally. Resin-filled bile ducts'

terminal branches (in wild-type mice) are faintly visible at the liver surface.

NOTE: Expected time to fill the liver is 30 -100 s.

15. Stop injecting the resin when dots of resin appear at the surface of the liver (**Figure 2Ci**, blue arrowheads) or when resistance is met.

NOTE: Work as fast as possible since the resin begins to harden after adding the resin curing agent. The working time from adding the curing agent is approximately 15 min.

16. Remove the tubing by pulling it out of the common bile duct and quickly tighten the silk knot using forceps to prevent the resin from leaking out. Cut away the loose ends of the silk suture, so they do not interfere with the portal vein injection.

17. Dispose of the tubing containing resin and the remaining resin into the hazardous waste and the needle into the sharps waste.

3. Resin injection - Portal vein resin casting

1. Clear the portal vein (area ~5 mm) from its surrounding tissue about 2 cm from its entry to the liver using straight forceps. Place silk suture thread (size 4-0, 0.17 mm, 3 - 5 cm long) under the cleared area of the portal vein (**Figure 2Ci**) and tie a loose overhand knot (**Figure 2Cii**).

2. Make a longitudinal incision in the portal vein distal to the liver and the knot (**Figure 2Ciii**).

3. Mix 1 mL of the green resin with 50 µL of the curing agent (by filling up and emptying a 1 mL syringe) and fill the 1 mL Luer syringe with the resin-curing agent mixture.

4. Connect the filled syringe with the tubing (set #2 for >P30 mice, new set #1 for <P30 mice). Press the plunger to fill the tubing completely. Ensure that the resin drips from the tip of the tubing.

   NOTE: Avoid and remove bubbles in the syringe and tubing for best results.

5. Using forceps, straighten the portal vein by pulling the surrounding tissue towards the experimenter and insert the tubing with the longest edge of the beveled tip towards the dorsal side of the vessel (**Figure 2Ciii**).

6. Tighten the silk thread to secure the tubing in the portal vein.

7. Inject the resin into the portal vein. Observe the blood vessels filling up with resin. Massage the liver with a PBS-wetted cotton swab to help spread the resin equally (**Figure 2Civ**).

8. Stop injecting the resin when all blood vessels are filled (ends of portal veins are visible at the liver periphery) or when resistance is met.

   NOTE: Work fast since the resin begins to harden after the addition of the curing agent. The working time from adding the curing agent is approximately 15 min for injection set#1 and 25 min for injection set #2.

9. Remove the tubing by pulling out the tubing from the portal vein and quickly tighten the silk knot using forceps to prevent the resin from leaking out.

10. Dispose of the tubing containing resin and the remaining resin into the hazardous waste and the needle into the sharps waste.

4. Liver dissection and fixation

1. Dissect out the whole liver by cutting it away from the surrounding tissue and the diaphragm.

2. Gently place the whole liver in an empty 50 mL conical tube with the ventral side facing up and the dorsal side resting on the wall of the conical tube to prevent deformation of the liver. Store the conical tube horizontally overnight at 4 °C for the resin to harden completely.

   NOTE: Any container that is big enough to fit the liver can be used instead of 50 mL conical tube. Using a flat bottom container will increase the likelihood that the liver is not deformed.

3. Separate the liver into individual lobes. Make a selection of the lobes that will be used for microCT analysis (1.4.4-1.4.5) or quality control (1.4.6-1.4.8). Optionally use the whole liver for both optical clearing and microCT without separating it into individual lobes.

   NOTE: Liver architecture of the biliary and vascular systems is different in each lobe, and matched lobe analyses are therefore required. The optical clearing does not interfere with microCT scanning, and the lobe(s) used for quality control can be subsequently scanned with microCT. Conversely, samples scanned with microCT can be subsequently optically cleared for comparison. The whole liver analysis is thus possible. In wild-type mice (C3H/C57bl6 genetic background), the right medial lobe is filled first by resin injections, making this a suitable lobe for microCT analysis, with the highest reproducibility. The left lateral lobe is the biggest lobe, in which it is therefore straightforward to pre-screen for injection quality. The selection of the lobe (or whole liver) used for quality control and

microCT scanning is dependent on the animal model and research question.

4. In a ventilated hood, prepare 4% formaldehyde solution (10 -20 mL per tube). Fix the lobes used for microCT with 4% formaldehyde overnight at 4 °C and afterward wash once with PBS (10 -20 mL per tube).

5. Collect formaldehyde waste in a separate container. Keep the liver lobes in PBS at 4 °C for short-term storage or 70% ethanol for long-term storage. Proceed with section 2: Micro-computed tomography.

CAUTION: Formaldehyde causes acute toxicity if swallowed, inhaled, or in contact with skin. Formaldehyde is a flammable liquid and vapor. It causes severe skin burns and eye damage. May cause an allergic skin reaction. Fatal if inhaled (concentrated or in powder). May cause respiratory irritation. Suspected of causing genetic defects. May cause cancer. Causes damage to organs (eyes, central nervous system). Precautionary statements - keep away from heat, hot surfaces, sparks, open flames, and other ignition sources. No smoking. Wear protective gloves and protective clothing. In case of spillage, immediately take off all clothing that was contaminated. If in contact with the skin: rinse the contaminated area with water. If inhaled: remove person to fresh air and monitor breathing if comfortable. Immediately call a poison center/ doctor. If in eyes: rinse eyes with water for several minutes. If present and possible, remove contact lenses.

6. For quality control, fix the remaining lobes (at least one) with 50% methanol (mixed with deionized water) for a minimum of 4 h, rocking at room temperature, followed by 100% methanol overnight rocking at room temperature. Collect methanol waste in a separate container.

CAUTION: Methanol causes acute toxicity if swallowed, inhaled, or in contact with skin. Methanol is a flammable liquid and vapor. Wear protective gloves and clothing. Avoid breathing when handling and keep away from fire and heat. Wash skin thoroughly after using. In case of spillage, immediately take off all contaminated clothing. Rinse skin with water. If inhaled: Remove person to fresh air and keep comfortable for breathing. If inhaled, swallowed, or exposed, call a poison center/ doctor.

7. In a ventilated hood, prepare benzyl alcohol and benzyl benzoate (BA: BB, 1:2) (5 -10 mL per lobe) solution.

8. Place the liver lobe in a 15- or 50- mL polypropylene tube (depending on the size of the lobe) containing BABB solution. Leave it rocking at room temperature until transparent. This step can take between 2-16 h depending on the size of the lobe.

NOTE: The BABB solution dissolves certain types of plastic. It is safe to store the samples in polypropylene tubes or glass containers.

CAUTION: Benzyl benzoate can cause acute toxicity when swallowed. It is toxic to aquatic life with long-lasting effects. Precautionary statements: wash skin thoroughly after handling. It is harmful when swallowed, in contact with skin, or inhaled. Avoid breathing fume/vapors. Wash hands thoroughly after handling. Do not eat, drink or smoke when using this product. If swallowed - call a poison center/doctor if unwell Use in ventilated areas.

jove.com   September 2021 · 175 · e62941 · Page 7 of 19

Collect spillage. Dispose of contents/container to an approved waste disposal plant.

9. Inspect the quality of the injection. Only well-injected liver should be scanned with microCT.

2. Micro-computed tomography

1. Sample preparation

    1. Prepare 1% agarose gel by mixing 100 mL of distilled water and 1 g of agarose powder. Place the mixture in a microwave and boil the solution until the agarose powder dissolves.

    2. Temper the 1% agarose gel to ~40 °C to avoid thermal damage to the liver sample.

    3. Place the lobe(s) of interest in a 15 mL conical tube and fill it with the 1% agarose gel to approximately 2/3 of the total volume of the tube. This step minimizes undesired sample motion during CT measurement.

2. CT measurement
   NOTE: The following steps are CT device-dependent, and specific settings and actions may differ for different CT devices and manufacturers. In this protocol, the micro-computed tomography scanner used was equipped with a nanofocus X-ray tube (180 kV/15 W), and flat-panel dynamic 41|100 (4048 px x 4048 px, pixel size 100 mm with binning 2) for the CT measurements.

    1. Mount the 15 mL conical tube with the sample on the rotational stage of a CT device and allow it to thermally adapt to the measurement chamber for at least 1 h.

    2. When the sample is thermally adapted, center it in the Field of View (FOV).

3. Optimize the source-sample and sample-detector distances (SSD, SDD) to reach sufficient voxel resolution, e.g., 12 µm for an adult murine liver sample or 6.5 µm for <P30 liver, corresponding to dimensions of FOV (for beforehand specified hardware) 24.3 mm × 24.3 mm and 13.2 mm × 13.2 mm respectively.

4. Set the acquisition parameters (i.e., accelerating voltage and current, exposure, binning, averaging) following the CT device manufacturer's recommendations to reach a sufficient level of detected signal.These parameters are not only CT device-dependent but also sample-dependent and should be optimized for each sample. In Hankeova et al.[9], the settings were: 80 kV accelerating voltage, 160 µA accelerating current, 400 ms exposure time, and 2000 images.

5. Start a CT measurement. Use a dedicated tomographic reconstruction software to reconstruct the CT data.

3. Analysis and data segmentation

NOTE: The following steps are image-processing software-dependent; specific settings and actions may differ depending on the software used.

1. Load the CT data: Select **File > Import > Command**. A further selection is dependent on the specific format of the CT data to be processed.

2. Use the function **Surface Determination** on the top panel to segment the resin in the data using global thresholding. In the dialog window, determine the threshold value with histogram evaluation by setting the position of the red "Isovalue" line to segment only the

resin-filled vessels (i.e., encompassed by the yellow line in the presented "Preview panel") (**Figure 3A**).

3. On the left panel, select the module **Create ROI from Volume/CAD/Mesh** to create a region of interest (ROI) of the resin-filled vessels. In the dialog window, use the option **Create ROI(s) from Solid**, select the name of the processed volume and confirm.

4. Eliminate erroneous segmentation of noise clusters in the background region of this ROI. Mark this ROI on the right panel, right-click on it and select the module **Split ROI**.

5. In the dialog window, set the **Minimum Volume [voxel]** parameter to exclude all the noise particles - this value is experiment- and data-dependent and must be optimized for each sample to be analyzed (**Figure 3B**).

6. Create smooth, continuous, and solid canal masks without artifacts in the resin-cast ROI - e.g., presence of air bubbles or resin leakage.

7. On the left panel, use the module **Smoothing**, set the **Smoothing Strength** parameter to 1 or 2 (depending on the individual data, when higher values might lead to model deformation, especially when dealing with fine structures). If needed, run this process twice (**Figure 3C**).

8. Identify and separate the individual tubular systems in the segmented resin mask.

   1. Create a separate ROI for the system filled with the more absorptive resin (the yellow resin used for the common bile duct injection) with higher intensity values in the CT data. Follow the procedure described in step 3.2. (**Figure 3Di**).

   2. Mark the new ROI and the resin mask ROI, right-click and select **Subtract ROI(S)** and subtract the new ROI from the resin mask ROI to create a new ROI for the remaining tubular system (**Figure 3Dii, iii**).

9. Export the resulting ROIs for both tubular systems in various formats, based on operator preferences, for subsequent processing in different software. Further, process the resulting ROIs in a volume graphics software to export the final visualization in the form of an image or a video.

Representative Results

What to do

Successful double resin injection is achieved when both the intrahepatic bile ducts and portal vein vasculature are well filled. As a quality control step, clearing one lobe (for example, the left lateral lobe) allows for verification of a successful injection, followed by imaging of lobes of interest. The optically cleared lobe can be scanned later using microCT; hence it is possible to optically clear the whole liver. In well-injected mouse liver, the portal vein vasculature should be filled with resin until the liver periphery and resin should be visible in side-branches (**Figure 4**), and this architecture is faithfully recapitulated in microCT scanned and segmented data. Further, well-injected intrahepatic bile ducts should be visible next to the main portal vein branches extending almost to the periphery, and resin should be visible in the major side branches. If the control lobe passes the quality control step, the lobes of interest (included the optically cleared one) can be scanned with microCT. The result of the segmented data from a well-injected liver is shown for a P15 mouse (**Figure 4A,B**) and an adult mouse (**Figure 4C,D**).

What not to do

Intact liver tissue is a prerequisite for successful injection. Take extra care when cutting the abdominal cavity and diaphragm not to accidentally nick the liver tissue. If there is

physical damage to the liver during this procedure, the resin is very likely to leak out during portal vein injection (**Figure 5A**). It is not possible to achieve a good injection of the vascular system if the liver is physically damaged.

One of the common mistakes is underfilling the liver with resin that can lead to challenges for visualization or analysis. One of the causes for system underfilling is resin hardening prematurely in the needle or the tip of the tubing before the injection is completed (**Figure 5B**, blue arrowheads, brackets depict large bubbles). A good practice is to use one injection set per animal and work fast after the curing agent is added to the resin. If the resin hardens during the injection (which can be observed by a half-filled system, here exemplified with a half-filled portal vein vasculature) remove the tubing, cut the tip of the tubing (always diagonally to create a beveled tip), and push the plunger. If resin begins to drip again, carefully re-insert the tubing and secure it with the suture. If the resin has hardened in the needle, replace the tubing completely, fill it with resin (avoiding bubbles), carefully re-insert the tubing, and secure it with the suture. It can be challenging to replace the tubing, especially in young postnatal mice <P30, as the tissue is more fragile. Another cause of poor resin filling of portal vein vasculature can be insufficient transcardial perfusion (**Figure 5C**, blue arrowheads denote blood visible in terminal branches). This can be observed when the tips of the vessels are filled with blood instead of resin. To avoid this, ensure that the portal vein (outside the liver) does not contain any blood before the injection. The third cause of underfilled liver is when the tubing is inserted too deep into the liver and enters a branch towards one of the lobes. To prevent this, insert the tubing at a minimum of 0.5 cm from the entry to the liver.

Conversely, one, or both, of the systems become overfilled with resin (**Figure 5D**). It is necessary to visually monitor the liver throughout the injection. Biliary system casting with resin is more challenging than portal vein resin casting since resin-filled ducts are only faintly visible on the liver surface, and it is difficult to assess when the system is nearly full and when to stop. When small yellow resin dots appear on the liver surface (**Figure 2Ci**, blue arrowhead), this is a sign that the biliary system is completely filled, and the resin is starting to leak out of the ducts. Minor resin leakage can be manually corrected during microCT data segmentation (**Figure 5D**, right panels).

If the injection pressure is too high, this can cause vessels or ducts to rupture (**Figure 5E**), irreversibly damaging vessel or duct architecture. The liver will not be suitable for microCT scanning or analysis. To avoid resin overfilling, optimize the right volume and pressure used for injection in each mouse model. When working with mice that have been challenged with a toxic diet, genetic modification, or liver injury that affects the biliary or venous systems, or liver stiffness, the injection pressure and volume may need to be adjusted as volume and pressure tolerated may be different from the wild type mice. This protocol describes the manual injection of the two systems, but it is possible to connect the syringe to a pump to standardize the injection pressure. Bubbles are another very common injection artifact that leads to sparse filling of the tubular networks (**Figure 5F-H**, blue arrowheads). To avoid bubble formation, make sure that the syringe and tubing do not contain any bubbles, are completely filled with resin, and the resin is dripping from the tip of the tubing before injection. Small bubbles that appear as negative areas on the microCT data can be manually corrected during post-processing steps, although this is laborious.

Fresh is the best

Using fresh yellow resin is a crucial factor, significantly affecting the contrast of the two resins and the microCT data segmentation. When the freshly opened resin is used (**Figure 6A**) there is a clear difference in contrast between the yellow resin-injected bile ducts (bright white) and the green resin-injected portal veins (bright grey). Liver that is injected with fresh resin is easily processed using automated global thresholding. With prolonged storage, the resin precipitates, and the contrast diminishes. After 3 months of storage, the contrast can still be sufficient to distinguish the portal vein from the bile duct (**Figure 6B**), but precipitation affects the mixing of the two resins, which is visible as a heterogeneous

opacity in the filled portal vein (Fig 6B, blue arrowheads). Heterogeneous contrast negatively affects the automated thresholding and necessitates manual corrections, which increases the processing time. If the resin is older than six months, the contrast has degraded to a point at which it is not possible to distinguish the yellow-injected bile duct from the green-injected portal vein based on their contrast alone (**Figure 6C**). In this case, the bile duct and portal vein must be segmented manually based on their diameter and position in the hilar region and followed manually throughout the entire microCT data. This procedure is extremely time-consuming and best avoided.
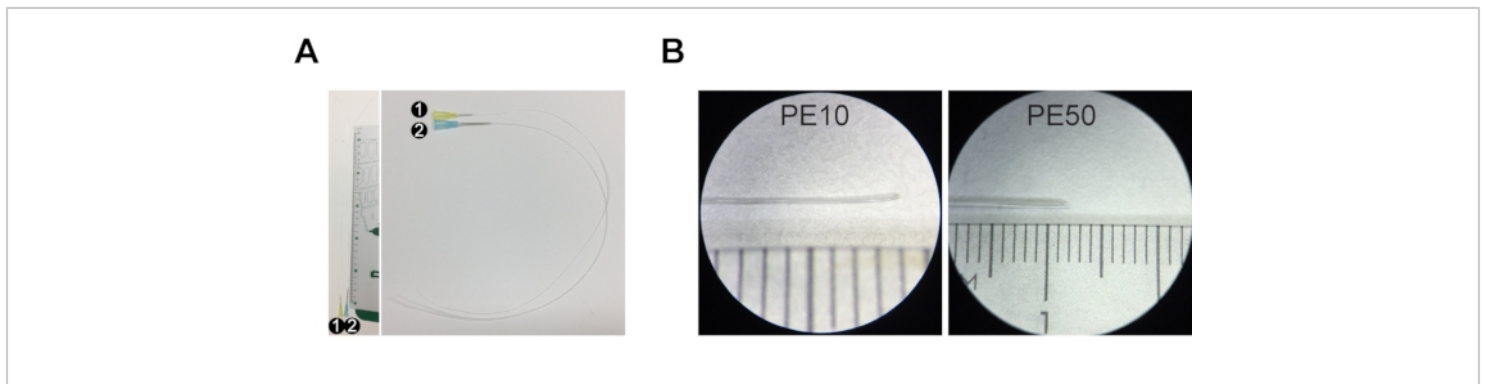

Figure 1: Injection set for resin casting. (**A**) Injection set #1 comprises a 30 G needle and PE10 tubing that is ~30 cm long. Injection set #2 is composed of a 23 G needle and PE50 tubing ~30 cm long. (**B**) The tip of the tubing is stretched and cut at an angle to create a beveled tip. The ruler in A and B is a centimeter ruler, with major increments of 1 cm, intermediate increments of 5 mm, and minor increments of 1 mm. Please click here to view a larger version of this figure.
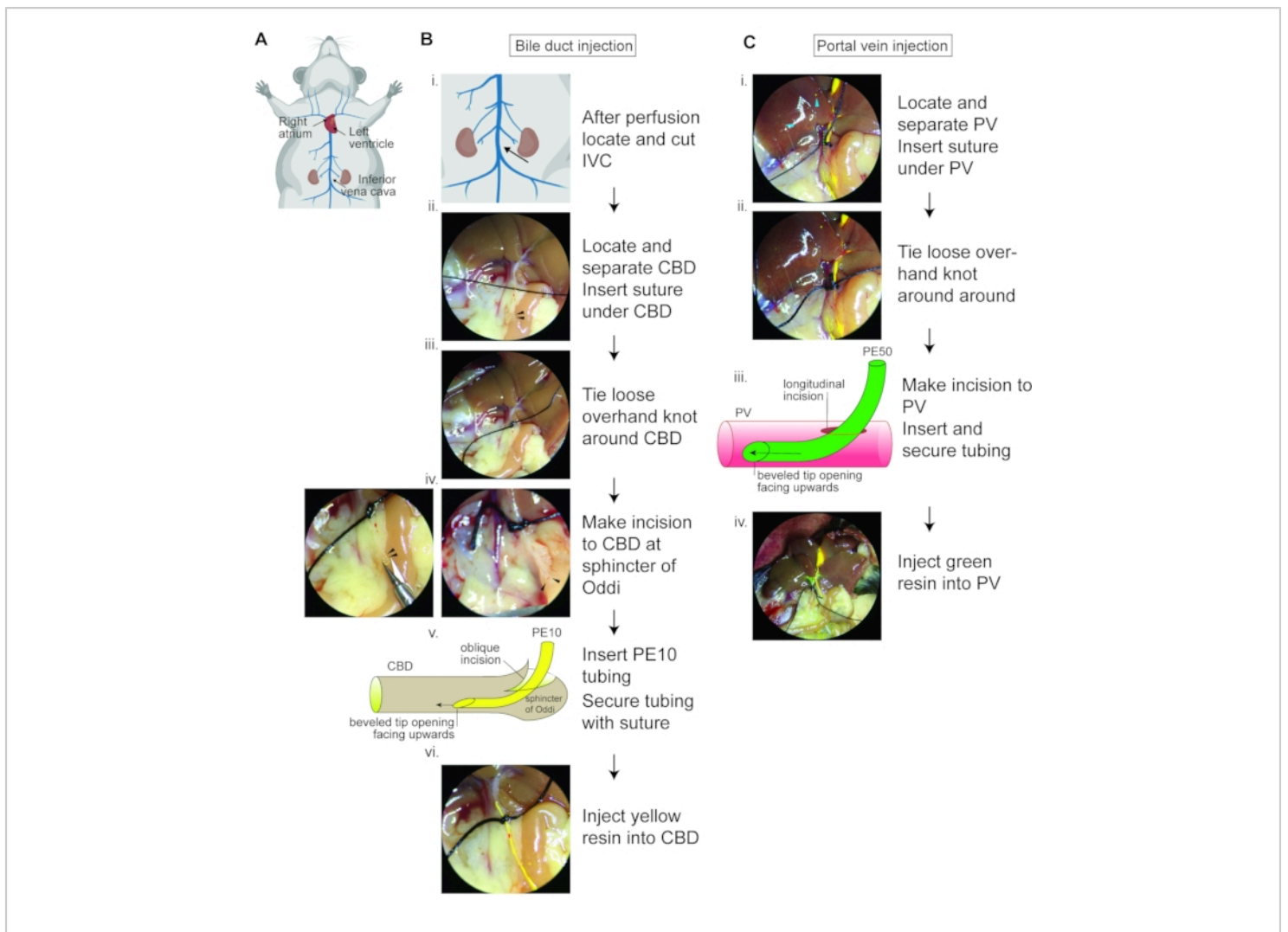
Figure 2: Double resin casting flow chart. (**A**) Schematic showing the murine venous circulatory system and the heart with highlighted right atrium, which should be cut away before perfusion, and the left ventricle into which the needle should be inserted for perfusion to wash away the blood from the circulatory system. The inferior vena cava should be severed under the kidneys to relieve vascular pressure. (**B**) Bile duct resin injection flow chart. (i) Zoom image of (**A**) depicting where to sever the IVC. (ii) Image depicting the common bile duct (yellow dotted line) from the liver hilar region to the sphincter of Oddi (black arrowheads), with suture thread under the cleared common bile duct. (iii) Suitable position for loose overhand knot around common bile duct. (iv) The yellow dotted line and black arrowheads label the sphincter of Oddi, demonstrating the oblique angle for incision and how the opening should appear after the oblique angle incision. (v) Schematic demonstrating the orientation of the PE10 tubing bevel opening (upwards) upon insertion. (vi) Appearance of yellow resin being injected; resin should easily pass the loosely tied knot. IVC, inferior vena cava; CBD, common bile duct. (**C**) Portal vein resin injection flow chart. (i) The green dotted line marks the portal vein from the hilar region. The blue arrowheads label the overfilled biliary system. (ii) Suitable location for loose overhand knot around portal vein. (iii) Schematic

demonstrating the bevel opening (upward) upon insertion. (iv) Appearance of liver upon injection of green resin and yellow resin; note the resin-filled blood vessel in the liver periphery. PV, portal vein. **Figure 2A** was created with Biorender.com. Please click here to view a larger version of this figure.
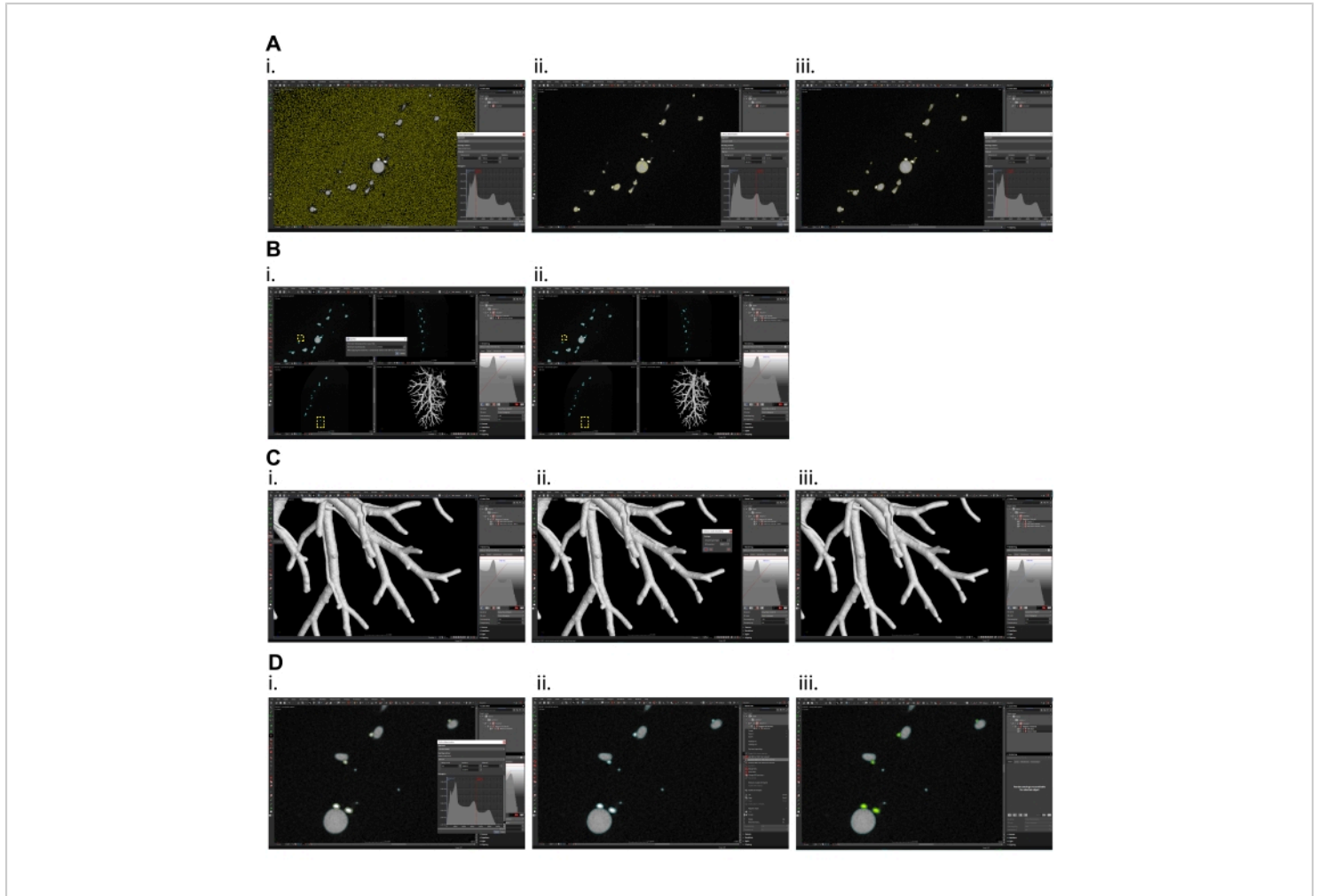

Figure 3: Micro CT data processing in volume graphics software. (**A**) Surface determination, (i) overestimated isovalue (current preview of selection is shown in yellow color), (ii) underestimated isovalue, (iii) optimal selection of isovalue for proper surface determination of portal vein and bile ducts. (**B**) Splitting region of interest (ROI) created by surface determination, (i) set the value in dialog window high enough that only one segment (the largest one) will remain, (ii) in yellow frames the smaller (excluded) particles are shown. (**C**) Surface smoothing of the data, (i) smoothing function is on the left panel, (ii) set the smoothing strength to 1 (max. 2) and create new smoothed ROI, (iii) smoothed data. (**D**) Separation of individual tubular systems, (i) in surface determination function set the isovalue so that only the biliary system is included in selection (current preview of selection is shown in yellow color), (ii) mark the ROI of both systems and ROI of only the biliary system and subtract biliary system ROI from ROI of both systems, (iii) Portal vein shown in grey, the biliary system shown in green. Please click here to view a larger version of this figure.
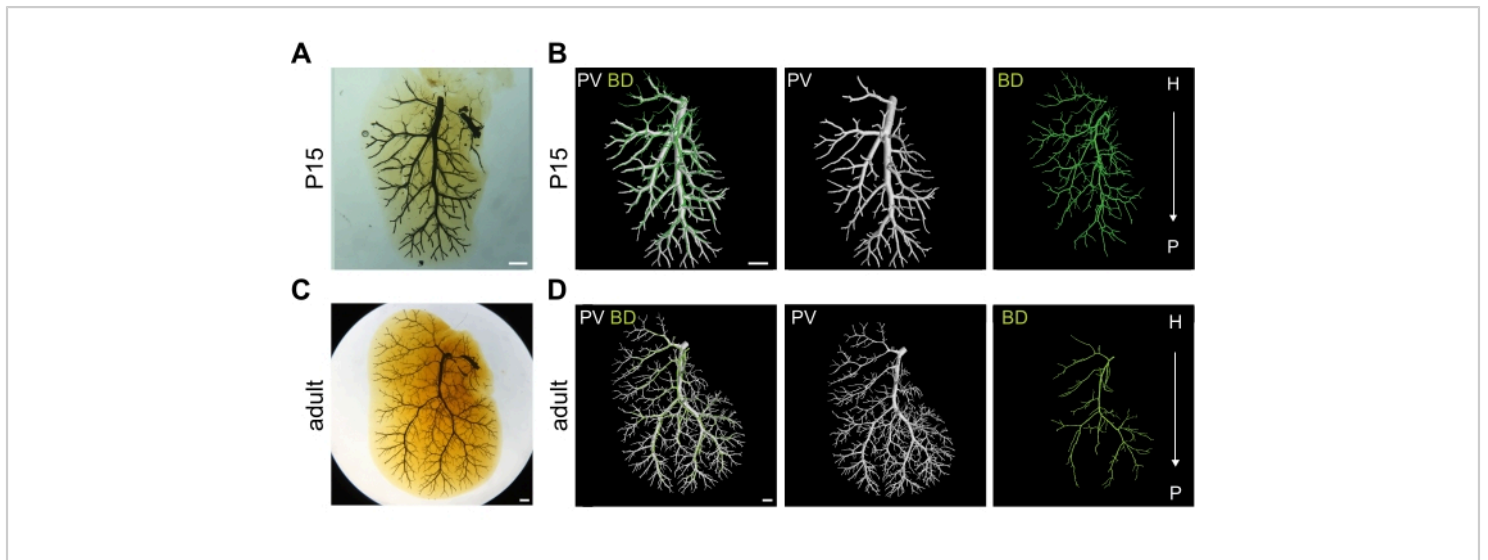
Figure 4: Well-injected bile duct (BD) and portal vein (PV) systems. (**A**) Optically cleared right medial lobe (RML) of postnatal day 15 (P15) liver injected with two resins into the two systems. Scale bar 1 mm. (**B**) 3D rendering of P15 RML shown in (**A**) depicting portal vein vasculature in white and biliary system in green. Scale bar 1 mm. (**C**) Optically cleared RML of adult liver injected with two resins into the two systems. Scale bar 1 mm. (**D**) 3D rendering of adult RML shown in (**C**) depicting portal vein vasculature in white and biliary system in green. H = hilar, P = peripheral. Scale bar 1 mm. Panels A, B, D are adapted with permission from Hankeova et al.[9]. Please click here to view a larger version of this figure.
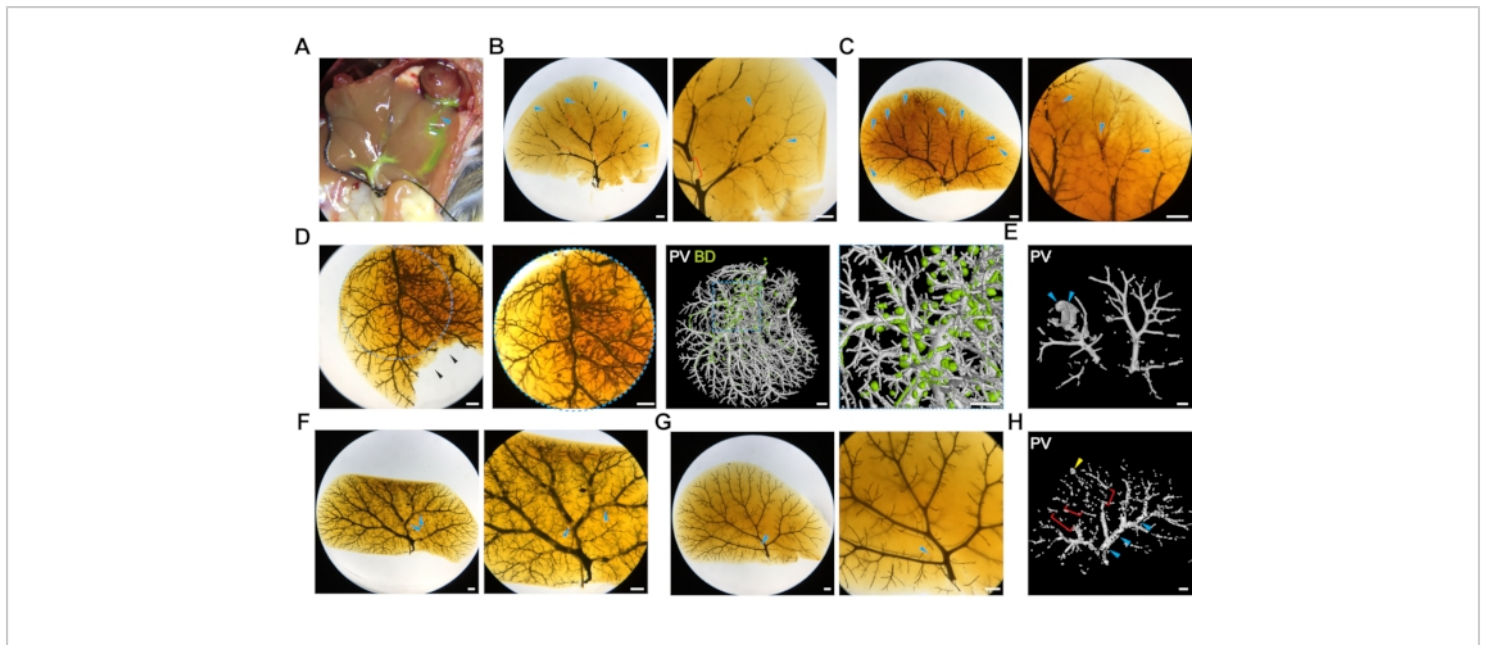
Figure 5: Common challenges of double resin liver injections. (**A**) The image depicts a liver that was accidentally nicked during the initial opening of the abdominal cavity, and the resin is leaking through the cut (blue arrowhead). (**B**) Poorly injected portal vein system due to resin hardening. Blue arrowheads label empty terminal branches, and red brackets label large bubbles. Scale bar 1 mm. (**C**) Poorly injected portal vein system due to poor transcardial perfusion. Blue arrowheads label blood visible in the terminal branches. Scale bar 1 mm. (**D**) Overfilled biliary system manifested by isolated balls of resin. The left panels show the optically cleared liver, and the right panels show the 3D microCT rendered image. The blue dotted outlines depict zoom-in regions. The black arrowheads label a part of the liver that was damaged during the optical clearing after microCT scanning. Scale bar 1 mm. (**E**) High pressure during resin injection can cause rupture of the portal vein (the animal in this panel carries a Jag1H268Q mutation), marked by blue arrowheads. Scale bar 1 mm. (**F**) Bubbles in the resin during portal vein injection (blue arrowheads) and (**G**) biliary system injection (blue arrowhead), scale bar 1 mm. (**H**) MicroCT scan of bubbles (blue arrowhead), poorly filled terminal branches (red brackets) and resin leakage (yellow arrowhead), scale bar 1 mm. Please click here to view a larger version of this figure.
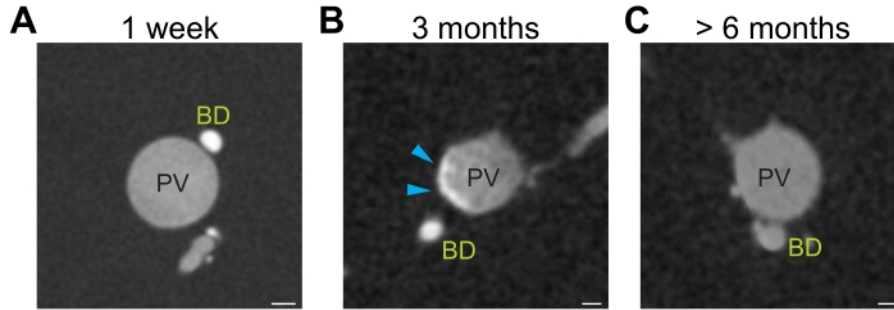
Figure 6: Differential resin contrast. (**A**) Freshly opened yellow resin generates sufficient contrast to distinguish resin injected portal vein (grey) and bile ducts (white). (**B**) Three months storage of yellow resin lead to precipitation of the resin resulting in heterogeneous opacity (grey-white portal vein, blue arrowhead). (**C**) Prolonged storage (>6 months) of yellow resin diminishes the contrast between the portal vein (grey) and bile ducts (grey). Scale bar 100 µm. Please click here to view a larger version of this figure.

Discussion

Several critical steps determine DUCT success, from sample preparation to the parameters of the CT device. To achieve the best results, well contrasted, well-injected, and bubble-free resin should be used to allow straightforward digital processing with automated thresholding to obtain 3D data, images, and movies. With training and following this protocol, 90% of injections are successful and result in reproducible data. It is important to use fresh yellow resin to achieve the best contrast between the two injected systems. The yellow resin has a very strong radiopacity, while the blue resin has undetectable radiopacity. Top results are achieved within the first three months after opening a new yellow resin bottle. With time, resin precipitates, and after longer storage (>6 months), the yellow and the green resins will no longer be distinguishable in CT scans. Images with poor contrast necessitate extensive and time-consuming manual tracing and segmentation of the two systems. Next, well-stretched tubing is indispensable to fit into the common bile duct of

adult mice and common bile duct and portal vein of postnatal mice. The entry point for the injection must be created with care. If the common bile duct is cut open transversally, it is likely to detach from the surrounding tissue, preventing successful entry of the tubing. This step is especially delicate for postnatal mice in which the common bile duct retracts and "curls up" if it has detached from its surrounding tissue, making insertion of the tubing extremely challenging. The common bile duct entry and injection may require some practice. While preparing the tubing with resin and throughout injection, avoid bubble formation as bubbles will create negative space in the CT images and require time-consuming manual correction. It is important to gently massage the liver by rolling over its surface with a wetted cotton swab during and after the injection procedure as this facilitates even resin spreading. After the completion of injection and removal of the tubing, the silk suture knot must be tightened quickly and carefully, so the resin does not flow out of the liver before it polymerizes completely. For successful microCT imaging,

the sample must be properly fixed in place with agarose and thermally adapted to eliminate movement artifacts in the CT data. The acquisition settings are also of key importance, which should be optimized to reach an adequate spatial resolution to resolve fine structures.

Technical modifications to the injection procedure can be made to achieve injection in younger mice. Currently, resin casting of younger mouse livers is limited by the availability of sufficiently thin tubing, with PE10 being the smallest commercially available tubing. Tanimizu et al. successfully injected carbon ink into embryonic day 17 (E17) common bile duct using glass capillaries[11]. Future testing of whether resin can be delivered via glass capillary would therefore be of interest. DUCT was further adapted to inject other tubular systems such as the airways and pulmonary artery vasculature of the lungs[9]. The double resin injection could also be modified to be used with other commercially available resins, or this protocol could be used for injections with carbon ink.

One of the main limiting factors of the DUCT pipeline is the resin viscosity. DUCT can only be used for resin casting of tubular structures above a diameter of 5 μm. In this data set, the resin could penetrate tubes with the smallest diameter of 5 μm[9]. This size limitation precludes the analysis of fine ductules and small capillaries. To further advance the DUCT pipeline to smaller caliber vessels, other commercially available resins should be tested, or the development of new low-viscosity radiopaque agents may improve the lumen penetration.

In Hankeova et al.[9], DUCT was compared to two other commonly used techniques, double carbon ink injections followed by tissue clearing and standard photography, and iDISCO+ with staining of the blood vessels with alpha-

smooth muscle cell actin and bile ducts with cytokeratin 7, followed by 3D imaging[9]. DUCT outperformed the other two methods in terms of dual analysis (which was challenging for iDISCO+ due to high liver autofluorescence), 3D imaging, and quantification (not possible with carbon ink injection), and lumenization (DUCT provides data for the internal lumen architecture and system perfusion). As mentioned above, the main limitation of DUCT is the minimum lumen size that can be injected and analyzed (5 μm limit), a parameter in which both carbon ink injection and iDISCO+ performed better. DUCT is superior to single system resin casting[3,5,6] because it allows analysis of each injected system separately and also facilitates dual 3D investigation to study the architectural relationship between the two systems.

DUCT can be applied to study any two tubular networks in 3D. As proof of principle, DUCT was used to visualize the liver biliary and portal vein systems and the pulmonary artery vasculature and airways in lung[9]. The intrahepatic bile ducts develop adjacent to the portal vein, and the portal vein provides a structural template and signaling center that regulates the growth and differentiation of the biliary tree[12]. In Hankeova et al.[9], DUCT explored biliary regeneration in a mouse model for the human pediatric disease Alagille syndrome. DUCT revealed previously unreported architectural mechanisms that the biliary system used to achieve a wild-type-like volume[9]. The Alagille syndrome mice utilized two different strategies: (1) in the hilar and central regions of the liver, the biliary system increased its branching, and (2) in the liver periphery, the de novo-generated bile ducts were highly tortuous. These two factors combined to yield a near-normal biliary system volume, despite the abnormal architecture. Furthermore, DUCT detected abnormal bile duct branching that occurred independent of portal vein branching and bile ducts forming connecting bridges between two portal

veins[9]. These phenotypes would be impossible to detect in single resin casting and could be misinterpreted in 2D histological sections as bile duct proliferation. DUCT thus provides data describing the 3D architecture of two tubular networks at the whole organ or lobe level with the possibility of qualitative and in-depth quantitative analysis. DUCT could be a new standard for postnatal liver development and liver regeneration analyses in different animal models.

Disclosures

Acknowledgments

References

1. Narat, J. K., Loef, J. A., Narat, M. On the preparation of multicolored corrosion specimens. *The Anatomical Record.* **64**, 155-160 (1936).

2. Ludwig, J. et al. Anatomy of the human biliary system studied by quantitative computer-aided three-dimensional imaging techniques. *Hepatology.* **27**, 893-899 (1998).

3. Masyuk, T. V., Ritman, E. L., LaRusso, N. F. Quantitative assessment of the rat intrahepatic biliary system by three-dimensional reconstruction. *American Journal of Pathology.* **158**, 2079-2088 (2001).

4. Masyuk, T. V., Ritman, E. L., LaRusso, N. F. Hepatic artery and portal vein remodeling in rat liver: Vascular response to selective cholangiocyte proliferation. *American Journal of Pathology.* **162**, 1175-1182 (2003).

5. Sparks, E. E. et al. Notch signaling regulates formation of the three-dimensional architecture of intrahepatic bile ducts in mice. *Hepatology.* **51**, 1391-1400 (2010).

6. Cuervo, H. et al. Endothelial notch signaling is essential to prevent hepatic vascular malformations in mice. *Hepatology.* **64**, 1302-1316 (2016).

7. Thakurdas, S. M. et al. Jagged1 heterozygosity in mice results in a congenital cholangiopathy which is reversed by concomitant deletion of one copy of Poglut1 (Rumi). *Hepatology.* **63**, 550-565 (2016).

8. Walter, T. J., Sparks, E. E., Huppert, S. S. 3-Dimensional resin casting and imaging of mouse portal vein or intrahepatic bile duct system. *Journal of Visualized Experiments: JoVE.* **68**, e4272 (2012).

9. Hankeova, S. et al. DUCT reveals architectural mechanisms contributing to bile duct recovery in a mouse model for Alagille syndrome. *Elife.* **1**, 1-29 (2021).

10. Andersson, E. R. et al. Mouse model of Alagille syndrome and mechanisms of Jagged1 missense mutations. *Gastroenterology.* **154**, 1080-1095 (2018).

11. Tanimizu, N. et al. Intrahepatic bile ducts are developed through formation of homogeneous continuous luminal network and its dynamic rearrangement in mice. *Hepatology.* **64**, 175-188 (2016).

12. Ober, E. A., Lemaigre, F. P. Development of the liver: Insights into organ and tissue morphogenesis. *Journal of Hepatology.* **68**, 1049-1062 (2018).

CCD and scientific-CMOS detectors for submicron laboratory based X-ray Computed Tomography

Jakub Salplachta[1], Tomas Zikmund[1], Martin Horvath[2], Yoshihiro Takeda[3], Kazuhiko Omote[3], Ladislav Pina[2], Jozef Kaiser[1]

[1]CEITEC - Central European Institute of Technology, Brno University of Technology, Purkynova 656/123, 612 00, Brno, Czech Republic, e-mail: jakub.salplachta@ceitec.vutbr.cz, tomas.zikmund@ceitec.vutbr.cz, jozef.kaiser@ceitec.vutbr.cz

[2]Rigaku Innovative Technologies Europe, s.r.o., Novodvorska 994, 142 21, Praha 4, Czech Republic, e-mail: Martin.Horvath@rigaku.com, Ladislav.Pina@rigaku.com

[3]Rigaku Corporation, 3-9-12, Matsubara-cho, Akishima-shi, Tokyo, 196-8666, Japan, e-mail: y-takeda@rigaku.co.jp, omote@rigaku.co.jp

Abstract

The key component of any CT (X-ray computed tomography) machine is a detection system. In area of scientific CT imaging applications three types of sensors are mainly used. These are amorphous silicon (α-Si) flat panels, complementary metal–oxide–semiconductor (CMOS) and charge-coupled device (CCD) sensors. Here the performance and comparison study of the two lastly named sensor types is conducted in field of high resolution CT imaging. CCD and novel sCMOS-based (scientific CMOS) detection systems are tested using high-resolution laboratory-based Rigaku nano3DX system (ability to achieve submicron voxel resolution). Properties of each camera were evaluated as well as the quality and noise properties of acquired data (both projection and CT data).

Keywords: X-ray imaging, X-ray Computed Tomography, image detectors, CCD, sCMOS, image quality evaluation

1 Introduction

For years, charge-coupled device (CCD) sensors have domininated scientific imaging applications. Recently, complementary metal-oxide semiconductor (CMOS) detectors and amorphous silicon (α-Si) flat panel detectors have become its main challengers [1]. CCD detectors poses the high image fidelity in terms of readout noise, quantum efficiency and dynamic range which were hardly met by other sensor types [1]. However, the CCD architecture, where each pixel is read sequentially, results in slow readout rate [1], which prevents its usage from measurement of fast dynamic processes. For area of CT imaging with high resolution (submicron range), detectors with pixel sizes of several hundred nanometers are utilized. This significantly improves detectability of CT system at submicron resolution even for a laboratory-based CT systems. To achieve the high image fidelity of CCD detector and preserving readout rate of standard CMOS sensors, new image sensors were developed specifically for scientific imaging applications. They were called scientific CMOS (sCMOS) [2].The purpose of this study was to compare the performance of a sCMOS-based detector with a CCD-based detector for submicron CT measurement at laboratory-based system in terms of image quality and scanning time. Rigaku nano3DX system [3] equipped with Rigaku's scientific X-ray CDD camera (XSight™ Micron LC X-ray CCD camera [4]) and scientific X-ray sCMOS camera (XSight™ Micron LC X-ray sCMOS camera [5]) was used in our study. Properties of each camera were evaluated as well as the quality and noise properties of acquired data. Several camera parameters were investigated e.g. achieved spatial resolution, modulation transfer function (MTF) and number of hot pixels. For data quality evaluation, acquired data of phantoms as well as selected samples were used. This evaluation was done in projection domain and also tomogram domain (i.e. CT data after tomographic reconstruction), for tomographic reconstruction ASTRA Tomography Toolbox [6] was used.

2 Materials and methods

2.1 Rigaku nano3DX

In our study the laboratory-based CT system Rigaku nano3DX [3] was used for data acquisition. This system is a true X-ray microscope which can be used for 3D CT data acquisition with submicron spatial resolution. Achieving such high resolution is accomplished by using a high power rotation anode X-ray source and high resolution detection system. For purposes or our comparison study this CT system was equipped with Rigaku's scientific X-ray CDD camera (XSight™ Micron LC X-ray CCD camera [4]) and scientific X-ray sCMOS camera (XSight™ Micron LC X-ray sCMOS camera [5]). In the nano3DX, the magnification takes place in the used detector using microscope optical elements which results in small sample to detector distances. Using such settings near-parallel beam geometry is achieved. This systems also enables switching anode materials to optimize contrast for specific sample types. In our study Cu and Mo targets materials were used. Apart from the material both targets differ in terms of used tube current and voltage (Cu: 40 kV and 30 mA, Mo: 50 kV and 24 mA) and also in shape and size of a X-ray spot (effective size at 6º take-off angle: Cu – 0.07 mm circle, Mo – 0.15 x 0.1 mm ellipse).

2.2 XSight™ Micron LC X-ray CCD/ sCMOS camera

As mentioned previously, Rigaku nano3DX CT system can be equipped by a CCD or sCMOS type X-ray camera, both using the same lens units set. The XSight™ Micron LC X-ray CCD camera is a scientific X-ray CCD camera whose imaging sensor is based on a full-frame CCD image sensor technology. The second tested camera was sCMOS version of the XSight™ Micron LC X-ray CCD camera whose imaging sensor is based on a sCMOS image sensor technology. Summary of the both cameras nominal parameters without a lens unit is listed below in Table 1.

Table 1: Nominal parameters of both tested cameras without a lens unit.

Technical features	CCD camera	sCMOS camera
Array size	3320(H) x 2500(V)	2048(H) x 2048(V)
Pixel size	5.4 μm	6.5 μm
Sensor diagonal	22.5 mm	18.8 mm
Nonlinearity	< 1%	0.2%
Dynamic range	2300 : 1	21 400 : 1
Acquisition gain	0.45 e$^-$/ADU	0.55 e$^-$/ADU
Readout noise	11 e$^-$ rms	1.4 e$^-$ rms
Readout rate	8 Mpix./s (approx. 1 fps)	40 fps (@ 16 bit)
Dark current	0.001 e$^-$/pix./s -35ºC	0.14 e$^-$/pix./s @ 0ºC
Binning	Independent on-chip binning in x, y	2 x 2, 3 x 3, 4 x 4, 8 x 8
Peak quantum efficiency	56% @ 540 nm	82% @ 550 nm
Shutter type	Electromechanical	Rolling shutter
Data interface	USB 2.0	USB 3.0

2.3 Acquired data

For comparison of both tested cameras various data types were acquired which are stated in Table 2, with used acquisition settings and evaluated parameters. For all measurements the sensors temperature was kept at 0 degrees. Used exposure times for X-ray projection data were selected based on optimal contrast (dependent on amount of detected signal) and also on analysis type. For comparison of both systems in terms of CT data acquisition the exposure time was first selected for CCD camera based on optimal contrast and the exposure for sCMOS camera was subsequently derived to achieve equal detected signal level as for CCD. The evaluated CT data of a ruby ball (0.3 mm diameter) and a glass cup sample were reconstructed, from only background and flat-field corrected projections, using ASTRA Tomography Toolbox [6] – FBP reconstruction with cosine filter. No data processing or corrections such as noise or ring artifacts reduction were used in our study. For some analysis DN (Digital numbers) of acquired data were converted to number of detected electrons using vendor's conversion specifications.

Table 2: List of acquired data with corresponding acquisition parameters and evaluated parameters.

Data	Acquisition parameters		Evaluated parameters
	CCD camera	sCMOS camera	
Bias frames	Exposure: 10 ms; Binning: 1x1; Pixel size: 5.5 μm; Frames: 10	Exposure: 10 ms; Binning: 1x1; Pixel size: 6.5 μm; Frames: 10	Read-out noise properties
Dark background frames	Exposure: 1-30 s; Binning: 1x1; Pixel size: 5.5 μm; Frames: 30	Exposure: 1-30 s; Binning: 1x1; Pixel size: 6.5 μm; Frames: 30	Dark current Number of hot pixels Number of random hot pixels
Bright frames	Target: Cu; Exposure: 1-30 s, 60 s; Binning: 1x1; Pixel size: 0.27 μm; Frames: 30, 20	Target: Cu; Exposure: 1-30 s, 30 s; Binning: 1x1; Pixel size: 0.32 μm; Frames: 30, 20	Noise properties Linearity
JIMA RT RC-02B frames	Target: Cu; Exposure: 30 s, 60 s; Binning: 1x1; Pixel size: 0.27 μm; Frames: 10/ chart position	Target: Cu; Exposure: 30 s; Binning: 1x1; Pixel size: 0.32 μm; Frames: 10/ chart position	Spatial resolution Data quality
CT data – Ruby ball (0.3 mm diameter)	Target: Mo; Exposure: 13 s; Binning: 2x2; Voxel size: 0.53 μm; Projections: 802	Target: Mo; Exposure: 4.5 s; Binning: 2x2; Voxel size: 0.64 μm; Projections: 802	Spatial resolution Data quality
CT data – Glass cup	Target: Cu; Exposure: 16 s; Binning: 2x2; Voxel size: 0.53 μm; Projections: 802	Target: Cu; Exposure: 6 s; Binning: 2x2; Voxel size: 0.64 μm; Projections: 802	Data quality

2.4   Evaluated properties

2.4.1   Noise properties

Noise is an inevitable compound of both CCD and sCMOS based images and can be described as unwanted variations of detected signal that result in non-exact representation of the original scene. Three main noise components in CCD and sCMOS data are shot (photon) noise, darkcurrent noise and readout noise. Shot noise is a property of quantum nature of light and arises from statistical fluctuations in the number of photons emitted from the object and can be described by Poisson statistics [7]. Darkcurrent noise comes from thermally generated electrons in the detector itself and is sometimes described as fixed pattern noise because it manifests as constant signal pattern. This type of noise is thermally dependent so it can be reduced by cooling the sensor. Readout noise represents a noise floor which is given by signal processing electronics. In our study we evaluated noise properties of CCD and sCMOS based sensors using bias frames, dark background frames and bright frames. From the bias frames readout noise was extracted using subtraction of average bias frame from other bias images. Readout noise was then quantified using standard deviation calculation. For quantification of dark current the linearity analysis of dark background frames was used. The dark background frames were acquired for exposures from 1 s to 30 s and from each frame mean bias frame was subtracted. Resulting dependence of average dark current signal on exposure time was then fitted using linear regression and the dark current was then defined as the slope of this fit. From the bright frames the total noise (compound of shot, dark current and readout noise) was quantified. Total noise was extracted from bright images using subtraction of average bright frame and quantified using standard deviation calculation and normalized noise power spectrum (NNPS). The NNPS is a characterization of the noise in the spatial frequency domain [8] and in our study we incorporated NNPS calculation as specified in IEC 62220-1: 2003(E) standard [9]:

$$NNPS\,(u,v) = \frac{1}{S^2} \cdot \frac{\Delta x \Delta y}{M \cdot 256 \cdot 256} \cdot \left(\left| DFT2(n_{ij}) \right|^2 \right), \tag{1}$$

where S denotes average signal in the subset, Δx and Δy are the pixel size in horizontal respectively vertical directions, M is number of subsets, DFT2 denotes the discrete 2D Fourier transform and $n_{i,j}$ is extracted 2D noise image from given subset.

2.4.2   Hot pixels

Hot pixels are considered as a type of fixed pattern noise. They can be defined as pixels with dark current significantly above the average [10]. Mostly they appear as bright dots, especially in dark frames, and their presence degrades image quality and is undesirable. Hot pixels can be detected by taking a long exposure image and creating a map of dark current across the image. Subsequently pixels that have a dark current value above a set threshold are labelled as hot pixels. In our study we implemented proposed procedure that involves analysis of dark background frames with 10 exposure levels from 20 s to 30 s. From such frames mean bias frames were subtracted so only dark current map images remained. In these images extreme dark values were detected using this formula:

$$g(x,y) = \begin{cases} 1, & if\ f(x,y) \geq\ M + 3 \cdot s \\ 0, & if\ f(x,y) <\ M + 3 \cdot s \end{cases} \tag{2}$$

where f(x,y) is analyzed dark current frame for given exposure, M is median dark current value and s is the standard deviation (both calculated from f) and g(x,y) is binary value of output binary image g both at corresponding spatial coordinates x, y. As hot pixels were then considered pixels with extreme dark current values whose positions was not changing within analyzed frames. In our study we also evaluated number of random hot pixels. These pixels are defined analogously as hot pixels but are mostly caused by scattered radiation. For detection similar scheme as for hot pixels was applied but in case of random hot pixels their positions were random within the frames.

2.4.3   Spatial resolution

For evaluation of spatial resolution of the nano3DX system with both tested cameras two approaches were used. In projection domain JIMA RT RC-02B resolution test [11] was conducted. Using such approach, spatial resolution was graphically analyzed by line profiles over selected pattern charts in both horizontal and vertical direction. Selected pattern charts were 0.5 µm, 0.6 µm and 0.7 µm. Projection data of each pattern were acquired in centered position regarding FOV (Field of View) and using best possible acquisition settings in terms of acquired contrast, effective pixel size and lowest binning. Such acquired data were subsequently background and flat-field corrected before the analysis. In resolution analysis representative frames for each pattern were used. Such frames were calculated by averaging of acquired frames where the extreme values were excluded from the calculation. This procedure was used to reduce noise in the data. To avoid any remaining effect of noise, analyzed line profiles were taken through a band of 100 pixels thickness. Second used approach was the evaluation of MTF (Modulation transfer function) which is considered as a measure of the spatial resolution of a liner imaging system. In our study, this function was calculated using procedure defined in: ASTM E1695-95(2013) standard [12]. As disk phantom a ruby ball with diameter 0.3 mm was used and corresponding CT data were acquired using acquisition parameters that simulated standard measurement scenario. From CT slice located at center of used phantom the composite edge disk profile was generated and used for calculation of the edge response function (ERF). From this function the point spread function (PSF) was obtained as the derivate. MTF was then calculated as unity normalized amplitude of PSF Fourier transform.

2.4.4 Linearity

Both tested cameras were also evaluated in terms of their linear response. In theory the detector detected signal should be linearly proportional to the amount of photons incident on the sensor. In our study the system linearity was verified using a graphical plot analysis of detected signal as a function of exposure time for bright frames. Linearity was then expressed as the root mean square of the distances between detected signal points and the linear regression fit line (a linear least-squares regression model was used).

2.4.5 Data quality

Image quality is one of the most influencing factors for subsequent data processing and analysis specifically for CT based dimensional metrology [13]. In our study we adopted image quality evaluation procedure presented by Kraemer et al. [13]. In their study they proposed utilization of several image quality measures based on projection data for optimization of CT acquisition parameters. These measures were: Contrast to Noise Ratio (CNR), Signal to Noise Ratio (SNR), Local Contrast (C), Variance (VAR), Sum of Modified Laplacians (SML) and Just Noticeable Blur (JNB). In our study those image quality measures were calculated for both projection and CT images and all measures were evaluated as average values of given parameter over 10 analyzed images. During these calculations operator manually selected evaluated areas such as background, object area or area covering object edges. In case of JNB calculation edge pixels were detected using Sobel edge detection operator and width parameter was calculated by performing an additional horizontal nonthinning Sobel operation on the original image. All quality measures were calculated for several data types stated in Table 2, evaluated was also situation when same exposure was used for both sensors. Apart from quantitative evaluation, quality of acquired data by tested cameras was also evaluated qualitatively.

3 Results and discussion

3.1 Noise properties and hot pixels analysis

Numerical results of conducted noise properties and hot pixels analysis are presented in Table 3. It is evident that CCD based camera poses higher readout noise and also the dark current compared to sCMOS based camera when cooling both sensors to 0 ºC. However, it was revealed that the total noise level was higher in sCMOS sensor acquired data (when equivalent signal was detected) which reflects the total noise standard deviation value (Table 3) and also both 1D and 2D normalized noise power spectras (Fig. 1 and Fig. 2). From these images it is evident that the biggest difference in total noise properties between both cameras was at lowest spatial frequencies. Specifically in sCMOS 2D total noise NNPS is evident high intensity cross (Fig. 2 b)). However, it was revealed that sCMOS based camera has higher hot pixels and random hot pixels rate. This results in reduced visual image quality of CT images as further discussed below.

Table 3: Results of noise properties and hot pixels analysis.

	Readout noise [e⁻ rms]	Dark current [e⁻/pix/s]	Total noise [e⁻ rms]	Hot pixels [%]	Random hot pixels [% / frame]
CCD	10.67	0.10	101.53	0.12	0.47
sCMOS	1.32	0.06	118.75	0.50	0.74

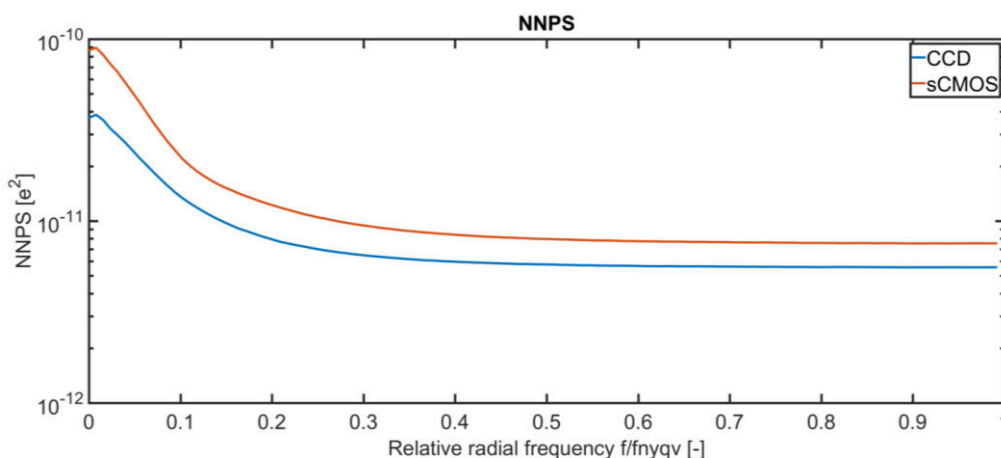Figure 1: 1D NNPS for both tested cameras.

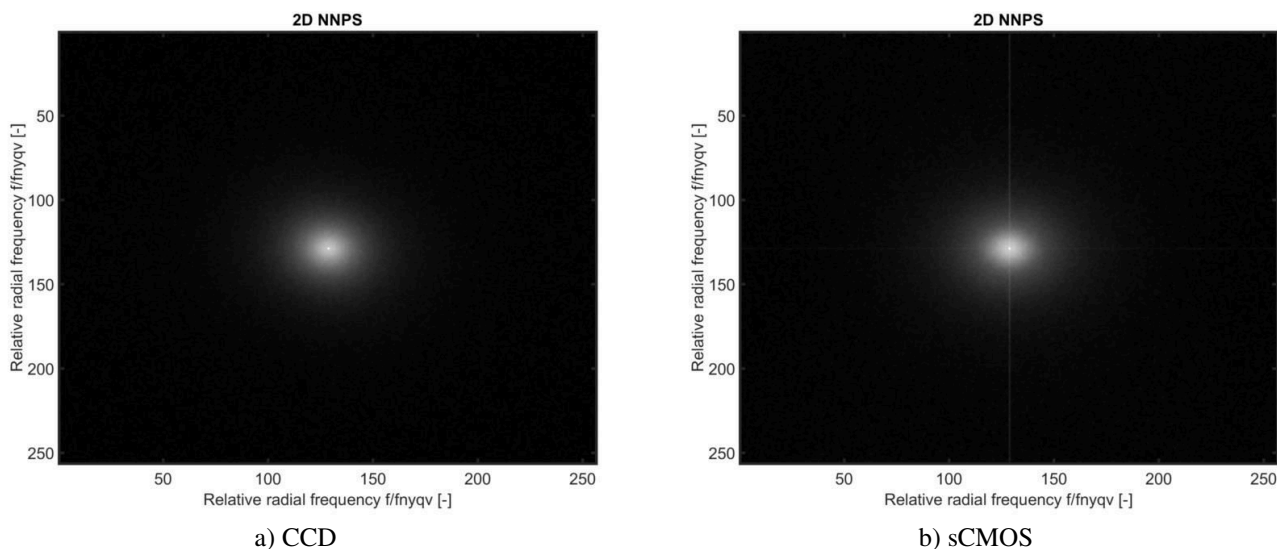a) CCD   b) sCMOS

Figure 2: 2D NNPS for both tested cameras.

3.2 Spatial resolution

Achieved spatial resolution of nano3DX system when using tested cameras was tested in both projection and tomogram domain using JIMA RT RC-02B resolution test and MTF analysis. It was revealed that in projection domain and the system was able to reach 0.5 µm resolution in both horizontal and vertical directions for both used cameras when using specified acquisition settings. In case of CCD based camera the resolution was comparable in both spatial direction (Fig. 3 a) and 3 b)). However in case of sCMOS, it was revealed that the resolution was higher in horizontal direction (Fig. 3 c) and 3 d)). In tomogram domain the numerical value of MTF at 10% level and known voxel size were used for spatial resolution calculation. It was revealed that there was slight difference between both systems in terms of MTF. The CCD based sensor reached 0.168 at 10 % level of MTF and the sCMOS based 0.167. Subsequently it was calculated that CCD based detection system achieved 1.58 µm spatial resolution and the sCMOS based system 1.91 µm for specified acquisition settings that reflected standard measurement scenario.

a) CCD – JIMA 0.5 µm chart, with labeled areas for spatial resolution line profile analysis.

b) CCD – JIMA 0.5 µm chart spatial resolution line profile analysis.

c) sCMOS – JIMA 0.5 µm chart, with labeled areas for spatial resolution line profile analysis.

d) sCMOS – JIMA 0.5 µm chart spatial resolution line profile analysis.
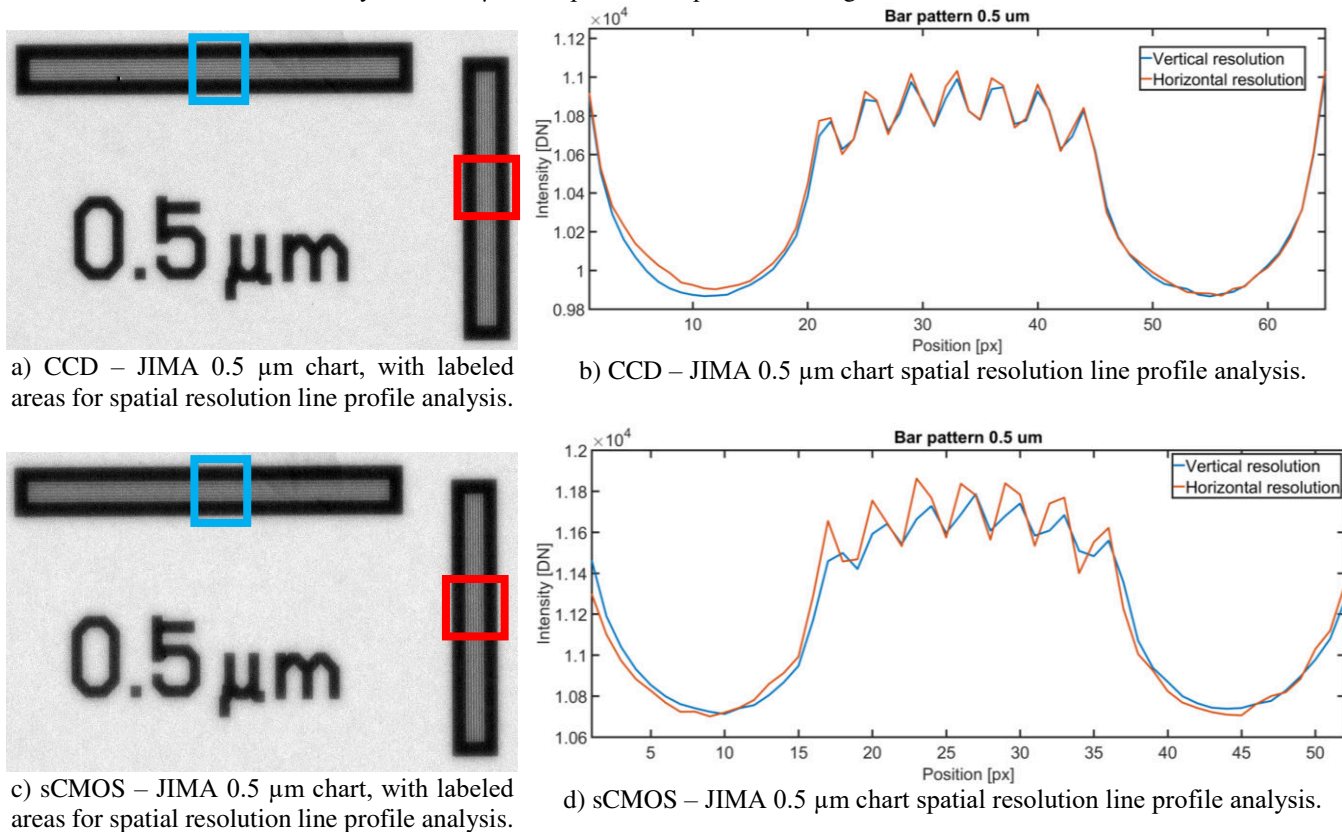
Figure 3: JIMA RT RC-02B resolution test

3.3 Linearity

Based on conducted linearity analysis of both tested cameras it was revealed that both detection systems have responses linearly proportional to amount of incident photons on the sensor (see. Fig. 4 and Fig. 5). For both cameras the root mean square error (RMSE) of the distances between detected signal points and the linear fit was found to negligible: for CCD sensor 9.93e-11 % and for sCMOS sensor 2.05e-10 %.
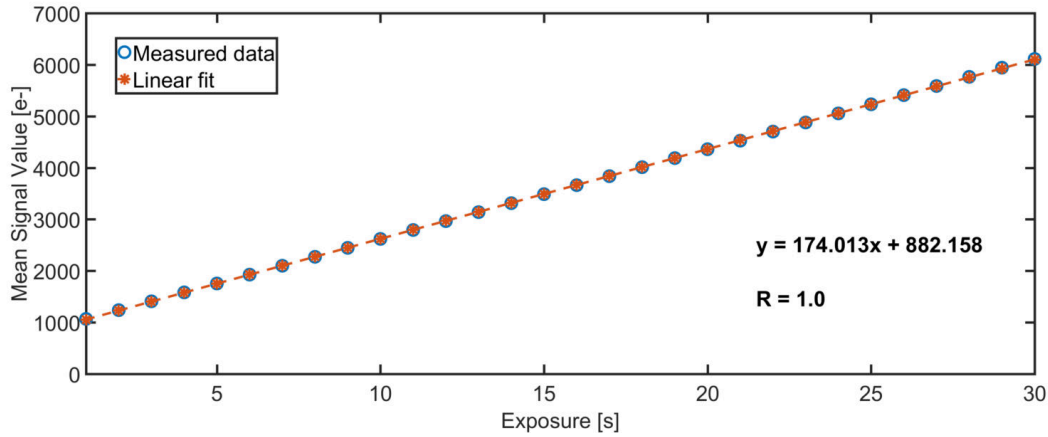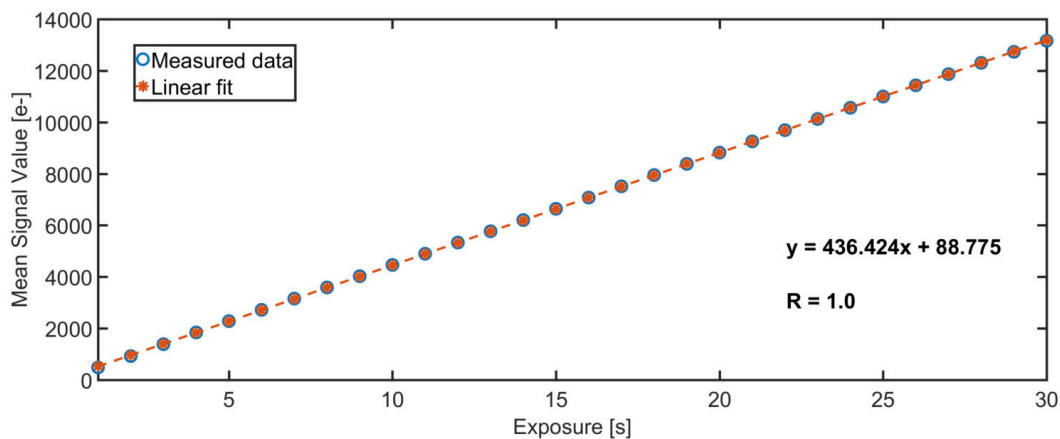

Figure 4: CCD bright frames linearity test.

Figure 5: sCMOS bright frames linearity test.

3.4 Data quality

As previously mentioned quality of data acquired by both tested cameras was evaluated quantitatively and qualitatively. Qualitative evaluation was done by visual perception of several operators. In projection domain there were no significant data quality differences between both cameras. However, in tomogram domain there were present severe ring artifacts in case of sCMOS acquired data (see Fig. 6). These artifacts were also present in CCD acquired data but not in such extent. This corresponds with results from hot pixels analysis where it was revealed that tested sCMOS sensor had four times larger percentage representation (related to sensor area) of hot pixels compared to tested CCD sensor. For quantitative quality evaluation six measures were calculated. These calculation was done in both projection and tomogram domain and the results are presented in Table 4 and Table 5. For all evaluated data the CCD sensor reached higher signal to noise ratio. Low SNR results in case of sCMOS sensor can correspond to hot pixels population that could affect the analysis, specifically in tomogram domain (see Table 5). In situation, when same exposure time was used during data acquisition of both tested cameras, sCMOS data of JIMA chart pattern reached better results compared to CCD data. Also for situations, when comparable signal was detected by both tested sensors, sCMOS based camera reached better or comparable results to CCD based camera.

a) Ruby ball – CCD

b) Ruby ball – sCMOS

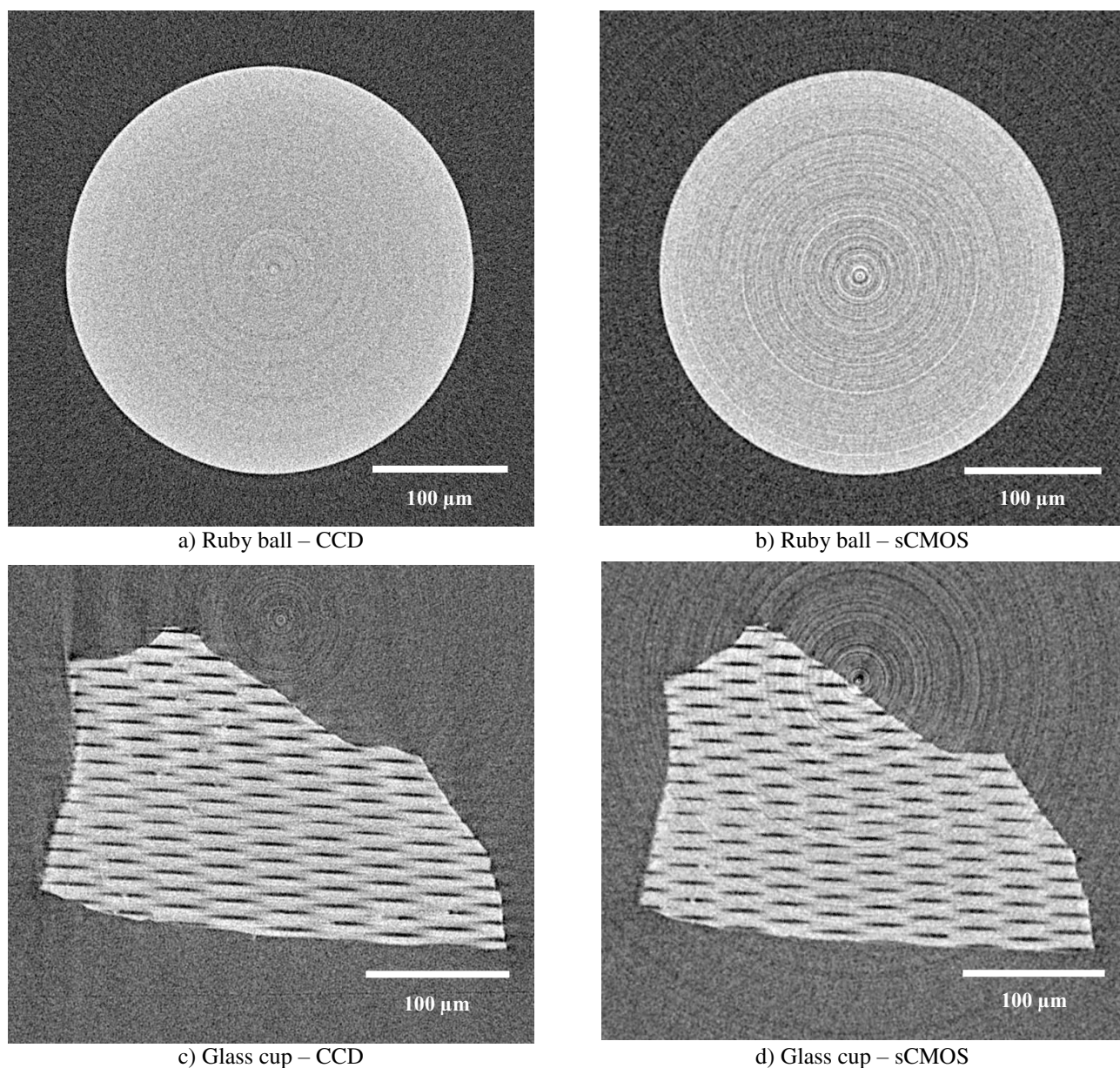c) Glass cup – CCD

d) Glass cup – sCMOS

Figure 6: Comparison of raw CT images without any processing (no ring artifacts and noise reduction) acquired by tested cameras.

Table 4: Results of data quality analysis for acquired projection data.

	CCD				sCMOS		
	JIMA (exp. = 30 s)	JIMA (exp. = 60 s)	Ruby ball	Glass cup	JIMA (exp. = 30 s)	Ruby ball	Glass cup
CNR	7.07	10.15	28.83	28.80	10.51	17.75	25.52
SNR	8.73	9.10	3.53	51.0	6.89	3.17	9.60
C	0.56	0.61	1.0	0.14	0.72	1.0	0.48
VAR	3e-3	4e-3	1.85e-5	1.47e-4	0.01	1e-3	8.91e-4
SML	184.76	185.48	381.94	280.53	164.25	3778.60	137.63
JNB	1.39	2.61	0.98	2.09	3.20	0.63	2.75

Table 5: Results of data quality analysis for tomographic data.

	CCD		sCMOS	
	Ruby ball	Glass cup	Ruby ball	Glass cup
CNR	6.15	4.44	6.11	4.41
SNR	79.28	278.15	26.63	26.06
C	0.08	0.03	0.39	0.40
VAR	1.98e-4	1.03e-4	2e-3	0.01
SML	1158.71	106.31	1682.12	519.72
JNB	7.89	4.52	6.94	5.13

4 Conclussion

In this study comparison of CCD and sCMOS based detectors in field of high resolution computed tomography imaging using laboratory-based CT system was conducted. For data acquisition Rigaku Nano3DX system was used. Both detector types were compared in terms of their properties and also acquired data quality and noise properties. For that, image data of phantoms as well as selected samples from material sciences were acquired and evaluated in projection and also tomogram domain. Acquired results showed that there were not negligible differences between both tested cameras, specifically in terms of noise properties, achieved spatial resolution and number of hot pixels. However, it was shown that sCMOS camera based detection system can be used for the task of submicron laboratory based X-ray Computed tomography. Specifically, it brings quality and noise properties improvements for low exposure time measurement scenarios compared to situation when CCD sensor is used.

References

[1] Gruner, S.M., Tate, M.W. and Eikenberry, E.F., Charge-coupled device area x-ray detectors. Review of Scientific Instruments, 2002, 73(8), pp.2815-2842.

[2] Mittone, A. et al. Characterization of a sCMOS-based high-resolution imaging system. Journal of Synchrotron Radiation, 2017, 24(6), pp.1226-1236.

[3] Rigaku Corporation, Nano3DX – X-ray microscope, https://www.rigaku.com/en/products/xrm/nano3dx, 2018 (accessed 6 December 2018).

[4] Rigaku Corporation, Compact two-dimensional CCD detector, https://www.rigaku.com/en/products/detectors/micron, 2018 (accessed 6 December 2018)

[5] Rigaku Corporation, Compact two-dimensional sCMOS detector, https://www.rigaku.com/en/products/detectors/micron-cmos, 2018 (accessed 6 December 2018).

[6] W. Van Aarle, W J. Palenstijn, J. Cant, E. Janssens, F. Bleichrodt, A. Dabravolski, J. De Beenhouwer, K. J. Batenburg, and J. Sijbers. Fast and Flexible X-ray Tomography Using the ASTRA Toolbox. Optics Express, 2016, vol. 24, no. 22, pp. 25129-25147.

[7] Dussault, D., Dereniak, E.L, Sampson, R. E., Hoess, P. and Johnson, C. B. Noise performance comparison of ICCD with CCD and EMCCD cameras. 2004-10-21, pp. 195-205. DOI: 10.1117/12.561839.

[8] Friedman, S.N. et al., A simple approach to measure computed tomography (CT) modulation transfer function (MTF) and noise-power spectrum (NPS) using the American College of Radiology (ACR) accreditation phantom. Medical Physics, 2013, 40(5).

[9] IEC 62220-1:2003(E), Medical electrical equipment – Characteristics of digital X-ray imaging devices – Part 1: Determination of the detective quantum efficiency. International Electrotechnical Commission, 2003, Switzerland.

[10] YU, Jonathan, Francisco IMAI, Nitin SAMPAT, David J. COLLINS, Alireza YASAN, Feng XIAO, Sanghoon BAE and Shri RAMASWAMI. Hot pixel reduction in CMOS image sensor pixels. 2010, 7537

[11] X-RAY WorX, JIMA RT RC-02B Resolution test, https://www.x-ray-worx.com/x-ray-worx/index.php/en/microfocus-x-ray-tubes-overview/jima-resolution-test/jima-rt-rc-02b-resolution-test, 2018 (accessed 6 December 2018)

[12] ASTM E1695-95(2013), Standard Test Method for Measurement of Computed Tomography (CT) System Performance, ASTM International, West Conshohocken, PA, 2013, www.astm.org

[13] Kraemer, A., Kovacheva, E. and Lanza, G. Projection based evaluation of CT image quality in dimensional metrology. Digital Industrial Radiology and Computed Tomography (DIR 2015). Belgium, Ghent, 2015.